

Preparation of calcium carbonate particles for application in natural rubber composites

Khansinee Longkaew

▶ **To cite this version:**

Khansinee Longkaew. Preparation of calcium carbonate particles for application in natural rubber composites. Polymers. Le Mans Université; Mahidol University (Bangkok, Thaïlande), 2024. English. ⟨NNT : 2024LEMA1003⟩. ⟨tel-05437658⟩

HAL Id: tel-05437658

https://theses.hal.science/tel-05437658v1

Submitted on 2 Jan 2026

HAL is a multi-disciplinary open access archive for the deposit and dissemination of scientific research documents, whether they are published or not. The documents may come from teaching and research institutions in France or abroad, or from public or private research centers.

L'archive ouverte pluridisciplinaire **HAL**, est destinée au dépôt et à la diffusion de documents scientifiques de niveau recherche, publiés ou non, émanant des établissements d'enseignement et de recherche français ou étrangers, des laboratoires publics ou privés.



HAL Authorization

COLLEGE DOCTORAL PAYS DE LA LOIRE
ED MATIERE, MOLECULES MATERIAUX ET GEOSCIENCES

Le Mans Université

Mahidol University

THESE DE DOCTORAT

DE
LE MANS UNIVERSITE ET MAHIDOL UNIVERSITY

ECOLE DOCTORALE N° 596
Matière, Molécules, Matériaux et Géosciences
Spécialité : *Chimie et Physico-chimie des polymères*

Par
Khansinee LONGKAEW

Preparation of calcium carbonate particles for application in natural rubber composites

Thèse présentée et soutenue à Bangkok, Thaïlande, le 28 Mars 2024
Unité de recherche : : Institut des Molécules et Matériaux du Mans, UMR CNRS 6283, Avenue Olivier Messiaen, 72085 Le Mans Cedex 09, France
Department of Chemistry, Faculty of Science, Mahidol University
272 Rama VI road, Bangkok 10400, Thaïlande

Thèse N° : 2024LEMA1003

Rapporteurs avant soutenance :

Sophie BISTAC	Professeur, Université de Haute Alsace, Mulhouse
Chor. Wayakron PHETPHAISIT	Assoc. Prof. Dr, Naresuan University, Thaïlande

Composition du Jury :

Président :	Jareerat RUAMCHAROEN	Asst. Prof. Dr., Prince of Songkla University, Thaïlande
Examinateurs :	Philippe DANIEL	Professeur, Le Mans Université, Le Mans
	Preeyanuch JUNKONG	Asst. Prof. Dr., Mahidol University, Thaïlande
Dir. de thèse :	Alain GIBAUD	Professeur, Le Mans Université, Le Mans
Co-dir. de thèse :	Pranee PHINYOCHEEP	Professeur, Mahidol University, Thaïlande

PREPARATION OF CALCIUM CARBONATE PARTICLES FOR APPLICATION IN NATURAL RUBBER COMPOSITES

KHANSINEE LONGKAEW

A THESIS SUBMITTED IN PARTIAL FULFILLMENT
OF THE REQUIREMENTS FOR
THE DEGREE OF DOCTOR OF PHILOSOPHY
(POLYMER SCIENCE AND TECHNOLOGY)
FACULTY OF GRADUATE STUDIES
MAHIDOL UNIVERSITY
BANGKOK, THAILAND

AND

ÉCOLES DOCTORALES
MATIÈRES, MOLÉCULES ET MATÉRIAUX
LE MANS UNIVERSITÉ
LE MANS, FRANCE
2024

Thesis
entitles

PREPARATION OF CALCIUM CARBONATE PARTICLES FOR APPLICATION IN NATURAL RUBBER COMPOSITES

…….
Ms. Khansinee Longkaew
Candidate

…….
Prof. Alain Gibaud,
Doctorat de l'Université du Maine
(Physics)
Co-advisor

…….
Prof. Pranee Phinyocheep,
Ph.D. (Polymer Chemistry)
Major advisor

…….
Asst. Prof. Preeyanuch Junkong,
Ph.D. (Material and Life Science)
Co-advisor

…….
Assoc. Prof. Taweechai Amornsakchai,
Ph.D. (Polymer Physics)
Program Director
Doctor of Philisophy in
Polymer Science and Technology
Faculty of Science
Mahidol University

…….
Prof. Chartchalerm Isarankura-Na-Ayudhya,
Ph.D. (Medical Technology)
Dean
Faculty of Graduate Studies
Mahidol University

Thesis
entitles

PREPARATION OF CALCIUM CARBONATE PARTICLES FOR APPLICATION IN NATURAL RUBBER COMPOSITES

was submitted to the Faculty of Graduate Studies, Mahidol University
for the degree of Doctor of Philosophy (Polymer Science and Technology)
and
Institut des Molécules et Matériaux du Mans, Le Mans Université
for the doctoral degree in Material Science
on
March 28th, 2024

…….
Ms.Khansinee Longkaew
Candidate

…….
Prof. Alain Gibaud,
Doctorat de l'Université du Maine
(Physics)
Member

…….
Asst. Prof. Jareerat Ruamcharoen,
Ph.D. (Polymer Science and
Technology)
Chair

…….
Prof. Philippe Daniel,
Doctorat de l'Université du Maine
(Physics)
Member

…….
Prof. Pranee Phinyocheep,
Ph.D. (Polymer Chemistry)
Member

…….
Prof. Sophie Bistac,
Doctorat de Université de Haute Alsace
(Physical Chemistry)
Member

…….
Asst. Prof. Preeyanuch Junkong,
Ph.D. (Materials and Life Science)
Member

…….
Assoc. Prof. Chor.Wayakron
Phetphaisit,
Ph.D. (Polymer Science and
Technology)
Member

…….
Assoc. Prof. Prasit Suwannalert,
Ph.D. (Pathobiology)
Dean
Faculty of Science
Mahidol University

…….
Prof. Chartchalerm Isarankura-Na-
Ayudhya,
Ph.D. (Medical Technology)
Dean
Faculty of Graduate Studies
Mahidol University

ACKNOWLEDGEMENTS

First of all, I would like to express my sincere gratitude and appreciation to my great major advisor, Prof. Pranee Phinyocheep, for her valuable guidance, excellent supervision, providing me with many opportunities, and powerful encouragement throughout this research. I equally express my sincere gratefulness to my co-advisor, Prof. Alain Gibaud for his professional vision, and kind supervision, for providing many opportunities in lab work and also for his kindness in taking care during my stay at Le Mans University, France. Their professional visions provided me with many experiences for various practical skills which inspired, useful, and encouraged me for my further career.

My appreciation is also given to Prof. Philippe Daniel for his valuable suggestions and support during my research work at Le Mans University, in particular for his supervision of vibrational spectroscopy.

I want to thank Assoc. Prof. Chor. Wayakron Phetphaisit, and Prof. Sophie Bistac for being examiners and Asst. Prof. Dr. Jareerat Ruamcharoen for being chair of the examination committee. Their valuable suggestions to accomplish my thesis are very much appreciated.

I also would like to express my special gratitude to my co-advisor and committee in my thesis defense, Asst. Prof. Preeyanuch Junkong, for the valuable suggestions and comments to complete this research. I wish also to express my sincere thanks to Assoc. Prof. Taweechai Amorsakchai for valuable suggestions during the thesis proposal examination.

I am sincerely grateful to the Sritrangthong Scholarship from the Faculty of Science, Mahidol University for providing financial support throughout my Ph.D. study in Thailand, together with ERASMUS+ (2019-1-FR01-KA107-062076) for my stay at Le Mans University.

Furthermore, I would like to thank all lecturers and staff members from both universities: the Polymer Science and Technology Program at the Department of Chemistry, and Rubber Technology Research Center, Faculty of Science, Mahidol University, and scientific staff member from Le Mans University, for all knowledge and facilities through my research work. Last but not least, I would like to thank my good colleagues from PP Lab members for their help, and time spent together in the laboratory with borderless friendships.

Finally, I would like to express my deepest thanks to my Longkaew family for their infinite encouragement. The endless value and usefulness of this thesis, I dedicate to my father, my mother, my brothers and sister for their entire care and support to make me overcome the tough time.

Khansinee Longkaew

CONTENTS

	Page
ACKNOWLEDGEMENTS	**ii**
ABSTRACT	**iv**
LIST OF TABLES	**xi**
LIST OF FIGURES	**xiii**
LIST OF ABBREVIATIONS	**xxvi**
CHAPTER I INTRODUCTION	**1**
CHAPTER II OBJECTIVES	**5**
CHAPTER III LITERATURE REVIEWS	**8**
3.1 Calcium carbonate	8
3.1.1 Mechanism of calcium carbonate crystal growth formation	10
3.2 Polymorphic phase of calcium carbonate	12
3.2.1 Vaterite phase	14
3.2.1.1 Vaterite structure	14
3.2.1.2 Vaterite shape	16
3.2.1.3 Characterization of vaterite	18
3.2.1.4 Chemical and physical properties of vaterite	20
3.2.1.5 Application of vaterite	20
3.2.2 Aragonite phase	22
3.2.2.1 Aragonite structure	22
3.2.2.2 Aragonite shape	23
3.2.2.3 Characterization of aragonite	27
3.2.2.4 Physical properties of aragonite	28
3.2.2.5 Application of aragonite	29
3.2.3 Calcite phase	29

CONTENTS (cont.)

	Page
3.2.3.1 Calcite structure	29
3.2.3.2 Calcite shape	30
3.2.3.3 Characterization of calcite	33
3.2.3.4 Chemical and physical properties of calcite	34
3.2.3.5 Application of calcite	34
3.3 Synthesis method and its parameter in calcium carbonate particle	35
3.3.1 Synthetic methods	35
3.3.2 Synthetic parameters	37
3.3.2.1 Temperature	38
3.3.2.2 Supersaturation activity	39
3.3.2.3 Mixing mode or stirring rate	40
3.3.2.4 Solubility constant (K_{so})	42
3.3.2.5 Mixing time	44
3.3.2.6 Effect of additive or aqueous medium	46
3.3.3 $CaCO_3$ surface modification	48
3.4 Commercial or industrial calcium carbonate	51
3.4.1 Ground or grinded calcium carbonate (GCC)	51
3.4.2 Precipitated calcium carbonate (PCC)	51
3.5 Natural rubber (NR)	53
3.5.1 Composition and structure of natural rubber	53
3.5.2 Concentrated natural rubber latex	55
3.5.2.1 Evaporation	55
3.5.2.2 Creaming	56
3.5.2.3 Centrifugation	56
3.5.3 Natural rubber compounding	56
3.5.4 Vulcanization systems and components	57

CONTENTS (cont.)

Page

3.5.4.1 Rubber 59
3.5.4.2 Vulcanizing agent 59
3.5.4.3 Activator 59
3.5.4.4 Accelerator 60
3.5.5 Filler systems 65
3.6 Calcium carbonate filled rubber composite 72
3.6.1 $CaCO_3$ in natural rubber composite 72
3.6.2 $CaCO_3$ in synthetic rubber composite 75

CHAPTER IV MATERIALS AND METHODS 78

4.1 Materials 78
4.2 Instruments 80

Part I: Preparation and polymorphic characterization of calcium carbonate ($CaCO_3$) particles

4.3 Preparation of $CaCO_3$ powders 82
4.3.1 Preparation of spherical $CaCO_3$ 82
4.3.2 Preparation of bundle-liked $CaCO_3$ 83
4.3.3 Preparation of fiber $CaCO_3$ 83
4.4 Preparation of treated $CaCO_3$ powders 84
4.4.1 Preparation of olive soap 84
4.4.2 Preparation of treated spherical $CaCO_3$ 85
4.4.3 Preparation of treated bundle-liked $CaCO_3$ 85
4.4.4 Preparation of treated fiber $CaCO_3$ 86
4.5 Characterization of $CaCO_3$ particles 87
4.5.1 Morphology of $CaCO_3$ particles 87
4.5.2 Polymorphic phase of $CaCO_3$ particles 87
4.5.3 Chemical and physical properties of $CaCO_3$ powders 88

CONTENTS (cont.)

Page

4.5.4 Thermal property of $CaCO_3$ powders 88

Part II: Preparation of natural rubber (NR)/$CaCO_3$ composites and its mechanical properties

4.6 Preparation of NR/$CaCO_3$ composites 89

4.6.1 Preparation of pre-dispersed NR/$CaCO_3$ compounds 89

4.6.2 Preparation of NR/$CaCO_3$ vulcanizates 89

4.7 Characterization of NR/$CaCO_3$ composites 96

4.7.1 Determination of cure characteristics 96

4.7.2 Preparation of rubber vulcanizates 97

4.7.3 Chemical structure of NR/$CaCO_3$ composites 97

4.7.3.1 Fourier transform infrared spectroscopy (FTIR) 97

4.7.3.2 X-ray diffraction analysis (XRD) 97

4.7.3.3 X-ray fluorescence microscope (micro-XRF) 98

4.7.4 Thermal analysis of the rubber vulcanizates 98

4.7.4.1 Thermogravimetric analysis (TGA) 98

4.7.4.2 Differential scanning calorimeter (DSC) 98

4.7.5 Mechanical properties of rubber vulcanizates 98

4.7.5.1 Tensile properties 98

4.7.5.2 Tear properties 99

4.7.5.3 Hardness (Shore A) 100

CHAPTER V RESULTS AND DISCUSSION 101

Part I: Preparation and polymorphic characterization of calcium carbonate ($CaCO_3$) particles

5.1 Saponification of soap and its use as surface modification of $CaCO_3$ 101

5.2 Preparation of untreated and treated $CaCO_3$ 103

CONTENTS (cont.)

	Page
5.2.1 Physical appearance of precipitated solution and $CaCO_3$ powders	104
5.2.1.1 Precipitated solutions	104
5.2.1.2 $CaCO_3$ powders	105
5.2.2 Morphological features of $CaCO_3$ particles	105
5.2.2.1 Scanning electron microscope (SEM)	105
5.2.2.2 Transmission electron microscope (TEM)	111
5.2.2.3 Effect of solution viscosity on the particle size of spherical $CaCO_3$ powder	113
5.2.2.4 Brunauer, Emmett and Teller (BET) analysis	115
5.2.3 Polymorphic phases and chemical structure of $CaCO_3$ particles	117
5.2.3.1 X-ray diffraction (XRD)	118
5.2.3.2 Attenuated total reflection-Fourier infrared (ATR-FTIR) analysis	122
5.2.3.3 Raman spectroscopy	124
5.2.4 The wettability of $CaCO_3$ particles	126
5.2.4.1 Contact angle	126
5.2.5 Thermal property of $CaCO_3$ particles	129
5.2.5.1 Thermogravimetric analysis	129
Part II: Preparation of NR/$CaCO_3$ composites and their mechanical properties	
5.3 Chemical and physical properties of NR/$CaCO_3$ compound	132
5.3.1 Physical appearance of pre-dispersed NR/$CaCO_3$ and NR/CB compounds	132
5.3.1.1 Morphology of $CaCO_3$ in NR and water	135
5.3.2 Cure measurement of NR/$CaCO_3$ and NR/N330 compounds	138

CONTENTS (cont.)

	Page
5.3.3 Chemical and crystal characterization of NR/$CaCO_3$ composites	145
5.3.3.1 XRD analysis	145
5.3.3.2 ATR-FTIR analysis	147
5.3.4 Morphology of NR/$CaCO_3$ composites	149
5.3.5 Element distribution analysis of NR/$CaCO_3$ composites	151
5.4 Mechanical property of NR/$CaCO_3$ composites	155
5.4.1 Tensile strength	155
5.4.2 Elongation at break	164
5.4.3 Modulus	165
5.4.4 Tear strength	167
5.4.5 Hardness Shore A	167
5.5 Thermal properties of NR/$CaCO_3$ composites	168
5.5.1 Thermogravimetric analysis (TGA)	168
5.5.2 Differential scanning calorimeter (DSC)	171
5.6 Mechanical property of NR/$CaCO_3$ compared with NR/N330 Composites	173
5.6.1 Tensile strength of NR/N330 composite	175
5.6.2 Elongation at break of NR/N330 composite	176
5.6.3 Modulus of NR/N330 composite	178
CHAPTER VI CONCLUSIONS	**181**
REFERENCES	**187**
APPENDIX	**206**
BIOGRAPHY	**232**
ABSTRACT	**234**

LIST OF TABLES

Table		Page
2.1	Fillers used in this work	7
3.1	Assignment of the IR absorption and vibration bands of vaterite phase	19
3.2	Chemical and physical properties of vaterite phased $CaCO_3$	20
3.3	Assignment of the IR absorption bands of aragonite phase	28
3.4	Physical properties of aragonite phased $CaCO_3$	28
3.5	Assignment of the IR absorption bands of calcite phase	34
3.6	Chemical and physical properties of calcite phased $CaCO_3$	34
3.7	Temperature ranges of $CaCO_3$ crystals precipitation for different polymorphs	39
3.8	The K_{so} values of $CaCO_3$ polymorphs at 25^oC	43
3.9	Main features of sulphur and peroxide curing systems	58
3.10	Accelerators used in rubber industry	60
3.11	Types of vulcanization system used in rubber	64
3.12	Shape and aspect ratio of various fillers	66
3.13	Particle size and surface area of different type of carbon black	68
3.14	Grades, production processes, selected properties and uses of different types of CB	69
4.1	Information of chemicals and materials used in this work	78
4.2	Instruments used in this work	80
4.3	Mixing formulation of NR/$CaCO_3$ composites used in this study	90
4.4	Mixing schedule of NR/$CaCO_3$ composites used in this study	90
4.5	Composite formulations prepared in this work	92
5.1	Viscosity of the sucrose and reactant solutions	114
5.2	Average particle size and BET specific surface area of as-precipitated and commercial $CaCO_3$ powders	117
5.3	%Crystallinity of different types of $CaCO_3$ powders	122

LIST OF TABLES (cont.)

Table		Page
5.4	Specific IR wavenumber in cm^{-1} of $CaCO_3$ polymorphs	124
5.5	Raman peak maxima in cm^{-1} of polymorphic phases of $CaCO_3$	126
5.6	Contact angle and wettability of different type of $CaCO_3$ powders	129
5.7	Thermal decomposition temperature of different types of $CaCO_3$	131
5.8	ATR-FTIR peak assignment of NR in NR/$CaCO_3$	138
5.9	Cure characteristic of neat NR, NR/$CaCO_3$ and NR/CB composites	142
5.10	Results of tensile properties of NR/$CaCO_3$ composites at different types loading of $CaCO_3$	157
5.11	Glass transition temperature (T_g) of NR/$CaCO_3$ composites at filler loading 20 phr	172
5.12	Physical and chemical properties of N330 CB used in this study (From BIRLA N330 company)	173
5.13	Tensile properties of NR/N330 composites	174

LIST OF FIGURES

Figure		Page
3.1	Main calcium source from marine organism: crustacean shells, coral, shells, fishbones, red seaweed	9
3.2	Greater Ani Crotophaga major's egg shell: (a) recently laid egg with white vaterite coating intact, (b) natural abrasion of the vaterite coating during incubation and patches of the blue calcite shell underneath, (c) the removal of entire vaterite coating	9
3.3	Optical limestone extracted from the Aruma formation	10
3.4	Schematic of sphere vaterite $CaCO_3$ microparticle formation	10
3.5	Stage and pathways of precipitation processes	12
3.6	Schematic of crystallographic unit cells of (a) calcite, (b) isostructural dolomite (isostructural to calcite), (c) aragonite, and (d) vaterite	13
3.7	Schematic formation of $CaCO_3$ spherulites and the transformation amorphous phase to typical calcite	13
3.8	SEM images of the solid phases that form during the ACC phase to vaterite and calcite crystals: (a) amorphous calcium carbonate (ACC), (b, c) ACC and vaterite nanoaggregates, (d, e) vaterite nanoaggregates, (f) vaterite nanoaggregates and first calcite crystals, (g) calcite crystals attached to vaterite spheres with the development of growth steps on the calcite surface, (h) calcite growth steps and vaterite nanoparticulate subunits, and (i) calcite crystals with vaterite casts	14
3.9	Vertical projection of vaterite showing orientation of carbonate group (CO_3^{2-}) relative to calcium (Ca^{2+}) atoms	15
3.10	Vaterite unit cell structure	15
3.11	Proposed structures for the vaterite polymorph of $CaCO_3$	15

LIST OF FIGURES (cont.)

Figure		Page
3.12	SEM image of vaterite $CaCO_3$ particles at different magnifications	16
3.13	SEM images of (a) broken vaterite $CaCO_3$ particle and (b) inner structure structure of broken micro sphere presenting a hollow core, and (c) hollow vaterite $CaCO_3$	16
3.14	SEM images of ellipsoidal shape of vaterite $CaCO_3$	17
3.15	SEM image of (a, b) vaterite grain composed of 10 – 20 μm flakes, and (c, d) each flake is composed of numerous 1 μm hexagonal pieces	17
3.16	SEM images of flower-liked vaterite nanostructures at (a, b) low and (c) high magnification	17
3.17	Morphology of hexagonal shaped vaterite: (a) SEM image and (b) TEM image of an isolated hexagonal particle	18
3.18	XRD patterns of vaterite $CaCO_3$	18
3.19	FTIR spectrum of as-prepared vaterite $CaCO_3$ crystals	19
3.20	Raman spectrum of vaterite phase	19
3.21	Using of vaterite assited-$CaCO_3$ drug delivery	21
3.22	Enzyme superoxide dismutase (SOD) encapsulated in vaterite $CaCO_3$ crystals	21
3.23	(a) Proposed formation mechanism of $CaCO_3$ and (b) the optimal Cu^{2+} adsorption conditions for $CaCO_3$ in the study of the amount of adsorbent added	22
3.24	Orthorhombic, P*mcn* of aragonite unit cell (Calcium, carbon, and oxygen atoms represent as blue, ochre, and red spheres, respectively in the unit cell	22
3.25	Aragonite crystal structure: (a) schematic combination form structure, (b and c) crystal structure crystallographic directions	23
3.26	SEM images of aragonite synthesized under high pressure ultrasound	23

LIST OF FIGURES (cont.)

Figure		Page
3.27	SEM images of nano aragonite whisker $CaCO_3$ particles in the function of time at 25, 30, 40, and 50^oC	24
3.28	FE-SEM images of meso-rod aragonite synthesized under 70 – 80^oC	25
3.29	SEM, TEM images and electron diffraction patterns of (a) aragonite precipitated in one-pot synthesis or direct precipitation, and (b) precipitated aragonite from transformation route	26
3.30	Possible growth of needle-liked shape: (a) spiral growth begins at a dislocation on the crystal face, (b) possible shape of final crystal, (c) formation of a step induces rapid growth along the face, and step sweeps around in a spiral	26
3.31	XRD diffraction of aragonite crystals synthesized at 95^oC of mixing temperature	27
3.32	FTIR spectrum of aragonite crystals in the range of 600 – 1200 cm^{-1}	28
3.33	Crystal structure of the R3c space group of calcites $CaCO_3$ (CO_3 groups: carbon atoms represented as gray spheres, oxygen atoms as red spheres in 0001 trigonal planes) separated by layers of calcium atoms (pink spheres)	29
3.34	Growth process of a calcite crystal from a cubic-shaped seed particle	30
3.35	Growth rate of (a) spherical growth and (b) cubic growth	30
3.36	(a) SEM and (b) TEM image of calcite crystals	31
3.37	SEM images at (a) low, and (b) high magnification of calcite particles precipitated from 0.1 M of CO_3^{2-} and Ca^{2+} sources, 30^oC and 300 rpm	31
3.38	SEM images of calcite crystals at low and high magnification	31
3.39	SEM images at low and high magnification of (a, c) aragonite powders, and (b and d) calcite powders	32
3.40	TEM images and SAED single-crystalline of (a) needle-liked aragonite	32

LIST OF FIGURES (cont.)

Figure		Page
	particle, and (b) needle-liked calcite particle	
3.41	XRD pattern of calcite $CaCO_3$	33
3.42	FTIR spectrum of calcite $CaCO_3$	33
3.43	SEM image of calcite $CaCO_3$ particles in paper sheet	35
3.44	The main $CaCO_3$ synthesis methods: (a) the spontaneous precipitation method, (b) the slow carbonation method, (c) the reverse emulsion method, and (d) CO_2 bubbling method	37
3.45	Illustration of the (a) ‘‘chemical route’’ and the (b) ‘‘scCO_2 route’’ pathways for the synthesis of $CaCO_3$ vaterite particles	37
3.46	Schematic of synthesized factors controlling the polymorphic crystallization	38
3.47	Plots of abundance crystalline form of $CaCO_3$ polymorphs at the early metastable stage as a function of temperature	38
3.48	SEM and CXDI images of (a-c) initial $CaCO_3$ particles, and (d-f) $CaCO_3$ particles immerse in tap water	39
3.49	Schematic of $CaCO_3$ particle formation under different treatments: (a) ultrasonic agitation, (b) stirring with magnetic bar, and (c) control experiment without any treatment	41
3.50	Schematic representation of formation of spindly and spherical vaterite particles with and without stirring	41
3.51	SEM images of ellipsoidal $CaCO_3$ obtained at different stirring speed during synthesis	42
3.52	Solubility product of ACC and crystalline phase (vaterite, aragonite , calcite) at different temperature	43
3.53	Schematic Ostwald–Lussac step ripening processes occurring upon immersion of $CaCO_3$ polymorphs in water	44

LIST OF FIGURES (cont.)

Figure		Page
3.54	Gibbs free energy at 25^{o}C for ACC, vaterite, and calcite	44
3.55	Proposed schematic of multistage of $CaCO_3$ from ACC → vaterite → calcite crystallization pathway in the function of time	45
3.56	Schematic representation of the kinetic mechanisms of $CaCO_3$ formation	45
3.57	Sketch map of the growth process of various-morphology $CaCO_3$ crystals under different conditions in the presence of DTAB	46
3.58	The (a, b) SEM and (c-e) TEM images of vaterite hollow microspheres in the presence of PSS	47
3.59	Decrement of $CaCO_3$ particle size by using polyol as additive	47
3.60	Precipitated procedure of sphere $CaCO_3$ by using sucrose as aqueous medium resulting 0.4 μm in diameter	48
3.61	TEM images with water contact angle of ultra-hydrophobic $CaCO_3$, unmodified (left) and modified (right) with sodium oleate	49
3.62	Illustration of surface treatment process of superhydrophobic aragonite $CaCO_3$ coated on filter paper: (a) deposition of titania gel film filer paper, (b) prenucleation of $CaCO_3$ on surface of cellulose, (c) crystal growth process/polymorph transformation of $CaCO_3$, (d)surface modification of $CaCO_3$ by sodium stearate	49
3.63	Water droplets on (a) polished aluminum, and (b) superhydrophobic surface	50
3.64	Contact angle of $CaCO_3$ precipitated at 30 and 80^{o}C with and without soap	50
3.65	SEM images of GCC micro-particles	51
3.66	Steps of PCC nanoparticle precipitation	52
3.67	PCC Manufacturing: (1) Limestone bin, (2) Lime kiln, (3) Gas filter,	52

LIST OF FIGURES (cont.)

Figure		Page
	(4) Gas scrubber, (5) Calcium oxide bin and slaker with cooling, (6) Slaked lime tank, (7, 8) Precipitation reactors, (9) Prescreen tank, (10) Screening for unreacted calcium hydroxide, (11) Postscreen tank, (12) Filter press and dryer, and (13) Gas filter	
3.68	(a) SEM images of PPC typed $CaCO_3$ particles, and (b) TEM image of PCC nanoparticles	53
3.69	*Hevea brasiliensis* tree plantation and NR latex exuded from the tree	54
3.70	NR structure (*cis*-1,4 polyisoprene)	54
3.71	Proposed *Hevea* rubber particle model in the latex form	54
3.72	Strain-induced crystallization (SIC) of NR	55
3.73	Water droplet on NR surface	55
3.74	Types of tyres and (a) micro- and (b) macroscopic of tyre composites	57
3.75	Compositions by weight % of a tyre	57
3.76	Bridging bidentate of Zinc/stearate complex in sulfur crosslinking of rubber	59
3.77	Common vulcanization accelerator structures	61
3.78	Formation of a crosslinked molecular network of sulphur crosslink system in rubber or elastomeric materials	62
3.79	Sulphur vulcanization systems	62
3.80	Rheometer curve of vulcanization	64
3.81	Classification of fillers according to average particle size	65
3.82	The different levels of structure and chemical structure of carbon black: (a) TEM image of N660 carbon black, (b) schematic of a primary particle (cut in half to show the internal structure) that is composed of stacks of graphene sheets, and (c) depiction of the different chemical groups on a graphene sheet in CB along with possible defects in the sheet	67

LIST OF FIGURES (cont.)

Figure		Page
3.83	Physical and chemical interaction between silica, silane coupling agent and NR	71
3.84	SEM images of NCC with (a) spherical, (b) chain, (c) cubic shapes	73
3.85	Tensile strength and elongation at break of NR/NCC composites at different of NCC amounts	73
3.86	Mechanical properties of NR/$CaCO_3$ films at filler contents 0, 5, 10, 15, and 20 phr: (a) tensile strength, (b) modulus at 100%, (c) elongation at break, and (d) tear strength	74
3.87	SEM micrographs of fracture surface of (a) unfilled NR film and NR/$CaCO_3$ film with different filler loading: (b) 5, (c) 10, and (d) 20 phr	75
3.88	Plots of tensile strength and elongation of BR/nano-sized $CaCO_3$ composites at various $CaCO_3$ loading	77
3.89	(a) hardness and (b) crosslink density of SBR/CRr/CB and SBR/CRr/$CaCO_3$ blends	77
4.1	Schematic diagram for preparation of spherical $CaCO_3$ powders	82
4.2	Schematic diagram for preparation of bundle-liked $CaCO_3$ powders	83
4.3	Schematic diagram for preparation of fiber $CaCO_3$ powders	83
4.4	Schematic diagram for preparation of olive soap	84
4.5	Schematic diagram for preparation of treated spherical $CaCO_3$ powders	85
4.6	Schematic diagram for preparation of treated bundle-liked $CaCO_3$ powders	86
4.7	Schematic diagram for preparation of treated fiber $CaCO_3$ powders	86
4.8	Preparation of pre-dispersed NR/$CaCO_3$ compounds	89
4.9	Preparation of rubber/inorganic filler compound	91
4.10	Typical cure characteristic curve of vulcanized rubber compound	97

LIST OF FIGURES (cont.)

Figure		Page
4.11	Dimensions of a tensile specimen	99
4.12	Dimension of a tear specimen (Die B – ASTM D624)	100
5.1	Fatty acid composition of olive oil: oleic acid, linoleic acid, and palmitic ester	102
5.2	Proposed formation of (a) soap molecule structure and (b) soap molecules coated on the surface of $CaCO_3$ nanograin	103
5.3	Images of precipitated $CaCO_3$ powders: (a) untreated and (b) treated by soap after solution mixing of reactants	104
5.4	Physical appearance of $CaCO_3$ white powders: (a) after drying in an oven, and (b) storing $CaCO_3$ powders in vial or closed container	105
5.5	SEM images at low magnification (2500x, 10 µm scale bar) of $CaCO_3$ particles: (a) untreated spherical, (b) treated spherical, (c) untreated bundle-liked, (d) treated bundle-liked, (e) untreated fiber, (f) treated fiber, (g) NCC, (h) 9QQ, and (i) 4QC commercial $CaCO_3$	108
5.6	SEM images at high magnification (10000x, 1 µm scale bar) of $CaCO_3$ particles: (a) untreated spherical, (b) treated spherical, (c) untreated bundle-liked, (d) treated bundle-liked, (e) untreated fiber, (f) treated fiber, (g) NCC, (h) 9QQ, and (i) 4QC commercial $CaCO_3$	110
5.7	TEM images of $CaCO_3$ particles: (a) untreated spherical, (b) treated spherical, (c) untreated bundle-liked, (d) treated bundle-liked, (e) untreated fiber, (f) treated fiber, and (g) NCC commercial $CaCO_3$	112
5.8	Plot of shear rate and viscosity of 1.0 M $CaCl_2$ reactant solution in water medium and 50 wt% of sucrose mediums compared with pure 50 wt% of sucrose without reactant (in preparation of spherical $CaCO_3$ powder)	113
5.9	Plot of shear rate and shear stress of 50 wt% sucrose and 1M	114

LIST OF FIGURES (cont.)

Figure		Page
	$CaCl_2$ reactant in water and 50 wt% sucrose mediums (in preparation of spherical $CaCO_3$ particles)	
5.10	Polymer-liked structure of Ca^{2+} ions and sucrose structure	115
5.11	The (a) BET isotherm linear plot and (b) BET surface area values of obtained $CaCO_3$ (untreated and treated ones) together with commercial $CaCO_3$ (NCC)	116
5.12	The X-ray diffractograms of obtained and commercial $CaCO_3$ particles in the range of 20 – 40^o (Θ)	119
5.13	Rietveld refinement patterns of X-ray diffraction from MAUD software of $CaCO_3$ powders: (a) Untreated spherical, (b) Treated spherical, (c) Untreated bundle-liked, (d) Treated bundle-liked, (e) Untreated fiber, (f) Treated fiber, (g) NCC, (h) 9QQ, and (i) 4QC commercial $CaCO_3$	121
5.14	FTIR spectra of different types of $CaCO_3$ particles in the range of (a) 500 - 2500 cm^{-1}, (b) 1200 – 1700 cm^{-1}, and (c) 650 – 900 cm^{-1}	123
5.15	Raman spectra of (a) Untreated spherical, (b) treated spherical, (c) untreated bundle-liked, (d) treated bundle-liked, (e) untreated fiber, (f) treated fiber, (g) NCC commercial $CaCO_3$ particles	125
5.16	Contact angle of water droplet on the solid surface	127
5.17	Photographs of water droplets of (a) untreated spherical, (b) treated spherical, (c) untreated bundle-liked, (d) treated bundle-liked, (e) untreated fiber, (f) treated fiber, (g) NCC, (h) 4QC, and (i) 9QQ commercial $CaCO_3$ powders	128
5.18	TGA thermograms and derivative thermogravimetric curves of (a) untreated spherical, (b) treated spherical, (c) untreated bundle-liked, (d) treated bundle-liked, (e) untreated fiber, (f) treated fiber, (g) NCC, (h) 4QC, and (i) 9QQ commercial $CaCO_3$ powders	130
5.19	Photograph of a water droplet on NR vulcanizate sheet without filler	133

LIST OF FIGURES (cont.)

Figure		Page
5.20	Physical appearance of different types of pre-dispersed $CaCO_3$ in NR latex	134
5.21	SEM images at 1000x, 10 µm scale bar of (a) as-prepared untreated spherical $CaCO_3$, (b) spherical $CaCO_3$ dispersed in water, and (c) untreated spherical $CaCO_3$ incorporated in NR	136
5.22	(a) XRD diffractions of $CaCO_3$ particles in water and NR, and (b) XRD refinement deduced from the Rietveld analysis for MAUD software of $CaCO_3$ in water for calculating the percentage of polymorph transformation	137
5.23	ATR-FTIR spectra of $CaCO_3$ particles dispersing in water and NR in the range of (a) 500 – 4000 cm^{-1}, and (b) 680 – 780 cm^{-1}	138
5.24	Cure behaviors of rubber compounds: (a) NR/untreated spherical $CaCO_3$, (b) NR/treated spherical $CaCO_3$, (c) NR/untreated bundle-liked $CaCO_3$, (d) NR/treated bundle-liked $CaCO_3$, (e) NR/untreated fiber $CaCO_3$, (f) NR/treated fiber $CaCO_3$, (g) NR/NCC $CaCO_3$, (h) NR/4QC $CaCO_3$, (i) NR/9QQ $CaCO_3$, and (j) NR/N330	140
5.25	Physical appearance of neat NR, NR/$CaCO_3$, and NR/N330 CB sheets	144
5.26	The XRD diffractions of neat NR and NR/$CaCO_3$ composites at 20 phr Filler loading	146
5.27	The XRD patterns of neat NR, N330 carbon black and NR/N330 composite at 40 phr filler loading	147
5.28	ATR-IR spectra of neat NR and NR/$CaCO_3$ composites at filler loading 40 phr in the range of (a) 500 – 4000 cm^{-1}, (b) 850 – 890 cm^{-1}, And (c) 680 – 780 cm^{-1}	148
5.29	SEM images of tensile-fractured surface at 2500x, 10 µm scale bar of (a) Neat NR, (b) NR/untreated spherical $CaCO_3$, (c) NR/treated	150

LIST OF FIGURES (cont.)

Figure		Page
	spherical $CaCO_3$, (d) NR/untreated bundle-liked $CaCO_3$, (e) NR/treated bundle-liked $CaCO_3$, (f) NR/untreated fiber $CaCO_3$, (g) NR/treated fiber $CaCO_3$, (h) NR/NCC $CaCO_3$, (i) NR/4QC $CaCO_3$, and (j) NR/9QQ $CaCO_3$ composites	
5.30	XRF imaging and components analysis detailed element distribution images including Ca, Zn and S of NR/$CaCO_3$ composites at 5 phr filler loading	153
5.31	XRF imaging and components analysis detailed element distribution images including Ca, Zn and S of NR/$CaCO_3$ composites at 20 phr filler loading	154
5.32	Tensile strength of NR/$CaCO_3$ composites at different types and loading	160
5.33	Plots of tensile strain and tensile strength of NR/$CaCO_3$ composites at different types and filler loading of (a) 5, (b) 10, (c) 20, (d) 40, and (e) 60 phr	161
5.34	Plots of tensile strength values of NR/$CaCO_3$ composites at different types and loading of $CaCO_3$	163
5.35	Plots of tensile strength values of NR/$CaCO_3$ composites comparing the different shapes of filler and surface treatment: (a) NR/spherical $CaCO_3$, (b) NR/bundle-liked $CaCO_3$, (c) NR/fiber $CaCO_3$, and (e) NR/commercial (rhombohedral) $CaCO_3$ composites	164
5.36	Elongation at break of NR/$CaCO_3$ composites at different types and loading of $CaCO_3$	165
5.37	100% Modulus (M100) of NR/$CaCO_3$ composites at different types and loading of $CaCO_3$	166
5.38	300% Modulus (M300) of NR/$CaCO_3$ composites at different types and loading of $CaCO_3$	166

LIST OF FIGURES (cont.)

Figure		Page
5.39	Tear strength of NR/$CaCO_3$ composites at different types and loading of $CaCO_3$	167
5.40	Hardness (Shore A) of NR/$CaCO_3$ composites at different types and loading of $CaCO_3$	168
5.41	TGA thermograms of (a) neat NR, and NR/$CaCO_3$ composites at 60 phr (b) NR/Untreated spherical, (c) NR/Treated spherical, (d) NR/Untreated bundle-liked, (e) NR/Treated bundle-liked, (f) NR/Untreated fiber, (g) NR/Treated fiber, (h) NR/NCC, (i) NR/4QC, and (j) NR/9QQ composites	170
5.42	DSC thermograms of neat NR and NR/$CaCO_3$ (20 phr) composites in the range of (-80) – 80^oC, and (-70) – (-50) ^oC deducing the glass transition temperature (Tg) of rubber vulcanizates	172
5.43	Plots of tensile strain and tensile strength of NR/N330 composites	174
5.44	Tensile strength of NR/N330 carbon black composites compared with NR/untreated (spherical, bundle-liked and fiber shaped) $CaCO_3$ composites	175
5.45	Tensile strength of NR/N330 carbon black composite compared with NR/treated (spherical, bundle-liked and fiber shaped) $CaCO_3$ composites	176
5.46	Elongation at break of NR/N330 carbon black composites compared with different shapes of $CaCO_3$: spherical, bundle-liked and fiber filled rubber vulcanizates (a) NR/untreated $CaCO_3$, and (b) NR/treated $CaCO_3$ composites	177
5.47	M100 of NR/N330 CB composites and NR/$CaCO_3$ composites: (a) NR/untreated $CaCO_3$ and (b) NR/treated $CaCO_3$ composites	178
5.48	300% Modulus (M300) of NR/N300 composites and NR/$CaCO_3$ composites: (a) NR/Untreated $CaCO_3$, and (b) NR/Treated $CaCO_3$ composites	179

LIST OF FIGURES (cont.)

Figure		Page
5.49	Radar chart comparison the mechanical properties of NR/untreated fiber $CaCO_3$ and NR/N330 composites at filler content 10 phr including tensile strength, elongation at break, M100 and M300	180

LIST OF ABBREVIATIONS

α_v	Volumetric coefficient of thermal expansion
ν	Vibrational mode
A	Accelerator
ABS	Acrylonitrile-butadiene-styrene
ACC	Amorphous calcium carbonate
ATR-FTIR	Attenuated total-Fourier transform infrared
BET	Brunauer, Emmett and Teller
BR	Butadiene rubber
C_2H_6O	Ethanol
Ca^{2+}	Calcium cation
$CaCl_2$	Calcium chloride
$CaCO_3$	Calcium carbonate
$Ca(OH)_2$	Calcium hydroxide
CB	Carbon black
CBS	N-cyclohexyl-2-benzothiazole sulfonamide
CO_2	Carbon dioxide
CO_3^{2-}	Carbonate anion
CR	Chloroprene rubber
CRI	Cure rate index
DI	Deionized
DRC	Dry rubber content
DPG	1,3-diPhenyl guanidine
DSC	Differential scanning calorimeter
DOTG	1,3-di-o-tolylguanidine
DTAB	Dodecyltrimethylammonium bromide
DTG	Derivative thermogravimetric
EV	Efficient vulcanizing system

LIST OF ABBREVIATIONS (cont.)

GCC	Grounded/grinded calcium carbonate
HA	High ammonium
HNRL	High ammonia natural rubber latex
KOH	Potassium hydroxide
K_{so}	Solubility constant
Ksp	Solubility product constant
LA	Lauryl alcohol
MBS	2-(4-morpholinothio) benzothiazole
MCC	Calcium carbonate monohydrate
MDR	Moving die rheometer
M_H	Maximum torque
M_L	Minimum torque
N_2	Nitrogen gas
Na_2CO_3	Sodium carbonate
$NaHCO_3$	Sodium bicarbonate
NaOH	Sodium hydroxide
NCC	Nanocalcium carbonate
$(NH_4)_2CO_3$	Ammonium carbonate
NPCC	Nano-sized precipitated calcium carbonate
NR	Natural rubber
OAN	Oil absorption number on compressed sample
OH^-	Hydroxyl group
PCC	Precipitated calcium carbonate
PE	Polyethylene
phr	Part per hundred of rubber
PP	Polypropylene
PVC	Polyvinyl chloride

LIST OF ABBREVIATIONS (cont.)

PSS	Sodium poly(4-styrenesulfonate)
RCOONa	Sodium carboxylate
S	Supersaturation activity
S_8	Sulphur
SAED	Selected area electron diffraction
SAP	Saponification number
SBR	Styrene-butadiene copolymer rubber
$ScCO_2$	supercritical carbon dioxide
SEM	Scanning electron microscope
Si-747	3-mercaptopropyl-ethyoxyl-di(tridecyl-pentamethoxy)-silane
SIC	Strain-induced crystallization
SiO_2	Silica dioxide
SR	Synthetic rubber
TBBS	N-tertbutyl-2-benzothiazole sulfonamide
t_c90	Curing time
TEM	Transmission microscope
TMTD	Tetramethylthiuram disulfide
TMTM	Tetramethylthiuram monosulfide
Tg	Glass transition temperature
TGA	Thermogravimetric analysis
t_s2	Scorch time
XRD	X-ray diffraction
XRF	X-ray fluorescence microscope
ZDEC	Zinc diethyldithiocarbamate
ZnO	Zinc oxide

CHAPTER I
INTRODUCTION

Calcium carbonate ($CaCO_3$) is one of the abundant and versatile mineral materials. It is found in nature [1; 2] and can be obtained from synthetic methods [3; 4]. Generally, $CaCO_3$ can be found as an amorphous phase $CaCO_3$ (ACC), three anhydrous crystalline forms including vaterite, aragonite, and calcite, and two hydrated crystalline forms: calcium carbonate hexahydrate (ikaite) and calcium carbonate monohydrate (MCC). [5] The ACC is highly unstable and rapidly transforms into other metastable polymorphs such as vaterite and aragonite or the most thermodynamically stable calcite polymorph. [3] The different polymorphs of $CaCO_3$ of each anhydrous crystalline forms show different typical morphology. [6] The metastable or kinetically favored vaterite phase has a typical hexagonal or spheroidal shape or "framboid" particle. [7] Another metastable phase is aragonite exhibiting in rhombohedral or needle-liked shape. [8] The stable calcite phase is presented in a rhombohedral crystal. [6] Nonetheless, the abundance of each polymorph strongly depends on the reaction conditions. [3] There are four main $CaCO_3$ precipitation routes consisting of solution precipitation, reverse emulsion, slow carbonation, and carbon dioxide (CO_2) bubbling. [9] Among these synthesis methods, solution precipitation is the simplest method. The submicrometric vaterite particle (0.4 – 0.5 μm) with a spherical shape could be obtained by precipitation using sucrose as an aqueous medium. [10; 11] Additionally, the suitable temperature for synthesizing vaterite particles is in the range of 25 – 50^oC while aragonite $CaCO_3$ crystals are produced under high temperatures (60 – 90^oC). [12] The aragonite crystals with short needle-like particles agglomerated together were produced under the high temperature of the mixing system. [13] From thermodynamics viewpoint, the metastable phases could be transformed into higher stable phases when the $CaCO_3$ crystals were dispersed in water. [14] The long nanowire $CaCO_3$ with aragonite polymorphs could be synthesized via the polymorphic transformation route. The CO_2 bubbling or carbonation method is the main industrial method resulting in the nano-sized calcite $CaCO_3$ (NCC)

and is also called precipitated $CaCO_3$ (PCC). [15] Another commercial $CaCO_3$ widely used in industry is ground $CaCO_3$ (GCC). It is produced by grinding the limestone or rock into a micro-scale of particle size with broad particle size distribution. [16]

From these varieties of polymorphs and shapes of $CaCO_3$ crystals, $CaCO_3$ is widely used in various industrial fields. Generally, $CaCO_3$ limestone is used in construction [17] and there is a strong demand for abrasive or absorbent fillers in polymer materials to improve the rheological and mechanical properties. [18; 19; 20] Due to the unique porous property of spherical shape, high surface, non-toxicity, and non-biological concerns of vaterite $CaCO_3$, this polymorph is used in biomedical application or personal care such as drug delivery, encapsulation with protein or enzyme or growth factors. [21; 22; 23] The needle-liked shape of aragonite $CaCO_3$ is used as filler in materials to improve the mechanical properties. [24] Turning to the application of calcite $CaCO_3$, the rhombohedral crystals with white or colorless properties are used as additives for enhancing the brightness or porosity of paper. [19] Commercial or industrial $CaCO_3$ powders are often added to rubber materials as additives or diluents due to their cost-effectiveness. There are many approaches to incorporate $CaCO_3$ as filler in natural rubber (NR) or synthetic rubber (SR) vulcanizates.

Natural rubber (NR) is one of the most important elastomer materials which is widely used for the manufacturing of gloves for NR latex and tire manufacturing for solid NR. [25; 26] NR latex is tapped or freshly collected in colloidal form deriving from the rubber tree *Hevea brasiliensis*. [27] The key parameter to stabilize this colloidal form is a negative charge on the surface of rubber particles. [28] Practically, ammonia solution is commonly used to maintain the negative charges for the preservation of NR colloidal particles in latex. [29] NR has to be mixed with curing agents and fillers to improve its mechanical properties such as tensile strength, and hardness, especially in tire manufacturing. [25] Many fillers have the potential to improve the mechanical properties of a rubber material such as carbon black (CB), precipitated silica (SiO_2), clay or inorganic filler $CaCO_3$. [25; 30; 31] The particle size, shape, and surface area of filler play important factors in reinforcing capability. [30; 32; 33] Many researchers have indicated that the addition of CB and SiO_2 can be used as reinforcing fillers resulting in significant improvement in the mechanical properties of rubber composite. [34; 35] Meanwhile, $CaCO_3$ is categorized as a semi-reinforcing or

non-reinforcing filler. [32] The major drawback for $CaCO_3$ is its particle size in micro-scale or larger than 100 nm with no reinforcing efficiency. [36] Additionally, the mechanical property improvement of micro-scaled filler is comparably weaker than nanofillers. The filler with a particle size smaller than 100 nm has greater polymer-filler interaction. [37] For these reasons, it has been reported that $CaCO_3$ is widely used as an additive or diluent filler but not as a mechanical modifier. [32] However, $CaCO_3$ remains a good option as an additive filler in some applications due to its cost-effectiveness and processability. [38] The percentage of micro-scaled $CaCO_3$ particles in rubber is in the range of 10 – 50% resulting in a weaker mechanical property than nano-scaled $CaCO_3$. [30; 32] The significant increase in specific surface area and interfacial adhesion of nano-$CaCO_3$ results in the enhancement of the mechanical property of rubber. [30] The particle size of filler is not only an important factor on the mechanical property of rubber but the compatibility between polymer matrix and filler is also concerned. [39] Due to the hydrophilicity of the $CaCO_3$ surface, it becomes more difficult to interact with the non-polar or hydrophobic properties of NR. Some attempts have been made to improve or change the surface of fillers such as using a silane coupling agent for SiO_2 filler [40] or incorporating oily chemicals into $CaCO_3$ filled NR compounds. [41] The results have shown that the degree of dispersion and rubber to modified-filler interactions were enhanced resulting in improved mechanical properties. [41] Based on these findings, up to now, the study of the incorporation of different aspect ratios, different shapes, and surface treatment of synthesized $CaCO_3$ powders in NR composite has still not been reported in the scientific literature.

According to the above reasons, we precipitated different shapes including spherical, bundle-liked, and fiber of $CaCO_3$ together with surface treatments labelled untreated hydrophilic and treated hydrophobic $CaCO_3$ particles under different precipitating procedures. The polymorphic phase, morphological shape, and other properties of as-prepared $CaCO_3$ particles were examined. Furthermore, the incorporation of different types of $CaCO_3$ in NR/$CaCO_3$ composites was extensively studied in mechanical behaviors. In this research, we pointed out which type of $CaCO_3$ filler could provide the reinforcing efficiency. The micro- and nano-$CaCO_3$ in commercial were also compared and used in this work. Moreover, the NR/carbon black

composites were also prepared at the same variation of filler loading as $CaCO_3$ for comparison.

To sum up, this work focused not only on the procedure of precipitation of different types of $CaCO_3$ but also on studying the mechanical properties of $CaCO_3$ in NR composites as a reinforcing agent to broaden the application of $CaCO_3$ in the future. These different types of $CaCO_3$ should pave the way to widen or broaden the applications to improve the mechanical properties of polymers.

CHAPTER II
OBJECTIVES

This research aims to study the synthesis of different shapes, aspect ratios, and surface treatments of calcium carbonate ($CaCO_3$) particles by using olive soap. The use of prepared $CaCO_3$ as reinforcing fillers in natural rubber (NR) composites was also investigated. Normally, particle size, shape, aspect ratio and surface property of the filler play important roles and are directly related to the mechanical properties of the NR/$CaCO_3$ composites. Furthermore, the NR is hydrophobic due to its cis-1,4-polyisoprene structure while $CaCO_3$ particles are hydrophilic. In this work, $CaCO_3$ particles without and with surface modification to hydrophobic character were included in NR and their mechanical behavior was studied. In addition, commercial $CaCO_3$ powders in nano (NCC) and micro-scale (4QC and 9QQ) were added into NR to compare their mechanical properties with the prepared $CaCO_3$. Moreover, commercial carbon black (grade N330) was used as a reinforcing filler in NR for comparison. The mechanical and other properties of NR/$CaCO_3$ were also assessed.

The scope of this research has been divided into two parts as below.

Part I: Preparation and polymorphic characterization of $CaCO_3$ particles

1.1 Preparation of $CaCO_3$ particles

In this part, $CaCO_3$ particles in different shapes: spherical, bundle-liked, and fiber were prepared through precipitation reaction and transformation pathway. The spherical and bundle-liked $CaCO_3$ precipitations were carried out under the direct mixing of CO_3^{2-} solution with Ca^{2+} solution as schematized in equation 2.1 with the different aqueous medium, mixing temperature and mixing speed. Fiber $CaCO_3$

particles were carried out by the transformation and recrystallization pathway of dried spherical shaped $CaCO_3$ to fiber shape under high temperature in water together with stirring.

$$Ca^{2+} + CO_3^{2-} \rightarrow CaCO_3 \text{ (s)} \quad (2.1)$$

1.2 Preparation of treated $CaCO_3$ particles

In this section, the surface of $CaCO_3$ particles (spherical, bundle-liked and fiber shapes) was modified by treating with olive soap. The soap was prepared via a saponification reaction of olive oil and sodium hydroxide (NaOH). The soap solution was added to the reactants before the precipitation started using a similar pathway to Part 1.1.

1.3 Polymorphic characterization

The morphological shape of obtained $CaCO_3$ was analyzed by scanning electron microscopy (SEM) and transmission electron microscopy (TEM) to measure the particle size resulting aspect ratio. The polymorphic phase of the crystals and chemical structure of $CaCO_3$ powders were characterized using X-ray diffraction (XRD), the attenuated total reflection-Fourier transform infrared (ATR-FTIR) and Raman spectroscopy. The % crystallinity of the polymorphs (vaterite, aragonite and calcite) was calculated by MAUD software based on Rietveld refinement. The wettability of the powder was determined as hydrophobic or hydrophilic using contact angle. To measure the porosity and the surface area of powders, the Brunauer, Emmett and Teller (BET) analysis technique was investigated. The thermal decomposition temperature of $CaCO_3$ powder was assessed using thermogravimetric analysis (TGA).

Part II: Preparation of NR/$CaCO_3$ composites and their mechanical properties

In this part, the reinforcing efficacy of the prepared $CaCO_3$ to NR was investigated. The prepared $CaCO_3$ powders were incorporated into NR latex as presented in Table 2.1. The amount of filler was varied as 5, 10, 20, 40 and 60 phr

compared to neat NR. The curing ingredients were added to NR/$CaCO_3$ composites, including ZnO 1.8 phr, stearic acid 2.0 phr, CBS 1.0 phr and sulfur 1.5 phr.

Table 2.1 Fillers used in this work

No	Filler	Filler type	Name of filler
1	**$CaCO_3$**	Synthesized	Untreated spherical $CaCO_3$
2			Untreated bundle-liked $CaCO_3$
3			Untreated fiber $CaCO_3$
4			Treated spherical $CaCO_3$
5			Treated bundle-liked $CaCO_3$
6			Treated fiber $CaCO_3$
7		Commercial	Nano $CaCO_3$ (NCC)
8			4QC
9			9QQ
10	**Carbon black (CB)**	Commercial	N330

The cure measurement of composites was measured using a Moving die rheometer (MDR). The morphological aspect of the prepared NR/$CaCO_3$ composites was observed using the SEM technique. Several techniques were used to assert the chemical and crystallographic structure of as-prepared $CaCO_3$ particles in NR, including XRD, ATR-FTIR and Raman spectroscopy. The mechanical properties including tensile properties (modulus, tensile strength, elongation at break and tear), and hardness (Shore A) of NR/$CaCO_3$ and NR/N330 composites were investigated. The TGA and differential scanning calorimeter (DSC) were used to analyze the thermal analysis of NR/$CaCO_3$ vulcanizates.

CHAPTER III
LITERATURE REVIEWS

In this research, the reinforcing efficiency of different shapes, sizes, aspect ratios and polymorphic phases of calcium carbonate ($CaCO_3$) in natural rubber (NR) are focused, together with the modification of $CaCO_3$ surface filled in NR. This chapter was categorized into seven main topics relative to the general introduction of calcium carbonate, polymorphic phase of calcium carbonate, synthesis method and its parameter on calcium carbonate, commercial and industrial calcium carbonate, application of calcium carbonate, natural rubber and calcium carbonate filled natural rubber composites.

3.1 Calcium carbonate

Calcium carbonate ($CaCO_3$) is one of the most abundant minerals which can exist in nature such as crustaceans (Figure 3.1) [42; 43], fish organs (Figure 3.1) [43; 44] eggshells (Figure 3.2) [45], and limestone (Figure 3.3) [46; 47]. It can be also obtained by synthetic methods [3; 4]. $CaCO_3$ exists mainly as six polymorphic phases: amorphous calcium carbonate (ACC), calcium carbonate monohydrate (MCC), calcium carbonate hexahydrate (ikaite), and three crystalline phases; vaterite, aragonite, and calcite. [5] From a thermodynamical point of view, calcite is the most stable phase among the other phases at ambient temperature and atmospheric pressure. Vaterite is the most unstable polymorph and kinetically favored while the ACC phase is also unstable and relatively short-lived phase. [3; 4] Due to its different types of polymorphs, $CaCO_3$ particles exhibit different morphological shapes. The typical shape of vaterite is hexagonal, spherulitic or framboid particle. Aragonite displays orthorhombic or needle-liked shapes. Calcite shows typical trigonal morphology. [48; 49; 50] Nevertheless, the shapes of these polymorphs can be changed or transformed by altering conditions and reaction methods. [51; 52] Due to its simple synthesis, non-toxicological concerns,

biocompatibility, and inexpensive cost [9], $CaCO_3$ is widely used in various industrial fields such as construction [17], medical treatment e.g., bone cement [53], bone scaffolds [54], bone tissue engineering [55], and dental implants [56]. In addition, $CaCO_3$ powders also have strong demand for use as filler, absorbent or abrasive in papers, paints, plastics, and rubbers aiming to improve the rheology, dilute the suing of raw materials as dilution, and improve some mechanical properties of products. [18; 19; 20]



Figure 3.1 Main calcium source from marine organism: crustacean shells, coral, shells, fishbones, red seaweed [43]

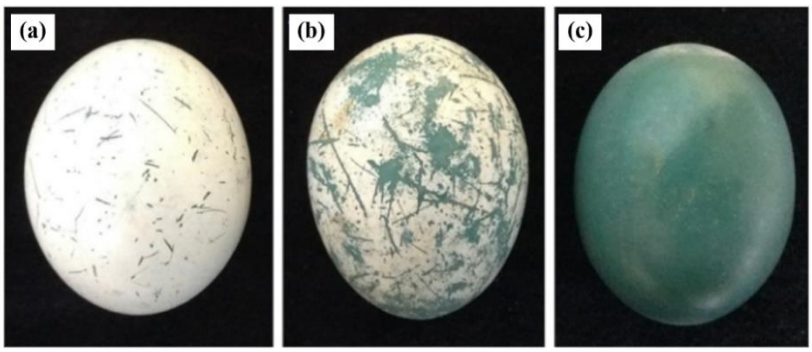


Figure 3.2 Greater Ani Crotophaga major's egg shell: (a) recently laid egg with white vaterite coating intact, (b) natural abrasion of the vaterite coating during incubation and

patches of the blue calcite shell underneath, (c) the removal of entire vaterite coating [45]



Figure 3.3 Optical limestone extracted from the Aruma formation [46]

3.1.1 Mechanism of calcium carbonate crystal growth formation

The formation of the solid phase of $CaCO_3$ occurs spontaneously through nucleation in a supersaturated solution. For the formation of primary polycrystalline vaterite spheres, Trushina et al. provided two explanations as follows. [57]

1. The nano-aggregation concept describes the rapid aggregation of initially formed nano-sized crystals resulting in the spherical vaterite schematized in Figure 3.4. According to the crystal growth theory, the precipitation starts from nucleation which initially forms nuclei that grow into crystallites.

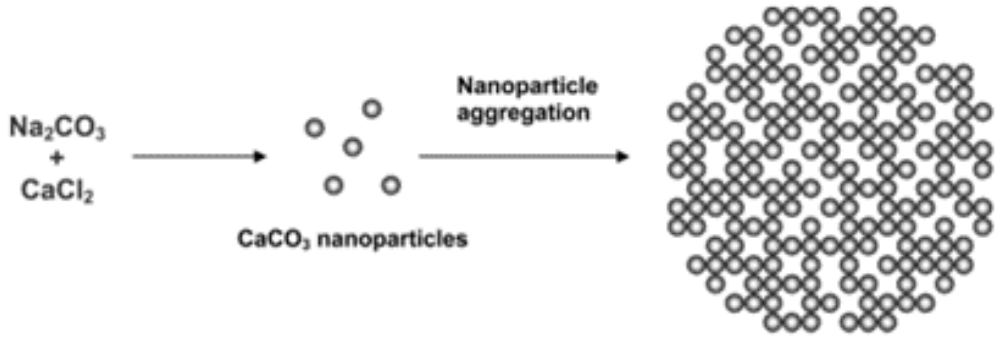


Figure 3.4 Schematic of sphere vaterite $CaCO_3$ microparticle formation [57]

2. The classical spherulite vaterite growth concept proposes the formation of a single nucleus followed by the branching of small crystals. Crystal growth is a complex process comprising two elementary processes which processes the following.

- Diffusion and/or convection of growth units through the bulk toward the crystal-solution surface
- Surface integration processed at the crystal-solution interface

The secondary changes would occur under equilibrium conditions. Theoretically, the precipitation will be terminated when one crystal is formed in equilibrium with the saturated solution. Nevertheless, in practice, the precipitation is completed when the crystal reaches a size that causes sedimentation. Ageing is the process that leads to equilibrium. At the early stage of the precipitate formation, several mechanisms probably occur including: dissolution of small particles, simultaneous growth of large particles, and recrystallization followed by coagulation, agglomeration, sintering change, and the initial dispersion of the system by formation of more stable large aggregates. [58] The stage and pathways of precipitation processes are presented in Figure 3.5.

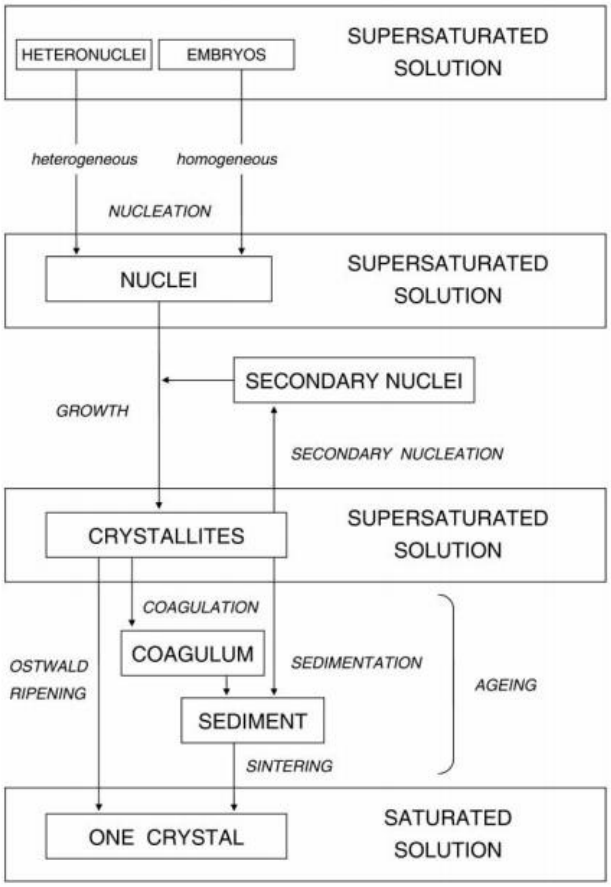


Figure 3.5 Stage and pathways of precipitation processes [58]

3.2 Polymorphic phase of calcium carbonate

The morphological shapes and crystal structure of $CaCO_3$ depend on the relative differences in the behavior of the in-plane and out-of-plane bending modes among different carbonate minerals unit cells as in Figure 3.6. [59] Under ambient condition, the less stable thermodynamically of vaterite phase, is transformed into the most stable calcite phase as depicted in Figure 3.7. [60] The SEM photomicrographs in Figure 3.8 revealed that ACC is obtained immediately after mixing and vaterite is crystallized after ACC, forming large aggregates. [50] When prolonging the crystallization, the amount of vaterite decreases and calcite crystals are formed on the surface of the vaterite aggregates. More details of polymorph structure, morphological appearance, characterization, chemical and physical properties, and applications of different $CaCO_3$ phases are explained in this section.

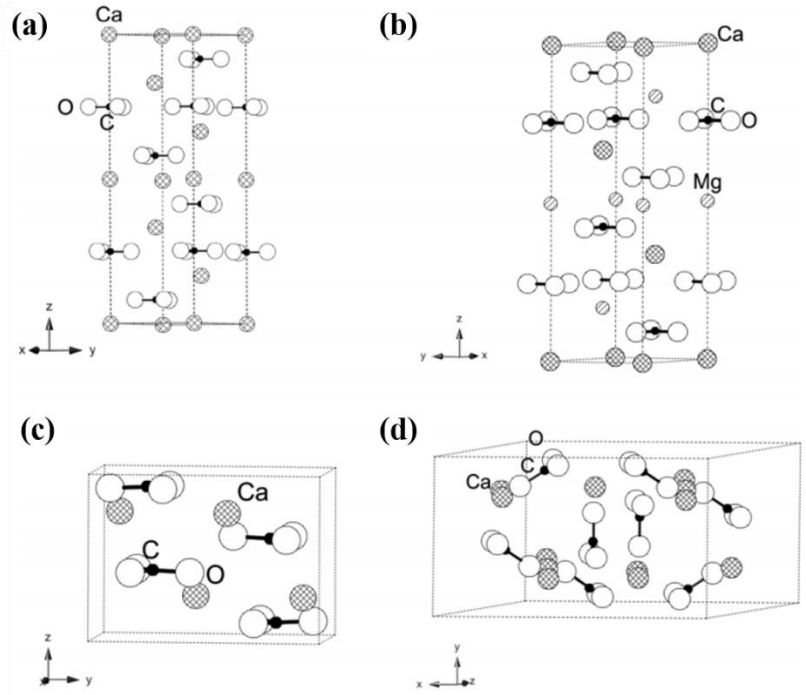


Figure 3.6 Schematic of crystallographic unit cells of (a) calcite, (b) isostructural dolomite (isostructural to calcite), (c) aragonite, and (d) vaterite [59]

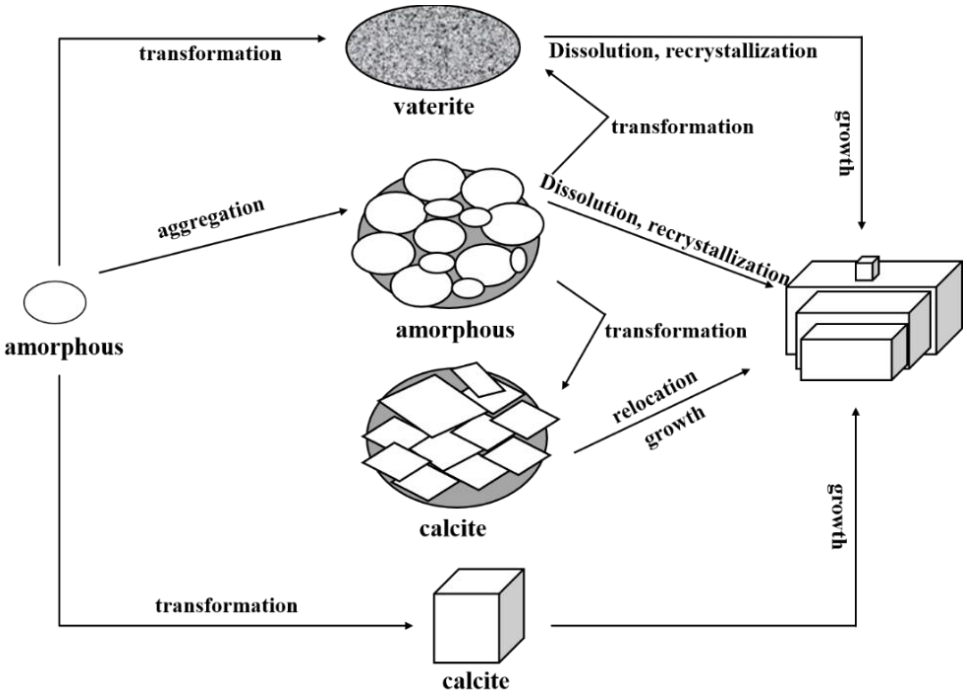


Figure 3.7 Schematic formation of $CaCO_3$ spherulites and the transformation from amorphous phase to typical calcite [61]

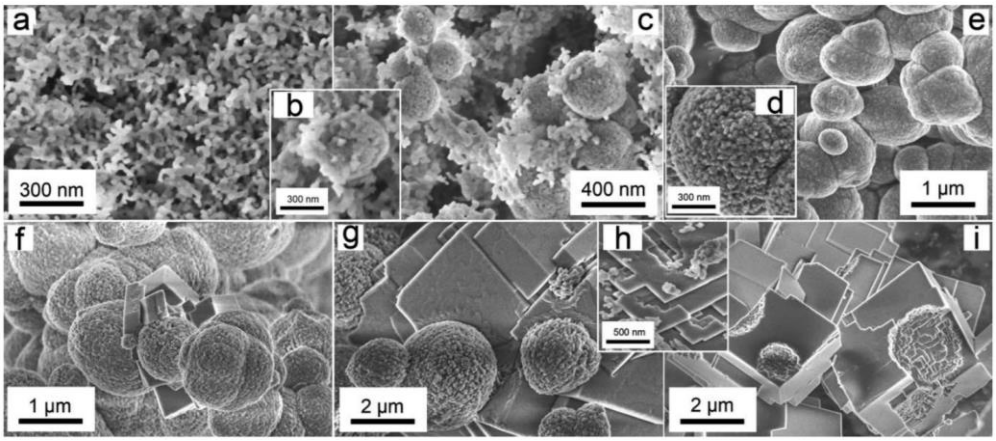


Figure 3.8 SEM images of the solid phases that form during the ACC phase to vaterite and calcite crystals: (a) amorphous calcium carbonate (ACC), (b, c) ACC and vaterite nanoaggregates, (d, e) vaterite nanoaggregates, (f) vaterite nanoaggregates and first calcite crystals, (g) calcite crystals attached to vaterite spheres with the development of growth steps on the calcite surface, (h) calcite growth steps and vaterite nanoparticulate subunits, and (i) calcite crystals with vaterite casts [51]

3.2.1 Vaterite phase

3.2.1.1 Vaterite structure

Vaterite is a thermodynamically metastable phase of $CaCO_3$. Normally, the synthesis of vaterite particles usually produces polycrystalline spheres. The most widely accepted fact is that the vaterite phase has a hexagonal crystal symmetry with and P63/mmc space group. [49; 61] Kamhi et al. presented the atomic arrangement constructed based on the symmetry elements of P63/mmc space group as Figure 3.9. [49] This model is occupied by calcium and one-third by carbonate group. From diffraction data, the structure of vaterite unit cell is presented in Figure 3.10 by Meyer et al. [62; 63] M. Burgess and coworkers used ^{43}Ca solid-state NMR spectroscopy to simulate the structure of the vaterite polymorph as shown in Figure 3.11. [64] The models are based on hexagonal ($P3_221$), monoclinic lattice (C2), or orthorhombic lattices.

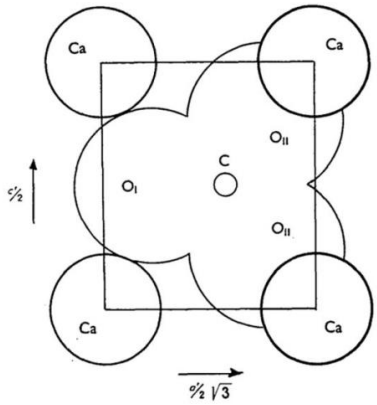


Figure 3.9 Vertical projection of vaterite showing orientation of carbonate group (CO_3^{2-}) relative to calcium (Ca^{2+}) atoms [49]

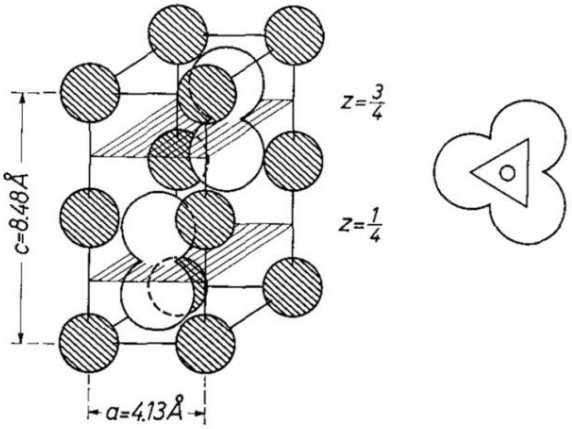


Figure 3.10 Vaterite unit cell structure [62]

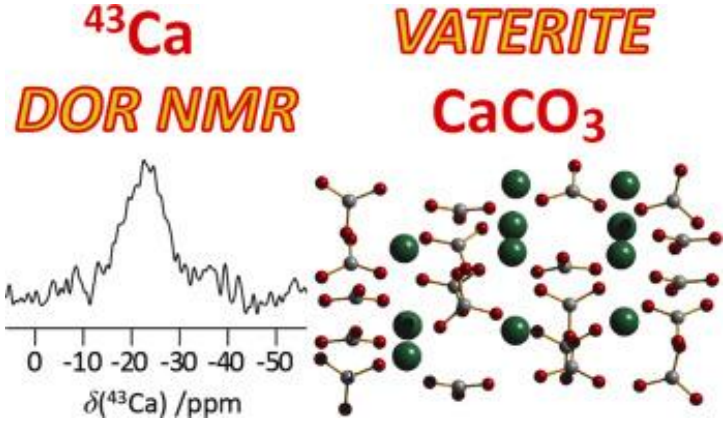


Figure 3.11 Proposed structures for the vaterite polymorph of $CaCO_3$ [64]

3.2.1.2 Vaterite shape

The morphological particle of $CaCO_3$ may display a great deal of variety. The main crystal structure of polycrystalline vaterite is hexagonal with typically a spherical crystal habit. This spherical form can be called “framboid” ((‘la framboise’ in French) (see Figure 3.12). [65] The sphere shape of the $CaCO_3$ particle is composed by self-assembly of the nanograin $CaCO_3$. Figure 3.13 shows the cross-section of broken $CaCO_3$ microparticle illustrating the internal structure with a specific channel-like structure formed or porous and high surface area of 8.8 ± 0.3 m^2/g. [66] Vaterite is only on phase of $CaCO_3$ polymorph which has unique porous properties.

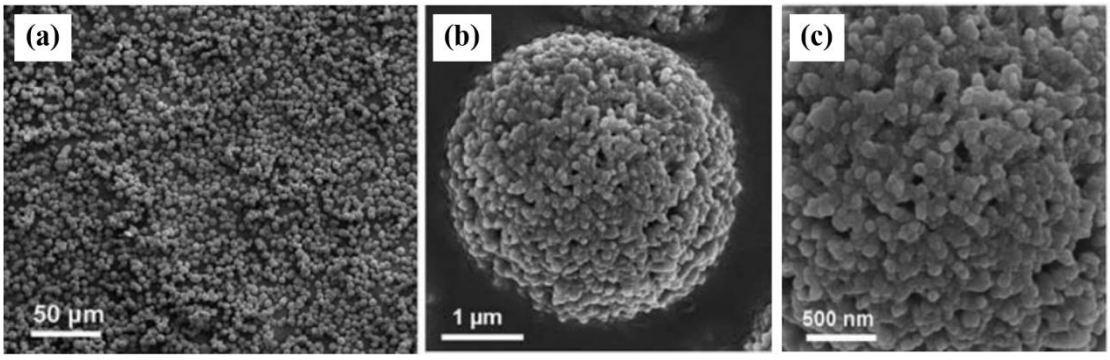


Figure 3.12 SEM image of vaterite $CaCO_3$ particles at different magnifications [65]

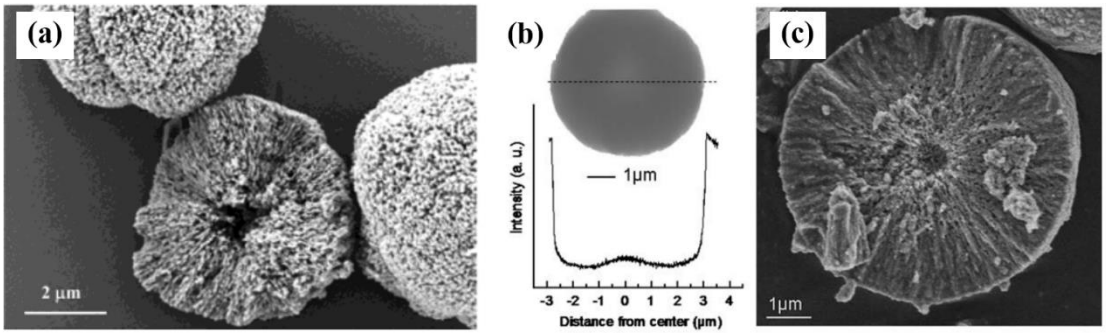


Figure 3.13 SEM images of (a) broken vaterite $CaCO_3$ particle [66] and (b) inner structure of broken micro sphere presenting a hollow core, and (c) hollow vaterite $CaCO_3$ [67]

Besides the typical spherical shape of vaterite, it often presents in a variety of shapes such as ellipsoidal (Figure 3.14) [68], flower-liked with flakes (Figure 3.15)

[69], flower-like (Figure 3.16) [70], and hexagonal (Figure 3.17). [61] These different particle shapes were prepared under different mixing conditions.

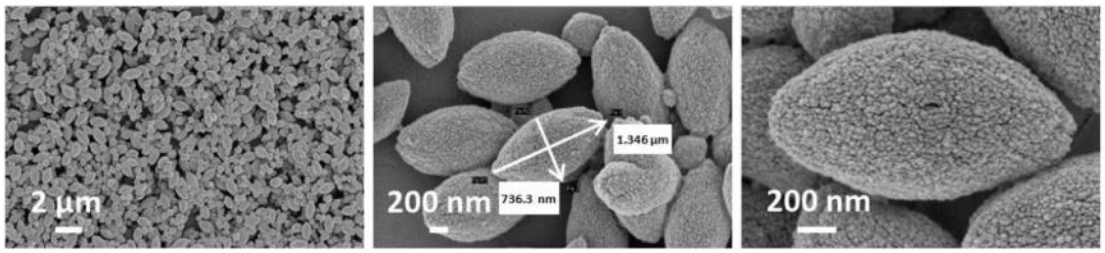


Figure 3.14 SEM images of the ellipsoidal shape of vaterite $CaCO_3$ [68]

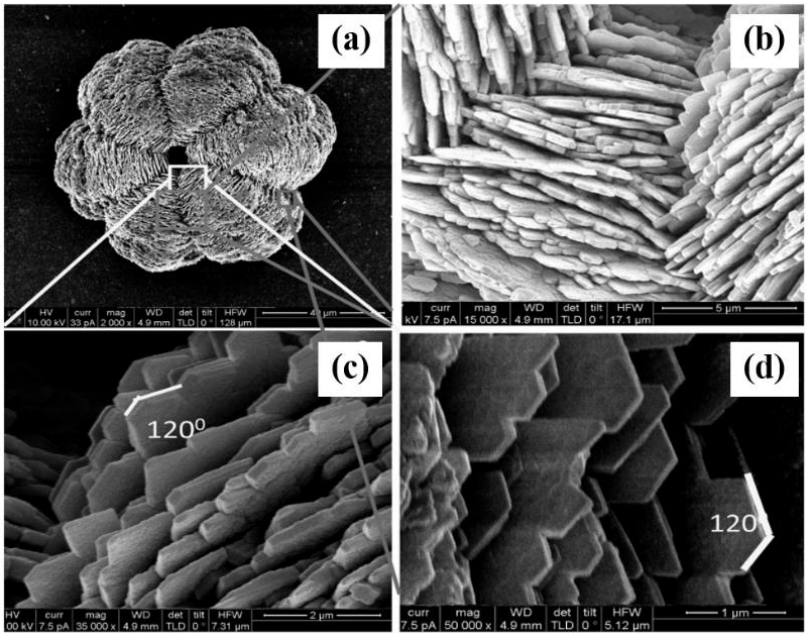


Figure 3.15 SEM image of (a, b) vaterite grain composed of 10 – 20 µm flakes, and (c, d) each flake is composed of numerous 1 µm hexagonal pieces [69]

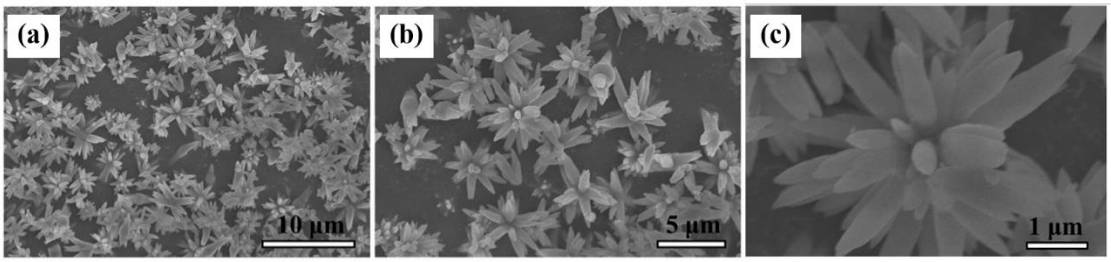


Figure 3.16 SEM images of flower-liked vaterite nanostructures at (a, b) low and (c) high magnifications [70]

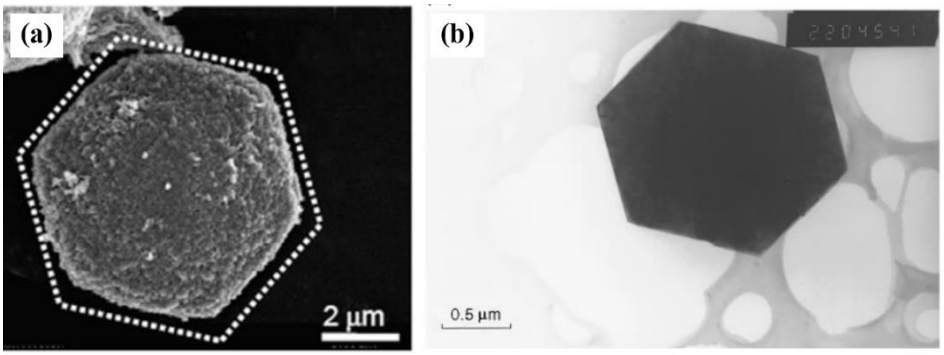


Figure 3.17 Morphology of hexagonal-shaped vaterite: (a) SEM image and (b) TEM image of an isolated hexagonal particle [61]

3.2.1.3 Characterization of vaterite

Due to its variety of morphological shapes of vaterite, the X-ray diffraction, FTIR and Raman spectroscopy are widely used to characterize the polymorphs of $CaCO_3$ for more exhaustive information.

The XRD patterns of vaterite in Figure 3.18 obtained from the synthesis of using 2.0 M of [Na_2CO_3] and 4.0 M of [$NaHCO_3$] in the presence of urea at 120 min. [70] The Bragg reflection peaks for the typical vaterite crystal located at 20.77, 24.70, 26.90, 32.60, 38.65, 43.65, 48.75, 49.70, and 55.50^o in 2Ɵ which were corresponding to (004), (110), (112), (114), (211), (300), (304), (118) and (224) crystallographic planes, respectively.

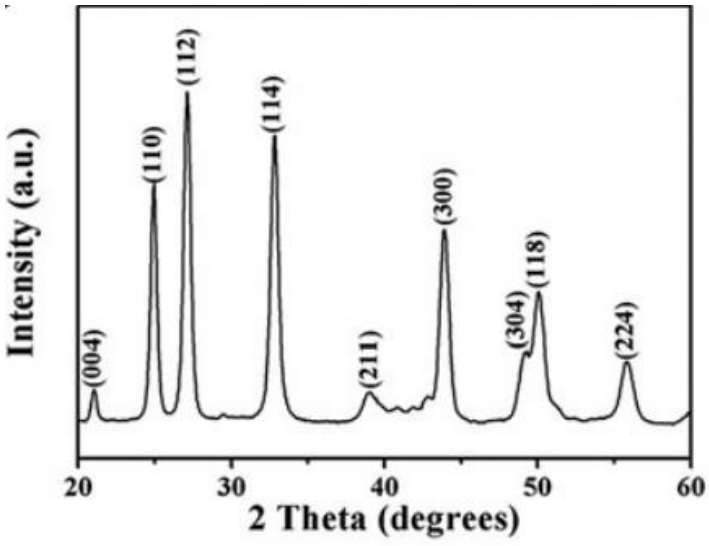


Figure 3.18 XRD patterns of vaterite $CaCO_3$ [70]

Figure 3.19 shows FT-IR spectrum of the absorption bands of typical vaterite located at 744.86, 877.02, 1085.31 and 1409.38 cm^{-1} corresponding to in-plane OCO deformation bending, CO_3 out-of-plane bending, symmetric C-O stretching, and C-O stretching, respectively. [70] The typical absorption bands of the different crystallographic of vaterite $CaCO_3$ are listed in Table 3.1. [61] Raman spectrum of vaterite is presented in Figure 3.20. [57]

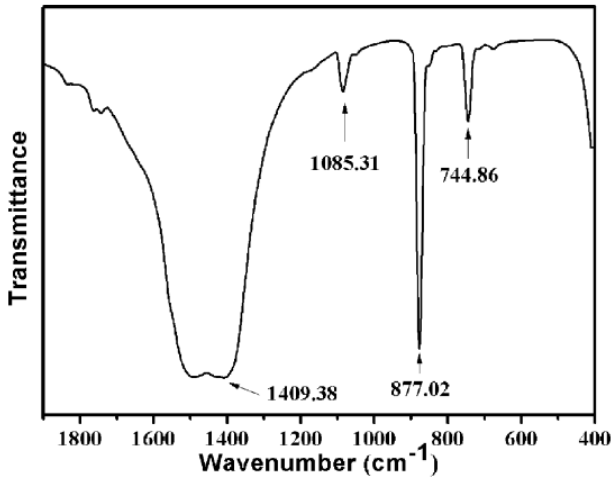


Figure 3.19 FTIR spectrum of as-prepared vaterite $CaCO_3$ crystals [70]

Table 3.1 Assignment of the IR absorption and vibration bands of vaterite phase [61]

Polymorph	**υ_1, cm^{-1}**	**υ_2, cm^{-1}**	**υ_3, cm^{-1}**
Vaterite	1087	877	745

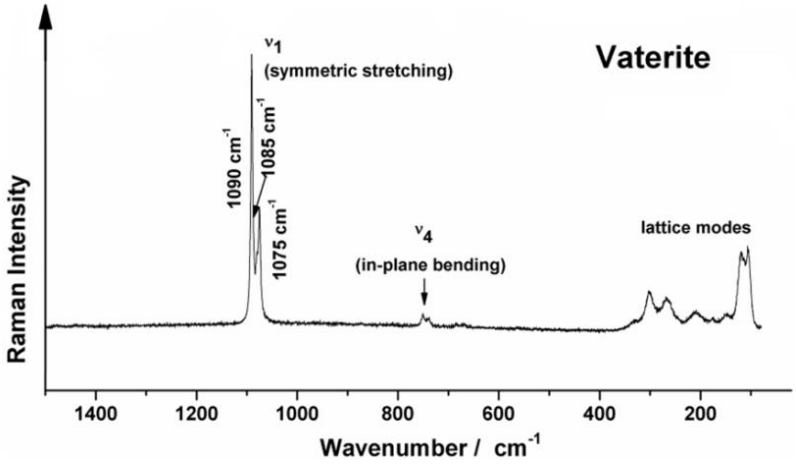


Figure 3.20 Raman spectrum of vaterite phase [57]

3.2.1.4 Chemical and physical properties of vaterite

The chemical and physical properties of vaterite are listed in Table 3.2. The mechanical property of synthesized vaterite particles were determined by nano-indentation analysis. [71] Naturally, the surface of $CaCO_3$ is hydrophilic. The values of the ζ-potential are negative which are -4 mV at pH 9.0 and - 26 mV at pH 10.6. [72]

Table 3.2 Chemical and physical properties of vaterite phased $CaCO_3$

Properties	Values	References
Chemical properties		
Density	2.54 – 2.65 g/cm^3	[48]
BET specific surface area	3.2 – 8.8 m^2/g	[66; 73; 74]
Surface energy	Calculated: 90 mJ/m^2 Experimental: 34-73 mJ/m^2	[76]
Physical properties		
Effective birefringence	Δn = 0.06-0.1	[75]
Reflective index	n_ω = 1.55 n_ε = 1.65	[48]
Volumetric coefficient of thermal expansion (α_v) α_V^2 at 25°C	35.5 x 10^{-6} K^{-1}	[71]
Optical property	Semitransparent / colorless	[75]
Wettability	Hydrophilic	[72]
Elastic modulus	16-61 GPa (μ = 31 GPa)	[71]
Hardness	0.3 – 4.2 GPa (μ = 0.9 GPa)	[71]

3.2.1.5 Application of vaterite

Spherical vaterite $CaCO_3$ particles have greater advantages over other morphological forms. Vaterite has unique porous properties, high surface area, low toxicity, greater hydrophilicity without any causing organic damage and pathological tissue calcification, and biological inertness in comparison to more stable calcite or aragonite. [60; 77] Vaterite has higher solubility in water than other phases and is easily transformed into more stable phases, i.e. aragonite or calcite in presence of water. [14] This property is an advantage of vaterite as a carrier when it is delivered to the human

body and in contact with water in the blood. These spherical vaterite particles are actively used in personal care and biomedical products as encapsulation with protein, enzyme, DNA, and growth factor or lysozyme, and especially in drug delivery (Figures 3.21 and 3.22). Vaterite particles can be successfully loaded with diagnostics and therapeutic drugs. Additionally, porous $CaCO_3$ can be used for copper ions (Cu^{2+}) removal by adsorption process (see Figure 3.23). [78] It is shown that the adsorption efficiency increases continuously with increasing amounts of $CaCO_3$. The process for Cu^{2+} adsorption onto the $CaCO_3$ is based on chemisorption, and the number of active sites on the surface of $CaCO_3$ is proportional to the reaction rate. The Cu^{2+} removal mechanism by the aggregated $CaCO_3$ in aqueous solution is based on two simultaneous processes: adsorption and ion exchange chemical precipitation.

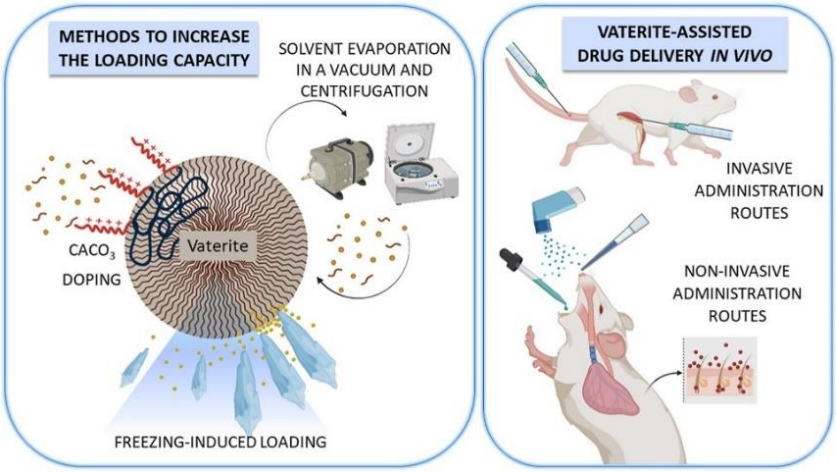


Figure 3.21 Using of vaterite assisted-$CaCO_3$ drug delivery [79]

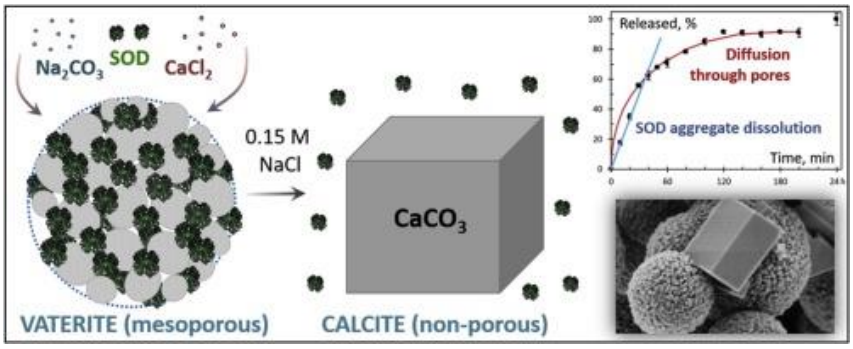


Figure 3.22 Enzyme superoxide dismutase (SOD) encapsulated in vaterite $CaCO_3$ crystals [80]

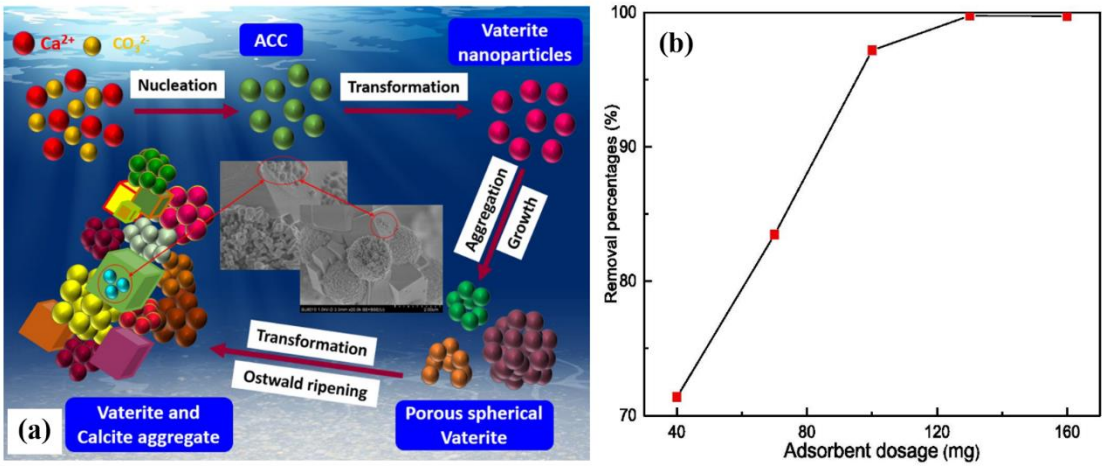


Figure 3.23 (a) Proposed formation mechanism of $CaCO_3$ and (b) the optimal Cu^{2+} adsorption conditions for $CaCO_3$ in the study of the amount of adsorbent added [78]

3.2.2 Aragonite phase

The aragonite polymorph is also one of the metastable phases of $CaCO_3$ under atmospheric conditions.

3.2.2.1 Aragonite structure

The orthorhombic aragonite crystals crystallize in the space group P*mcn*. [24] The aragonite unit cell is exhibited in Figure 3.24. [81] Figure 3.25 describes the aragonite crystal structure. The centrosymmetric orthorhombic lattice of aragonite crystals alternating Ca^{2+} cations and CO_3^{2-} anions layers are repeated along the directions of [110], [010], and [001], respectively. [82]

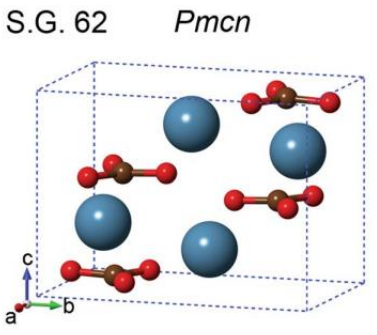


Figure 3.24 Orthorhombic, P*mcn* of aragonite unit cell (Calcium, carbon, and oxygen atoms represent as blue, ochre, and red spheres, respectively in the unit cell [81]

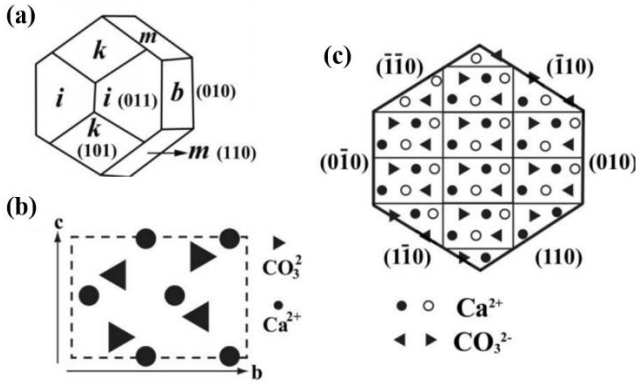


Figure 3.25 Aragonite crystal structure: (a) schematic combination form structure, (b and c) crystal structure crystallographic directions [82]

3.2.2.2 Aragonite shape

- By *'one-pot synthesis or direct precipitation'*

Generally, the morphology of aragonite $CaCO_3$ is presented in needle-liked, rod-liked, spindle-shaped or fiber shape depending on the synthesized system under high temperature (> 40^{o}C) or high pressure (ultrasound irradiation). Z. Gen-Tao et al. precipitated $CaCO_3$ under ambient temperature but using a high-intensity ultrasonic '*One-pot synthesis or direct precipitation'*. At the range of acoustic amplitudes 60% - 70% led to pure aragonite with a rod-shaped structure (the rod size is about 10 ± 2 mm with an aspect ratio of 5) as shown in Figure 3.26. [83]

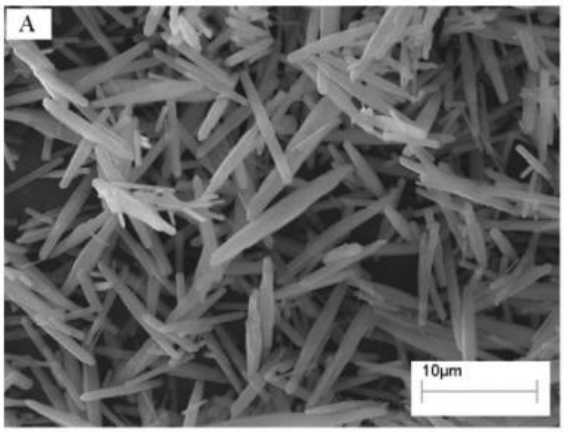


Figure 3.26 SEM images of aragonite synthesized under high-pressure ultrasound irradiation [24]

C. Ramakrishna and coworkers precipitated $CaCO_3$ particles by using 0.1 M of Na_2CO_3 and $CaCl_2$ under reaction temperatures of 25 – 50°C. They revealed that the temperature is the key factor of whisker precipitation and the composition and high fraction of aragonite was dependent on the temperature higher than 50°C. [84]

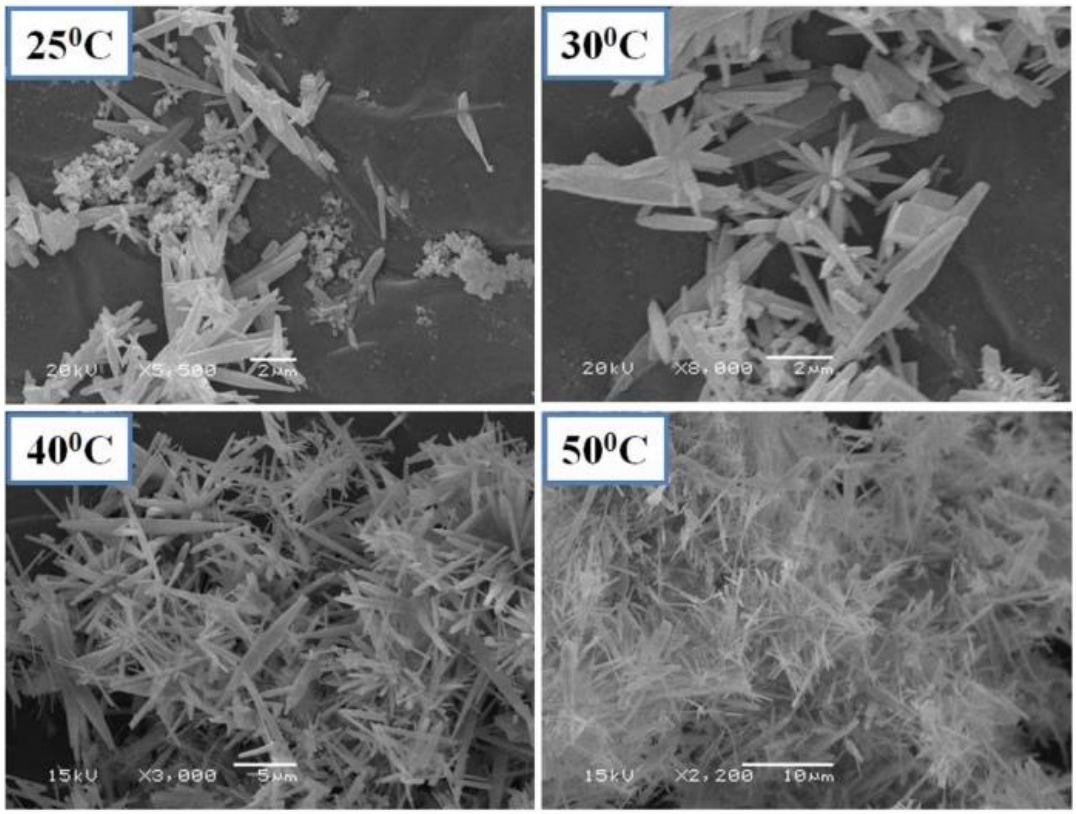


Figure 3.27 SEM images of nano aragonite whisker $CaCO_3$ particles as the function of temperatures at 25, 30, 40, and 50°C [84]

This study also supported that the selection of $CaCO_3$ polymorph depends significantly on the experimental condition. The meso-rods aragonite $CaCO_3$ particles precipitated under high temperatures of 70 – 80°C are exhibited in Figure 3.28. At 70°C, the results showed aggregates of meso-rods (Figure 3.28(c)). At 80°C, SEM demonstrated a rod-liked structure assembled with microrods in Figure 3.28(b). [82]

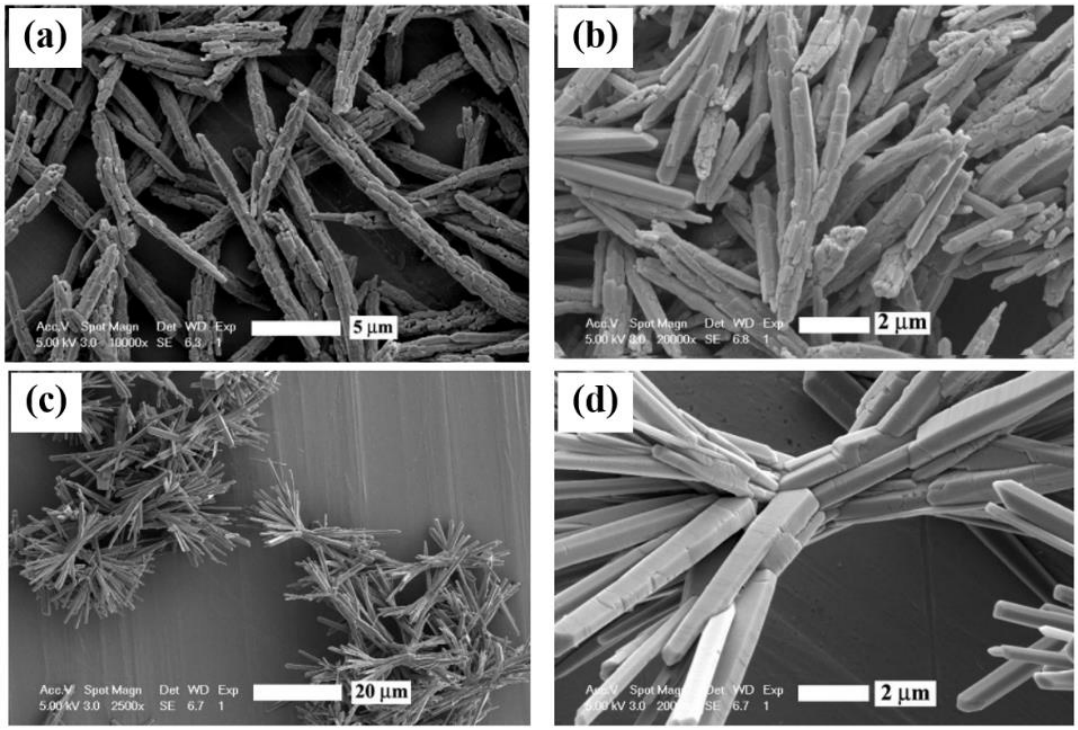


Figure 3.28 FE-SEM images of meso-rod aragonite synthesized under 70 – 80ºC [82]

-By *'polymorph transformation'*

The needle-liked aragonite not only precipitated by the mixing of Ca^{2+} and CO_3^{2-} solutions under high temperatures but it can be occurred by the crystal transformation when the $CaCO_3$ particles were immersed in hot water at 80ºC. [14] The direct precipitation gives aggregated wires of aragonite with short in length. While, the transformation of dry vaterite to aragonite, one gets long nano-wired with poorly aggregated as shown in Figure 3.29.

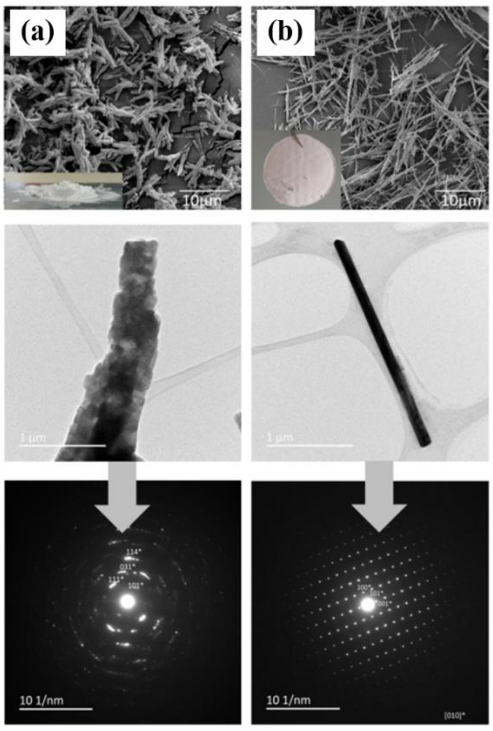


Figure 3.29 SEM, TEM images and electron diffraction patterns of (a) aragonite precipitated in one-pot synthesis or direct precipitation, and (b) precipitated aragonite obtained from the transformation route [14]

Figure 3.30 represents a needle-like or slender crystal with smooth layer offset which dislocation formed on a crystal face. [85] This possible mechanism can describe the growth of long nanowire $CaCO_3$ particles.

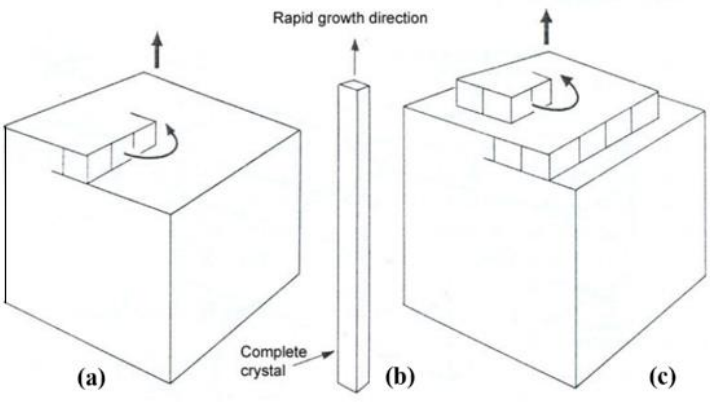


Figure 3.30 Possible growths of needle-liked shape: (a) spiral growth begins at a dislocation on the crystal face, (b) possible shape of the final crystal, (c) formation of a step induces rapid growth along the face, and step sweeps around in a spiral [85]

3.2.2.3 Characterization of aragonite

Phase identification of aragonite is presented in Figure 3.31. [82] The crystallographic planes of typical aragonite consist of (110), (111), (021), (121), (0.12), (200), (031), (112), (130) in the range 20 – 40^{o} in 2Ɵ. The FTIR technique is also a sensitive and useful tool for the identification of aragonite phase shown in Figure 3.32. The typical vibrational bands of aragonite located at 1079 and 854 cm^{-1} are attributed to the characteristic symmetric carbonate stretching (ν_1 mode) and carbonate out-of-plane bending (ν_2 mode) vibrations, respectively. The characteristic pair of bands at wavenumber 713, and 700 cm^{-1} is assigned to the in-plane bending modes (ν_4 mode) of aragonite. [82] The assignment of the IR absorption bands of the aragonite phase is listed in Table 3.3.

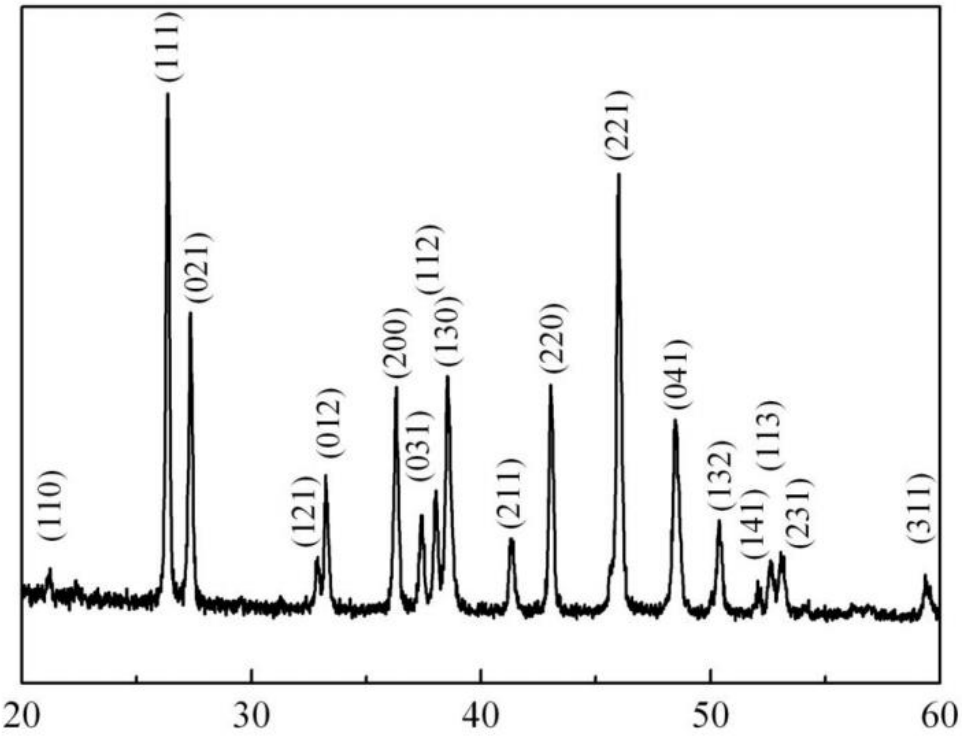


Figure 3.31 XRD diffraction of aragonite crystals synthesized at 95^{o}C of mixing temperature [82]

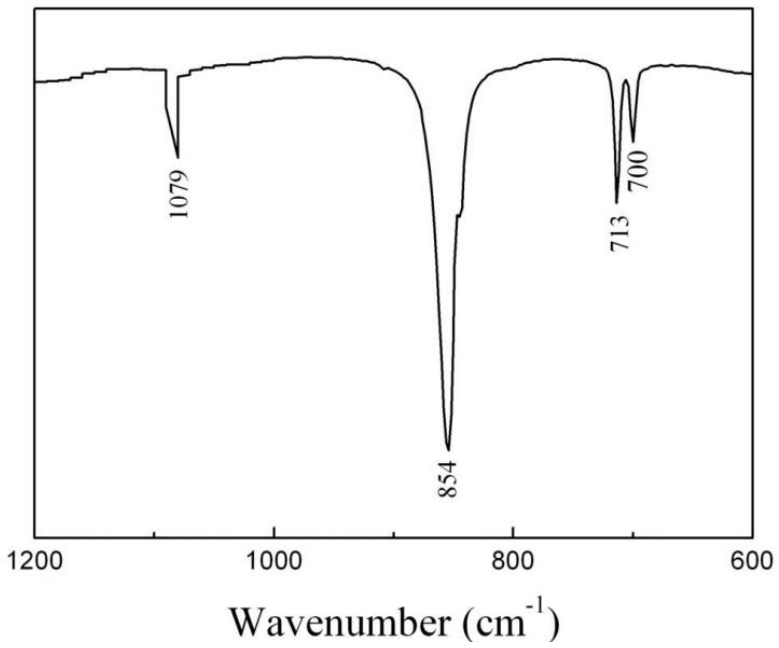


Figure 3.32 FTIR spectrum of aragonite crystals in the range of 600 – 1200 cm^{-1} [82]

Table 3.3 Assignment of the IR absorption bands of aragonite phase [61, 82]

Polymorph	**υ_1, cm^{-1}**	**υ_2, cm^{-1}**	**υ_3, cm^{-1}**
Aragonite	1079	854	700, 713

3.2.2.4 Physical properties of aragonite

The physical properties of aragonite $CaCO_3$ are listed in Table 3.4.

Table 3.4 Physical properties of aragonite phased $CaCO_3$

Property	**Value**	**Reference**
Density	2.93 - 3.00 g/cm^3	[86]
Optical property	White / colorless	[87]
Wettability	Hydrophilic / Soluble in organic solvent	[87]
Hardness	3.5 – 4 Mohs scale	[88]

3.2.2.5 Application of aragonite

$CaCO_3$ with the aragonite polymorph has been applied in many industries as fillers and pigments. [24] Recently, the interest in needle-like aragonite crystals is increasing which is applied using as fillers for the improvement of the mechanical properties of paper and polymer materials. In the paper industry, aragonite crystals are added to improve the quality of the paper such as printing characteristics, luster, and color. [83] The needle-like aragonite $CaCO_3$ particles with a very high aspect ratio are particularly employed as fillers in rubber and plastic: polypropylene and polyvinyl alcohol because they increase the strength of these materials. [89]

3.2.3 Calcite phase

According to a theoretical thermodynamics study, calcite is the most stable phase of $CaCO_3$ polymorph.

3.2.3.1 Calcite structure

The space group of the calcite phase is assigned to R3c. [68] The crystal structure of the calcite phase is presented in Figure 3.33. [90] There are many approaches to the mechanism of crystal growth. Sinkakas and coworkers proposed the possible crystal growth mechanism of calcite developing from cube-shaped or block-shaped seeds, assuming that the atomic attractions on the surface of cube seeds are the same, then the cube seeds get closer and form the calcite crystals (see Figure 3.34). [85]

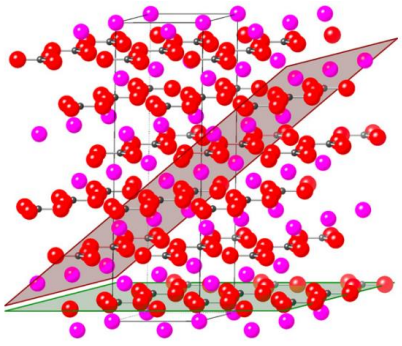


Figure 3.33 Crystal structure of the R3c space group of calcites $CaCO_3$ (CO_3^{2-} groups: carbon atoms represented as gray spheres, oxygen atoms as red spheres in 0001 trigonal planes) separated by layers of calcium atoms (pink spheres) [90]

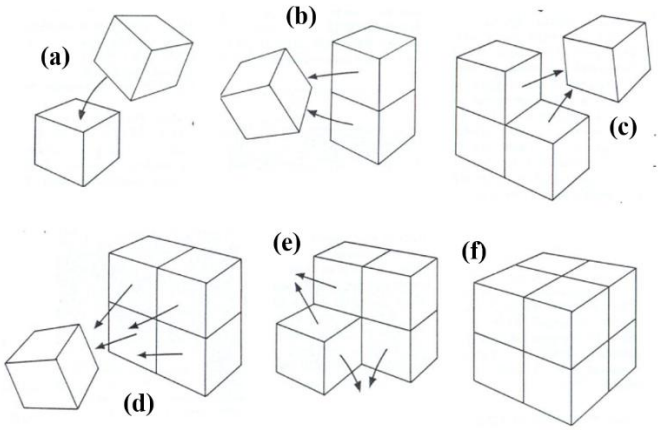


Figure 3.34 Growth process of a calcite crystal from a cubic-shaped seed particle [85]

Figure 3.35 shows the growth rate of spherical and cubical crystals. The spherical-shaped crystal has a uniform rate of growth while it is a non-uniform rate of growth for cubic crystals. [85] In addition, the growth of crystals is rapid or precipitated immediately which causes being found on crystals of various species.

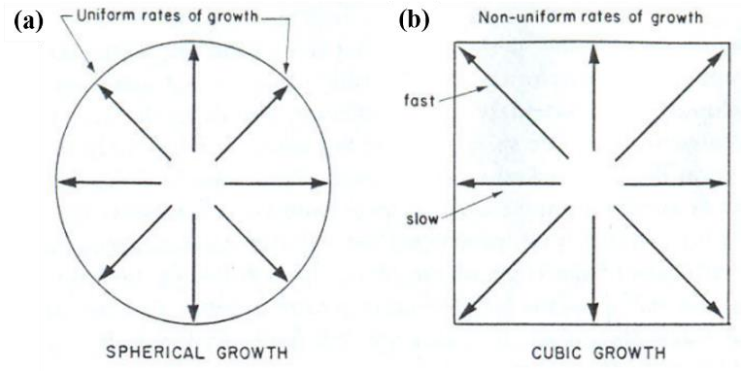


Figure 3.35 Growth rate of (a) spherical growth and (b) cubic growth [85]

3.2.3.2 Calcite shape

According to the previous part, typical shapes of calcite can be exhibited in rhombohedral structures or cubical shapes. [91] The $CaCO_3$ crystals with a rhomboherdral shaped structure is presented in Figures 3.36, 3.37 and 3.38. [92] The average particle size was more than 100 μm in length. [58]

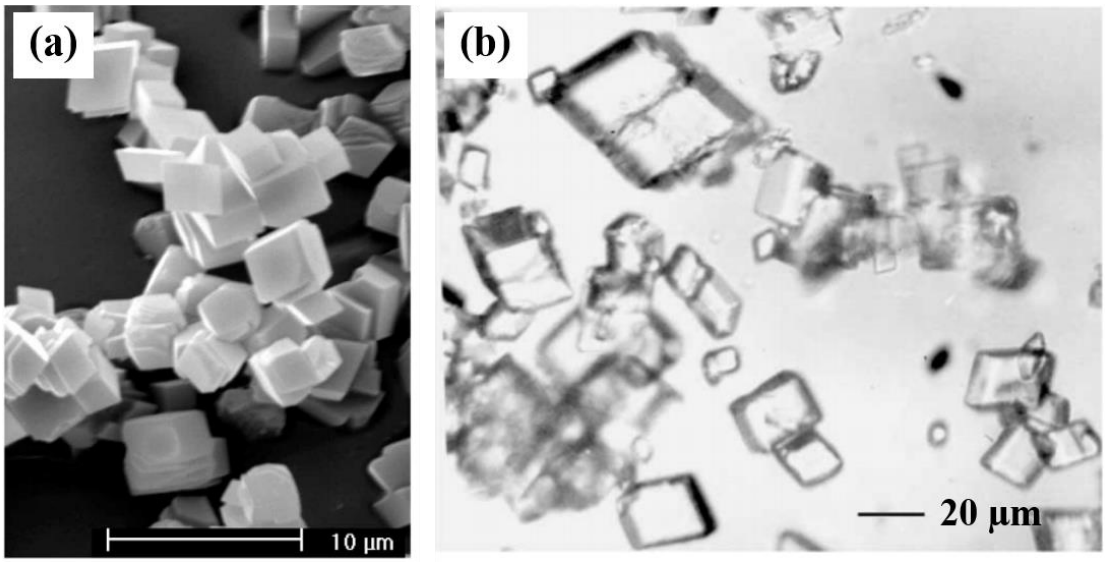


Figure 3.36 (a) SEM and (b) TEM image of calcite crystals [58]

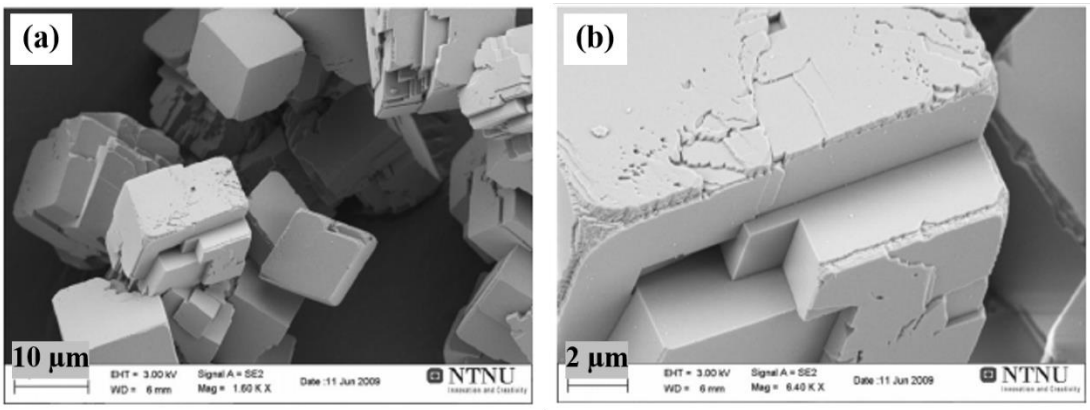


Figure 3.37 SEM images at (a) low, and (b) high magnification of calcite particles precipitated from 0.1 M of CO_3^{2-} and Ca^{2+} sources, 30 ºC and 300 rpm [91]

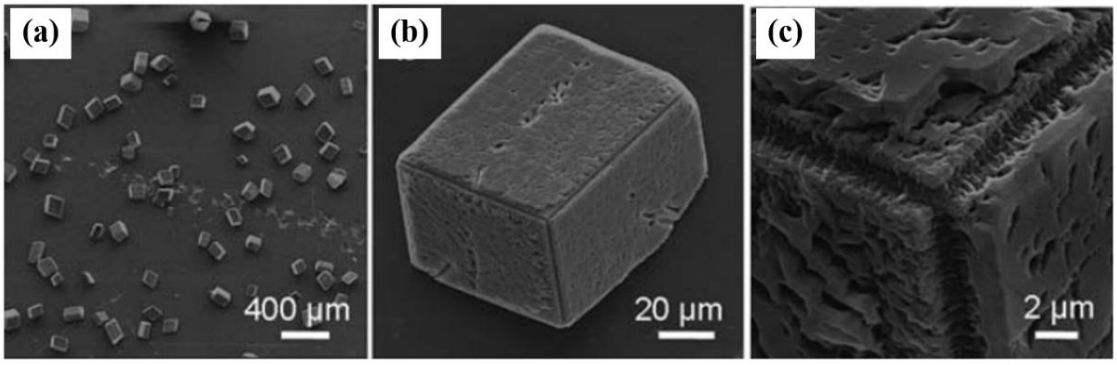


Figure 3.38 SEM images of calcite crystals at low and high magnification [92]

No only does aragonite demonstrate a whisker shape, but the calcite phase also could be exhibited in a whisker shape or needle-liked shape as well, as shown in Figure 3.39. [93] To identify the polymorphic phase of similar needle-liked shapes, the X-ray diffraction and TEM are carried out. A single-crystalline aragonite structure is observed at [110] axis with a smooth surface as shown in Figure 3.40(a). Meanwhile, the needle-liked calcite is presented in a rough or zigzag surface with a selected area electron diffraction (SAED) pattern taken along the [241] axis (Figure 3.40(b)).

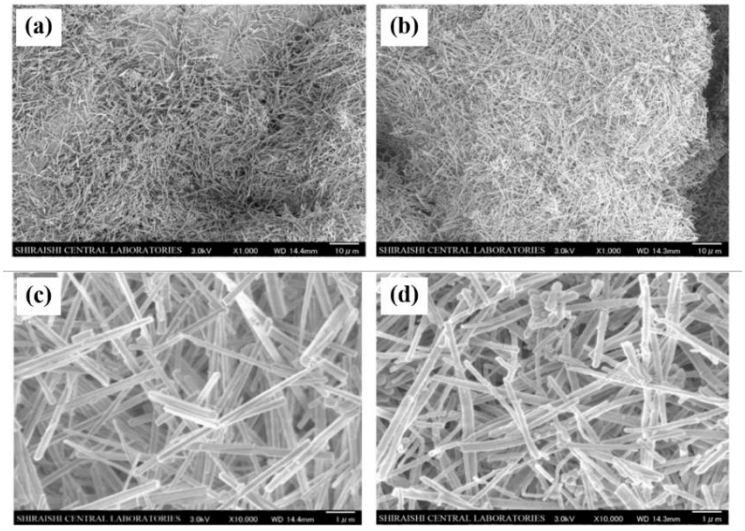


Figure 3.39 SEM images at low and high magnification of (a and c) aragonite powders, and (b and d) calcite powders [93]

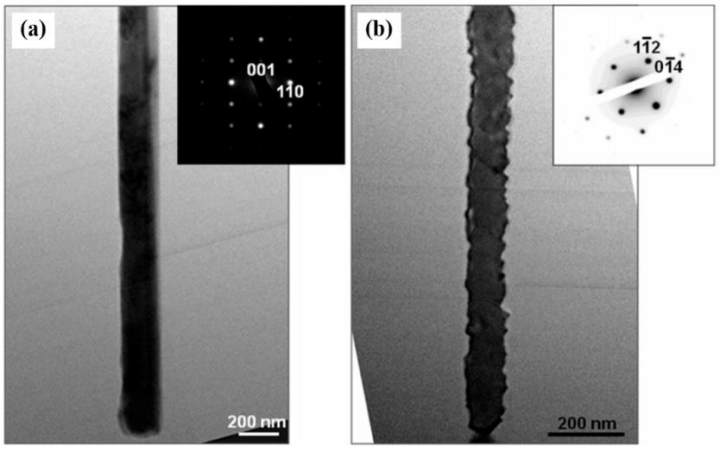


Figure 3.40 TEM images and SAED single-crystalline of (a) needle-liked aragonite particle, and (b) needle-liked calcite particle [93]

3.2.3.3 Characterization of calcite

The XRD pattern and FTIR result of calcite $CaCO_3$ are presented in Figure 3.41 and Figure 3.42, respectively. [94] The assignment of the IR absorption bands of the calcite phase is listed in Table 3.5.

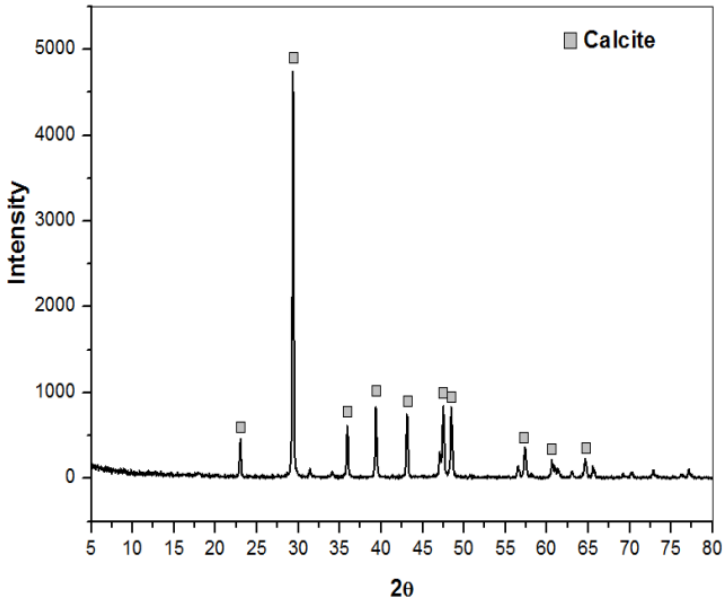


Figure 3.41 XRD pattern of calcite $CaCO_3$ [94]

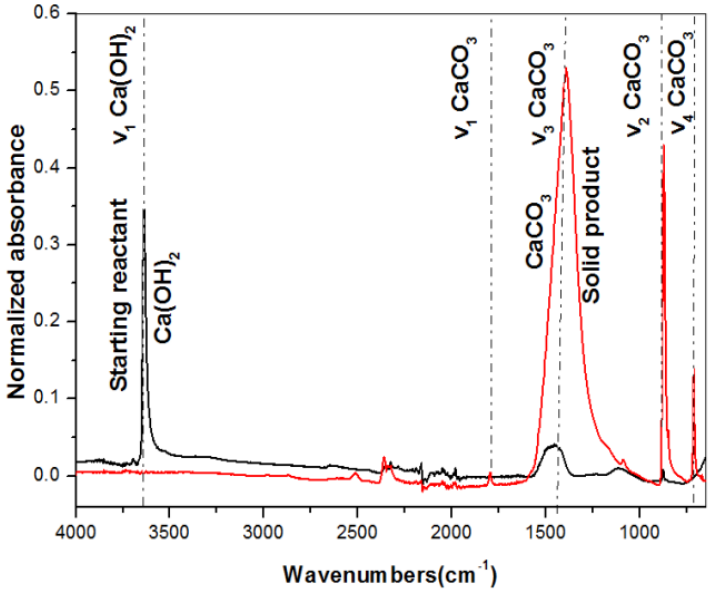


Figure 3.42 FTIR spectrum of calcite $CaCO_3$ [94]

Table 3.5 Assignment of the IR absorption bands of calcite phase [61]

Polymorph	υ_1, cm^{-1}	υ_2, cm^{-1}	υ_3, cm^{-1}
Calcite	1435	879	713

3.2.3.4 Chemical and physical properties of calcite

The chemical and physical properties of calcite crystals are summarized in Table 3.6.

Table 3.6 Chemical and physical properties of calcite phased $CaCO_3$

Property	Value	Reference
Chemical property		
Element content of purest calcite	56.03% CaO 43.97% CO_2	[95]
Physical property		
Optical property	Milky white	[95]
Hardness	3 Mohs scale	[88]
Density	2.75 g/cm^3	[86]
Specific gravity	2.71 g/cm^3	[95]

3.2.3.5 Application of calcite

Calcite $CaCO_3$ is the most widely used mineral in papermaking since sizing in the paper industry is inverted from acid to neutral. The calcite $CaCO_3$ is used in the paper as a filler (Figure 3.43) to provide specific properties to the paper like brightness, porosity, and so on. [19]

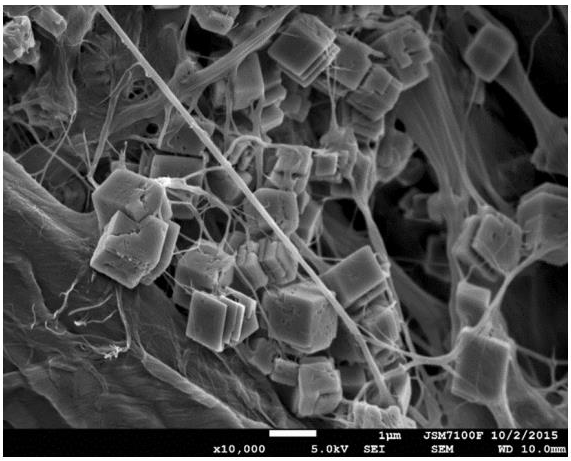


Figure 3.43 SEM image of calcite $CaCO_3$ particles in paper sheet [19]

3.3 Synthesis methods and parameters affecting calcium carbonate particles

3.3.1 Synthetic methods

There are four main synthetic methods of $CaCO_3$ precipitation. [3] The simplified method which is the spontaneous precipitation involves the mixing of carbonate (CO_3^2) anions and calcium (Ca^{2+}) cations. The sodium carbonate (Na_2CO_3), ammonium carbonate ($(NH_4)_2CO_3$) or sodium bicarbonate ($NaHCO_3$) solutions are normally used as CO_3^{2-} reactants. Meanwhile, calcium chloride ($CaCl_2$), and calcium hydroxide ($Ca(OH)_2$) solutions are widely used as Ca^{2+} reactants. [14; 60] E. Y. Zeynep and coworkers evaluated $CaCO_3$ morphologies and properties by the difference of performed preparation (i) chemical pathway involving $CaCl_2$ and Na_2CO_3 and (ii) supercritical carbon dioxide ($ScCO_2$) technology in which CO_3^{2-} ions are generated in aqueous media and react with Ca^{2+} ions shown in Figure 3.44 and Figure 3.45, respectively. [96] These synthesis methods are described below.

- *Spontaneous precipitation method*

The spontaneous precipitation method consists of the mixing of a calcium salt solution with a carbonate salt solution, as illustrated in Figure 3.44(a) and 3.45(a). The most used calcium salts are calcium chloride ($CaCl_2$), calcium sulfate ($CaSO_4$), and calcium nitrate ($Ca(NO_3)_2$). Meanwhile, sodium carbonate (Na_2CO_3), ammonium

carbonate ($(NH_4)_2CO_3$), potassium carbonate (K_2CO_3) and magnesium carbonate (Mg_2CO_3) are employed as carbonate sources for this synthesis method.

- *Slow carbonation method*

This method consists of spontaneous precipitation (Figure 3.44(b)), where CO_3^{2-} ions are produced from the dissolution of the CO_2 gas in an alkaline solution typically from $(NH_4)_2CO_3$. The $CaCl_2$ solution, with or without additives, is introduced in a desiccator, where crushed $(NH_4)_2CO_3$ is also placed. The $(NH_4)_2CO_3$ releases NH_3 and CO_2 gases, which are consecutively absorbed in the calcium solution, and the $CaCO_3$ formation takes place.

- *Reverse emulsion method*

The reverse emulsion (Figure 3.44(c)) is a thermodynamic dispersion of water and oil channels stabilized by interfacial layers of surfactants with or without co-surfactants and consisting of bi-continuous microstructures. It can be used as “micro-reactors” and templates for preparing nanomaterials.

- *Carbon dioxide (CO_2) bubbling method or Carbonation method*

The carbonation method (Figure 3.44(d) and supercritical CO_2 ($ScCO_2$) method in Figure 3.4(b)) consists of CO_2 gas stream reaction with a calcium-alkaline solution. This process was already employed at the industrial stage for the production of $CaCO_3$.

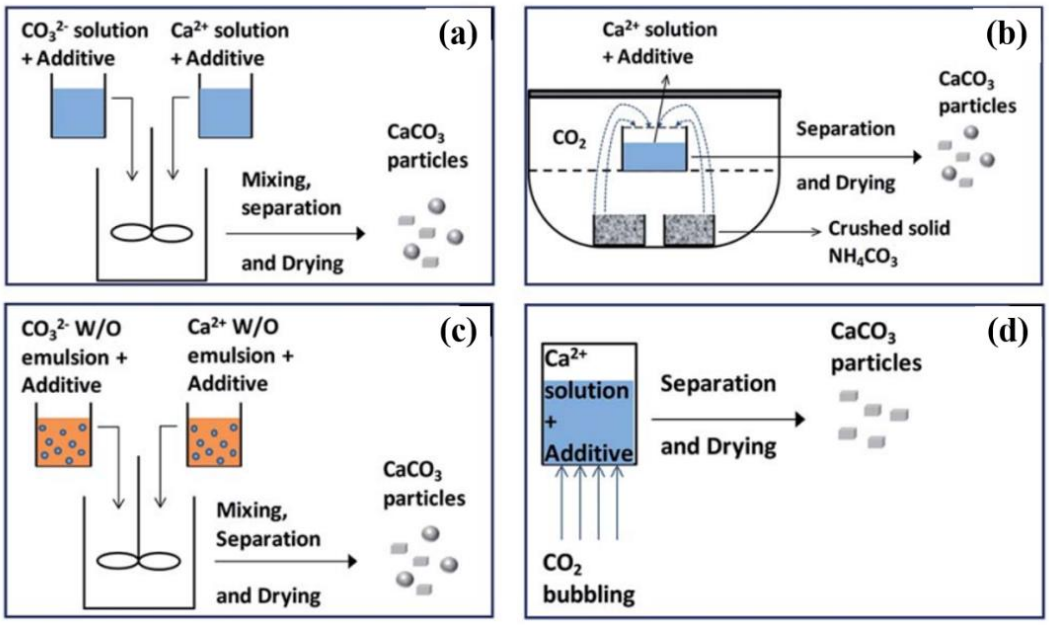


Figure 3.44 For main $CaCO_3$ synthesis methods: (a) the spontaneous precipitation method, (b) the slow carbonation method, (c) the reverse emulsion method, and (d) CO_2 bubbling method [3]

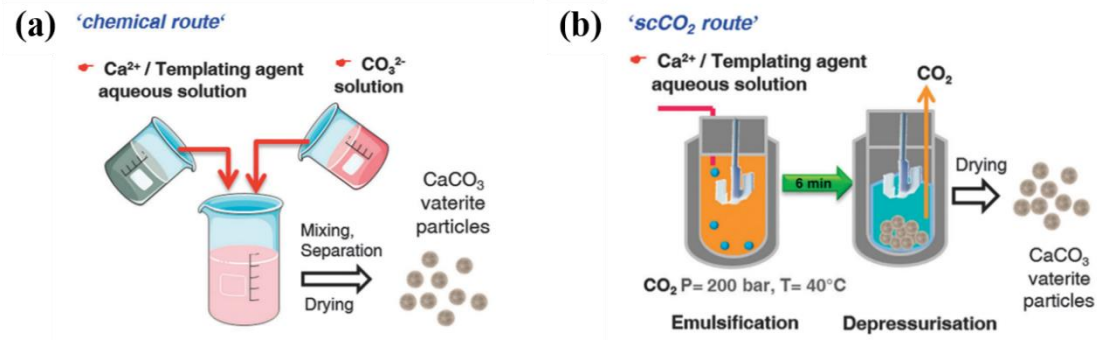


Figure 3.45 Illustration of (a) ‘‘chemical route’’ and the (b) ‘‘$scCO_2$ route’’ pathways for the synthesis of $CaCO_3$ vaterite particles [96]

3.3.2 Synthetic parameters

The morphological shape and polymorphic phase of $CaCO_3$ particles depend on the synthesis conditions. Among the synthesis factors, the temperature, supersaturation, and stirring rate play the primary factors in the crystallization of polymorph (Figure 3.46). Meanwhile, the solvent and additive in the mixing system are secondary factors. [4; 97]

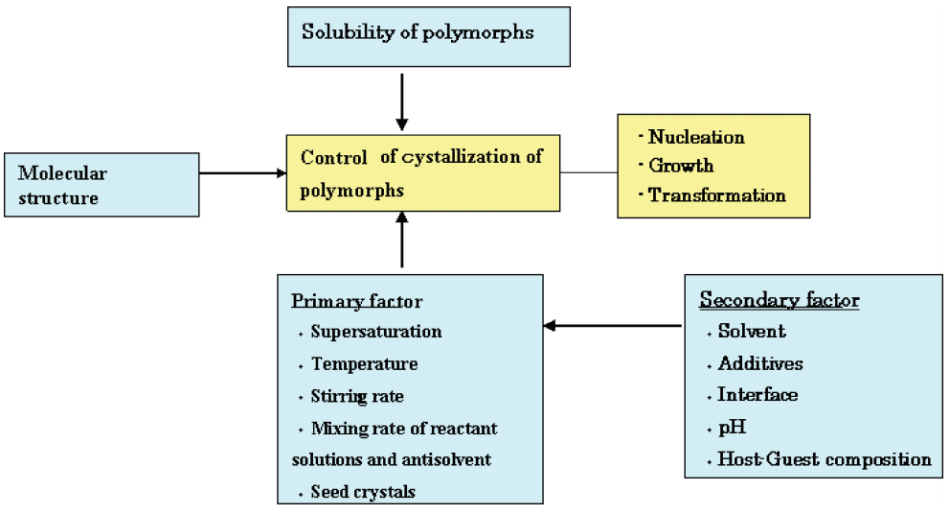


Figure 3.46 Schematic of synthesized factors controlling the polymorphic crystallization [97]

3.3.2.1 Temperature

The temperature affects directly the polymorphs of $CaCO_3$ crystals as presented in Figure 3.47. The polymorph composition of $CaCO_3$ precipitated particles in the early metastable stage presented as a function of temperature. The initial ACC will be transformed to form calcite particles at low temperatures (14 – 30 ^oC). The vaterite crystal occurs predominantly at 30 – 40 ^oC. At the temperature above 60^oC, the aragonite polymorph is observed. [98] The occurring temperatures of $CaCO_3$ crystalline polymorphs are listed in Table 3.7.

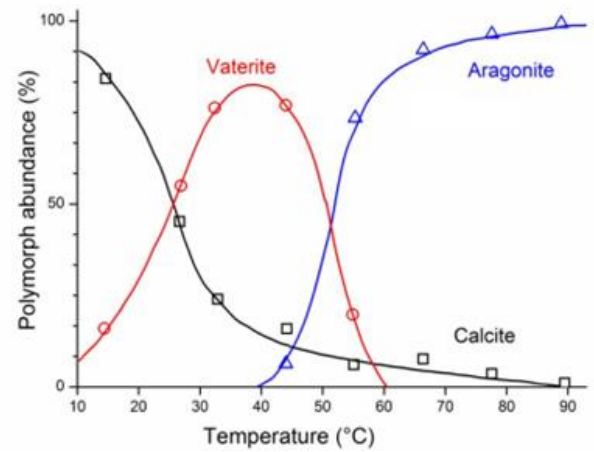


Figure 3.47 Plots of abundance crystalline form of $CaCO_3$ polymorphs at the early metastable stage as a function of temperature [98]

Table 3.7 Temperature ranges of $CaCO_3$ crystal precipitation for different polymorphs

Polymorphs	Temperature (°C)	Reference
Vaterite	30 – 40	[98]
Aragonite	> 60	
Calcite	14 – 30	

O. Cherkus et al. precipitated rapidly vaterite particles under stirring using an equal volume of 0.5 M of $CaCl_2$ and 0.5 M of Na_2CO_3 solutions in deionized (DI) water at room temperature and 300s of mixing time. The phase transformation from spherical vaterite particle to calcite phase after immersing in tap water was captured by using SEM and Coherent X-ray Diffraction Imaging (CXDI) techniques in Figure 3.48.

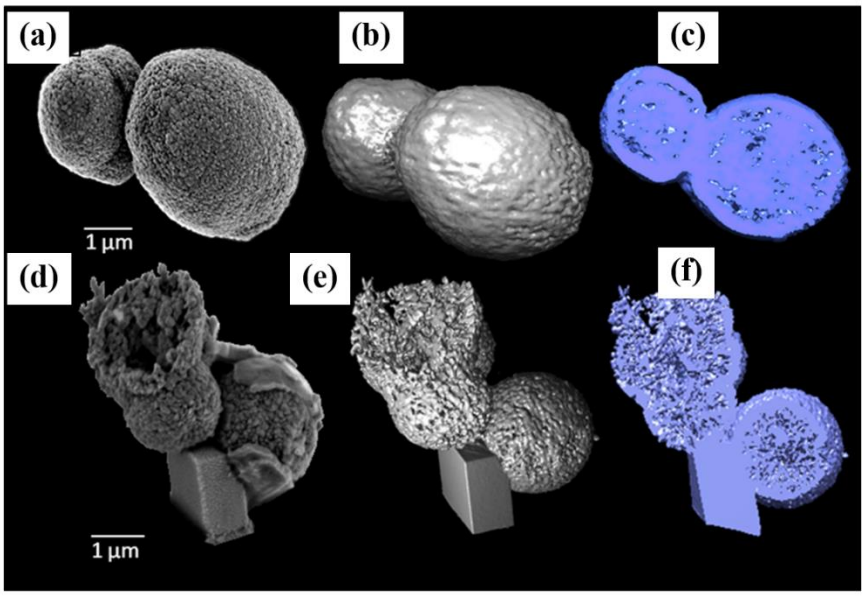


Figure 3.48 SEM and CXDI images of (a-c) initial $CaCO_3$ particles, and (d-f) $CaCO_3$ particles immerse in tap water [14]

3.3.2.2 Supersaturation activity

The factors influencing the morphology of $CaCO_3$ crystals are the affecting of supersaturation activity. The supersaturation (*S*) is the solution containing more solute than present at equilibrium. It provides a relative measure of the system's deviation from its nonequilibrium state. The supersaturation activity in equation 3.1 illustrates the relation between supersaturation of the system and solubility product of a solid phase

while $\Delta\mu$ is the difference of chemical potential between non-equilibrium and equilibrium state, $a_{CO_3^{2-}}$ is activity of carbonate ion (CO_3^{2-}), $a_{Ca^{2+}}$ is activity of calcium cations (Ca^{2+}), and K_{sp} is solubility product constant. Base on Ostwald's law of stages, the metastable stage form, or the most soluble phase of $CaCO_3$ is crystallized at high supersaturation. [99] The next phase of stability of $CaCO_3$ is developed by the transformation of the initial form via the dissolution and re-crystallization process. In the liquid-liquid mixing method, vaterite $CaCO_3$ particles precipitate at room temperature when S < 6.5. [4]

$$\text{In S} = \frac{\Delta\mu}{RT} = \text{In}\frac{a_{CO_3^{2-}}\ a_{Ca^{2+}}}{(a_{CO_3^{2-}}\ a_{Ca^{2+}})^{eq}} = \text{In}\ \frac{a_{CO_3^{2-}}\ a_{Ca^{2+}}}{K_{sp}} \quad (3.1)$$

3.3.2.3 Mixing mode or stirring rate

The size of the formed particles and distribution of $CaCO_3$ particles depend on the mixing mode and mixing rate strongly. [100] The ultrasonication is one of the most effective agitation methods resulting in the formation of smaller particles with lower dispersity (Figure 3.49(a)). The $CaCO_3$ sample was stirred with a magnetic bar. The result of $CaCO_3$ particles using only stirring contains the amount of spherical $CaCO_3$ particles with polydisperse particle size as shown in Figure 3.49(b). The system of control without any treatment by ultrasonic agitation or stirring presents cubic-like shaped particles represented by calcite modification as can be seen in Figure 3.49(c).

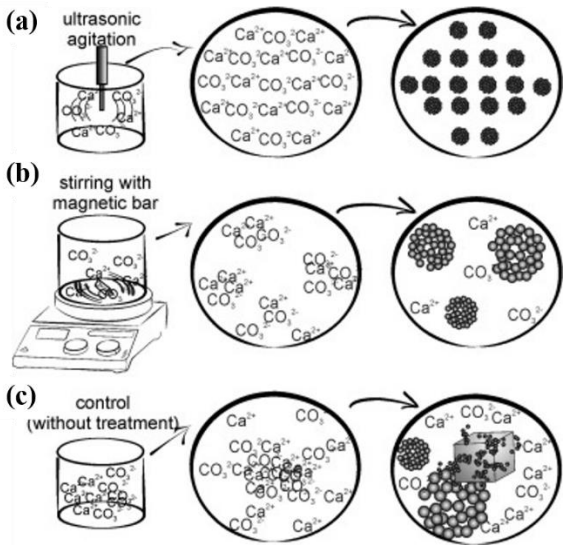


Figure 3.49 Schematic of $CaCO_3$ particle formation under different treatments: (a) ultrasonic agitation treatment, (b) stirring with magnetic bar treatment, and (c) control experiment without any ultrasonic agitation or stirring treatment [100]

The mixing rate of the reactant solutions is also an important factor in the precipitation process. The stirring intensity, stirring rate, or high shear can affect the activation energy of nucleation of $CaCO_3$ in an aqueous system as shown in Figure 3.50. [101] The $CaCO_3$ nuclei will be formed to be spindly particles with smaller particle sizes when the stirring is used in the mixing system. In the other way, the bigger spherical $CaCO_3$ particle will further grow without stirring.

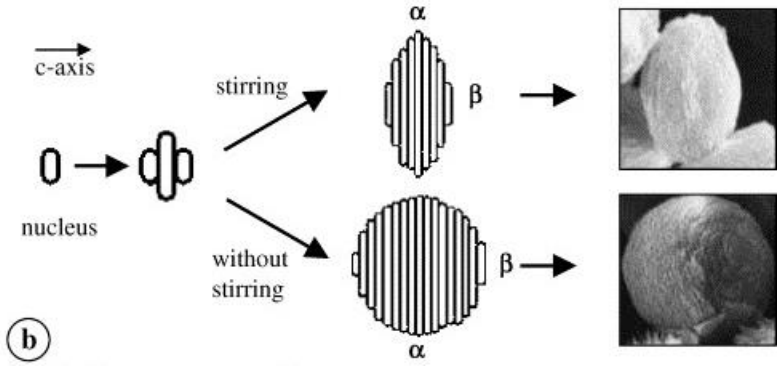


Figure 3.50 Schematic representation of the formation of spindly and spherical vaterite particles with and without stirring [101]

Imai and coworkers synthesized ellipsoidal $CaCO_3$ particles by varying the stirring speed 250, 500, 1000, and 1400 rpm. [68] The stirring speed affected directly in diameter of the particles. At 250 rpm of mixing speed, the diameter of the ellipsoid is 1.512 µm. The diameter decreased when the mixing speed increased and the diameter was decreased down to 736.3 nm at 1400 rpm of stirring rate (Figure 3.51).

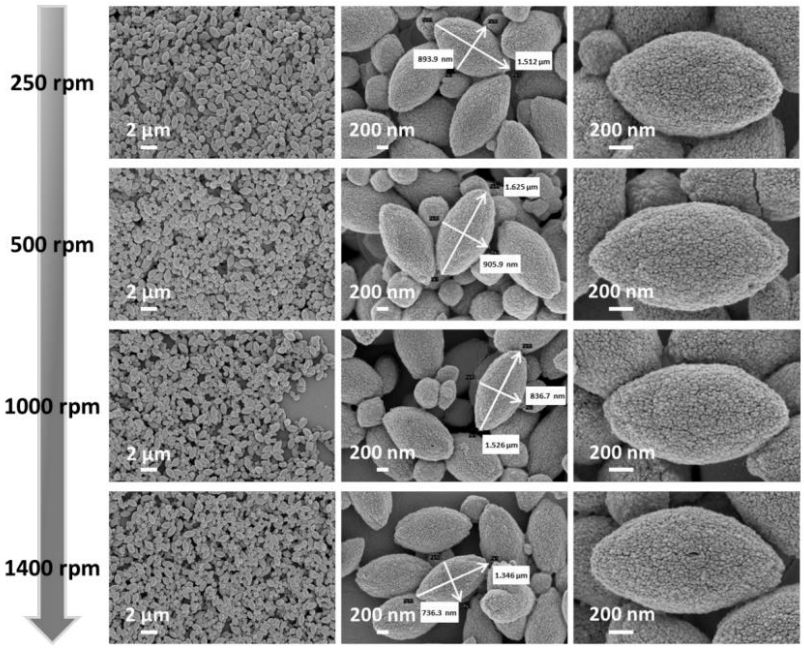


Figure 3.51 SEM images of ellipsoidal $CaCO_3$ obtained at different stirring speed during synthesis [68]

3.3.2.4 Solubility constant (K_{sp})

According to the vaterite form is metastable stage, it has the highest solubility among other polymorphs and will be the first form precipitated. The K_{sp} values of $CaCO_3$ at 25°C forms are listed in Table 3.8. [14] The different temperatures also provide the different ranges of respective solubility product constant (K_{sp}) values as shown in Figure 3.52. [102] The K_{sp} values of different polymorphs decrease at higher temperatures. The metastable crystal (vaterite) is transformed to the most stable form of calcite at all temperatures corresponding to a result of water induced dissolution recrystallization process.

Table 3.8 The K_{sp} values of $CaCO_3$ polymorphs at 25°C

Polymorph	Solubility constant (K_{sp})	Reference
Vaterite	$10^{-7.91}$	[102]
	$1.22 \times 10^{-8.0}$	[74]
Aragonite	$10^{-8.30}$	[102]
	$10^{-8.36}$	[74]
Calcite	$10^{-8.45}$	[102]
	$10^{-8.475}$	[74]

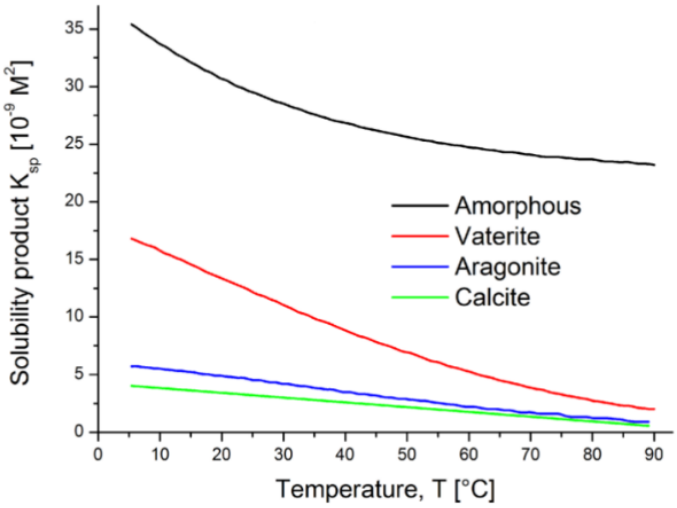


Figure 3.52 Solubility product of ACC and crystalline phases (vaterite, aragonite, calcite) at different temperatures [102]

B. Myszka et al. revealed that the vaterite and aragonite can be transformed into stable calcite phase when brought into contact with water, obeying the Ostwald–Lussac step rule as in Figure 3.53. [103] Also the Gibbs free energy presenting the stability of ACC, vaterite, and calcite are presented in Figure 3.54. [104] The ACC was formed spontaneously and then further growth as vaterite particle in hexagonal or spheroidal shapes. After dispersing the vaterite particles in water, the particles were transformed to the more stable phases: aragonite or calcite.

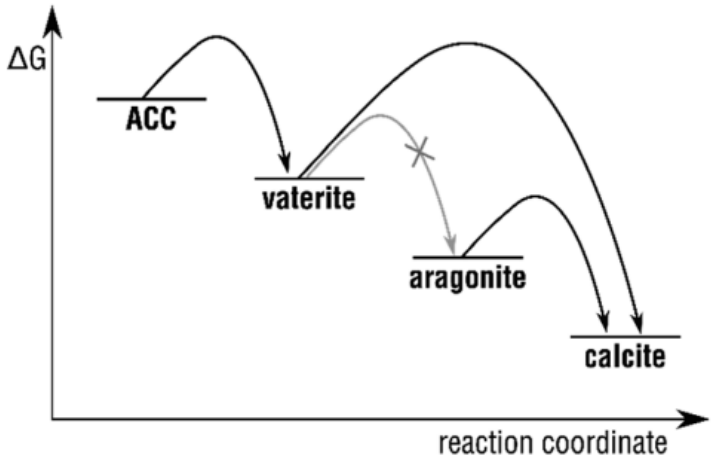


Figure 3.53 Schematic Ostwald–Lussac step ripening processes occurring upon immersion of $CaCO_3$ polymorphs in water [103]

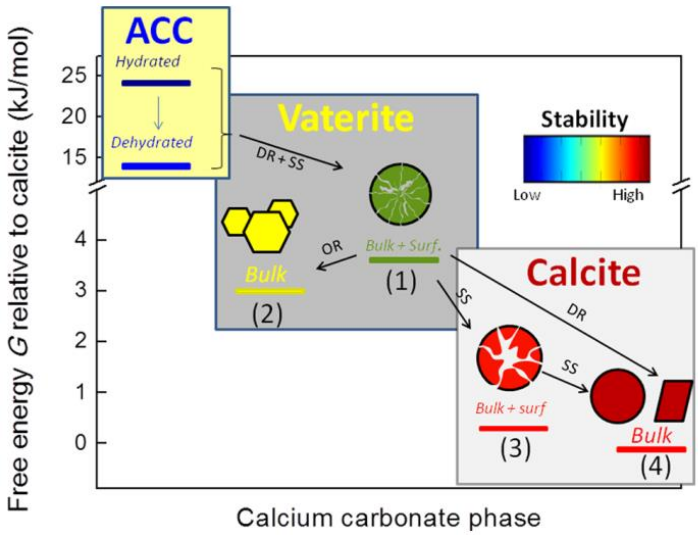


Figure 3.54 Gibbs free energy at 25°C for ACC, vaterite, and calcite [104]

3.3.2.5 Mixing time

According to the thermodynamic stability of the polymorph and solubility of $CaCO_3$ phases are different, prolonging the reaction or mixing time results in the transformation of the polymorphic phase. The immersing of metastable vaterite particles in the aqueous solutions leads to its recrystallization to the more stable phases (aragonite or calcite). [105] The transformation of vaterite to calcite is usually in the range of a few minutes to several hours including the ordering-dehydration, spherulitic growth,

dissolution-reprecipitation, and ripening steps (Figure 3.55). [106] The kinetic model of $CaCO_3$ formation in the function of time is also presented in Figure 3.56. [107]

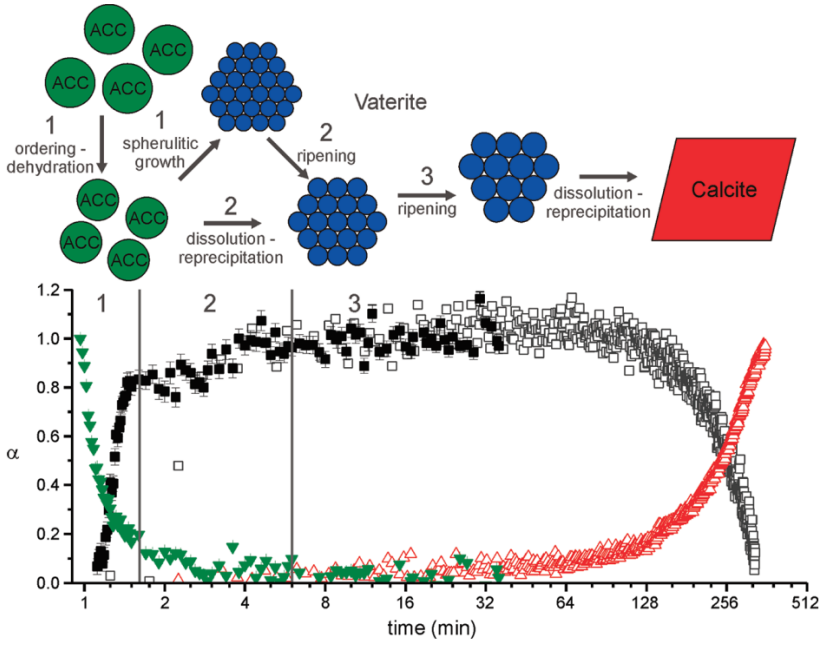


Figure 3.55 Proposed schematic of multistage of $CaCO_3$ from ACC → vaterite → calcite crystallization pathway in the function of time [106]

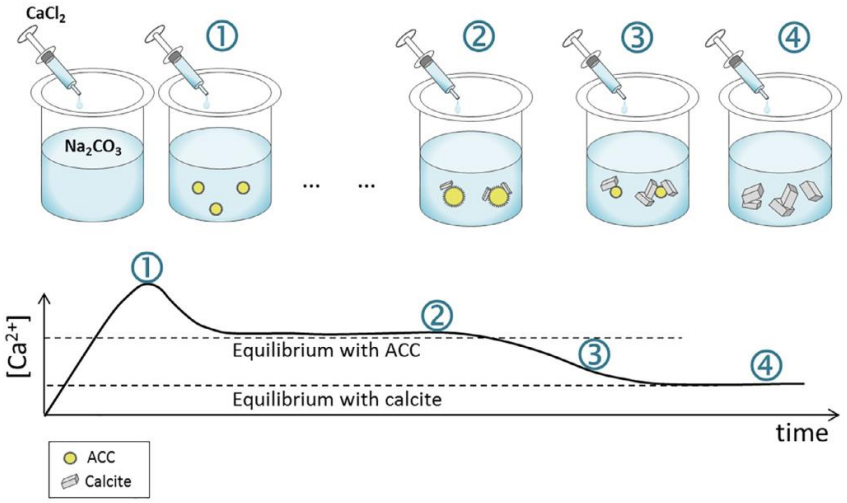


Figure 3.56 Schematic representation of the kinetic mechanisms of $CaCO_3$ formation [107]

3.3.2.6 Effect of additive or aqueous medium

The presence of additives or change of aqueous medium in the reaction system affects the precipitation of $CaCO_3$ particles. The additive in the mixing system changes the solubility of a forming substance by influencing the reactivity of crystallization rate, nucleation, crystal growth, supersaturation and activity of Ca^{2+} cation and CO_3^{2-} anion which directly effect on the morphology of $CaCO_3$ forming crystals. [108]

L. Shuxia et al. precipitated various shapes of $CaCO_3$ by using dodecyltrimethylammonium bromide (DTAB) micellar as additive as seen in Figure 3.57. [109] It can be confirmed that the additive affect directly to the morphology and size of $CaCO_3$ particles.

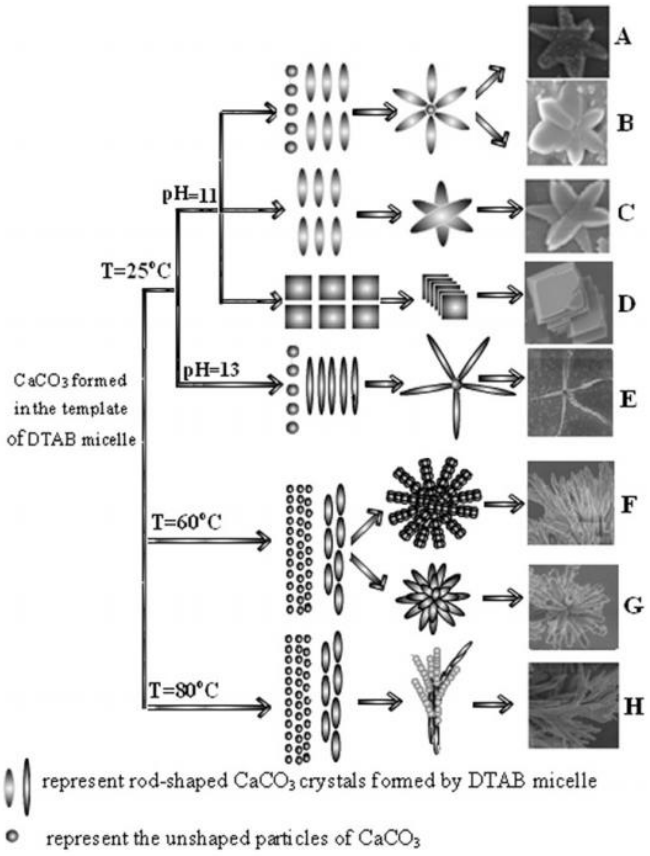


Figure 3.57 Sketch map of the growth process of various morphology $CaCO_3$ crystals under different conditions in the presence of DTAB [109]

There was a fabrication of vaterite hollow microsphere of $CaCO_3$ by using sodium poly(4-styrenesulfonate) (PSS) as a stabilizing agent together with adjusting the

pH value in the mixing system as Figure 3.58. [110] The average particle size was found to be 2.56 µm.

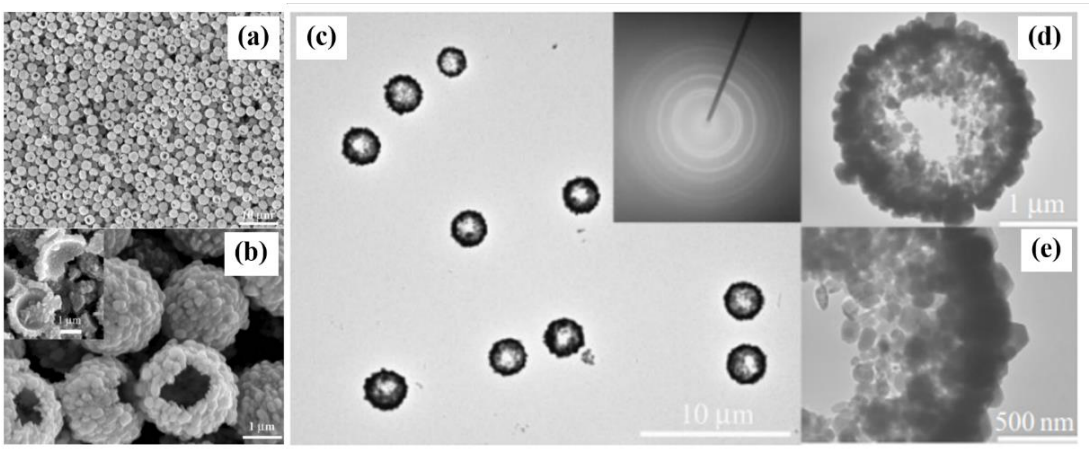


Figure 3.58 The (a, b) SEM and (c-e) TEM images of vaterite hollow microspheres in the presence of PSS [110]

The polyol additives including ethylene glycol, glycerol, and erythritol were other additives added into the mixing system to reduce the particle size of sphere $CaCO_3$ in Figure 3.59. This study revealed that the hydroxyl groups (OH^-) in polyol structure play an important role in the particle size by binding with Ca^{2+} of $CaCl_2$ reactant resulting in the prevention of further growth of crystals. [60] The smallest spherical framboid particles were reduced to 200 – 350 nm by using glycerol as an additive. In addition, higher viscosity of polyol/water mixtures was found to decrease the particle size at the same amount of hydroxyl groups in the system.

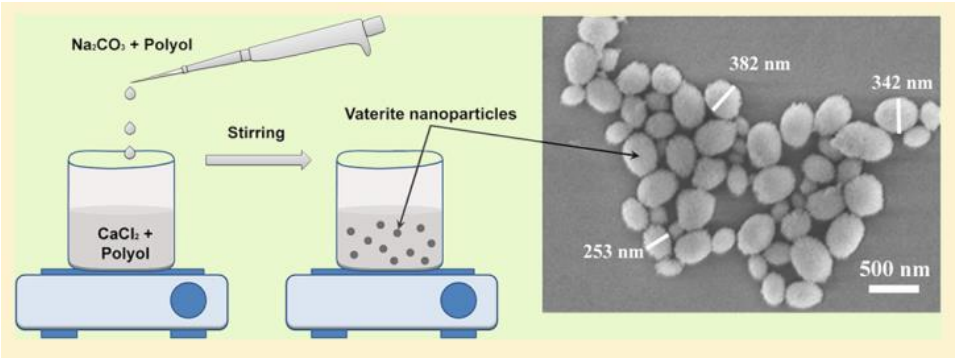


Figure 3.59 Decrement of $CaCO_3$ particle size by using polyol as an additive [60]

Moreover, there was research to study the effect of OH groups in the additives on the particle size of $CaCO_3$ particles. Sucrose consisting of plenty of hydroxyl groups in its structure also used as an aqueous medium in reactant solution. [11] The OH groups can form the polymer-liked structure with Ca^{2+} increasing the viscosity of the mixing system. This increment of viscosity is also an important factor to prevent the formation of bigger spherical vaterite particles. The smallest particle size with over 99% of vaterite phase was reduced to about 400 nm by using the 50 %wt sucrose as aqueous medium under high-speed mixing 10000 rpm, 60s at room temperature (Figure 3.60). [10]

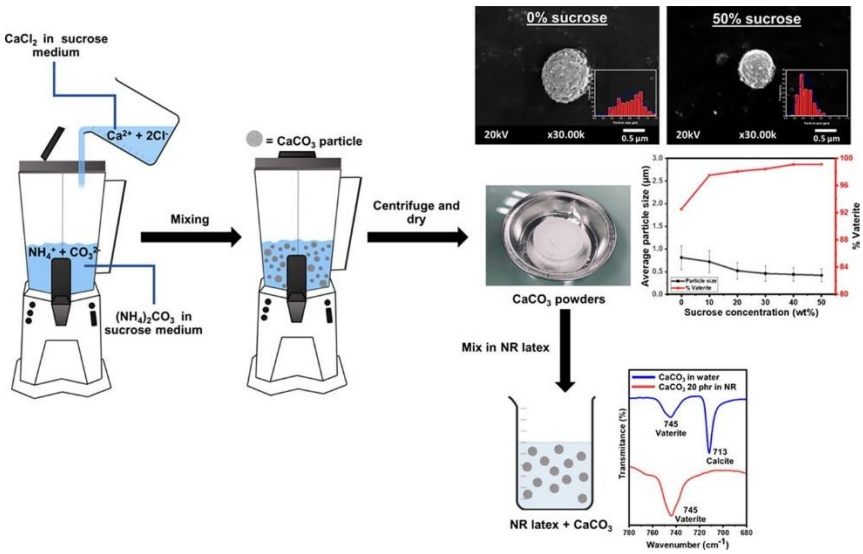


Figure 3.60 Precipitation procedure of sphere $CaCO_3$ by using sucrose as an aqueous medium resulting in 0.4 µm diameter [10]

3.3.3 $CaCO_3$ surface modification

$CaCO_3$ is a naturally hydrophilic particle. There are many researches to change the surface property of $CaCO_3$ can be modified by treatment with chemicals such as sodium oleate [111], sodium stearate [83], stearic acid [16] and olive soap [13].

A. Barhoum et al. used anionic surfactants based on fatty acids (sodium oleate) to modify the surface of $CaCO_3$ particles. [111] Using 2 wt% sodium oleate in the monodistilled water of CO_2 carbonation system showed that rhombohedral particles having the average water contact angle raised to 130° (see Figure 3.61).

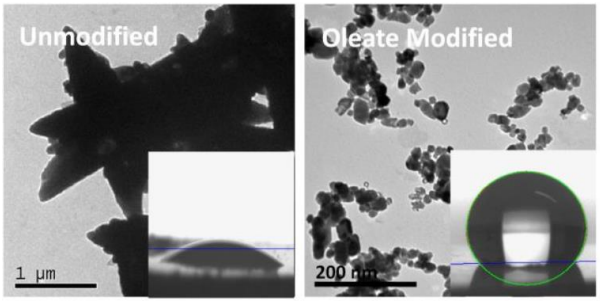


Figure 3.61 TEM images of water contact angle of ultra-hydrophobic $CaCO_3$, unmodified (left) and modified (right) with sodium oleate [111]

N. Tao et al. fabricated cellulose/$CaCO_3$ composites by firstly coating spherical $CaCO_3$ on the surface of ultrathin titania gel film-modified filter paper as shown in Figure 3.62(b). [83] The spherical particles on the filter paper were transformed into needle-like aragonite crystals (Figure 3.62(c) via a crystal growth process. Figure 3.62(d) presented the $CaCO_3$ surface modification by immersing in sodium stearate resulting in super hydrophobicity with 153^o of contact angle.

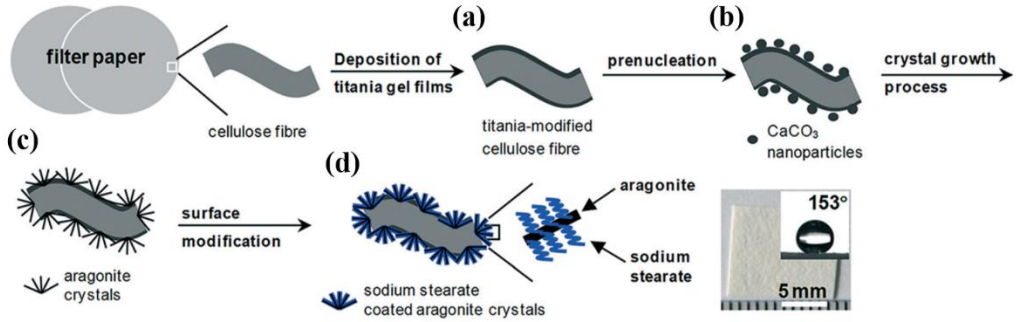


Figure 3.62 Illustration of the surface treatment process of superhydrophobic aragonite $CaCO_3$ coated on filter paper: (a) deposition of titania gel film filler paper, (b) prenucleation of $CaCO_3$ on the surface of cellulose, (c) crystal growth process/polymorph transformation of $CaCO_3$, and (d) surface modification of $CaCO_3$ by sodium stearate [83]

R. Jafari et al. prepared a superhydrophobic surface by spray coating a mixture of $CaCO_3$ particles, stearic acid and polymer latex suspensions on an aluminum substrate. [16] The results as presented in Figure 3.63 showed that stearic acid plays the most significant role in affecting the wettability of the coating surface.

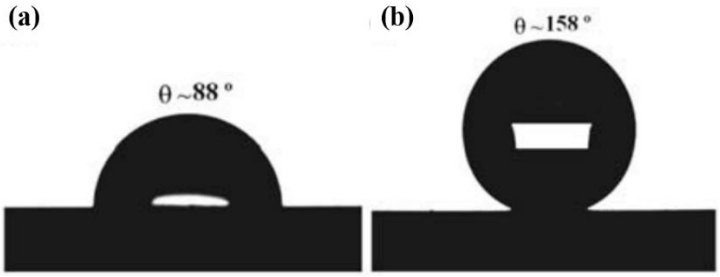


Figure 3.63 Water droplets on (a) polished aluminum, and (b) superhydrophobic surface [16]

L. Abidi and coworkers added olive soap to the Na_2CO_3 reactant before the mixing step started. [13] The contact angle result showed that in the presence of 0.4 g soap, the angle between the powder surface and water droplet is changed from 0 to 163^o for 30^{o}C, and 175^o at 80^{o}C which can be concluded that the wettability of treated $CaCO_3$ can be categorized as superhydrophobic $CaCO_3$. According to SEM results at 30^{o}C of mixing temperature, the morphology of $CaCO_3$ is spherical but aggregated needle-liked shape with rough surface at 80^{o}C of precipitated temperature. This rough surface provided the contact angle value higher than spherical $CaCO_3$. The contact angle of obtained $CaCO_3$ powders is exhibited in Figure 3.64.

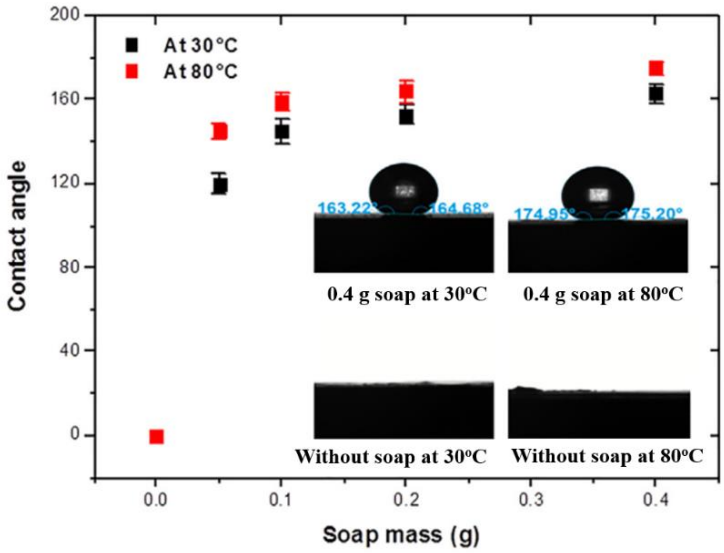


Figure 3.64 Contact angle of $CaCO_3$ precipitated at 30 and 80^{o}C with and without soap [13]

3.4 Commercial or industrial calcium carbonate

Corresponding to $CaCO_3$ naturally occurs abundantly in the forms of limestone, chalk, and marble, the ground $CaCO_3$ (GCC) and precipitated $CaCO_3$ (PCC), hence they have been used in many industrial fields. [112]

3.4.1 Ground calcium carbonate (GCC)

The GCC particles are produced by grinding or crushing the $CaCO_3$ deposits such as limestone or chalk. Generally, the particle size of GCC is bigger than 1 μm (Figure 3.65). The particle size distribution and degree of whiteness of GCC depend on the raw materials significantly. It was revealed that GCC produced from limestone and marble give narrative particle size distribution than GCC produced from chalk. [112]

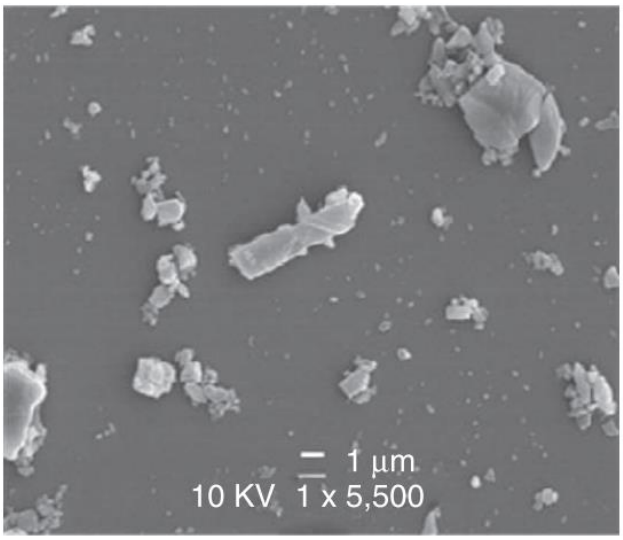


Figure 3.65 SEM images of GCC micro-particles [112]

3.4.2 Precipitated calcium carbonate (PCC)

PCC is precipitated by bubbling CO_2 through a solution of calcium hydroxide ($Ca(OH)_2$) (Figure 3.66). The final $CaCO_3$ powders of PCC have high purity with controllable particle size in the range of 0.02 to 2 μm in diameter. [112] The PCC Manufacturing is presented in Figure 3.67. [15] The SEM and TEM images of PCC nanoparticles are presented in Figure 3.68.

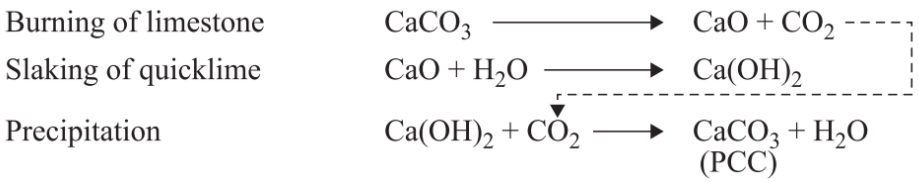


Figure 3.66 Steps of PCC nanoparticle precipitation

Generally, the calcination starts with the limestone being decomposed into $Ca(OH)_2$ and carbon dioxide (CO_2) at > 900°C. After that, the lime is slaked with water for purification and carbonization with the CO_2. The particle size and shape of PCC are controlled by reaction temperature, reaction time, and reactant concentration. [15; 112] Naturally, $CaCO_3$ surface is hydrophilic, to modify the surface to be hydrophobic, fatty acid such as stearic acid is commonly used as a surfactant and added prior to the process of filtration. [112]

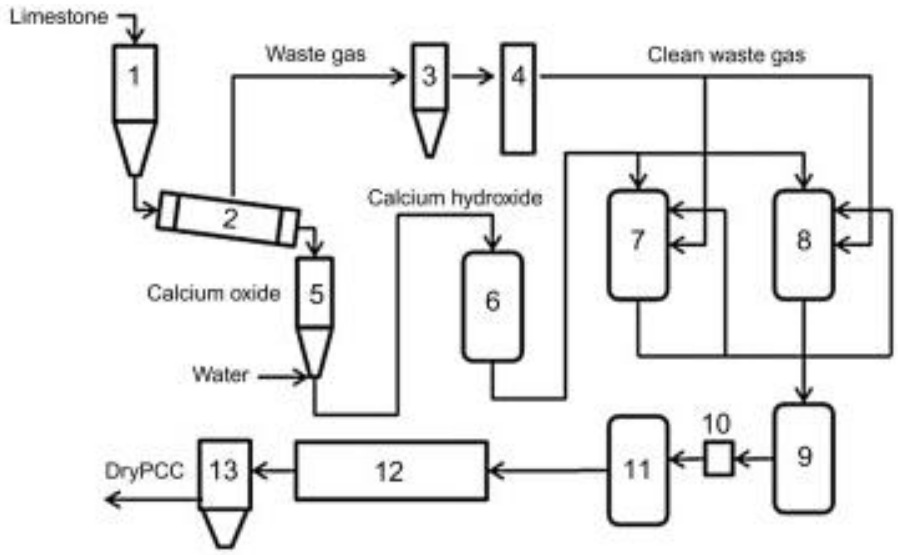


Figure 3.67 PCC Manufacturing: (1) Limestone bin, (2) Lime kiln, (3) Gas filter, (4) Gas scrubber, (5) Calcium oxide bin and slaker with cooling, (6) Slaked lime tank, (7,8) Precipitation reactors, (9) Prescreen tank, (10) Screening for unreacted calcium hydroxide, (11) Postscreen tank, (12) Filter press and dryer, and (13) Gas filter [15]

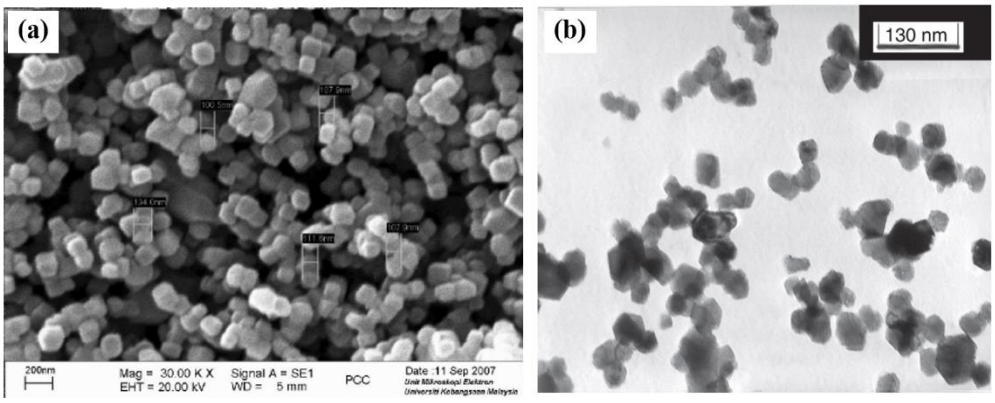


Figure 3.68 (a) SEM images of PPC typed $CaCO_3$ particles [110], and (b) TEM image of PCC nanoparticles [112]

3.5 Natural rubber (NR)

In this section, the composition of NR structure, NR compounding and vulcanizate system of NR are described.

3.5.1 Composition and structure of natural rubber

Natural rubber (NR) is an elastomeric material derived from plants in milky fluid or latex. There are many plant resources such as *Hevea brasiliensis* or Para rubber, *Parthenium argentatum* or Guayule, and *Taraxacum brevicorniculatum* or dandelion. Among rubber plants, *Hevea brasiliensis* (Figure 3.69) is the main plant that produces NR for commercial in the form of NR latex and dry NR. [27; 113]. The NR latex is freshly collected in a colloidal form which is stabilized by negative charges on the surface of rubber particles. [28] The NR is composed of rubber molecules of *cis*-1,4 polyisoprene structure (Figure 3.70) and also a few percent of non-rubber components (proteins, lipids, etc.) dispersed or dissolved in aqueous phase and adsorbed on the rubber particles. The proposed *Hevea* rubber particle is presented in Figure 3.71. [29]

NR provides several properties such as excellent flexibility, high tensile strength, high tear strength, low heat build-up, high fatigue resistance. [114; 115] Furthermore, the outstanding characteristic known as ‘strain-induced crystallization’ (SIC) under uniaxial tensile deformation with growth resistance of NR is derived from prominent self-reinforcement effect (Figure 3.72). [116; 117, 118] This unique property of NR describes the reason why NR cannot be fully replaced by synthetic rubber.

Corresponding to NR chemical structure with high content of unsaturated isoprene units along the rubber backbones, NR has some drawbacks including insufficient resistance to ozone, oxidation, weathering, solvents, chemical compared to synthetic rubbers. [119] According to its hydrocarbon structure, NR is a non-polar rubber and hydrophobic material evidenced by water droplet (Figure 3.73). [120]



Figure 3.69 *Hevea brasiliensis* tree plantation and NR latex tapped from the Para rubber tree

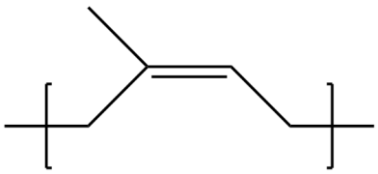


Figure 3.70 NR structure (*cis*-1,4 polyisoprene)

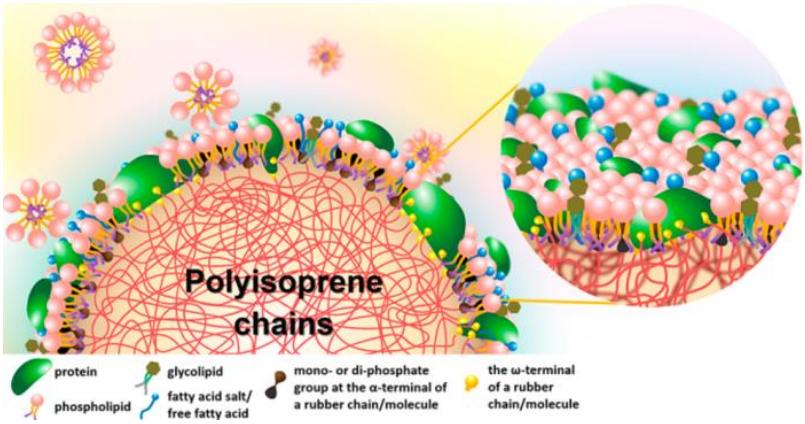


Figure 3.71 Proposed *Hevea* rubber particle model in the latex form [29]

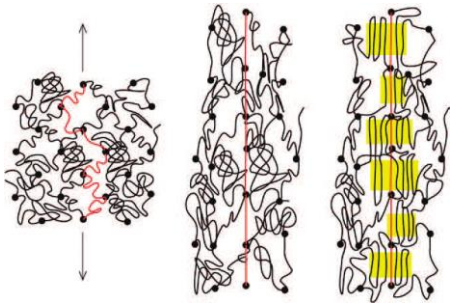


Figure 3.72 Strain-induced crystallization (SIC) of NR [117]

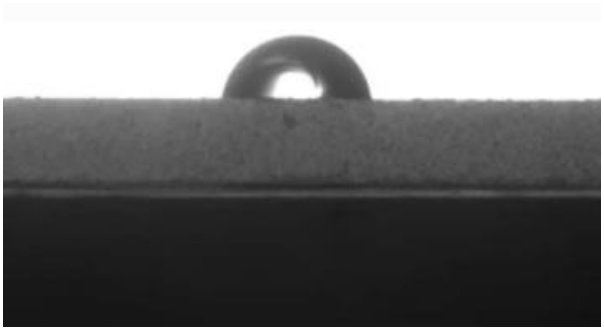


Figure 3.73 Water droplet on NR surface [120]

3.5.2 Concentrated natural rubber latex

The NR latex tapping from *Hevea* plants mostly contains about 30% dry rubber content (DRC). Generally, after tapping the latex from the rubber tree is called fresh NR latex or fresh field latex which is immediately preserved by ammonia solution. [121] The NR latex is concentrated to be 60% DRC due to the economic point during transportation. This strategy also helps in the partial elimination of non-rubber components which are soluble in water. There are three main methods applied to increase the concentration of fresh latex: evaporation, creaming, and centrifugation. [122]

3.5.2.1 Evaporation

The water in fresh NR latex is evaporated by a hot air stream in a rotating barrel. The rotating barrel is partially filled with latex and air steam passes through the barrel. Inside this rotating barrel, there is a hollow iron roller partially dipped in the latex. Ammonia is not suitable as a preservation agent for this evaporation method because ammonia can also be evaporated when water evaporates. Thus, the potassium hydroxide

(KOH) is suitable for this type of concentrating method. The evaporation method is only used in small-scale productions.

3.5.2.2 Creaming

The creaming agents, sodium alginate, are added to the preserved latex. The creaming agents increase the volume of rubber particles and therefore the density is decreased. This method required only simple equipment and the process is easy to operate but the major disadvantage of this process is time-consuming (40 – 60 hours) and used a lot of water. So, this process is not widely used in the large-scale production.

3.5.2.3 Centrifugation

This centrifugation method is the most and practical method in industrial scale. Firstly, the DRC, ammonia content, volatile fatty acid (VFA) number, and Mg^{2+} ion contents are measured. Then, to remove the Mg^{2+} ion, diammonium hydrogen phosphate (15% DAHP) is added to the latex with stirring for 20 hours resulting the precipitated magnesium sludge ($MgNH_4PO_4$). This $MgNH_4PO_4$ sludge was removed afterwards. Then, the latex is taken to the centrifuge machine and stored afterwards.

3.5.3 Natural rubber compounding

NR is the most important raw material used in motor transport or tyre manufacturing. [25] Figure 3.74 depicts the classification of tyres by the target value such as passenger car tyres, light truck tyres, truck or bus tyres, and motorcycle or industrial vehicle tyres. The tyre rubber consists of natural rubber and/or synthetic rubber as raw materials, reinforcing fillers (carbon black, silica or other inorganic fillers) A tyre comprises about 30% by weight of NR, and 20% by weight of synthetic rubber as in Figure 3.75. It means that the tyre has slightly less than 60% of polymer component with about 26% weight of filler. [25] Addition of filler in rubber has the potential to improve the stiffness and mechanical properties of NR. [123] However, some fillers are added to rubber to reduce the cost of production simultaneously. [33] From these reasons, formulating NR with some ingredients is important which has been practiced to render a rubber compound suitable for targeted applications. There are five categories

of reagents or chemicals filled in rubber compounding which are vulcanizing agent, accelerator, activator, retarder, and fillers. [124]

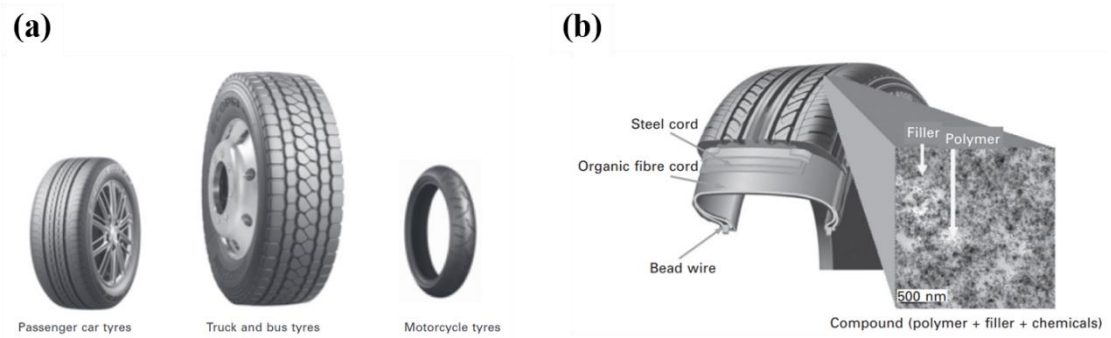


Figure 3.74 Types of tyres; (a) micro- and (b) macroscopic of tyre composites [25]

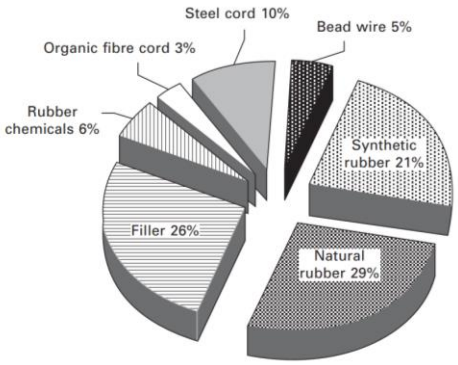


Figure 3.75 Compositions by weight % of a tyre [25]

3.5.4 Vulcanization systems and components

The vulcanization of rubber is the process of inserting crosslinks between adjacent polymer chains. This vulcanization plays an important role in the mechanical property or elasticity of the desired product such as tensile strength, elongation at break, modulus and tear strength. The vulcanization systems of rubber can be classified as sulphur vulcanization and peroxide curing system. The typical sulphur vulcanization system in a rubber compound consists of four main components: rubber, vulcanizing agent, activator, and accelerator. The peroxide curing in NR consists of the use of co-agents Type I and Type II. Typically, Type I co-agents are polar molecules, low molecular weight multifunctional compounds (e.g. N,N'-m-phenylenedimaleimide, bismaleimides), which dissociate into very reactive radicals and initiate primarily the

addition reactions. Meanwhile, Type II co-agents are polar molecules such as triallyl cyanurate, and triallyl isocyanurate, which able to form more stable free radicals. [125] Generally, these co-agents are multifunctional low molecular weight organic compounds, which are highly reactive towards free radicals. The co-agents can react in the peroxide vulcanization of unsaturated elastomers by addition and hydrogen abstraction, or by only addition reactions. The advantages and disadvantages of both curing systems are listed in Table 3.9. In this section, we will discuss in more detail only the sulphur vulcanization system.

Table 3.9 Main features of sulphur and peroxide curing systems [126]

Vulcanization systems	**Advantages**	**Disadvantages**
Sulphur-cured vulcanizates	- Good tensile and tear strength - Good dynamical properties - Good abrasion resistance - Good regulation of scorch safety and optimal cure time - Good resistance to dynamic fatigue	- Low resistance to thermo-oxidative aging - High compression set - Possibility of reversion during vulcanization
Peroxide-cured vulcanizates	- Good heat-ageing stability - Good electrical properties - Low compression set - Simple formulation of rubber compounds - Rapid vulcanization without reversion - No discoloration of finished parts	- Possibility of preparing transparent products - Worse tensile, elastic and dynamic properties - Low scorch safety - Sensitivity to elemental oxygen during curing certain components of rubber compounds, such as anti-degradants, may consume peroxide radicals generally higher cost

3.5.4.1 Rubber

Solid rubber or rubber latex can be considered. Solid rubber is useful in the tyre industry. [127] While, rubber latex is used in dipping goods applications such as glove, toy, balloon, and preservative. [128; 129]

3.5.4.2 Vulcanizing agent

A typical vulcanizing agent is sulphur for sulphur crosslinking system due to its cheap price, and abundant material. [130] Moreover, element sulphur is mixed easily and readily soluble in the rubber matrix.

3.5.4.3 Activator

The activator in the vulcanization system consists of zinc oxide (ZnO) and stearic acid. These chemicals form zinc stearate which promotes the vulcanization reaction. [131] The bridging bidentate of zinc/stearate complex in sulfur crosslinking of rubber is presented in Figure 3.76. The complex plays an important role to accelerate the sulfur crosslinking reaction caused by the high Lewis activity of ZnO.

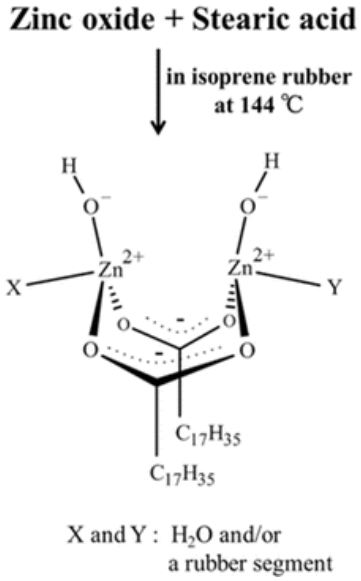


Figure 3.76 Bridging bidentate of Zinc/stearate complex in sulfur crosslinking of rubber [131]

3.5.4.4 Accelerator

The accelerators are products that increase both the rate of sulphur crosslinking and the crosslink density of rubber compounds. Most accelerators are categorized into five groups which are guanidines, mercaptobenzothiazoles, sulfenamides, thiurams, and dithiocarbamates. [132] The scorch safety, cure rate, and crosslink density obtained from different types of accelerators are listed in Table 3.10. Figure 3.77 demonstrates the chemical structure of common accelerators used in the rubber industry.

Table 3.10 Accelerators used in rubber industry [132]

Accelerator type	**Scorch safety**	**Cure rate**	**Crosslink length**
None	-	Very slow	Very long
Guanidines (DPG, DOTG)	Moderate	Moderate	Medium-long
Mercaptobenzothiazoles	Moderate	Moderate	Medium
Sulfenamides (MBS, TBBS, CBS)	Long	Fast	Short-medium
Thiurams (TMTD, TMTM)	Short	Very-fast	Short
Dithiocarbamates (Zinc dimethyldithiocarbanate, Zinc dibutyldithiocarbamate)	Least	Very-fast	Short

The sulfenamides group (CBS, TBBS, and MBS) is widely used due to its superior scorch safety. Meanwhile, the thiurams and dithiocarbamates accelerator are short on scorch safety thus they are used as primary accelerator at low levels to help activate the cure. [132] The sulphur vulcanization without any accelerator takes several hours compared to the presence of accelerators which reduces the time required for vulcanization. [133] The benefits of using accelerators in rubber are such as economy of heat, greater uniformly of final products, improved physical appearance and property, and better resistance to deterioration. [134]

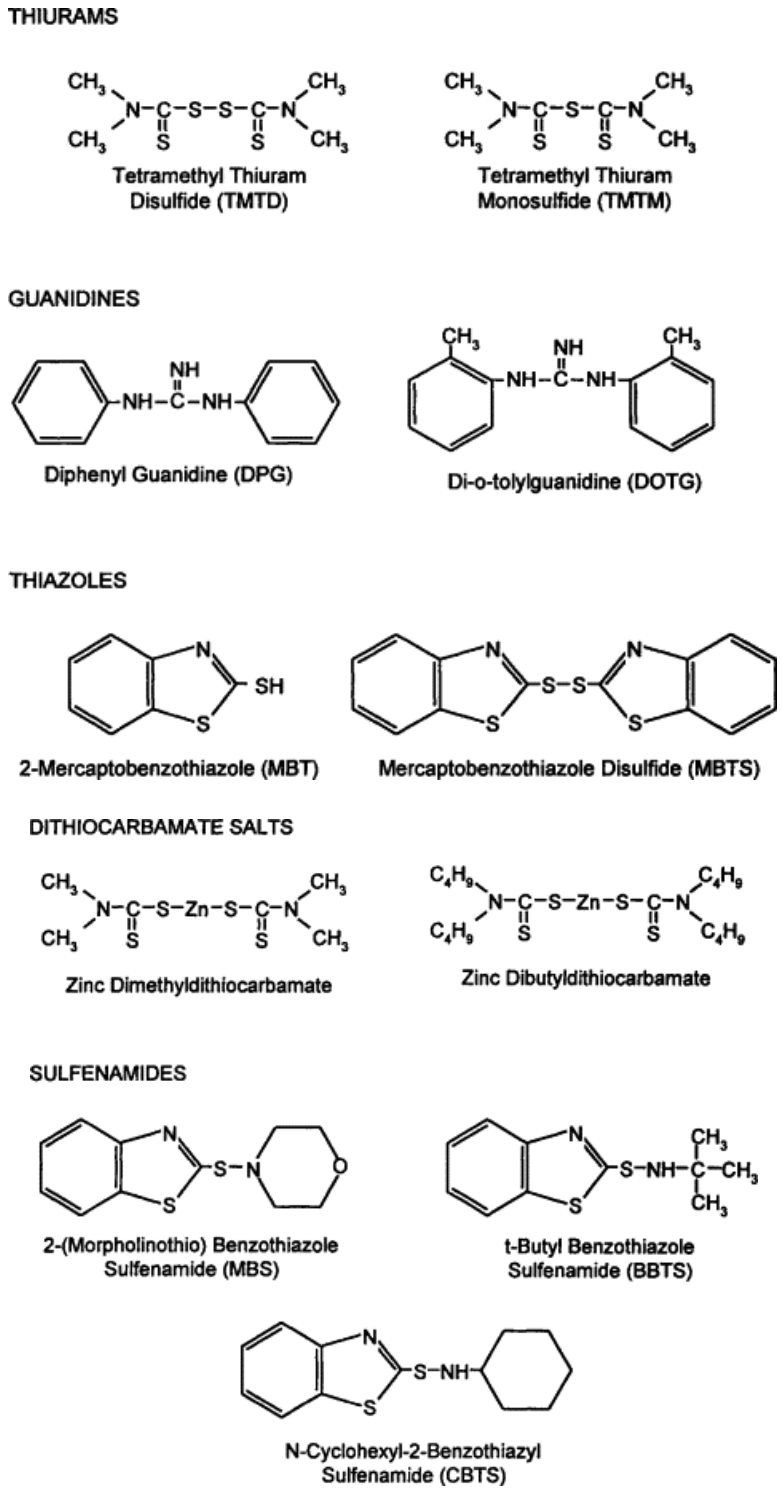


Figure 3.77 Common vulcanization accelerator structures [133]

After vulcanization process, the rubber chains were crosslinked as shown in Figure 3.78. [135] The vulcanization is a process of chemically producing network junctures by the insertion of crosslinks between polymer chains through the action of heat and pressure. The strength, modulus, hardness, abrasion resistance, and also chemical stability of rubber materials are improved. The vulcanization introduces monosulfidic, disulfidic, polysulfidic, main chain bound sulphur chains, and cyclic sulphur structures linkages in the rubber vulcanizates as exhibited in Figure 3.79. [136]

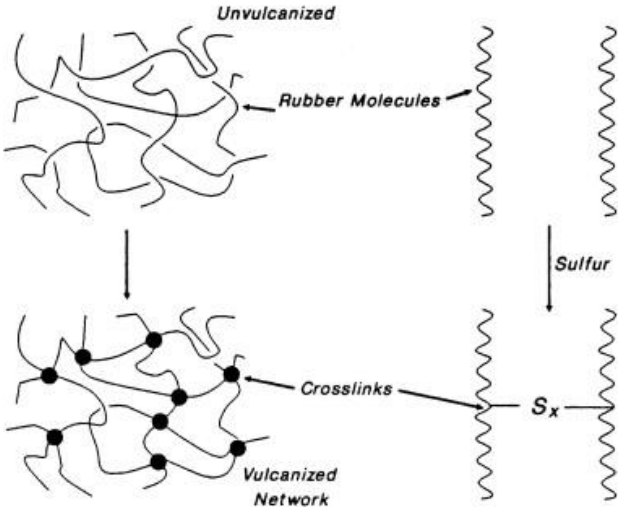


Figure 3.78 Formation of a crosslinked molecular network of sulfur crosslink system in rubber or elastomeric materials [135]

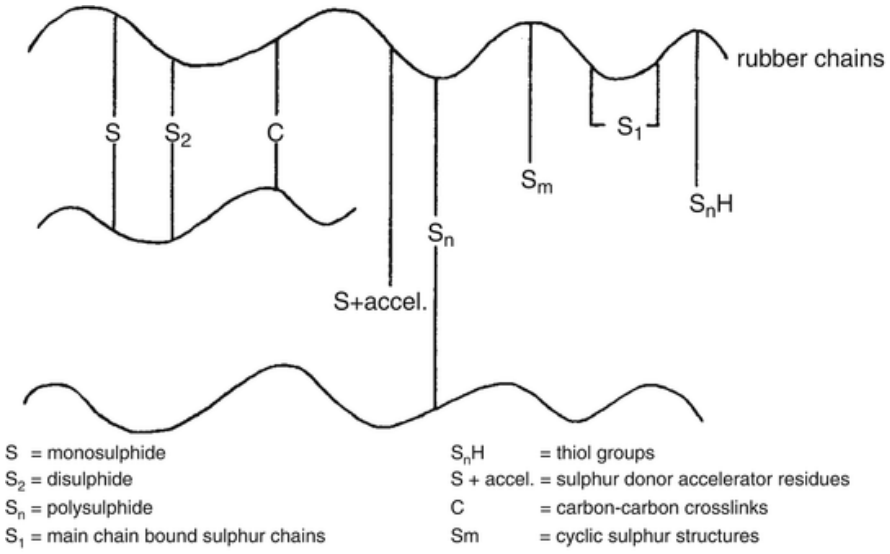


Figure 3.79 Sulphur vulcanization systems [136]

As vulcanization is an important process in rubber manufacturing, it is conducted at relatively high temperatures in the range of 140 – 200^{o}C. [130] The different ratios between sulphur and accelerator result in different types of crosslinking in the rubber matrix. Table 3.11 summarizes the types of sulphur vulcanization systems including conventional, efficient (EV), and semi-efficient (semi-EV) systems. The sulphur vulcanization provides flexibility because it can design the type of crosslink intended for specific uses or applications.

To prepare NR vulcanizates, the typical temperature of rubber vulcanization is in the range of 150 – 190 ^{o}C with an oscillation frequency of 1 Hz and the deformation of ± 1.5^{o}. [126] The characteristic rheometer of the crosslinking reaction is demonstrated in Figure 3.80. The force generated by the deformation resistance of rubber specimen is measured as torque or *M*. The rheometric behaviors of rubber can be divided into three stages of vulcanization process, including induction period, crosslinking or curing, and over crosslink stage. In the first stage (induction period), the crosslinks are not formed yet, or only small amount. The second stage is main vulcanization process. At over crosslink stage, the rubber is cured longer than optimum. No change in torque with time after attainment of maximum torque is defined as *plateau behavior*. A decrement in torque after the maximum value indicated as *reversion behavior* which means the loss of network structure by thermal aging. In the other hand, a slow increase torque after the maximum torque is defined as *marching behavior*.

Table 3.11 Types of vulcanization system used in rubber [130]

Vulcanization systems	Sulphur (S)	Accelerator (A)	Type of crosslink linkages	Technological properties
Conventional (S > A)	2.0 – 3.5	1.0 – 0.4	Polysulfidic	Increase tensile and tear strength, high compression set, and poor heat aging
Efficient (EV) (A > S)	0.3 – 0.8	6.0 – 2.5	Monosulfidic	Excellent heat aging, low compression set, low tensile, and tear strength
Semi-EV	1.0 – 1.7	2.5 – 1.0	Mixture of poly, di- and monosulfidic	Compromise or balance in terms of strength and heat aging

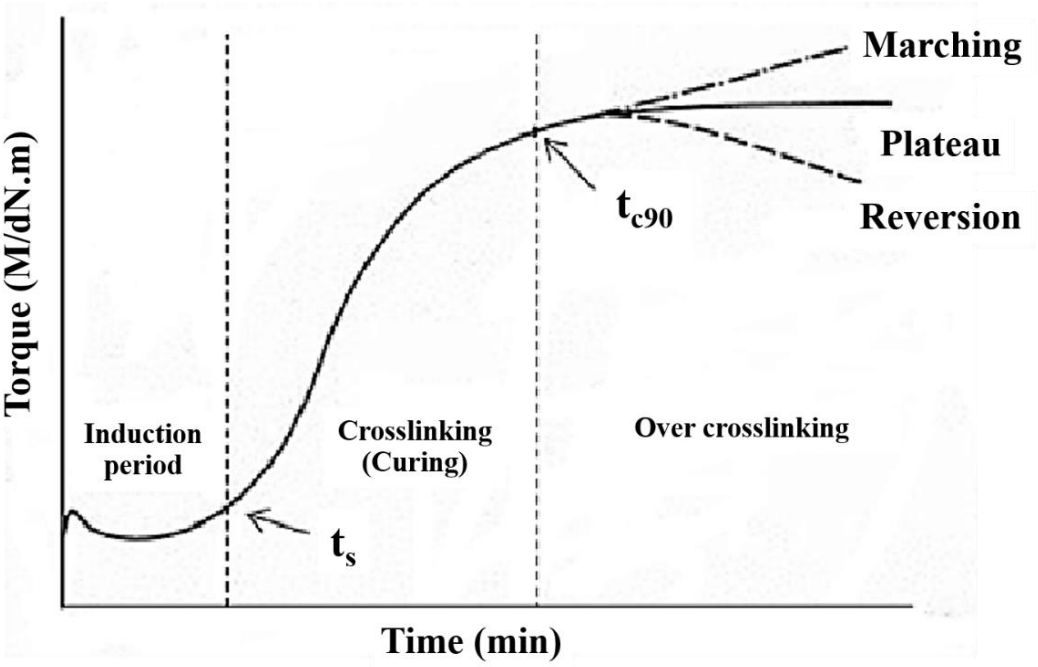


Figure 3.80 Rheometer curve of vulcanization [126]

3.5.5 Filler systems

Several researchers have extensively reported the addition of filles into rubber. Filler or reinforcement aids such as carbon black, silica (SiO_2), clay or $CaCO_3$ are added into rubber formulations to find desired material properties such as tensile strength, and abrasion resistance. Theoretically, the nanoscale filler is considered as the appropriate filler material in term of aspect ratio (length/diameter) of surface area to volume and the compatibility with the polymeric materials.

J. Leblance described the nature of rubber-filler interactions and their effects on the rheological properties of uncured materials. [36] Considering the filler, the single most important parameter in such effects is the average particle size of the filler (Figure 3.81). The particles larger than 10^3 nm do not have reinforcing capabilities and generally increase viscosity by a mere hydrodynamic effect. Reinforcement is readily obtained with sizes smaller than 100 nm such as carbon black, and silica. For ground $CaCO_3$ (GCC), the particle size is in micro scale or in the range of 10^3 - 10^4 nm that can be used as a dilution filler while precipitated $CaCO_3$ (PCC) can be used as a semi-reinforcing filler due to its 10^2-10^3 nm of particle size. The shape and aspect ratio of fillers are presented in Table 3.12.

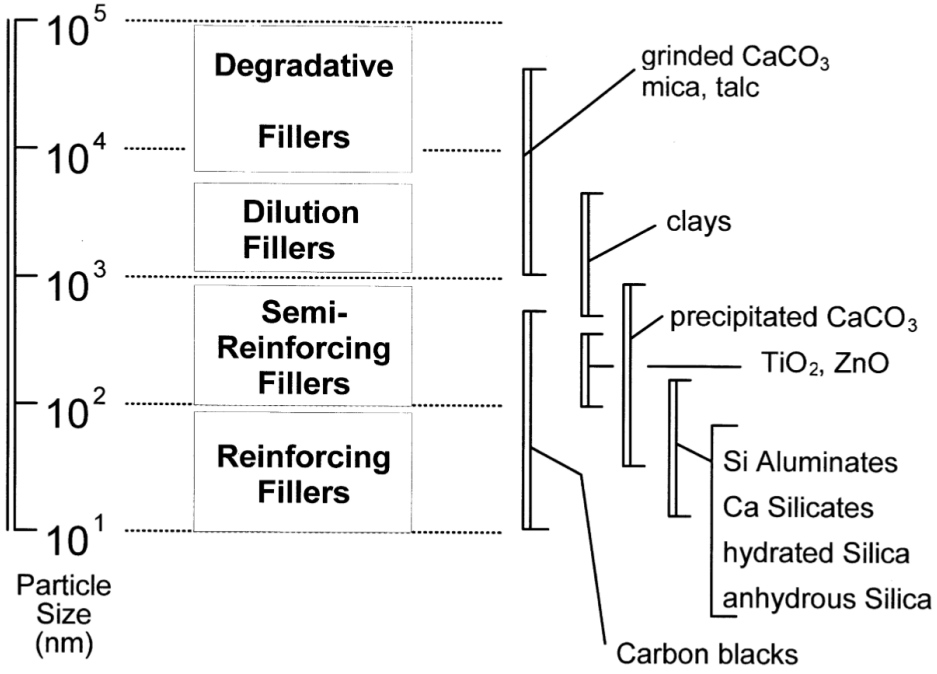


Figure 3.81 Classification of fillers according to average particle size [36]

Table 3.12 Shape and aspect ratio of various fillers [37]

Shape	Aspect ratio	Fillers
Sphere/cube	1	$CaCO_3$, feldspar, glass spheres
Block	1 – 4	Quartz, silica, barite
Platelet	4 – 30	Kaolin, talc
Flake	50 – 200+	Mica, graphite, nano clays
Fiber/needle shape	20 – 200+	Wollastonite, glass fibers, carbon fibers, carbon nanotubes etc.

Carbon Black (CB) is one of the most abundant carbon nanostructured materials. Approximately 70% of it is used as pigment and as reinforcing phase in rubber and plastics. [35] The CB materials are aggregates of nanoparticles of spheroidal shape, typically 10 to 100 nm in diameter, with an amorphous core surrounded by a shell of stacked graphene-like domains, each made of a nanometric stack of polyaromatic sheets. The CB structure is presented in Figure 3.82. [137] The unique structure and surface property of CB includes good thermal and electrical conductivity, low density, high specific surface area. The CB can be used as reinforcing agent to provide high mechanical strength of the material.[138] The utilization of CB incorporated with rubber has largely been published. [137]

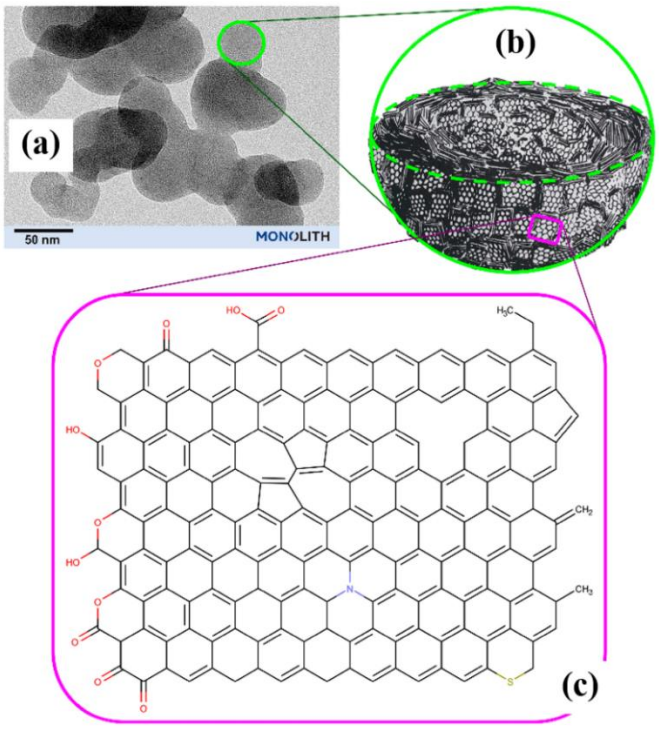


Figure 3.82 Different levels of structure and chemical structure of carbon black: (a) TEM image of N660 carbon black, (b) schematic of a primary particle (cut in half to show the internal structure) that is composed of stacks of graphene sheets, and (c) depiction of the different chemical groups on a graphene sheet in CB along with possible defects in the sheet [137]

A. R. Azura et al. investigated the effect of different types of CB including N220, N330, N550, N660, and N774 as filler loading 0, 10, 20, 30, 40, and 50 phr on mechanical properties of NR composites. [139] The particle size and surface area of CB are listed in Table 3.13. The rubber/CB and other ingredients were compounded using 2-rolls mill mixing machine. The results showed that N220 gave the highest tensile strength (29 – 30 MPa) at 20 phr filler loading, compared to other types of CB. The N220 has small particle size with high specific surface area. While, the N330 distributed and interacted well with rubber matrix.

Table 3.13 Particle size and surface area of different types of carbon black [139]

Carbon black	Particle size (nm)	Average surface area (m^2/g)
N220	20 – 25	112 – 115
N330	28 – 36	76 – 80
N550	39 – 55	39 – 41
N660	56 – 70	34 – 36
N774	71 – 96	31 – 32

Tensile strength of rubber increases when the CB loading increases. [140] Helson M. da Costa and team added N774 in NR vulcanizate. The N774 CB was varied from 0, 10, 20, 30, 40 and 50 phr. The results provided that the tensile strength of NR/N774 composite increased when filler loading increased until maximum loading value was 20 phr. The tensile strength of NR/N774 composite at 20 phr of CB loading was 25 – 26 MPa.

Among many types of CB, N330 is widely used as a reinforcing filler in NR. [141] The grades, production processes, selected properties and uses of different types of CB are demonstrated in Table 3.14.

Table 3.14 Grades, production processes, selected properties and uses of different types of CB [141]

Type	ASTM	Production process and/or feedstock	Average primary particle diameter (nm)	Primary rubber processing properties and uses
Super-abrasion furnace black	**N110**	Oil furnace	17	High reinforcement; used in special and off-road tyre products for which high abrasion resistance is required.
Intermediate Super-abrasion furnace black	**N220**	Oil furnace	21	High reinforcement and tear strength, good processing; used in passenger, off-road and special tyres for which good abrasion resistance is required.
High-abrasion furnace black	**N330**	Oil furnace	31	Medium-high reinforcement, low modulus, high elongation, good flex, tear and fatigue resistance; used in tyre tread, carcass and sidewall compounds, motor mounts, weather-stripping and bicycle tyres
Fast-extruding furnace black	**N550**	Oil furnace	53	Medium-high reinforcement, high modulus and hardness, low die swell and smooth extrusion; used in tyre inner liners, carcass and sidewall compounds and other extruded goods
General purpose furnace black	**N660**	Oil furnace	63	Medium reinforcement and modulus, good flex and fatigue

Table 3.14 (cont.) Grades, production processes, selected properties and uses of different types of CB [141]

Type	ASTM	Production process and/or feedstock	Average primary particle diameter (nm)	Primary rubber processing properties and uses
				resistance, low heat build-up; used in tyre carcass, inner liners andsidewalls, sealing rings, cable jackets, hose and extruded goods
Semi-reinforcing furnace black	**N762**	Oil furnace	110	Medium reinforcement, high elongation and resilience, low compression set; used in mechanical goods, footwear, inner tubes and floor mats
Medium thermal black	**N990**	Natural gas	320	Low reinforcement, low modulus, hardness, hysteresis and tensile strength, high elongation and loading capacity; used in wire insulation and jackets, mechanical goods, footwear, belts, hose, gaskets, O-rings and tyre inner liners

Silica (SiO_2) is also one of the most important reinforcing fillers in the rubber industry. [34] As a reinforcing filler category, silica provides a unique combination of high tear strength, high modulus and fatigue resistance. The incorporation of SiO_2 in rubber was investigated from low (<50 phr) and high (>50 phr) loading. [142] The results showed that at low silica content, the hardness increased marginally with silica loading. While, at high silica loading, the filler–filler network should significantly increase the hardness. The NR/SiO_2 composite became harder and stiffer due to the silica–rubber interactions reducing the mobility of rubber chains,

making the compound more rigid, and the elasticity of the rubber chains decreased, resulting in the increase in the stiffness. Importantly, the tensile strength of NR/SiO_2 composites increased slightly with the filler content up to 50 phr and then increased significantly beyond 50 phr. As silica particles are small with a narrow particle size distribution, resulting in a uniform distribution in the rubber matrix. [142] However, using silica for rubber reinforcement, poor dispersion of the silica is obtained due to the polarity difference. It is required silane coupling agents to enhance silica-rubber interaction and dispersion of silica in the rubber matrix. Z. Junchi et al. used 3-mercaptopropyl-ethyoxyl-di(tridecyl-pentamethoxy)-silane (Si-747) as a silane coupling agent in NR/SiO_2 compounds. [143] They revealed that the physical and chemical interactions between silica and silane coupling agent effected on the property of NR/silica composites, caused by hydrogen bonding between Si-747 and silica (Figure 3.83). The property e.g. modulus, tensile strength, abrasion resistance was improved.

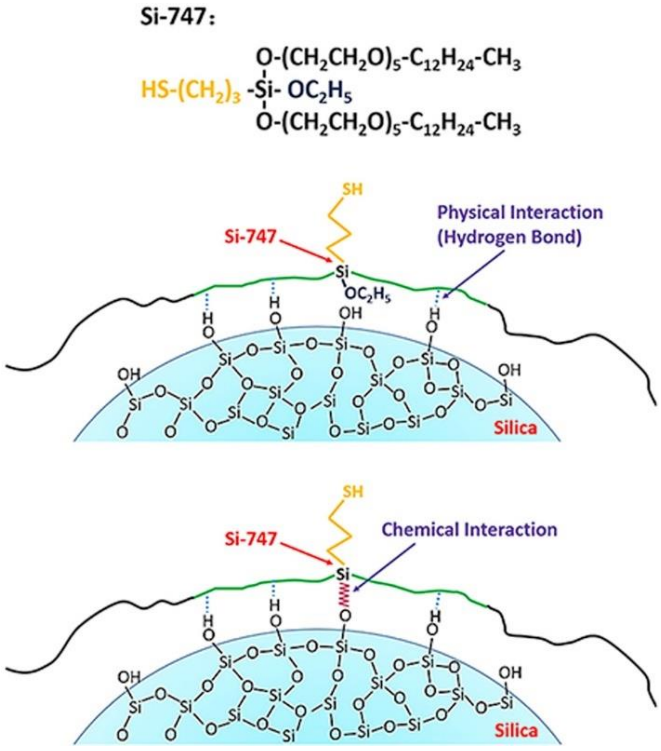


Figure 3.83 Physical and chemical interaction between silica, silane coupling agent and NR [143]

3.6 Calcium carbonate filled rubber composites

The definition of composite can be defined as a material formed by combining two or more materials of filler and polymer matrix to have unique and new properties. The constituents of the composite material must not dissolve or blend into each other and they retain their chemical and physical properties. [144]

3.6.1 $CaCO_3$ in natural rubber composite

$CaCO_3$ powders can be used as dilution and reinforcing fillers in polymer composites depending on its particle size and specific surface area. The nanosized $CaCO_3$ has prominent mechanical/optical properties in polymer composite due to its high specific surface area, chemical activity and superior barrier effects. Several researches were carried out to study the effect of $CaCO_3$ in NR composites.

Q. Fang et al. added nano-$CaCO_3$ (NCC) with different forms i.e. spherical, chain shape, and cube-shaped particles (Figure 3.84) with 30, 50, and 80 nm of size into NR matrix to prepare NR/NCC composites. [30] Various amount of $CaCO_3$ (20, 40, 60, 80, and 100 phr) were investigated. The tensile strength results revealed that when the amount of NCC increased, the tensile strength initially improved up to an optimum level at 60 – 80 phr. The spherical shape of NCC has a larger surface area compared to chain and cube shapes, resulting in better interaction well with the rubber matrix, hence the tensile strength of spherical NCC added NR vulcanizate exhibited the highest tensile strength (Figure 3.85). This excellent interfacial adhesion between spherical NCC particles and NR matrix could transfer the stress from rubber to filler effectively during stretching providing the reinforcing efficiency. Meanwhile, the chain and cube type of NCC particles tend to agglomerate into larger aggregated particles in rubber matrix. These agglomeration of NCC particles cause occurrence of voids and reduce the effective interfacial adhesion between NCC and NR. The 80 nm of cube shape had the lowest tensile strength value among the cube shape (30, 50, and 80 nm). Additionally, the hydrophilic surface of NCC also reduced the interfacial interaction with rubber vulcanizate matrix. The elongation at break analysis revealed that at low filler loading (< 60 phr) has higher elongation at break compared to high level of loading (Figure 3.85). The low quantities of NCC filler would not cause disruption to the entanglement of polymer chains to slide freely when subjected to extension. This is the evidence to

conclude that the particle size and shape of filler play important role in the mechanical property of rubber composite.

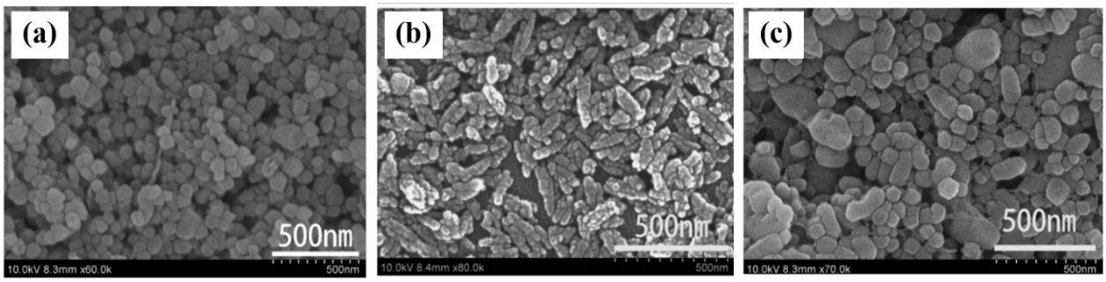


Figure 3.84 SEM images of NCC with (a) spherical, (b) chain, (c) cubic shapes [30]

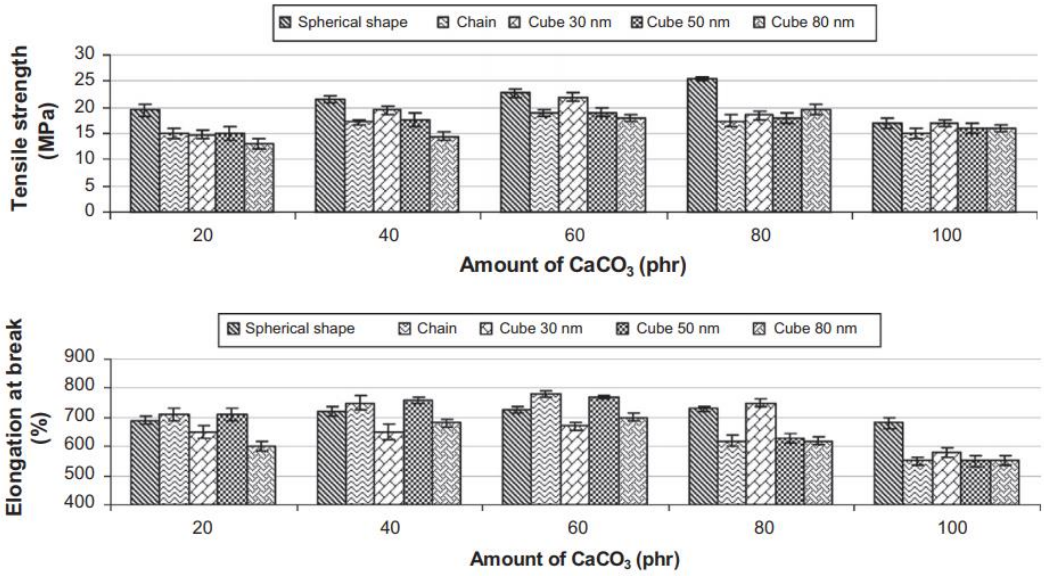


Figure 3.85 Tensile strength and elongation at break of NR/NCC composites at different of NCC load [30]

M. Lay et al. broke down the particle size of purchased $CaCO_3$ by using ball mill, ultrasonic techniques and prepared NR/$CaCO_3$ film. [33] The particle size of $CaCO_3$ decreased when the processing time increased in both mechanical methods. The particle size of $CaCO_3$ is reduced down from 5.21 µm to 1.4 µm with less agglomerate using ultrasonication (120 minutes) and ball mill (72 hours). The NR/$CaCO_3$ films were prepared in latex form using high ammonia (HA) NR latex, compounded with potassium hydroxide (KOH), sulfur, ZnO, ZDEC accelerator, antioxidant, and $CaCO_3$ (5 – 20 phr)

using mechanical stirring at room temperature. The vulcanizate NR/$CaCO_3$ film showed decreasing in viscosity and crosslink density but increased swelling index. The mechanical properties including tensile strength, modulus at 100%, elongation at break of $CaCO_3$/film were improved with the optimum $CaCO_3$ addition (10 phr) but decreased for other loading compared to the unfilled NR film as shown in Figure 3.86. The tear strength of rubber film increased at 5 phr of $CaCO_3$ loading. The micro scaled $CaCO_3$ particle size and broad particle size distribution reduced the mechanical property of the filled NR product as presented in Figure 3.87.

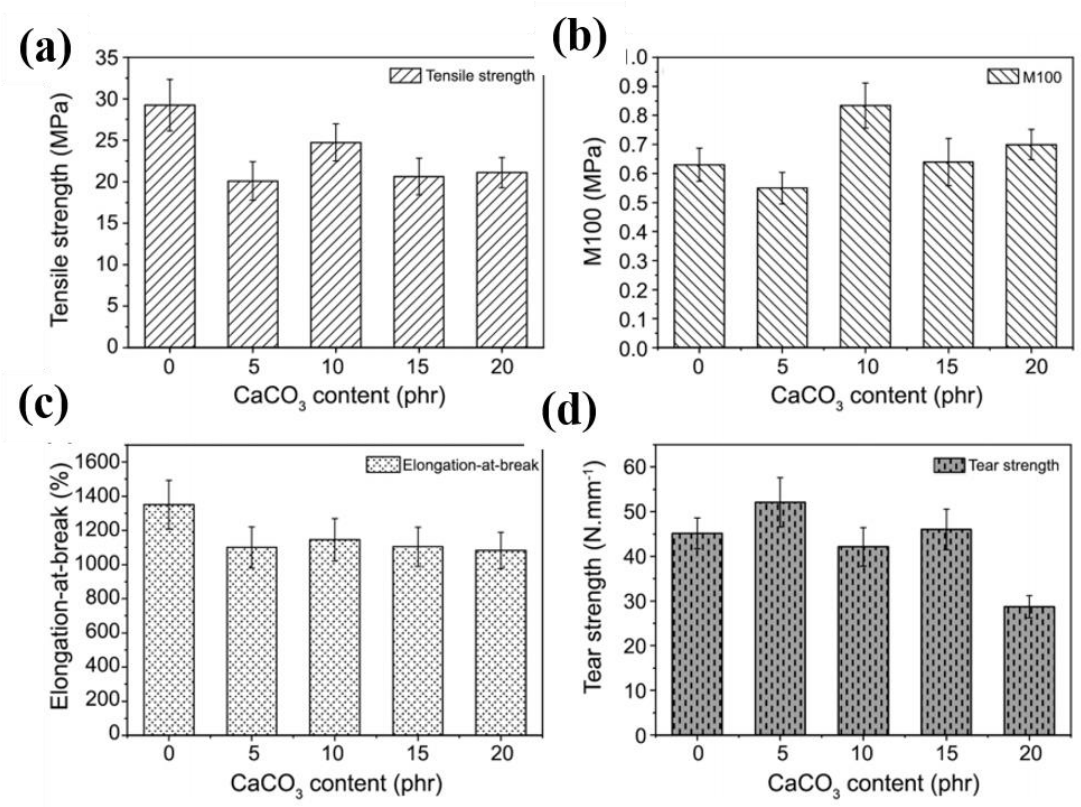


Figure 3.86 Mechanical properties of NR/$CaCO_3$ films at filler contents 0, 5, 10, 15, and 20 phr: (a) tensile strength, (b) modulus at 100%, (c) elongation at break, and (d) tear strength [33]

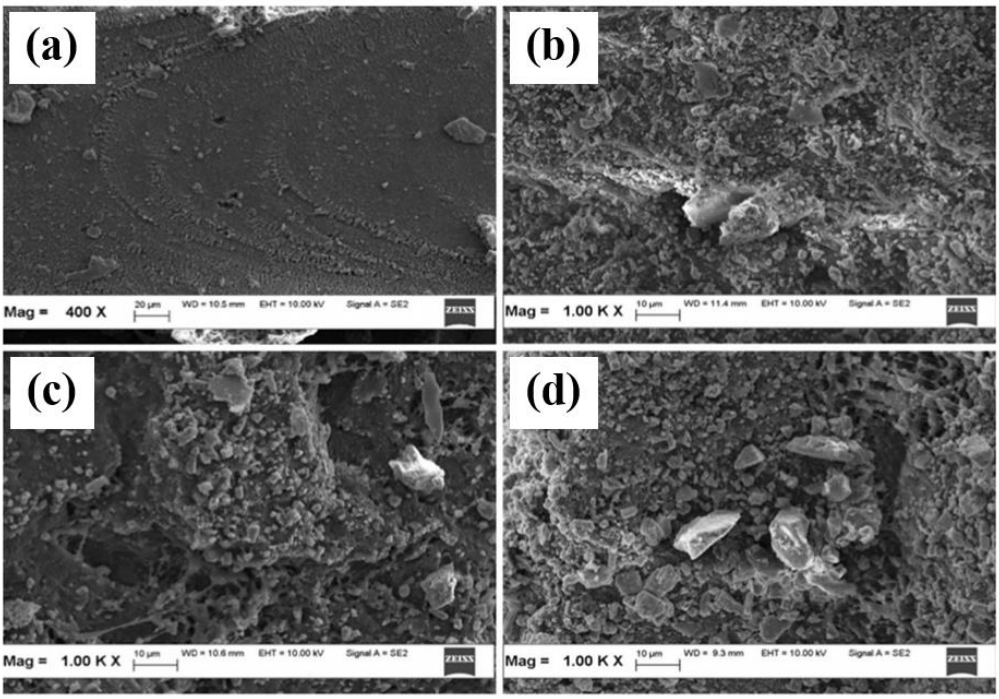


Figure 3.87 SEM micrographs of fracture surface of (a) unfilled NR film and NR/$CaCO_3$ film with different filler loading: (b) 5, (c) 10, and (d) 20 phr [33]

I. Surya et al. prepared $CaCO_3$ filled NR compounds without and with lauryl alcohol (LA) as a new rubber additive. [41] They studied the effect of oily LA as a compatibilizer to solve the incompatibility of hydrophilic $CaCO_3$ and NR (hydrophobic / non-polar rubber). The $CaCO_3$ (30 phr) was treated with LA (0, 1, 3, 5, and 7%) before addition into the NR. The results showed that tensile strength of NR/ $CaCO_3$ composite increased when LA content increased. The optimum loading is 5 % giving the tensile strength of 20.30 MPa compared to neat NR (15.70 MPa). The LA could enhance the dispersion of $CaCO_3$ in NR matrix and used as a compatibilizer to increase the flexibility of filled NR.

3.6.2 $CaCO_3$ in synthetic rubber composites

Synthetic rubber (SR) is generally comprised polymer by man-made which was developed during World War II. [145] Synthetic rubbers are synthesized from fossil petroleum, and used in tire manufacturing. [146] The most common synthetic rubbers are polybutadiene rubber (BR), acrylonitrile-butadiene-styrene (ABS), styrene-butadiene copolymer rubber (SBR). In tyre production, SBR rubber is used in tyre tread

due to its good abrasion resistance. [145] One tyre may contain of natural rubber, synthetic rubber, fillers such as carbon black, silica or $CaCO_3$, steel, plasticizers, lubricants, antioxidants, and other components. [146]

L. Jiang et al. prepared ABS composites reinforced by micro-$CaCO_3$ (MCC) and nano-sized precipitated $CaCO_3$ (NPCC). [147] The researchers used 23% of acrylonitrile, 13% of butadiene and 64% of styrene to produce ABS. The NPCC particulates are in cubic shape with average primary particle size of 40 nm. The MCC has a mean particle size of 5 μm. The MCC/ABS and NPCC/ABS composites were prepared by Haake Conical Twin Crew Extruder to disperse the NPCC and MCC homogeneously in ABS matrix. The mechanical properties revealed that MCC increased the modulus of neat ABS but decreased its tensile and impact strengths. NPCC/ABS composites showed superior properties over the MCC. This was attributed to the larger interfacial area of NPCC than that of MCC. Hence, the NPCC could be used as a reinforcing additive to improve the properties of materials while MCC is commonly used to increase modulus or reduce the cost of production line.

J. Fan-long and coworkers revealed that the thermal stabilities of BR/nano-sized $CaCO_3$ composites were increased by increment of $CaCO_3$ amounts but the glass transition of the composites remained approximately constant. [148] The nanosized $CaCO_3$ particles used in their study were in the range of 40 – 70 nm with specific surface area of 20 – 30 m^2/g. The $CaCO_3$ fillers were varied from 5 to 20 wt% in BR together with curing agent (ZnO, stearic acid, sulfur and accelerator) and antioxidant. The mechanical properties showed that the BR/nano-sized $CaCO_3$ composites were improved by addition of $CaCO_3$ fillers. The increased tensile strength and elongation of the rubber composites are shown in Figure 3.88. The nano-sized $CaCO_3$ was found to be a good reinforcing filler for BR composites.

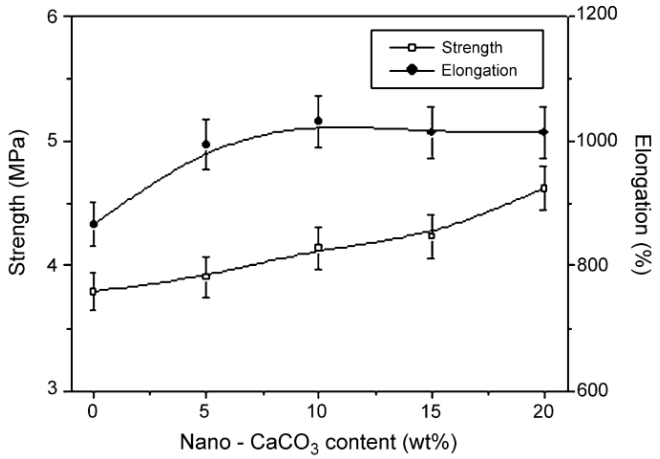


Figure 3.88 Plots of tensile strength and elongation of BR/nano-sized $CaCO_3$ composites at various $CaCO_3$ loading [148]

$CaCO_3$ could also be applied as a filler in a polymer blend. A.A. Azrem and coworkers studied the effects of different fillers of styrene butadiene rubber/recycled chloroprene rubber/carbon black (SBR/CRr/CB) blends and styrene butadiene rubber/recycled chloroprene rubber/calcium carbonate (SBR/CRr/$CaCO_3$). [149] Both SBR/CRr/CB blends and SBR/CRr/$CaCO_3$ blends were prepared using a 2-rolls mill at room temperature with blend ratios of 95/5, 85/15, 75/25, 65/35 and 50/50. The results showed that both hardness and crosslink density of SBR/CRr/CB blends and SBR/CRr/$CaCO_3$ blends increased with increasing CRr contents as shown in Figure 3.89. The increasing in hardness value was due to improvement in crosslink density in both blends.

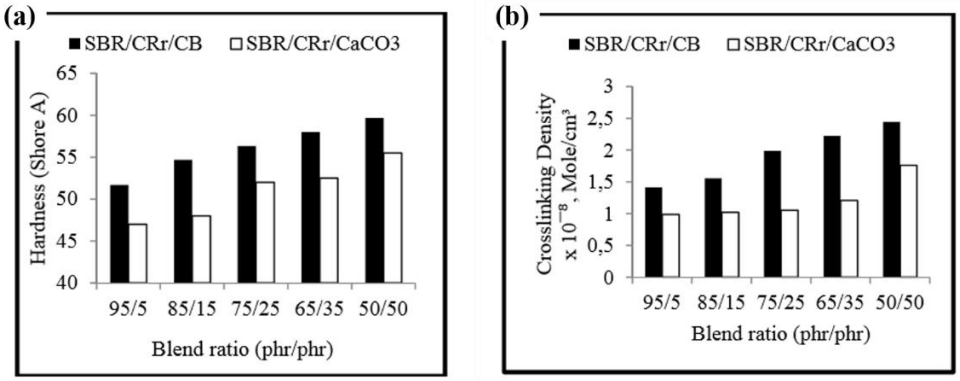


Figure 3.89 (a) hardness and (b) crosslink density of SBR/CRr/CB and SBR/CRr/$CaCO_3$ blends [149]

CHAPTER IV
MATERIALS AND METHODS

This chapter illustrates the materials and instruments used in this research work followed by the preparation procedure for different types of calcium carbonate ($CaCO_3$) including the use of olive soap for surface treatment. The procedure for incorporation of $CaCO_3$ powders into natural rubber (NR) producing NR/$CaCO_3$ composites was included. The characterization techniques and mechanical properties measurement were also covered.

4.1 Materials

The chemicals and materials used in the study are presented in Table 4.1.

Table 4.1 Information of chemicals and materials used in this work

Materials	Grade	Supplier
4QC $CaCO_3$	Commercial	Quality Minerals Public Co., Ltd (Bangkok, Thailand)
9QQ $CaCO_3$	Commercial	Quality Minerals Public Co., Ltd (Bangkok, Thailand)
Ammonium carbonate ($(NH_4)_2CO_3$)	Reagent	Acros-Organics (Paris, France)
Calcium chloride dihydrate ($CaCl_2.2H_2O$)	Reagent	Acros-Organics (Paris, France)
Carbon black (N330)	Commercial	Birla Carbon N330 (Angthong, Thailand)

Table 4.1 (cont.) Information of chemicals and materials used in this work

Materials	Grade	Supplier
Ethanol	Analytical	Merck (Delaware, USA)
High ammonia natural rubber latex (HNRL)	Commercial	Thai Rubber Latex Corporation (Bangkok, Thailand)
Nano-calcium carbonate (NCC)	Commercial	C.P. Chemical Industry Co., Ltd (Bangkok, Thailand)
N-cyclohexyl benzothiazole-2-sulfenamide (CBS)	Commercial	Kitpiboon chemical Ltd. (Bangkok, Thailand)
Stearic acid	Commercial	Kitpiboon chemical Ltd. (Bangkok, Thailand)
Sodium carbonate (Na_2CO_3)	Reagent	Acros-Organics (Paris, France)
Sodium hydroxide (NaOH)	Reagent	Honeywell (Offenbach am Main, Germany)
Sulphur (S_8)	Commercial	Kitpiboon chemical Ltd. (Bangkok, Thailand)
Sugar	Commercial	Pulverent Sugar Poedersuiker (Paris, France)
Tergitol-15-s-15	Commercial	East Asiatic Company (Bangkok, Thailand)
Toluene	Commercial	Labsystems (Bangkok, Thailand)

Table 4.1 (cont.) Information of chemicals and materials used in this work

Materials	Grade	Supplier
Olive oil	Commercial	Carrefour BIO Huile d'olive vierge extra Extraite a Froid (Massy Cedex, France)
Zinc oxide (ZnO)	Commercial	Kitpiboon chemical Ltd. (Bangkok, Thailand)

4.2 Instruments

The instruments utilized in this work are shown in Table 4.2.

Table 4.2 Instruments used in this work

Apparatus	Supplier/Trademark
Brunauer, Emmett and Teller (BET)	TriStar II 3020 V1.03 (Georgia, USA)
Blender	KENWOOD SB327 (London, United Kingdom)
Compression machine	Wabash, Genesis (Massachusetts, USA)
Centrifuge	Allegra X-22, Beckman Coulter (Indianapolis, USA)
Contact angle	SL200KS, Kino (Massachusetts, USA)
Differential scanning calorimetry (DSC)	DSC Q200, V24.11 (Delaware, USA)
Hardness tester (Shore A)	H17A, Wallace (Surrey, United Kingdom)

Table 4.2 (cont.) Instruments used in this work

Apparatus	Supplier/Trademark
Fourier Transform Infrared Spectrometer (FTIR)	Bruker Vertex (Massachusetts, USA)
Scanning Electron Microscopy (SEM)	JEOL JSM 65 VL (Massachusetts, USA)
Tensile tester	Instron Universal model 5566 (Massachusetts, USA)
Transmission electron microscopy (TEM)	JEM-2100 Electron Microscope (Massachusetts, USA)
Thermogravimetric analysis (TGA)	SDT 296 model, Universal V3.4C TA instrument (Delaware, USA)
Two-roll-mill	TEACH-LINE, Collin (Mühldorf, Germany)
Moving Die Rheometer (MDR)	Dynsic, MDR-CG (Massachusetts, USA)
Raman spectroscopy	Horiba Scientific XploRA (Lyon, France)
Rheometer	AR-G2 Magnetic Bearing Rheometer (Delaware, USA)
X-ray diffraction (XRD)	Panalytical Empyrean diffractometer (Malvern, United Kingdom)
X-ray fluorescence microscope (micro-XRF)	Horiba-XGT-9000 (Kyoto, Japan)

Part I: Preparation and polymorphic characterization of calcium carbonate ($CaCO_3$) particles

In this section, 3 different types which are spherical, bundle-liked and fiber shapes of $CaCO_3$ powders were synthesized under different mixing conditions. The

treated $CaCO_3$ powders with olive soap were also carried out to modify their surface characteristics. The preparation equipment (in Figure 4.1 – 4.8) were illustrated and created by BioRender.com with Academic institutional Plan provided by Mahidol University.

4.3 Preparation of $CaCO_3$ powders

The prepared $CaCO_3$ powders consist of spherical, bundle-liked, and fiber shapes. The preparations were synthesized under solution precipitation method.

4.3.1 Preparation of spherical $CaCO_3$

Spherical $CaCO_3$ was prepared from the reaction of $(NH_4)_2CO_3$ and $CaCl_2$. The reactants were dissolved in 50% by weight of sucrose as the aqueous medium. The preparation protocol (Figure 4.1) was carried out by mixing 1.0 M of $(NH_4)_2CO_3$ into 1.0 M of $CaCl_2$ followed by vigorous mixing conditions: 10,000 rpm of mixing speed using a blender (KENWOOD brand SB327) at 25 ± 1°C for 60 seconds. Due to the high viscosity of the solution, the precipitated powder was collected by centrifugation (Allergra X-22 Centrifuge, Beckman Coulter) at 4200 rpm for 6 minutes, then washed with ethanol 3 times. The $CaCO_3$ powder was dried in an oven at 70°C for 3 hours and stored in a dried form.

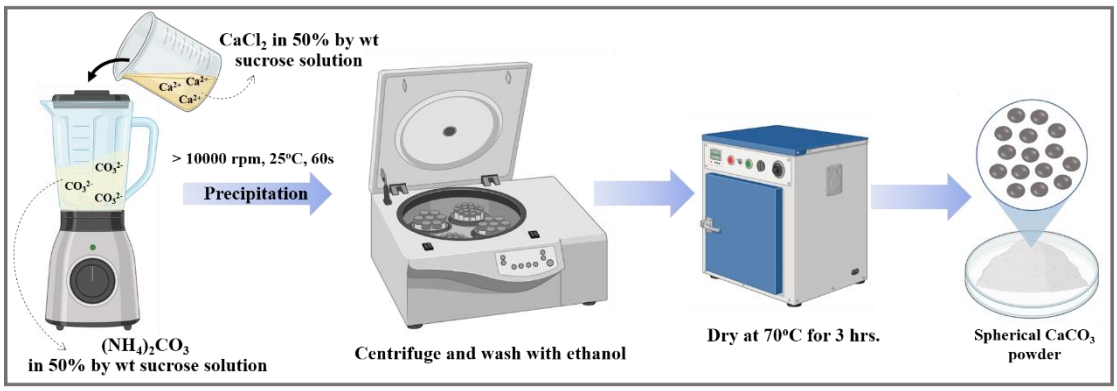


Figure 4.1 Schematic diagram for preparation of spherical $CaCO_3$ powders

4.3.2 Preparation of bundle-liked $CaCO_3$

The bundle-liked $CaCO_3$ was prepared from the reaction of 1.0 M Na_2CO_3 and 1.0 M $CaCl_2$ solutions using water as a medium (Figure 4.2). The mixing condition of Na_2CO_3 and $CaCl_2$ solutions was 80 ± 1°C, 1000 rpm using a magnetic stirrer for 60 seconds. The powders were obtained by vacuum filtration, washed with ethanol 3 times and dried in an oven at 70°C for 3 hours.

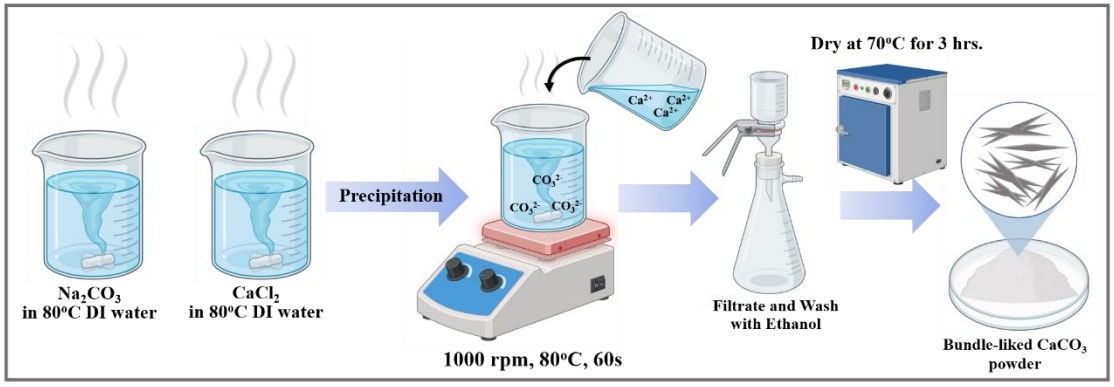


Figure 4.2 Schematic diagram for preparation of bundle-liked $CaCO_3$ powders

4.3.3 Preparation of fiber $CaCO_3$

The fiber $CaCO_3$ was prepared by using spherical $CaCO_3$ powders from 4.3.1, dispersed in DI water which was prior heated to 80°C (Figure 4.3). The transformation of the spherical shape to fiber shape was carried out by magnetic stirring at 1500 rpm for 90 minutes at 80°C. The transformed powders were filtered by vacuum filtration and washed with ethanol 3 times, then dried at 70°C in an oven for 3 hours.

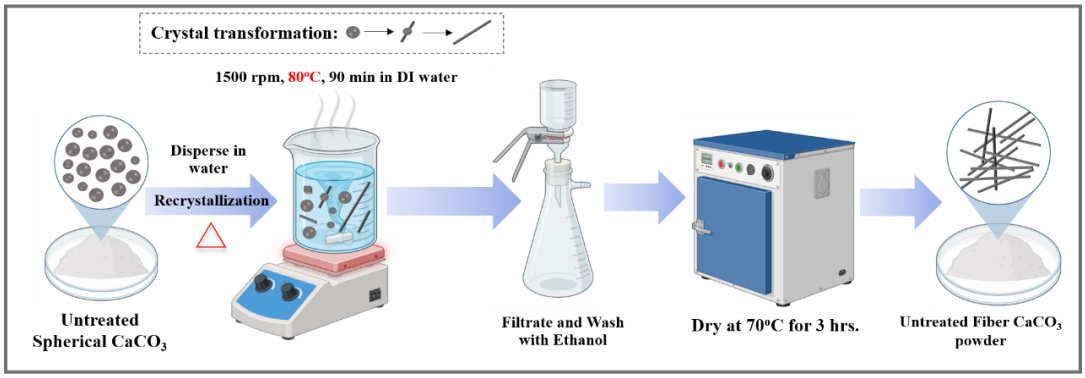


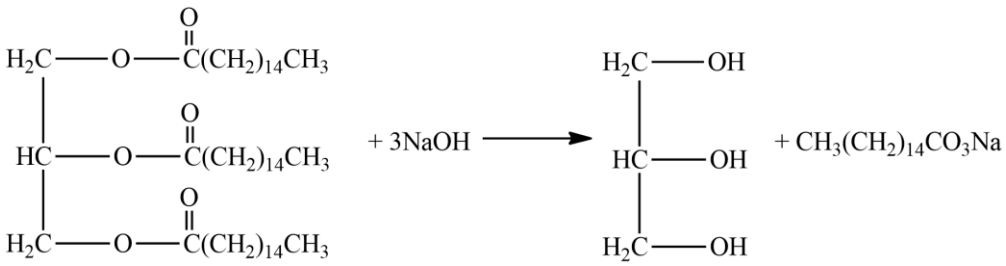
Figure 4.3 Schematic diagram for preparation of fiber $CaCO_3$ powders

4.4 Preparation of treated $CaCO_3$ powders

The prepared different shapes of $CaCO_3$ were treated with olive soap which was prepared by saponification of olive oil.

4.4.1 Preparation of olive soap

The olive soap was prepared via a saponification process between olive oil and NaOH. The triglyceride from olive oil reacted with NaOH producing glycerol and crude soap as schematized in equation 4.1. NaOH solution was prepared by dissolving 1.3 g of NaOH in solid pallets in 3.9 mL DI water (Figure 4.4). Then, the NaOH solution was mixed with olive oil 10 g.; based on the saponification number (SAP. no.) of olive oil = 184 [151]; at 500 rpm by magnetic stirring at room temperature for 3 hours. The definition of SAP. no. is the number of mg of KOH needed to neutralize the free acid in, and to hydrolyze the esters in, 1 g of substance oil. The prepared soap became more sticker during 3 hours of stirring. The obtained solid soap was dried at room temperature for a few days until became harder.



(4.1)

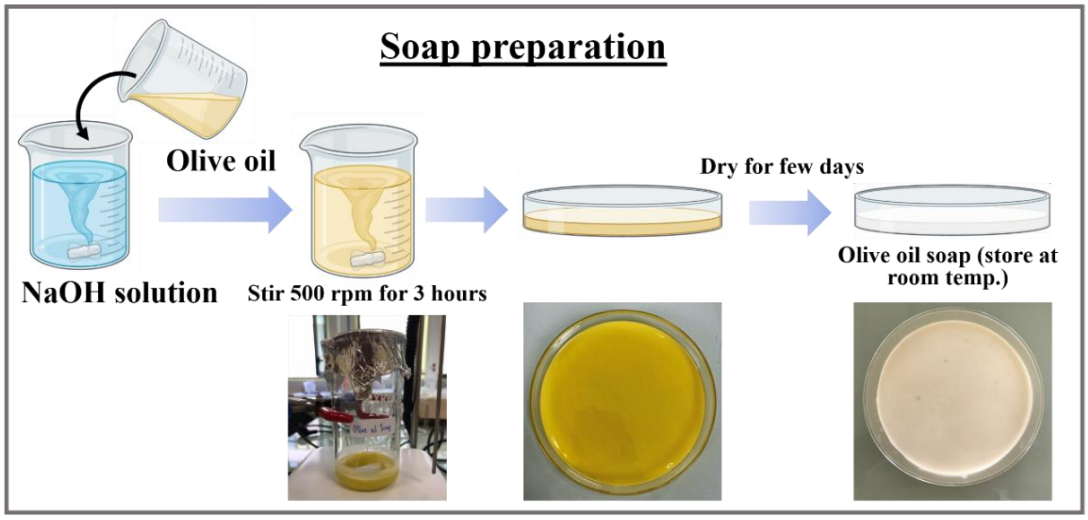


Figure 4.4 Schematic diagram for preparation of olive soap

4.4.2 Preparation of treated spherical $CaCO_3$

The 0.4 g of solid soap was dissolved in 10 mL of ethanol at 80°C. The soap solution was cooled down afterward. This soap solution was poured into 1.0 M $(NH_4)_2CO_3$ solution before mixing with 1.0 M $CaCl_2$ solution using 50% wt sucrose as an aqueous medium. The mixing speed of 10000 rpm at 25 ± 1°C was performed for 60 seconds. The turbid solution of $CaCO_3$ was found floating on the surface of the aqueous solution, indicating the change of surface property of $CaCO_3$. These treated precipitated $CaCO_3$ powder was collected by centrifugation at 4200 rpm for 6 minutes, then washed with ethanol 3 times. The obtained $CaCO_3$ powder was dried in an oven at 70°C for 3 hours and stored in a dried form.

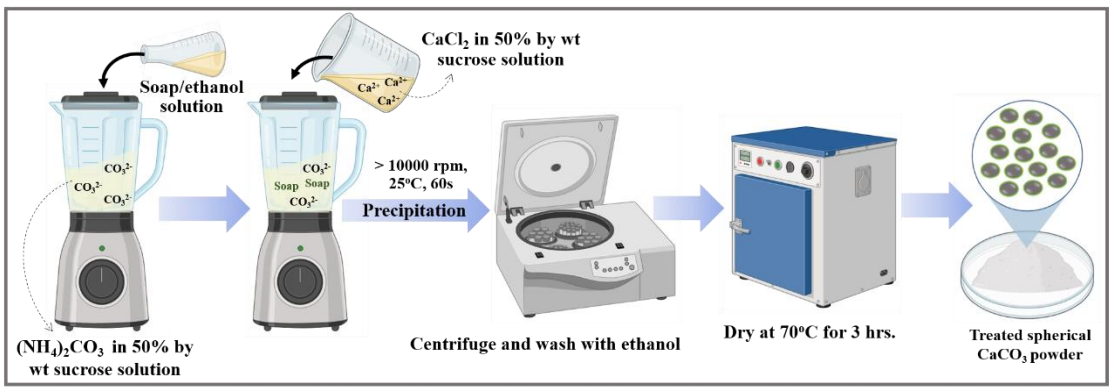


Figure 4.5 Schematic diagram for preparation of treated spherical $CaCO_3$ powders

4.4.3 Preparation of treated bundle-liked $CaCO_3$

The solid soap (0.4 g) was dissolved in 10 mL ethanol before addition to 1.0 M Na_2CO_3 solution in water. The mixed Na_2CO_3 in soap solution was mixed with 1.0 M $CaCl_2$ solutions at 80°C using magnetic stirring at 1000 rpm mixing speed for 60 seconds. The powders were collected by vacuum filtrating, and washing with ethanol 3 times. The powders were dried in an oven at 70°C for 3 hours and stored at room temperature.

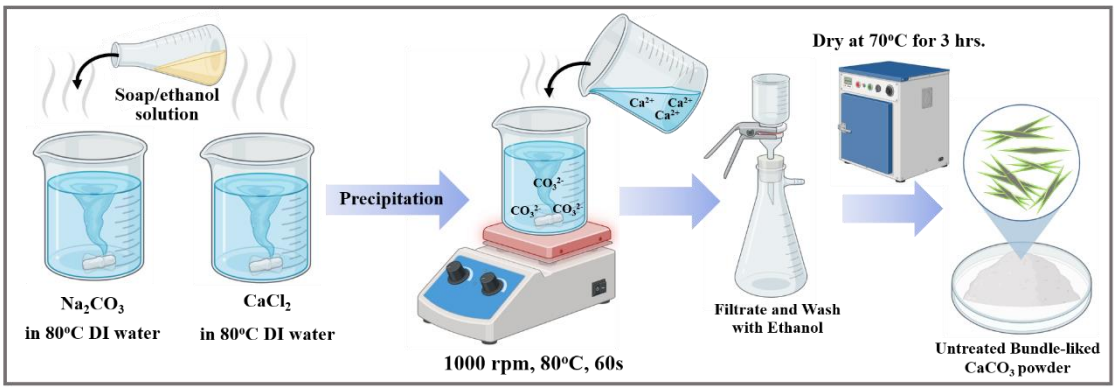


Figure 4.6 Schematic diagram for preparation of treated bundle-liked $CaCO_3$ powders

4.4.4 Preparation of treated fiber $CaCO_3$

The prepared fiber $CaCO_3$ powders were added into 80°C DI water, and stirred at 1500 rpm mixing speed. Then, the low concentration of 10 mM of Na_2CO_3 solution was freshly prepared by dissolving in DI water. The 0.4 g of soap was added into the Na_2CO_3 solution resulting in the Na_2CO_3/soap solution. This Na_2CO_3/soap solution was added to fiber dispersed in water. Then, the 10 mM $CaCl_2$ solution dissolving in DI water was added afterward. The stirring time was 30 minutes. The powders were collected by vacuum filtration, washing with ethanol 3 times, and drying at 70°C for 3 hours in the oven.

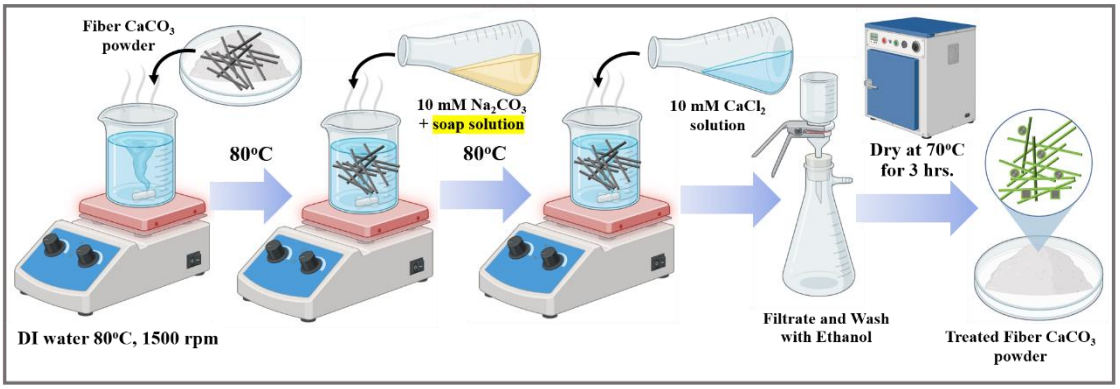


Figure 4.7 Schematic diagram for preparation of treated fiber $CaCO_3$ powders

4.5 Characterization of $CaCO_3$ particles

The morphology, polymorph, chemical structure, physical properties and thermal properties of $CaCO_3$ particles were characterized as follows.

4.5.1 Morphology of $CaCO_3$ particles

Scanning electron microscope (SEM) model JEOL JSM 65 VL operated at 20 kV with varying working distances from 10 to 11 mm was used to image the morphology of $CaCO_3$ particles coated with gold on the particle surface. The dimension, length, average size, and distribution of $CaCO_3$ particles were measured by ImageJ software (version 1.8.0). For measuring each $CaCO_3$ sample, the number of particles examined exceeded 150.

A transmission electron microscope (TEM, JEM-2100 Electron Microscope) was carried out to image the particle structure on the atomic scale. The $CaCO_3$ particles were dispersed in an ethanol solution. Then, the solution was deposited as a droplet onto a TEM grid coated with a carbon film layer.

4.5.2 Polymorphic phase of $CaCO_3$ particles

The crystal phases and polymorphs of $CaCO_3$ particles were investigated using the XRD diffractometer model Panalytical Empyrean. The XRD patterns were obtained from 2θ between 20° to 40° in a step size of 0.052° working with a monochromatic Cu-Kα radiation (λ = 1.54 Å), and 40 kV-30mA. The % polymorphs of $CaCO_3$ powders were calculated by MAUD software (version 2.94) based on Rietveld refinement. The Rietveld software MAUD was designed especially for calculating both the structural and phase parameters.

The vibration bands of the polymorphs of $CaCO_3$ particles were analyzed by Bruker Vertex 70v equipment in attenuated total reflection-Fourier transform infrared (ATR-FTIR) mode, working in the range from 4000 to 400 cm^{-1} with a resolution of 1 cm^{-1} and using 20 scanning numbers.

The XploRA Raman Microscope was used to characterize the polymorphs of $CaCO_3$ particles. The recorded spectra were operated from 400 to 4000 cm^{-1}, 785 nm, and 1200 gr/mm detector.

4.5.3 Chemical and physical properties of $CaCO_3$ powders

The surface properties or wettability of $CaCO_3$ particles were measured using a contact angle instrument (Kino, SL200KS model). A water droplet was applied on the surface of the $CaCO_3$ powder and NR vulcanizate sheet following the sessile drop method, with a capture speed of 7 frames per second, and axisymmetric drop shape analysis was performed with the Young–Laplace equation in fitting mode.

The BET surface area (m^2/g) of $CaCO_3$ powders was measured on a TriStar II 3020 V1.03 Micromeritics Instrument Corporation with nitrogen gas (N_2) analysis adsorption, using a sample mass of 2.5 g.

To study the viscosity behavior of the medium on particle size of $CaCO_3$ particles in the section of untreated and treated spherical $CaCO_3$ precipitation, the shear rate, shear stress and viscosity values of $(NH_4)_2CO_3$ in water and sucrose mediums were assessed by AR-G2 Magnetic Bearing Rheometer using Aluminum plate core 994327, 40 mm at temperature 20℃. The approximated 10 ml of solution was dropped on the aluminum plate to study the viscosity behaviors. The solutions were studied consisting of 50% wt of sucrose solution, 1.0 M of $CaCl_2$ in DI water, and 1.0 M of $CaCl_2$ in 50% wt sucrose solution.

4.5.4 Thermal properties of $CaCO_3$ powders

Thermogravimetric analysis (TGA) model SDT 296, Universal V3.4C TA instrument was used to investigate the thermal stability of prepared and commercial $CaCO_3$ powders. The 10 mg of powders were heated up from 0 – 800^oC under a nitrogen atmosphere with a heating rate of 10^oC/min.

Part II: Preparation of natural rubber (NR)/$CaCO_3$ composites and its mechanical properties

4.6 Preparation of NR/$CaCO_3$ composites

In this section, the NR/$CaCO_3$ composites were prepared by pre-dispersion of $CaCO_3$ powders into NR latex, drying and mixed with curing agents. The carbon black N330 filled NR vulcanizates also prepared as NR/N330 composites.

4.6.1 Preparation of pre-dispersed NR/$CaCO_3$ compounds

The $CaCO_3$ powders were added into 60%DRC NR latex, stirring at 600 rpm for 10 minutes by using overhead mechanical stirring. Each type of $CaCO_3$ powder was varied by 5, 10, 20, 40 and 60 phr to be filled in NR. The pre-dispersed of NR/$CaCO_3$ compounds were poured on an aluminum plate and dried at room temperature for about 2 weeks.

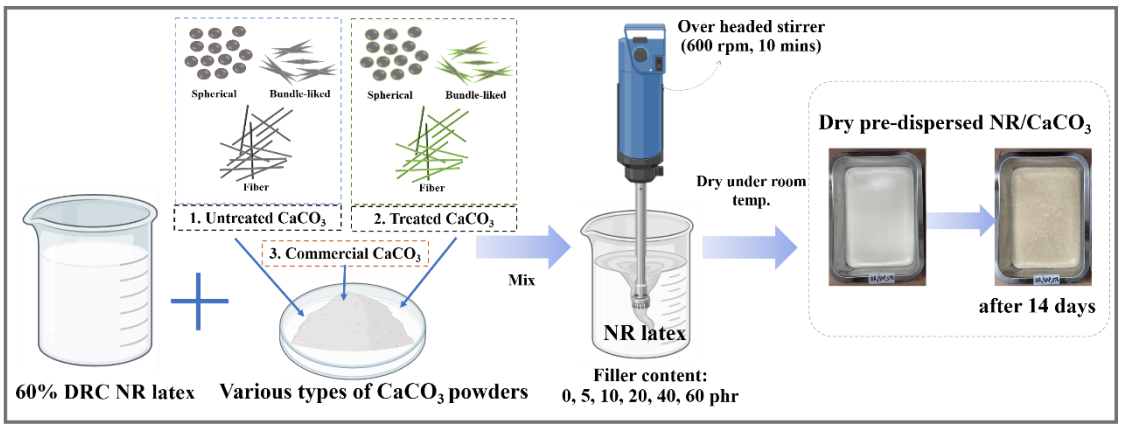


Figure 4.8 Preparation of pre-dispersed NR/$CaCO_3$ compounds

4.6.2 Preparation of NR/$CaCO_3$ vulcanizates

The dried NR/$CaCO_3$ mixture was compounded with ingredients using formulations shown in Table 4.3. All these ingredients were mixed by using a conventional COLLIN 2-roll mill mixing machine at room temperature for sulfur system crosslinking (Figure 4.9). The mixing schedule is shown in Table 4.4. Firstly, the pre-dispersed NR/$CaCO_3$ was masticated on the roll for 5 minutes. Next, the ZnO and stearic

acid were added and mixed for 5 minutes. Thereafter, the curative CBS and sulfur were added and mixed for 5 minutes. The overall mixing time was kept constant at 15 minutes. At the end of mixing, the 10 end-roll passe were made before sheeting the compound off.

Table 4.3 Mixing formulation of NR/$CaCO_3$ composites used in this study

Chemicals	**Content (phr)**
NR	100
$CaCO_3$ powders	0, 5, 10, 20, 40, 60
ZnO	1.8
Stearic acid	2.0
CBS	1.0
Sulphur	1.5

Table 4.4 Mixing schedule of NR/$CaCO_3$ composites used in this study

Mixing schedule	**Time (min)**
Load NR (Masticate rubber on roll)	0-5
Add ZnO and stearic acid	5
Add CBS and sulphur	5
10 end-roll passes	

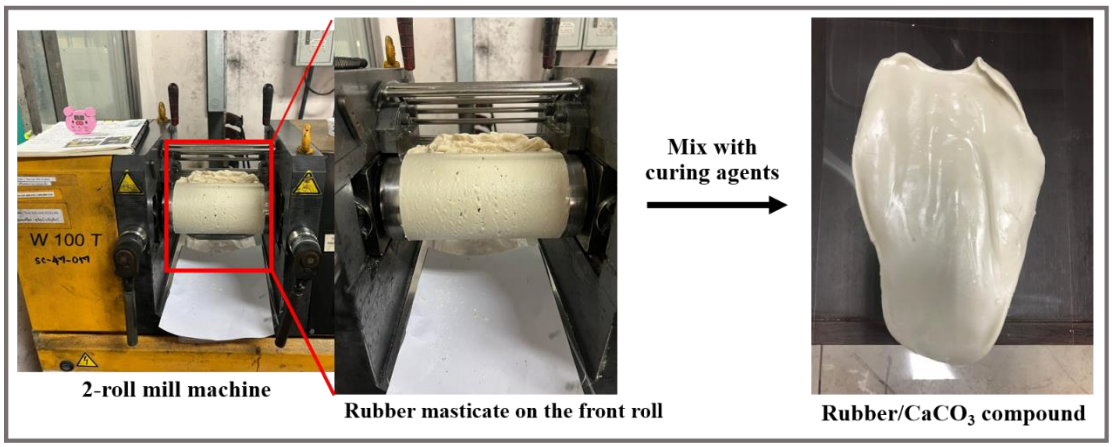


Figure 4.9 Preparation of rubber/inorganic filler compound

All formulations of prepared rubber composites including NR/$CaCO_3$ and NR/N330 are shown in Table 4.5.

Table 4.5 Composite formulations prepared in this work

Composites	NR (phr)	$CaCO_3$ (phr)									Carbon black (CB)	ZnO (phr)	Stearic acid (phr)	CBS (phr)	Sulphur (phr)
		Untreated			Treated			Commercial grade			N330 (phr)				
		Spherical	Bundle	Fiber	Spherical	Bundle	Fiber	NCC	9QQ	4QQ					
Neat NR	100	-	-	-	-	-	-	-	-	-	-	1.8	2.0	1.0	1.5
NR/Untreated Spherical $CaCO_3$ (5)	100	5	-	-	-	-	-	-	-	-	-	1.8	2.0	1.0	1.5
NR/Untreated Spherical $CaCO_3$ (10)	100	10	-	-	-	-	-	-	-	-	-	1.8	2.0	1.0	1.5
NR/Untreated Spherical $CaCO_3$ (20)	100	20	-	-	-	-	-	-	-	-	-	1.8	2.0	1.0	1.5
NR/Untreated Spherical $CaCO_3$ (40)	100	40	-	-	-	-	-	-	-	-	-	1.8	2.0	1.0	1.5
NR/Untreated Spherical $CaCO_3$ (60)	100	60	-	-	-	-	-	-	-	-	-	1.8	2.0	1.0	1.5
NR/Untreated Bundle-liked $CaCO_3$ (5)	100	-	5	-	-	-	-	-	-	-	-	1.8	2.0	1.0	1.5
NR/Untreated Bundle-liked $CaCO_3$ (10)	100	-	10	-	-	-	-	-	-	-	-	1.8	2.0	1.0	1.5
NR/Untreated Bundle-liked $CaCO_3$ (20)	100	-	20	-	-	-	-	-	-	-	-	1.8	2.0	1.0	1.5
NR/Untreated Bundle-liked $CaCO_3$ (40)	100	-	40	-	-	-	-	-	-	-	-	1.8	2.0	1.0	1.5
NR/Untreated Bundle-liked $CaCO_3$ (60)	100	-	60	-	-	-	-	-	-	-	-	1.8	2.0	1.0	1.5
NR/Untreated Fiber $CaCO_3$ (5)	100	-	-	5	-	-	-	-	-	-	-	1.8	2.0	1.0	1.5
NR/Untreated Fiber $CaCO_3$ (10)	100	-	-	10	-	-	-	-	-	-	-	1.8	2.0	1.0	1.5
NR/Untreated Fiber $CaCO_3$ (20)	100	-	-	20	-	-	-	-	-	-	-	1.8	2.0	1.0	1.5

Table 4.5 (cont.) Composite formulations prepared in this work

Composites	NR (phr)	$CaCO_3$ (phr)									Carbon black (CB)	ZnO (phr)	Stearic acid (phr)	CBS (phr)	Sulphur (phr)
		Untreated			Treated			Commercial grade			N330 (phr)				
		Spherical	Bundle	Fiber	Spherical	Bundle	Fiber	NCC	9QQ	4QQ					
NR/Untreated Fiber $CaCO_3$ (40)	100	-	-	40	-	-	-	-	-	-	-	1.8	2.0	1.0	1.5
NR/Untreated Fiber $CaCO_3$ (60)	100	-	-	60	-	-	-	-	-	-	-	1.8	2.0	1.0	1.5
NR/Treated Spherical $CaCO_3$ (5)	100	-	-	-	5	-	-	-	-	-	-	1.8	2.0	1.0	1.5
NR/Treated Spherical $CaCO_3$ (10)	100	-	-	-	10	-	-	-	-	-	-	1.8	2.0	1.0	1.5
NR/Treated Spherical $CaCO_3$ (20)	100	-	-	-	20	-	-	-	-	-	-	1.8	2.0	1.0	1.5
NR/Treated Spherical $CaCO_3$ (40)	100	-	-	-	40	-	-	-	-	-	-	1.8	2.0	1.0	1.5
NR/Treated Spherical $CaCO_3$ (60)	100	-	-	-	60	-	-	-	-	-	-	1.8	2.0	1.0	1.5
NR/Treated Bundle-liked $CaCO_3$ (5)	100	-	-	-	-	5	-	-	-	-	-	1.8	2.0	1.0	1.5
NR/Treated Bundle-liked $CaCO_3$ (10)	100	-	-	-	-	10	-	-	-	-	-	1.8	2.0	1.0	1.5
NR/Treated Bundle-liked $CaCO_3$ (20)	100	-	-	-	-	20	-	-	-	-	-	1.8	2.0	1.0	1.5
NR/Treated Bundle-liked $CaCO_3$ (40)	100	-	-	-	-	40	-	-	-	-	-	1.8	2.0	1.0	1.5
NR/Treated Bundle-liked $CaCO_3$ (60)	100	-	-	-	-	60	-	-	-	-	-	1.8	2.0	1.0	1.5
NR/Treated Fiber $CaCO_3$ (5)	100	-	-	-	-	-	5	-	-	-	-	1.8	2.0	1.0	1.5
NR/Treated Fiber $CaCO_3$ (10)	100	-	-	-	-	-	10	-	-	-	-	1.8	2.0	1.0	1.5

Table 4.5 (cont.) Composite formulations prepared in this work

Composites	NR (phr)	$CaCO_3$ (phr)									Carbon black (CB)				
		Untreated			Treated			Commercial grade			N330 (phr)	ZnO (phr)	Stearic acid (phr)	CBS (phr)	Sulphur (phr)
		Spherical	Bundle	Fiber	Spherical	Bundle	Fiber	NCC	9QQ	4QQ					
NR/Treated Fiber $CaCO_3$ (20)	100	-	-	-	-	-	20	-	-	-	-	1.8	2.0	1.0	1.5
NR/Treated Fiber $CaCO_3$ (40)	100	-	-	-	-	-	40	-	-	-	-	1.8	2.0	1.0	1.5
NR/Treated Fiber $CaCO_3$ (60)	100	-	-	-	-	-	60	-	-	-	-	1.8	2.0	1.0	1.5
NR/NCC (5)	100	-	-	-	-	-	-	5	-	-	-	1.8	2.0	1.0	1.5
NR/NCC (10)	100	-	-	-	-	-	-	10	-	-	-	1.8	2.0	1.0	1.5
NR/NCC (20)	100	-	-	-	-	-	-	20	-	-	-	1.8	2.0	1.0	1.5
NR/NCC (40)	100	-	-	-	-	-	-	40	-	-	-	1.8	2.0	1.0	1.5
NR/NCC (60)	100	-	-	-	-	-	-	60	-	-	-	1.8	2.0	1.0	1.5
NR/9QQ (5)	100	-	-	-	-	-	-	-	5	-	-	1.8	2.0	1.0	1.5
NR/9QQ (10)	100	-	-	-	-	-	-	-	10	-	-	1.8	2.0	1.0	1.5
NR/9QQ (20)	100	-	-	-	-	-	-	-	20	-	-	1.8	2.0	1.0	1.5
NR/9QQ (40)	100	-	-	-	-	-	-	-	40	-	-	1.8	2.0	1.0	1.5
NR/9QQ (60)	100	-	-	-	-	-	-	-	60	-	-	1.8	2.0	1.0	1.5
NR/4QQ (5)	100	-	-	-	-	-	-	-	-	5	-	1.8	2.0	1.0	1.5

Table 4.5 (cont.) Composite formulations prepared in this work

Composites	NR (phr)	$CaCO_3$ (phr)									Carbon black (CB)				
		Untreated			Treated			Commercial grade			N330 (phr)	ZnO (phr)	Stearic acid (phr)	CBS (phr)	Sulphur (phr)
		Spherical	Bundle	Fiber	Spherical	Bundle	Fiber	NCC	9QQ	4QQ					
NR/4QQ (10)	100	-	-	-	-	-	-	-	-	10	-	1.8	2.0	1.0	1.5
NR/4QQ (20)	100	-	-	-	-	-	-	-	-	20	-	1.8	2.0	1.0	1.5
NR/4QQ (40)	100	-	-	-	-	-	-	-	-	40	-	1.8	2.0	1.0	1.5
NR/4QQ (60)	100	-	-	-	-	-	-	-	-	60	-	1.8	2.0	1.0	1.5
NR/N330 CB (5)	100	-	-	-	-	-	-	-	-	-	5	1.8	2.0	1.0	1.5
NR/N330 CB (10)	100	-	-	-	-	-	-	-	-	-	10	1.8	2.0	1.0	1.5
NR/N330 CB (20)	100	-	-	-	-	-	-	-	-	-	20	1.8	2.0	1.0	1.5
NR/N330 CB (40)	100	-	-	-	-	-	-	-	-	-	40	1.8	2.0	1.0	1.5
NR/N330 CB (60)	100	-	-	-	-	-	-	-	-	-	60	1.8	2.0	1.0	1.5

4.7 Characterization of NR/$CaCO_3$ composites

Several techniques were utilized to analyze the prepared composites as follows.

4.7.1 Determination of cure characteristics

The cure measurements and cure behavior of rubber specimens were measured using the Moving die rheometer (MDR), Dynsico MDR-CG model. The uncured rubber was weighed about 5 g. Then, the sample was placed on the die of the rheometer cavity. The testing temperature was operated at 140^{o}C. The results were exported as scorch time (t_{s2}) and curing time (t_{c90}) of NR/$CaCO_3$ composites which were determined from the cure curve. The t_{s2} is the time to reach a 2 unit increase in torque above minimum (equation 4.1). The t_{c90} is the time at which the rheometer torque increases from the beginning of the test to 90% of the total torque change on the cure curve (equation 4.2). Meanwhile, M_L and M_H represent minimum torque and maximum torque, respectively.

$$T_{s2} = M_L + 2 \text{ units above it} \quad (4.1)$$

$$T_{c90} = 0.9(M_H - M_L) + M_L \quad (4.2)$$

Cure Rater Index (CRI) is a measure of the rate of vulcanization based on the difference between optimum vulcanization and incipient scorch time (equation 4.3). This correlates with a rise in the value of torque with time.

$$CRI = \frac{100}{(t_{c90} - t_{s2})} \quad (4.3)$$

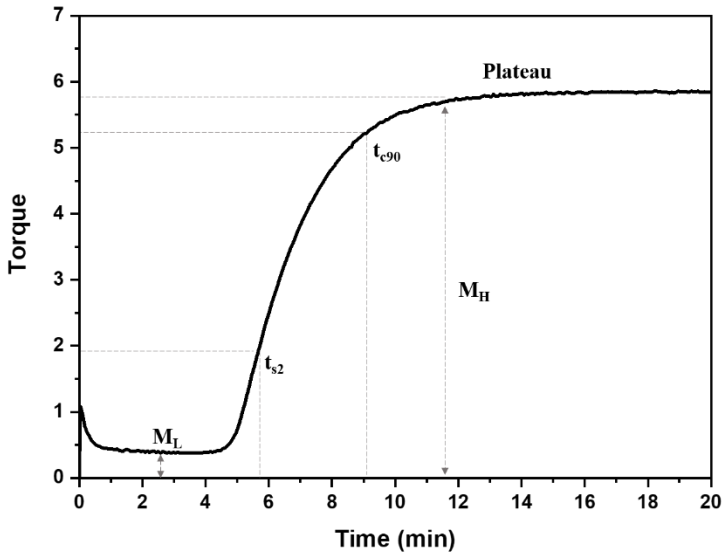


Figure 4.10 Typical cure characteristic curve of vulcanized rubber compound

4.7.2 Preparation of rubber vulcanizates

The rubber vulcanizate of NR compounds for various mechanical and dynamic testing was compressed or shaped at 140^{o}C (1 mm thickness) [152] using compression molding based on the t_{c90} time from the MDR result.

4.7.3 Chemical structure of NR/$CaCO_3$ composites

4.7.3.1 Fourier transform infrared spectroscopy (FTIR)

The chemical structure of natural rubber and other ingredients were evaluated using ATR-FTIR analysis via Bruker Vertex 70v equipment. The measurement was scanned in the range from 4000 to 400 cm^{-1} with a resolution of 1 cm^{-1} and using 20 scans.

4.7.3.2 X-ray diffraction analysis (XRD)

The crystal phases of $CaCO_3$ particles in NR, the amorphous phase of rubber and other ingredients were evaluated by the XRD analysis model Panalytical Empyrean. The X-ray diffractometer was equipped with a copper anode (Cu-Kα radiation) with λ = 1.54 Å operating at 30 mA and 40 kV. The XRD patterns were obtained from 2Θ from 20° to 40° in step size 0.052°.

4.7.3.3 X-ray fluorescence microscope (micro-XRF)

To measure Ca, Zn and S element analysis of the composites, micro-XRF was conducted by Horiba micro-XRF model XGT-9000. The measurement area is about 10 mm. The vacuum stops every 5 seconds together with the transmission image. The pixel X and Y is fixed at 512 pix and the pixel time is 15 ms. The capillary used in this work is 100 µm, 0.8 time/step and a voltage 30 kV.

4.7.4 Thermal analysis of the rubber vulcanizates

4.7.4.1 Thermogravimetric analysis (TGA)

Thermogravimetric analysis (TGA) model SDT 296, Universal V3.4C TA instrument was used to investigate the thermal stability of NR/$CaCO_3$ composites. Approximately 10 mg of rubber samples were heated up from 40-800^oC with a heating rate of 20^oC/min under N_2 gas. The thermal decomposition temperatures of rubber samples were investigated.

4.7.4.2 Differential scanning calorimeter (DSC)

The thermal analysis of NR/$CaCO_3$ (20 phr) composites was performed using DSC Q200 model under a nitrogen atmosphere, heating scan from -80 up to 80^oC with a heat rate of 10^oC/min. The glass transition temperature (Tg) was obtained by the apparatus software.

4.7.5 Mechanical properties of rubber vulcanizates

4.7.5.1 Tensile properties

Tensile tests were conducted as Instron ASTM D 412-98 Standard Test Methods, Instron 5566 model with cross-head speed rate 500 mm/min and with 1 mm thick type dumbbell specimens using type C die as in Figure 4.11. The specimen had a test length of 40 and a total length of 115 mm. Five specimens were tested for each composite and the average was taken from 3-5 specimens for calculations. The properties measured were recorded as tensile strength (MPa), elongation at break (%), 100% (M100) and 300% (M300) moduli (MPa) of the composites. The value of tensile strength, %elongation at break and moduli were calculated following the equations 4.4, 4.5 and 4.6, respectively.

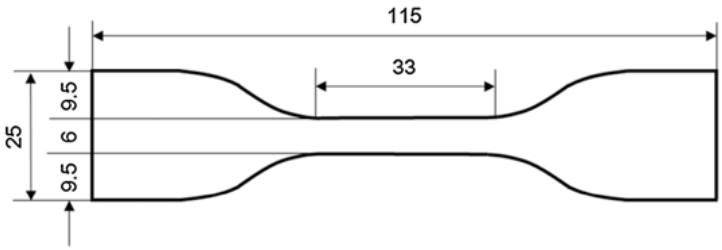


Figure 4.11 Dimensions of a tensile specimen

$$\text{Tensile strength (MPa)} = \frac{F}{A} \tag{4.4}$$

Where; F = force at break (N)

A = cross-sectional area of unstrained specimen (mm^2)

$$\text{\% Elongation at break} = \frac{L-L_0}{L_0} \times 100 \tag{4.5}$$

Where; L = observed distance between bench marks on the extended specimen

L_0= original distance between bench marks

$$M_{(100\%,\ 300\%)}\ (\text{MPa}) = \frac{F_{(100\%,\ 300\%)}}{A} \tag{4.6}$$

Where; $M_{(100\%,\ 300\%)}$ = modulus at 100 or 300% strain (MPa)

$F_{(100\%,\ 300\%)}$ = force at 100 or 300% strain (N)

4.7.5.2 Tear properties

The tear resistance properties of vulcanized NR/$CaCO_3$ composites were tested according to ASTM D624 using Instron 5566 Universal Tensile tester with a crosshead speed of 500 nm/min load cell 1 kN capacity. The 1 mm thickness of sample sheet were cut into specimen by using die B as Figure 4.12 along the mill direction. The tear resistance was calculated as equation 4.7.

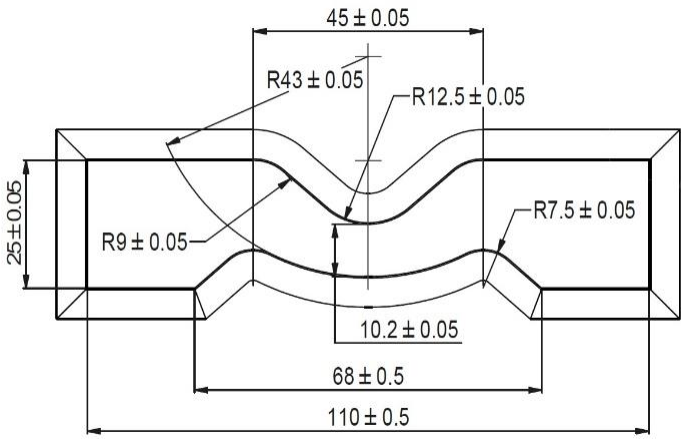


Figure 4.12 Dimension of a tear specimen (Die B – ASTM D624)

$$\text{Tear resistance} = \frac{F}{t} \tag{4.7}$$

Where, F = observed force

t = specimen thickness

4.7.6.3 Hardness (Shore A)

The hardness (Shore A) of rubber vulcanizates were examined by Wallace H17A hardness tester in accordance with standard ASTM D2240-97. The thickness of specimen is 6 mm. The specimen was placed on the platform of hardness tester. The testing was carried out at different positions on the specimen. The average hardness value of each specimen was calculated from 6 positions.

CHAPTER V
RESULTS AND DISCUSSION

The results and discussion of this research consisted of two main parts. The first part was the preparation of different shapes of calcium carbonate ($CaCO_3$) particles via precipitation methods. Plus, the surface treatment of $CaCO_3$ particles was prepared by using olive soap which was obtained from saponification reaction. The morphological shape, polymorphic phases, and wettability of $CaCO_3$ particles were investigated. The second part was to explore the incorporation of the prepared $CaCO_3$ powders in natural rubber (NR) for producing NR/$CaCO_3$ composites and to investigate their mechanical properties. NR/N330 carbon black composites were also carried out for comparison of the mechanical properties with the NR/$CaCO_3$ composites.

Part I: Preparation and polymorphic characterization of $CaCO_3$ particles

This part involved preparation by precipitation process of different shapes (spherical, bundle-liked and fiber-shaped) of $CaCO_3$ without and with surface treatment using olive soap. The obtained $CaCO_3$ and commercial $CaCO_3$ particles were characterized by their morphological shape, polymorphic phase, chemical structure, wettability, physical property, and thermal property.

5.1 Saponification of soap and its use as surface modification of $CaCO_3$

The chemical structures of the fatty acid component of olive oil are presented in Figure 5.1. The fatty acid compositions of olive oil consist of oleic acid (55 – 83%), linoleic acid (3.5 – 21%) and palmitic ester (7.5 – 20%). The ratio of the number

of carbons to double bond of oleic acid, linoleic acid and palmitic ester are 18:1, 18:2 and 16:0, respectively. [151] The saponification reaction of these fatty acids with sodium hydroxide (NaOH) produced sodium carboxylate and glycerol. The sodium carboxylate (RCOONa) then consists of sodium oleate, sodium linoleate and sodium palmitate. The obtained soap molecule contains two parts: hydrophilic head and hydrophobic tail. In water, the soap micelles are formed as in Figure 5.2(a). When the soap solution was added to the Ca^{2+} ions solution, these sodium carboxylate chains can bind with Ca^{2+} ions forming Ca-carboxylate ($R(COO^{-})_2Ca$). During the precipitation between Ca^{2+} and CO_3^{2-} ions, some of the carboxylate chains could be adsorbed on the surface of the $CaCO_3$ nanograins as shown in Figure 5.2(b). The soap used in the surface treatments of $CaCO_3$ was not only coated on the surface but also trapped inside the particles resulting in the particles becoming bigger, rougher, and more hydrophobic than untreated ones which will describe in next part.

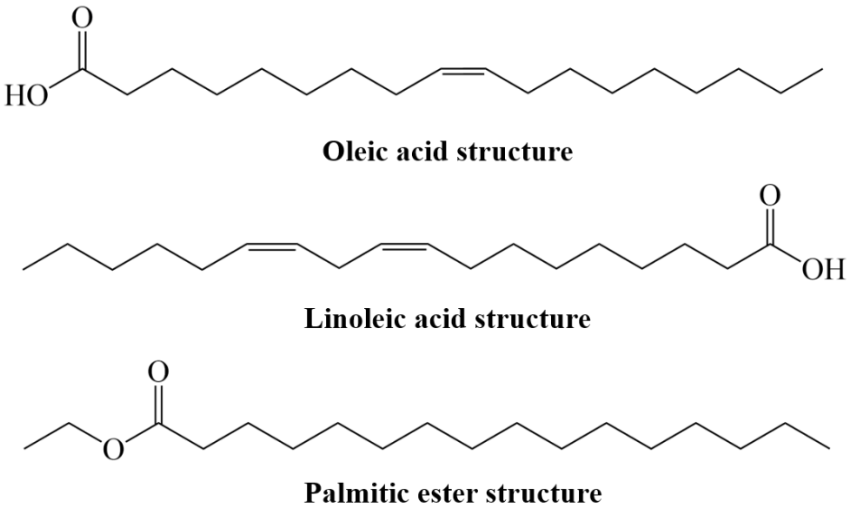


Figure 5.1 Fatty acid composition of olive oil: oleic acid, linoleic acid, and palmitic ester

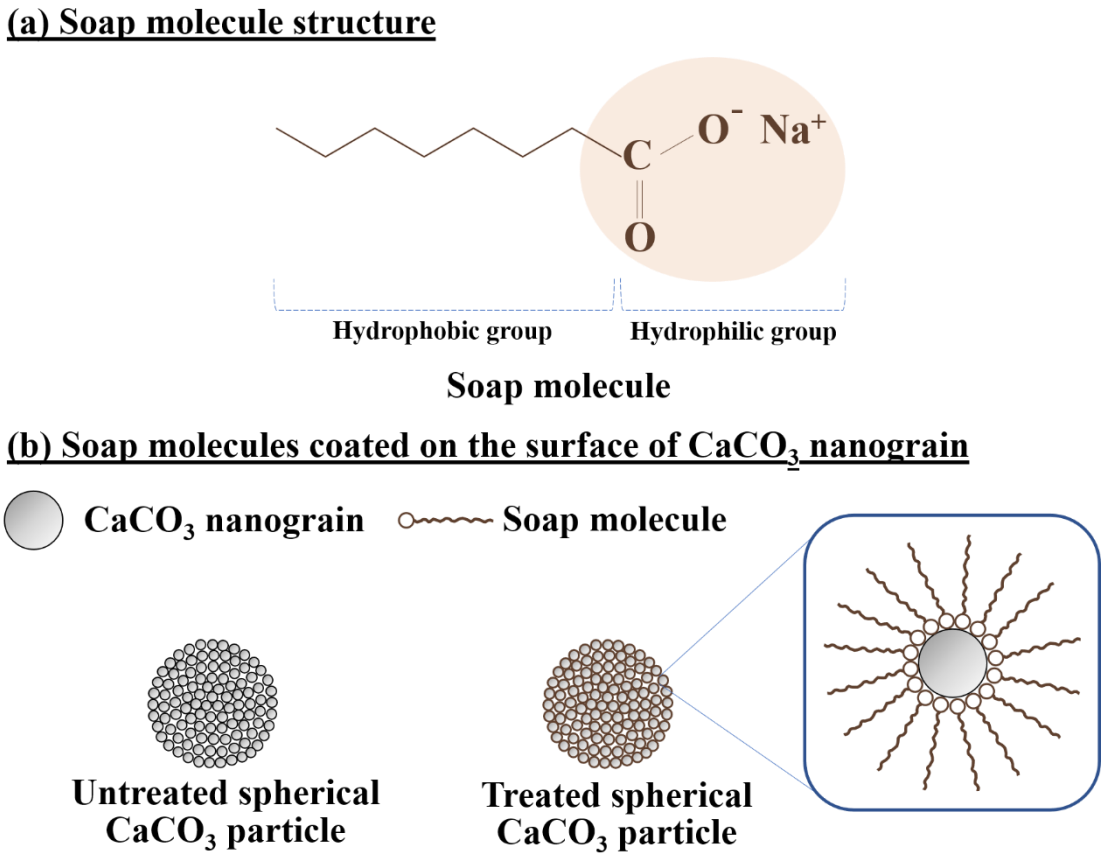


Figure 5.2 Proposed formation of (a) soap molecule structure and (b) soap molecules coated on the surface of $CaCO_3$ nanograin

5.2 Preparation of untreated and treated $CaCO_3$

The $CaCO_3$ particles were obtained by solution precipitation method using a simple mixing of carbonate (CO_3^{2-}) ions and calcium (Ca^{2+}) ions solution. The surface of $CaCO_3$ particles was also treated by the addition of soap solution in the Ca^{2+} reactant solution before further mixing with CO_3^{2-} solution. It was noted that the solvent used to dissolve the Ca^{2+} reactant was sucrose solution or water depending on the type of prepared $CaCO_3$ particles.

5.2.1 Physical appearance of precipitated solution and $CaCO_3$ powders

5.2.1.1 Precipitated solutions

Concerning the preparation of $CaCO_3$ particles using 50% by weight of sucrose solution as an aqueous medium for dissolving 1.0 M of $(NH_4)_2CO_3$ solution and 1.0 M of $CaCl_2$, solution, the precipitated solutions before the powder collecting step was shown in Figure 5.3(a). In the surface treatment process in which the olive soap was added to the CO_3^{2-} solution before mixing with the Ca^{2+} solution, the precipitated solution was demonstrated in Figure 5.3(b). Without soap treatment, the $CaCO_3$ powders were settled in the bottom of the precipitated solution. The simple logic assumes that as-prepared $CaCO_3$ particles are hydrophilic powder in the hydrophilic mediums whether using sucrose or water as an aqueous medium. On the other hand, it was seen that by adding soap to the reactant solution, the treated $CaCO_3$ particles floated on the surface of the precipitated solution (Figure 5.3(b)). Thus, it was identified as a surface modification of the hydrophilic $CaCO_3$ to hydrophobic $CaCO_3$ particles. The difference in the physical appearance of the $CaCO_3$ powders in the solution medium could be useful beforehand that the surface wettability by using the contact angle technique was measured afterward.

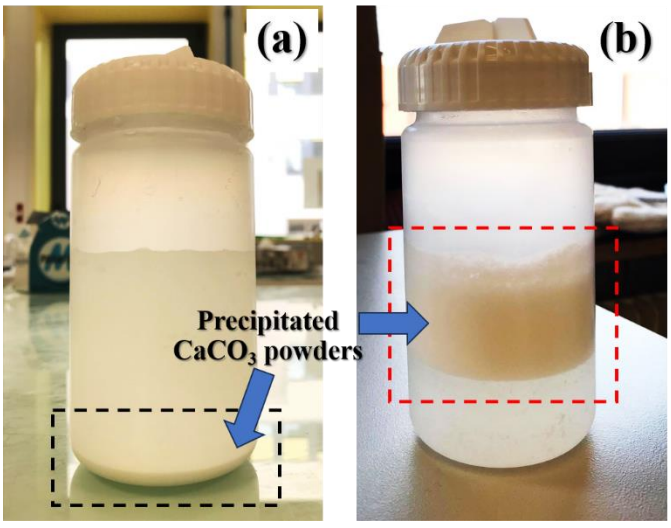


Figure 5.3 Images of precipitated $CaCO_3$ powders: (a) untreated and (b) treated by soap after solution mixing of reactants

5.2.1.2 $CaCO_3$ powders

The physical appearance of dried $CaCO_3$ powders after drying for 3 hours in the oven at 70°C was exhibited as colorless or white powders (Figure 5.4(a)). Generally, $CaCO_3$ powders appear as white crystals and are odorless. Due to some metastable polymorphs of $CaCO_3$ being sensitive to water [14], the $CaCO_3$ powders should be stored in a dried form at room temperature without contact with any water and avoid humidity shown in Figure 5.4(b).



Figure 5.4 Physical appearance of $CaCO_3$ white powders: (a) after drying in an oven, and (b) storing $CaCO_3$ powders in vial or closed container

5.2.2 Morphological features of $CaCO_3$ particles

The morphology of untreated and treated $CaCO_3$ particles with different shapes (spherical, bundle-liked and fiber) together with commercial ones were observed by SEM and TEM analyses, as illustrated in Figure 5.5 – Figure 5.7.

5.2.2.1 Scanning electron microscope (SEM)

Figure 5.5 presents the morphology of different types of $CaCO_3$ particles at low magnification. Figure 5.5(a) and 5.5(b) are $CaCO_3$ prepared by using $(NH_4)_2CO_3$ and $CaCl_2$ as reactants, 50%wt sucrose as aqueous medium without and with surface treatment with olive soap, respectively. The SEM images demonstrated spheroidal shape with the average diameter in sub-micro scale of 0.42 ± 0.14 µm and 0.51 ± 0.16 µm, respectively, having a narrow particle size distribution. The aspect ratio of spherical

particles of both spherical $CaCO_3$ is about 1 which is in good agreement with the aspect ratio of the sphere equal to 1, reported in the literature. [37] The treated spherical $CaCO_3$ provided a slightly bigger particle size caused of the soap chains were trapped on the surface of $CaCO_3$ nanograins. The proposed mechanism of surface treatment of treated $CaCO_3$, producing hydrophobic powders was discussed in section 5.1.

When the precipitation system using Na_2CO_3 and $CaCl_2$ in aqueous medium at 80^{o}C, the obtained $CaCO_3$ were rod-like particles which were agglomerated into bundles. Thus, it was named as "bundle-liked $CaCO_3$" particles. The untreated bundle-liked $CaCO_3$ (Figure 5.5(c)) was 4.44 ± 1.92 µm in length and 0.49 ± 0.08 µm in diameter, resulting in the aspect ratio of 9.06. Meanwhile, the treated bundle-liked $CaCO_3$ particles (Figure 5.5(d)) provided an aspect ratio value of 8.42 according to the length and diameter which were 4.38 ± 0.83 µm and 0.52 ± 0.39 µm, respectively.

Concerning the needle-liked or fiber $CaCO_3$, it was obtained by dispersion of prepared spherical $CaCO_3$ in water followed by heating up at 80^{o}C. The transformation of spherical $CaCO_3$ into the long nanowire, needle-liked or fiber morphology was shown in Figure 5.5(e), exhibiting the highest aspect ratio (156.9) over spherical and bundle-liked particles due to its diameter in nanoscale. The average length and diameter of untreated fiber were 20.40 ± 7.72 µm and 0.13 ± 0.04 µm (= 130 nm), respectively. Besides, the treated fiber $CaCO_3$ presented the mixture of spherical, cubic and fiber shapes as seen in Figure 5.5(f). This is caused by the treated $CaCO_3$ particles were formed and coated on the surface of fiber particles resulting in a bigger diameter. The morphology shown the most content of long nanowire particle together with some spheroidal and cubical particles. The average length and diameter of the treated fiber $CaCO_3$ were 19.05 ± 0.94 µm and 0.53 ± 0.05 µm, respectively. The aspect ratio was equal to 35.9 which is less than untreated fiber $CaCO_3$.

Figure 5.5(g) – 5.5(i) presents the morphological shapes of nano and micro-scale commercial $CaCO_3$ particles. The SEM image of nano calcium carbonate (NCC) is shown in Figure 5.5(g). These particles exhibited in rhombohedral or cubical shape which agglomerated together due to their particle size in nanoscale about 5 nm in diameter. Meanwhile, the micro-scale 9QQ (Figure 5.5(h)) and 4QC (Figure 5.5(i)) commercial powders show rhombohedral or cubical morphological shapes with very broad particle size distribution. The 9QQ and 4QC were produced throughout the

grinding process of limestones resulting in non-homogeneous particle size distribution. The average diameter of 9QQ and 4QC particles were 4.43 ± 3.46 μm and 3.16 ± 1.40 μm, respectively.

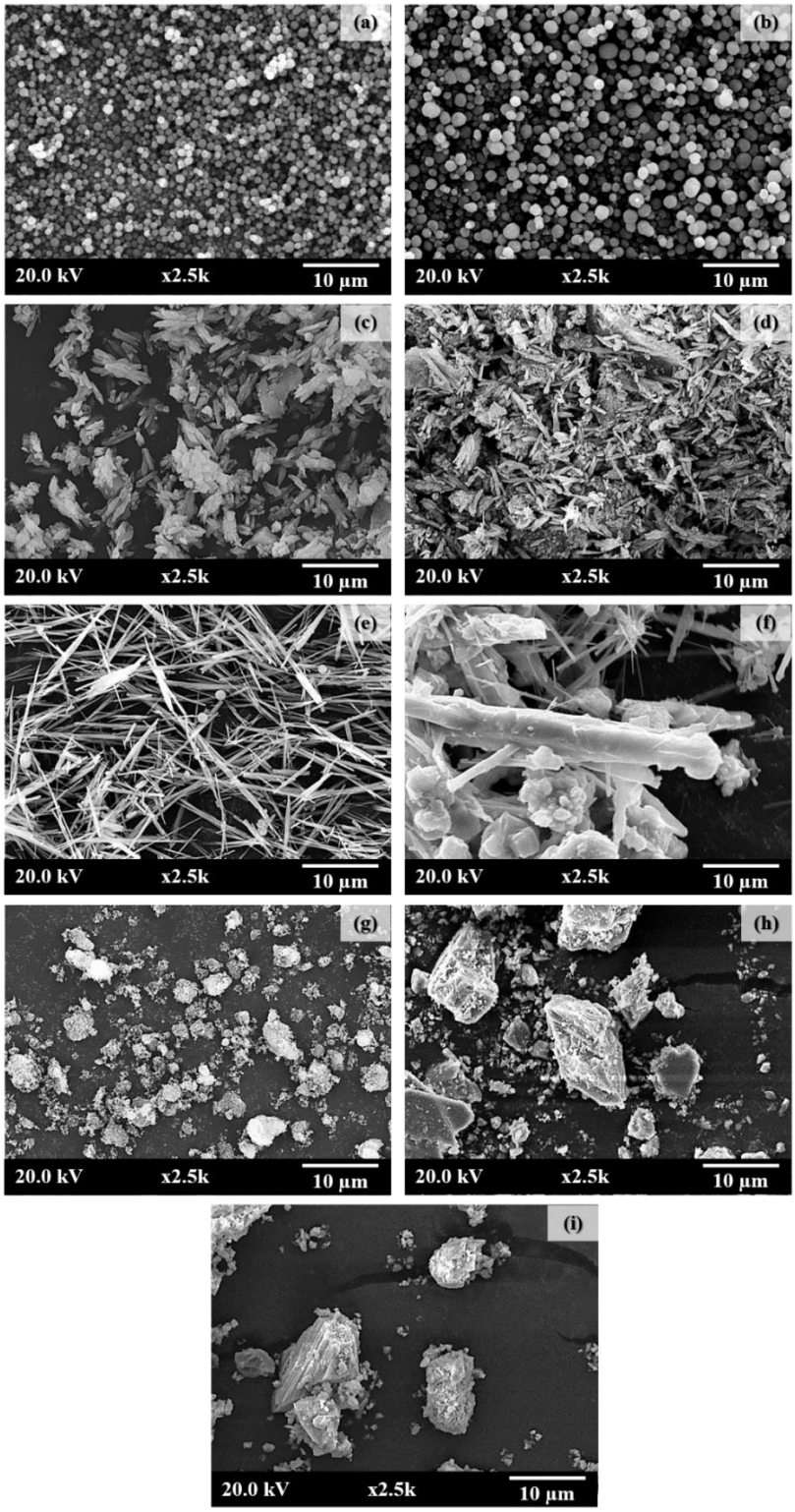


Figure 5.5 SEM images at low magnification (2500x, 10 µm scale bar) of $CaCO_3$ particles: (a) untreated spherical, (b) treated spherical, (c) untreated bundle-liked, (d) treated bundle-liked, (e) untreated fiber, (f) treated fiber, (g) NCC, (h) 9QQ, and (i) 4QC commercial $CaCO_3$

Figure 5.6 also presented SEM images of $CaCO_3$ particles in high magnification to observe the surface of $CaCO_3$ particles. The untreated spherical (Figure 5.6(a)), untreated bundle-liked (Figure 5.6(c)), and untreated fiber (Figure 5.6(e)) $CaCO_3$ particles presented a smooth surface morphology compared to the treated ones which were rougher. This was caused by the soap micelles were coated on the surface of the particles. It is seen that the morphology of NCC in Figure 5.6(g), the particle shapes are nano cubical particles. Commercial NCC or precipitated calcium carbonate (PCC) is produced via the carbonation process precipitating the nanoscale $CaCO_3$ particles. [9] The carbonation process was carried out by heating limestone at > 900^oC producing lime (CaO) following equation 5.1. The CaO and carbon dioxide (CO_2) interacted with water (H_2O) resulting in $Ca(OH)_2$ and H_2CO_3, as equations 5.2 and 5.3, respectively. The nanoscale $CaCO_3$ crystals of commercial PCC type was produced via the carbonation process as equation 5.4.

$$CaCO_3 \text{ (limestone)} \rightleftharpoons CaO + CO_2 \text{ (T~900}^oC) \quad (5.1)$$

$$CaO + H_2O \rightleftharpoons Ca(OH)_2 \quad (5.2)$$

$$CO_2 + H_2O \rightleftharpoons H_2CO_3 \quad (5.3)$$

$$H_2CO_3 + Ca(OH)_2 \rightleftharpoons CaCO_3 \text{ (crystal)} + 2H_2O \quad (5.4)$$

The morphologies of commercial micro-scale $CaCO_3$ particles of 9QQ and 4QC were presented in Figure 5.6(h) and 5.6(i), respectively. This type of commercial-grade $CaCO_3$ was categorized as ground or grinded calcium carbonate (GCC). [112] The natural limestones, chalk or rock were ground by using the blade in ball mill. As can be seen the blade masks on the particles of 9QQ and 4QC.

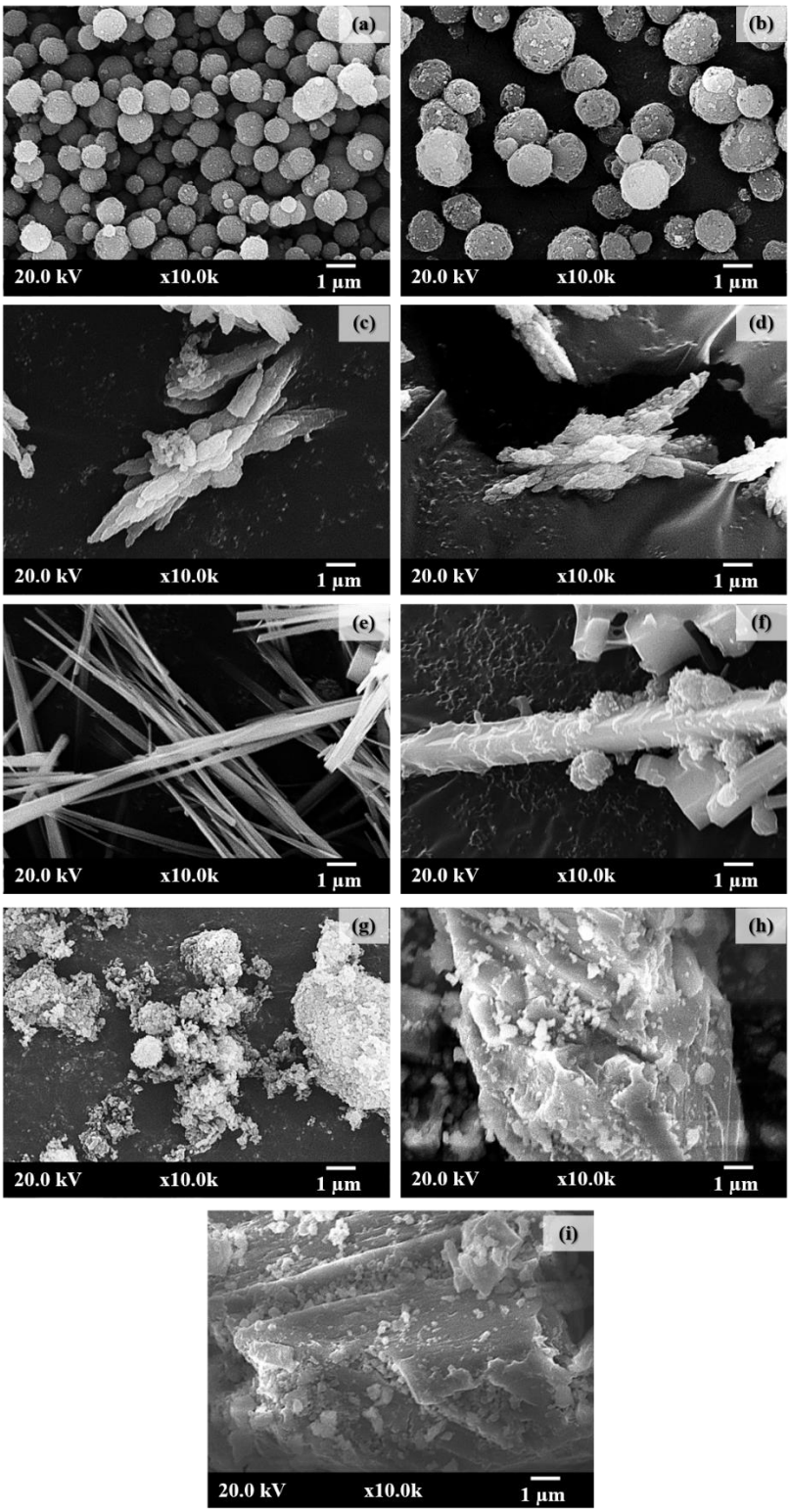


Figure 5.6 SEM images at high magnification (10000x, 1 µm scale bar) of $CaCO_3$ particles: (a) untreated spherical, (b) treated spherical, (c) untreated bundle-liked, (d) treated bundle-liked, (e) untreated fiber, (f) treated fiber, (g) NCC, (h) 9QQ, and (i) 4QC commercial $CaCO_3$

5.2.2.2 Transmission electron microscope (TEM)

TEM is another tool to visualize the microstructure of a material. Figure 5.7 shows TEM images of $CaCO_3$ without and with surface treatment with soap of different types of prepared $CaCO_3$ particles and commercial $CaCO_3$. The surface morphology of $CaCO_3$ after being treated with soap was different from the untreated particles, presenting rougher and bigger particles than the untreated ones. Figure 5.7(a) and 5.7(b) shows the porous structure of spherical-shaped $CaCO_3$ particles, demonstrating an obvious contrast difference between the paler edges and darker centers. This porous structure is a typical and unique property of vaterite polymorph. [66] The TEM images of bundle shapes of untreated and treated $CaCO_3$ particles are shown in Figure 5.7(c) and Figure 5.7(d), respectively. The results supported the SEM analysis conducted previously. In the case of fiber-shaped $CaCO_3$ particles, the TEM analysis revealed the long nanowire of fiber-shaped $CaCO_3$ in Figure 5.7(e). It can be seen for treated fiber-shaped $CaCO_3$, spherical particles attached on the surface of fiber particles (Figure 5.7(f)). The morphology of NCC particles is shown in the rhombohedral or cubical shapes in Figure 5.7(g). At a higher magnification image of NCC in Figure 5.7(h), the particle size of NCC was measured which is about 5 nm. The average particle size and aspect ratio of different types of $CaCO_3$ particles are listed in Table 5.2.

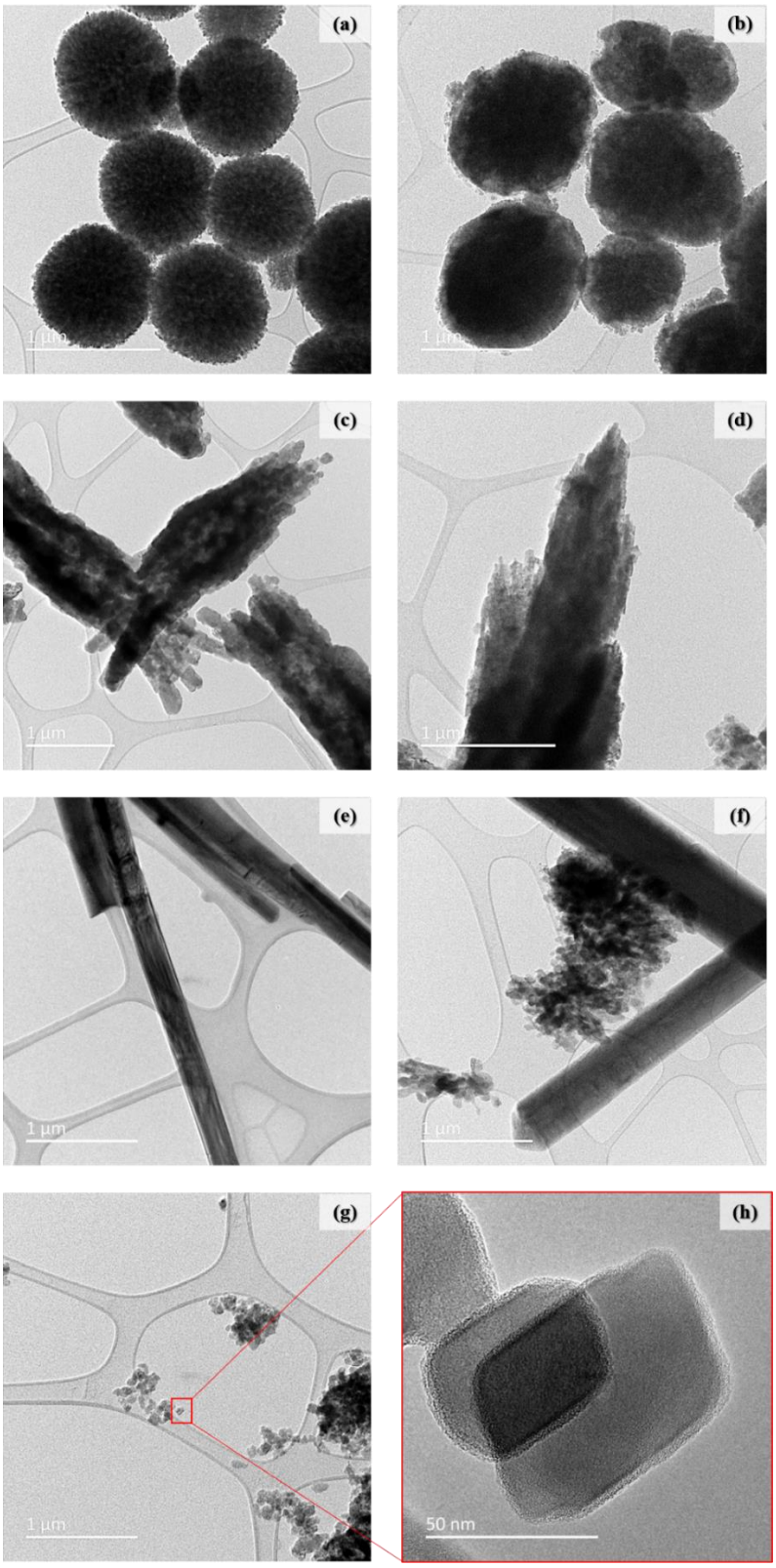


Figure 5.7 TEM images of $CaCO_3$ particles: (a) untreated spherical, (b) treated spherical, (c) untreated bundle-liked, (d) treated bundle-liked, (e) untreated fiber, (f) treated fiber, and (g,h) NCC commercial $CaCO_3$

5.2.2.3 Effect of solution viscosity on the particle size of spherical $CaCO_3$ powder

Concerning the preparation of spherical $CaCO_3$ particles, the effect of sucrose medium on the particle size of spherical $CaCO_3$ was studied. The plot between the shear rate and viscosity of pure 50 wt% sucrose medium, 1 M $CaCl_2$ reactant in water and sucrose medium is demonstrated in Figure 5.8. The fluids show Newtonian behavior which means the solutions are independent of both time and rate of shear similar to the published reference [10].

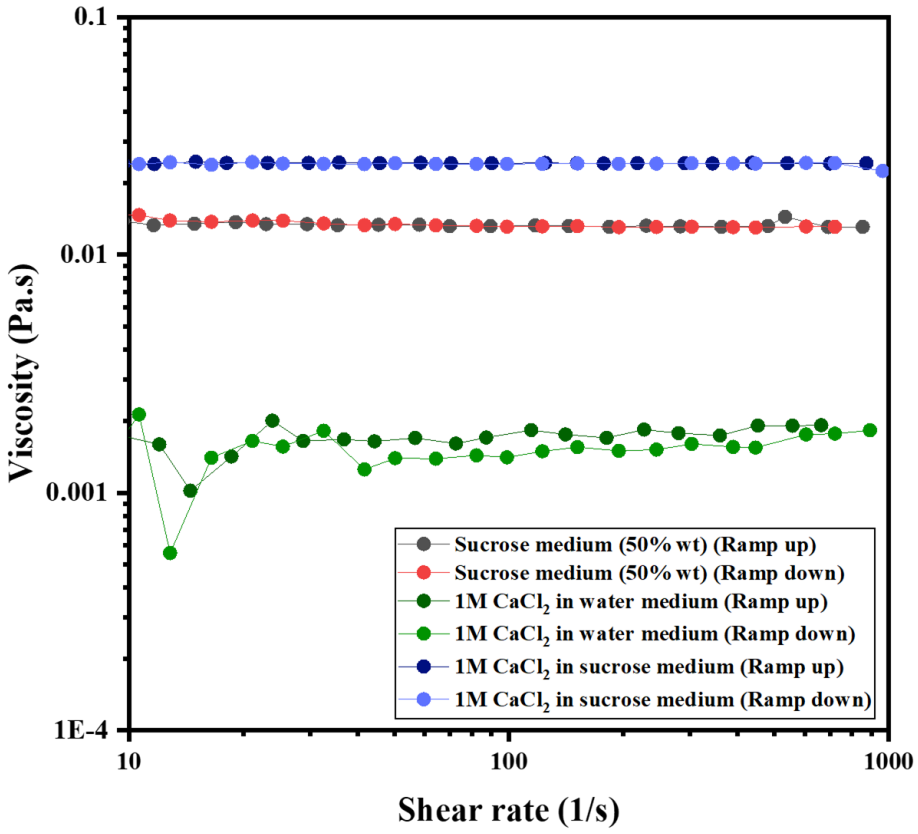


Figure 5.8 Plot of shear rate and viscosity of 1.0 M of $CaCl_2$ reactant solution in water medium and 50 wt% of sucrose mediums compared with pure 50 wt% of sucrose without reactant (in preparation of spherical $CaCO_3$ powder)

Figure 5.9 shows the plot of the shear rate and shear stress of sucrose medium, 1M $CaCl_2$ reactant in water and sucrose medium. The slope (shear stress divided by shear rate) represents the viscosity of the solution. The viscosity of pure 50

wt% sucrose medium is 0.0152 Pa.s. While the viscosity of 1M $CaCl_2$ reactants in water and sucrose medium are 0.0008 and 0.0240 Pa.s, respectively. The viscosity values of the solutions are summarized in Table 5.1.

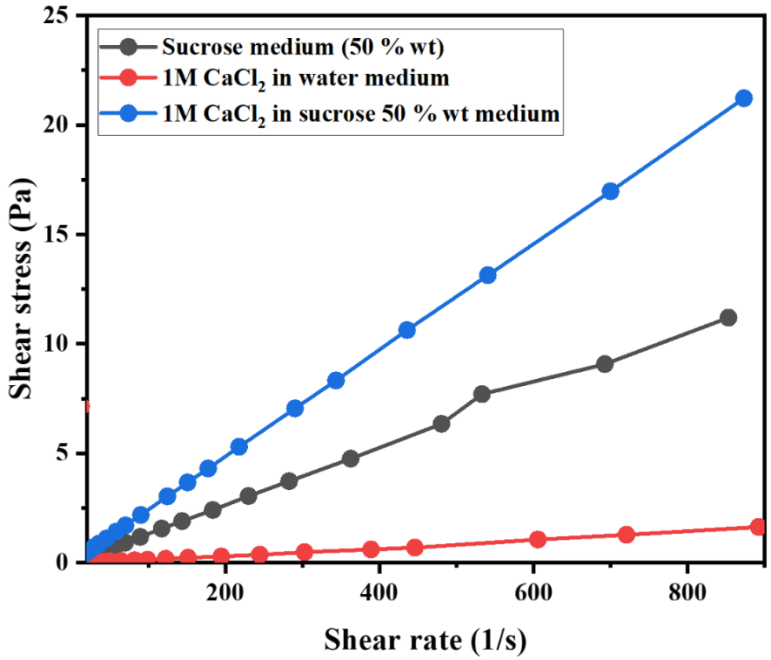


Figure 5.9 Plot of shear rate and shear stress of 50 wt% sucrose and 1M $CaCl_2$ reactant in water and 50 wt% sucrose mediums (in preparation of spherical $CaCO_3$ particles)

Table 5.1 Viscosity of the sucrose and reactant solutions

Solution	Viscosity (Pa.s)
Sucrose medium (50 wt%)	0.0152
1.0 M $CaCl_2$ reactant in water medium	0.0008
1.0 M $CaCl_2$ reactant in sucrose medium	0.0240

The drastic increase of viscosity of 1.0 M $CaCl_2$ reactant dissolved in sucrose solution over 30 times than in water affected the particle size of spherical-shaped $CaCO_3$ particles. [10] Naturally, the sucrose molecule is a disaccharide molecule consisting of two monosaccharides: glucose and fructose. [154] Sucrose contains plenty of hydroxy polar groups (-OH) which are miscible in water forming a three-dimension network of hydrogen-boned molecules. When the $CaCl_2$ reactant is dissolved in a

sucrose medium, the interaction of calcium cation (Ca^{2+}) and the hydroxy groups is polymer-liked complex between more than one Ca^{2+} per sucrose molecule as depicted in Figure 5.10. [155; 156] This interaction can prevent the contact of Ca^{2+} and CO_3^{2-} ions to form a bigger size of spherical $CaCO_3$ particles and slow down the kinetic of the precipitation. It could be summarized that sucrose plays an important role in promoting the viscosity of the mixing system leading to reduce the particle size of spherical $CaCO_3$ and promote a high percentage of vaterite polymorph. The average particle sizes of spherical $CaCO_3$ are 0.81 ± 0.26, 0.72 ± 0.24, 0.52 ± 0.18, 0.46 ± 0.17, 0.44 ± 0.15, 0.42 ± 0.14 by using sucrose 0, 10, 20, 30, 40, and 50 %wt as aqueous medium, respectively. Plus, the percentage of vaterite polymorphic phases also increases from 92.52, 97.50, 98.06, 98.43, 99.08, and 99.10% following the same variation of sucrose contents.

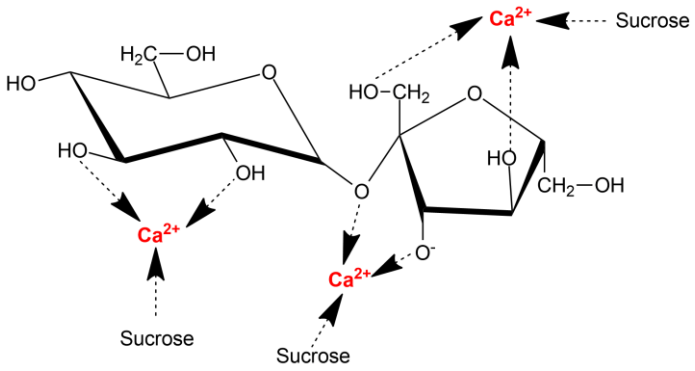


Figure 5.10 Polymer-liked structure of Ca^{2+} ions and sucrose structure

5.2.2.4 Brunauer, Emmett and Teller (BET) analysis

The BET isotherm linear plot and BET surface area value of as-prepared untreated and treated $CaCO_3$ powders, including NCC commercial $CaCO_3$ powders were presented in Figure 5.11. Figure 5.11(a) shows plots between relative pressure versus quantity of N_2 adsorbed by the $CaCO_3$ powders, representing the specific surface area and porosity of the powders. The BET surface area values of obtained and commercial $CaCO_3$ powder were presented in Figure 5.11(b). As aforementioned, the typical property of vaterite $CaCO_3$ is only one polymorph which is identified as a porous powder. [66] The BET values of untreated and treated vaterite $CaCO_3$ provided the highest specific surface area of 39.32 and 34.45 m^2/g, respectively. The treated spherical $CaCO_3$ provides a lower specific surface area value than the untreated one which relates

to the bigger particle size of the treated $CaCO_3$. The results supported the SEM images in Figure 5.6 that the average diameter of treated spherical $CaCO_3$ particles (0.51 ± 0.16 µm) was bigger than untreated spherical powder (0.42 ± 0.14 µm). In the case of bundle-liked and fiber $CaCO_3$ particles, these particles are solid crystals without pores. The specific surface area value of treated fiber $CaCO_3$ (7.93 m^2/g) is higher than untreated fiber $CaCO_3$ (0.29 m^2/g). This may be due to the presence of some spherical $CaCO_3$ particles during the precipitation. The particle size of commercial nano-calcium carbonate (NCC) is in the range of nanoscale material, then the BET specific surface value is 20.15 m^2/g which is higher than bundle-liked and fiber one. The BET specific surface area values were summarized in Table 5.2.

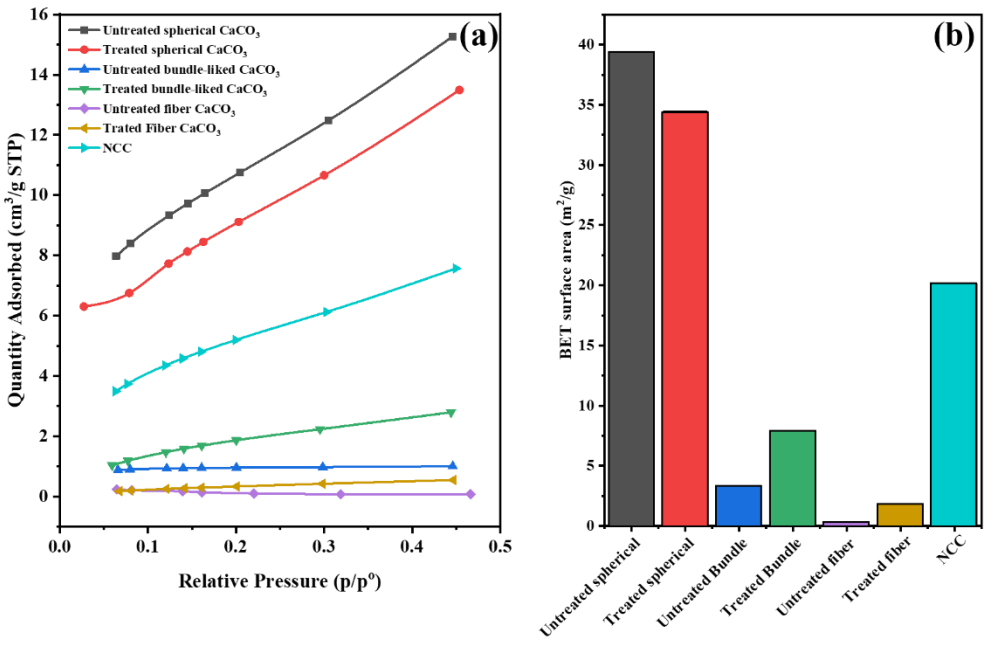


Figure 5.11 The (a) BET isotherm linear plot and (b) BET surface area values of obtained $CaCO_3$ (untreated and treated ones) together with commercial $CaCO_3$ (NCC)

The average particle size including length and diameter, aspect ratio, and specific surface area of $CaCO_3$ particles were summarized in Table 5.2.

Table 5.2 Average particle size and BET specific surface area of as-precipitated and commercial $CaCO_3$ powders

Type of $CaCO_3$	Particle size*			BET specific surface (m^2/g)
	Length (L) (μm)	Diameter (D) (μm)	Aspect ratio**	
1. Untreated spherical $CaCO_3$	0.44 ± 0.17	0.42 ± 0.14	1.04	39.32
2. Treated spherical $CaCO_3$	0.50 ± 0.19	0.51 ± 0.16	0.98	34.45
3. Untreated bundle-liked $CaCO_3$	4.44 ± 1.92	0.49 ± 0.08	9.06	3.27
4. Treated bundle-liked $CaCO_3$	4.38 ± 0.83	0.52 ± 0.39	8.42	7.93
5. Untreated fiber $CaCO_3$	20.40 ± 7.72	0.13 ± 0.04	156.9	0.29
6. Treated fiber $CaCO_3$	19.05 ± 0.94	0.53 ± 0.05	35.9	1.53
7. NCC $CaCO_3$	0.068 ± 0.011	0.049 ± 0.014	1.38	20.15
8. 4QC $CaCO_3$	3.16 ± 1.40	2.20 ± 2.92	1.58	N/A
9. 9QQ $CaCO_3$	4.43 ± 3.46	3.41 ± 0.70	1.29	N/A

* Particle size in length and diameter was measured by ImageJ by dragging the length of horizontal and vertical line.

**Aspect ratio = Length/Diameter

5.2.3 Polymorphic phases and chemical structure of $CaCO_3$ particles

The polymorphic phases of the prepared $CaCO_3$ particles were investigated by the XRD technique. The polymorph included vaterite, aragonite and calcite phases. The chemical structure of $CaCO_3$ crystals was determined from ATR-FTIR and Raman analysis

5.2.3.1 X-ray diffraction (XRD)

To identify the crystalline phases of the prepared $CaCO_3$, the XRD technique was employed in the range of 20 – 40º. Figure 5.12 shows the X-ray diffractograms of obtained $CaCO_3$ and commercial $CaCO_3$ particles. The peaks located at 20.0, 24.9, 27.0, and 32.7º in 2Θ assigning the reflection of XRD patterns of (004), (100), (101), and (102), respectively, could confirm the existence of untreated and treated vaterite $CaCO_3$ particles in Figure 5.12(a) and 5.12(b). When the preparation temperature was used at 80ºC, it affected the final grain morphology and polymorph of $CaCO_3$ particles. The bundle-liked $CaCO_3$ particles were revealed from the appearance of characteristic peaks at 26.1, 33.1, 36.1, 37.2, 37.8 and 38.9º in 2Θ which crystal planes could be assigned as (110), (111), (121+012), (031), (112) and (130), respectively in Figure 5.12(c) and 5.12(d). The typical peaks of vaterite and calcite at 29.3º of crystal plane (104) were also found. As a result, aragonite polymorph of bundle-liked $CaCO_3$ particles with the highest intensity over other polymorphs was identified. The fiber $CaCO_3$ particles were produced via the transformation from vaterite sphere particles under high temperature in a water medium. The XRD results of untreated fiber $CaCO_3$ particles are presented in Figure 5.12(e). There are two typical peaks appeared which are aragonite and vaterite for fiber $CaCO_3$ crystals. The XRD pattern of treated fiber $CaCO_3$ in Figure 5.12(f) revealed the mixing of the $CaCO_3$ polymorphs including vaterite, aragonite and calcite. This might come from the surface of untreated fiber $CaCO_3$ was coated by superhydrophobic sphere. In the case of commercial $CaCO_3$ consisting of NCC (Figure 5.12(g)), 4QC (Figure 5.12(h)), and 9QQ (Figure 5.12(i)), the Bragg peaks are located at 23.0, 29.3, 31.5, 35.9 and 39.5º in 2Θ, which could be assigned calcite polymorph.

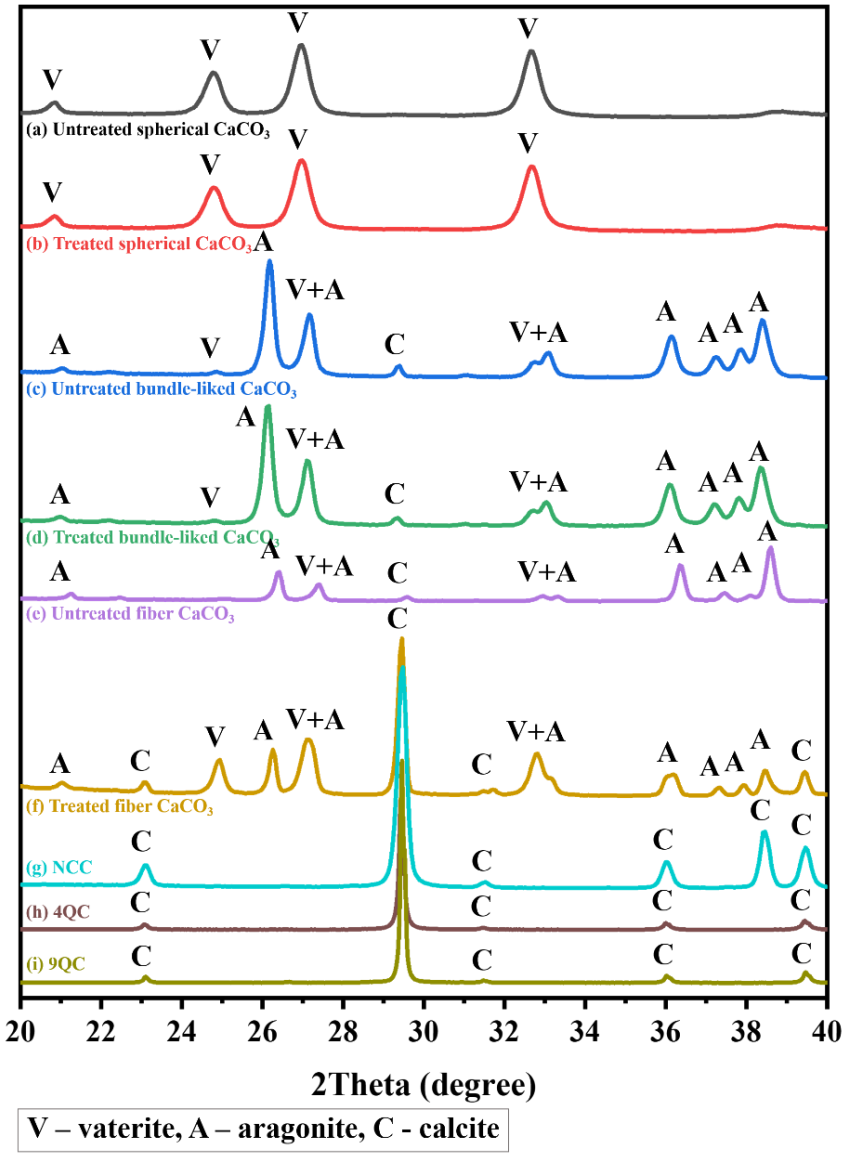


Figure 5.12 The X-ray diffractograms of obtained and commercial $CaCO_3$ particles in the range of 20 – 40° (Θ)

The percentage of each polymorph could be measured by calculating using MAUD software with refinement of the atomic fractions via the Rietveld method [157] shown in Figure 5.13. For the refinement step, the reference peaks informing the crystal structures of $CaCO_3$ polymorphs were first used. The quantitative XRD analysis of spherical shaped-$CaCO_3$ powders presents a high content of vaterite phase that is higher than 99%. The untreated spherical $CaCO_3$ gives a percentage of vaterite of 99.10% and calcite with a percentage of 0.10% as shown in Figure 5.13(a). The treated

spherical provided 99.80% of vaterite and 0.20% of calcite (Figure 5.13(b)). The bundle-liked $CaCO_3$ particles presented a high content of aragonite phase over vaterite and calcite. The percentage of vaterite, aragonite and calcite phases of untreated bundle-liked $CaCO_3$ in Figure 5.13(c) was found to be 22.00, 75.66, and 2.32%, respectively. While the treated bundle-liked $CaCO_3$ (Figure 5.13(d)) gave 12.17, 85.24, and 2.57% of vaterite, aragonite and calcite, respectively. The percentage of polymorphs of untreated fiber $CaCO_3$ (Figure 5.13(e)) consists of 84.92% of aragonite, 14.95% of vaterite, and 0.10% of calcite. The main polymorphic phase of treated fiber $CaCO_3$ (Figure 5.13(f)) is aragonite 72.24% following to vaterite (27.13%), and calcite (0.63%). The XRD refinement of three types of commercial $CaCO_3$ gave a volume fraction of calcite higher than 99.6% (Figure 5.13(g), 5.13(h) and 5.13(i)). These results are in good agreement with SEM images, the Bragg peaks of 9QQ and 4QC commercial $CaCO_3$ are narrower than the NCC indicating that the particle size of 9QQ and 4QC are bigger than NCC. The percentage of vaterite, aragonite and calcite polymorphs of $CaCO_3$ of different types of $CaCO_3$ used in this work were listed in Table 5.3.

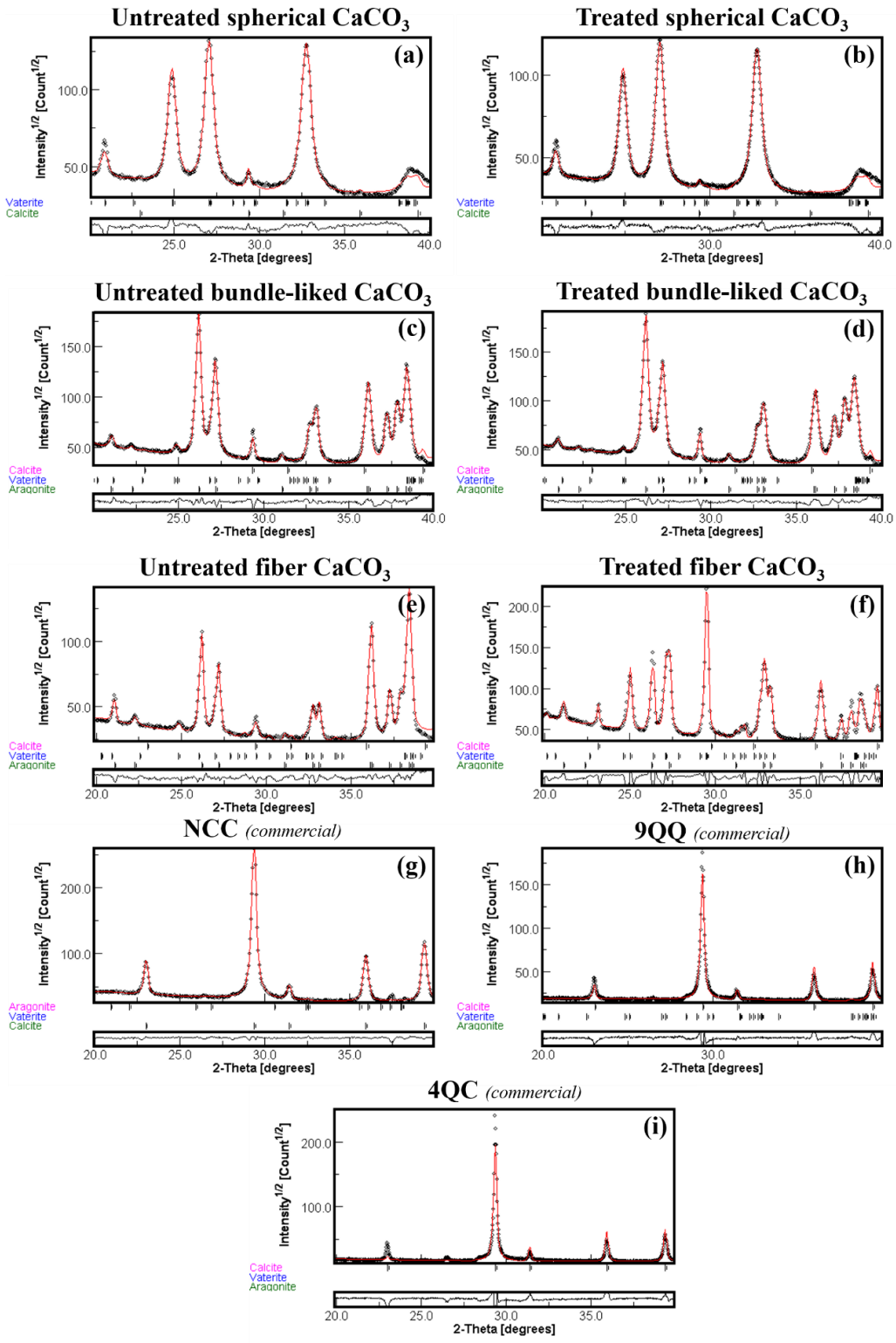


Figure 5.13 Rietveld refinement patterns of X-ray diffraction from MAUD software of $CaCO_3$ powders: (a) untreated spherical, (b) treated spherical, (c) untreated bundle-liked, (d) treated bundle-liked, (e) untreated fiber, (f) treated fiber, (g) NCC, (h) 9QQ, and (i) 4QC commercial $CaCO_3$

Table 5.3 %Crystallinity of different types of $CaCO_3$ powders

Type of $CaCO_3$	%Crystallinity		
	Vaterite	**Aragonite**	**Calcite**
1. Untreated spherical $CaCO_3$	**99.10**	0	0.90
2. Treated spherical $CaCO_3$	**99.80**	0	0.20
3. Untreated bundle-liked $CaCO_3$	22.00	**75.66**	2.32
4. Treated bundle-liked $CaCO_3$	12.17	**85.24**	2.57
5. Untreated fiber $CaCO_3$	14.95	**84.92**	0.10
6. Treated fiber $CaCO_3$	27.13	**72.24**	0.63
7. NCC	0.30	0	**99.60**
8. 4QC	1.90	0	**99.90**
9. 9QQ	0	0	**99.90**

5.2.3.2 Attenuated total reflection-Fourier transform infrared (ATR-FTIR) analysis

ATR-FTIR was employed to investigate the chemical structure of $CaCO_3$. The FTIR spectrum of each type of $CaCO_3$ is shown in Figure 5.14 and the band assignments are listed in Table 5.4. The absorption bands of $CaCO_3$ correspond to ν_1 mode: symmetric C-O stretching, ν_2 mode: CO_3^{2-} out-of-plane bending, and ν_3 mode: doubly degenerated asymmetric C-O stretching, and ν_4 mode: doubly degenerated in-plane OCO deformation bending. The characteristic absorption bands of vaterite located at 745 (ν_4), 876 (ν_2), 1424, 1450 and 1490 (ν_3) cm^{-1} for both spherical $CaCO_3$ with and without surface treatment. Moreover, there is no typical peak of calcite absorption bands observed in the system of spherical $CaCO_3$ precipitation. The result could support the use of sucrose as an aqueous medium leading to a considerably high impact of high percentage of vaterite polymorph. [10; 11] ATR-FTIR spectra of the bundle-liked shaped samples revealed the vibration modes characteristic bands of aragonite located at 700 and 712 (ν_4), 854 (ν_2) and 1475 (ν_3) cm^{-1}, clearly seen in Figure 5.14(b) and 5.14(c). The untreated and treated fiber $CaCO_3$ show typical absorption bands of vaterite and aragonite. There are some spheres remaining in the system but the aragonite provided the major form. The calcite absorption bands can be detected in the commercial

$CaCO_3$ (NCC) at 713, 874, and 1434 cm^{-1} corresponding to the ν_4, ν_2, and ν_3 vibration modes, respectively.

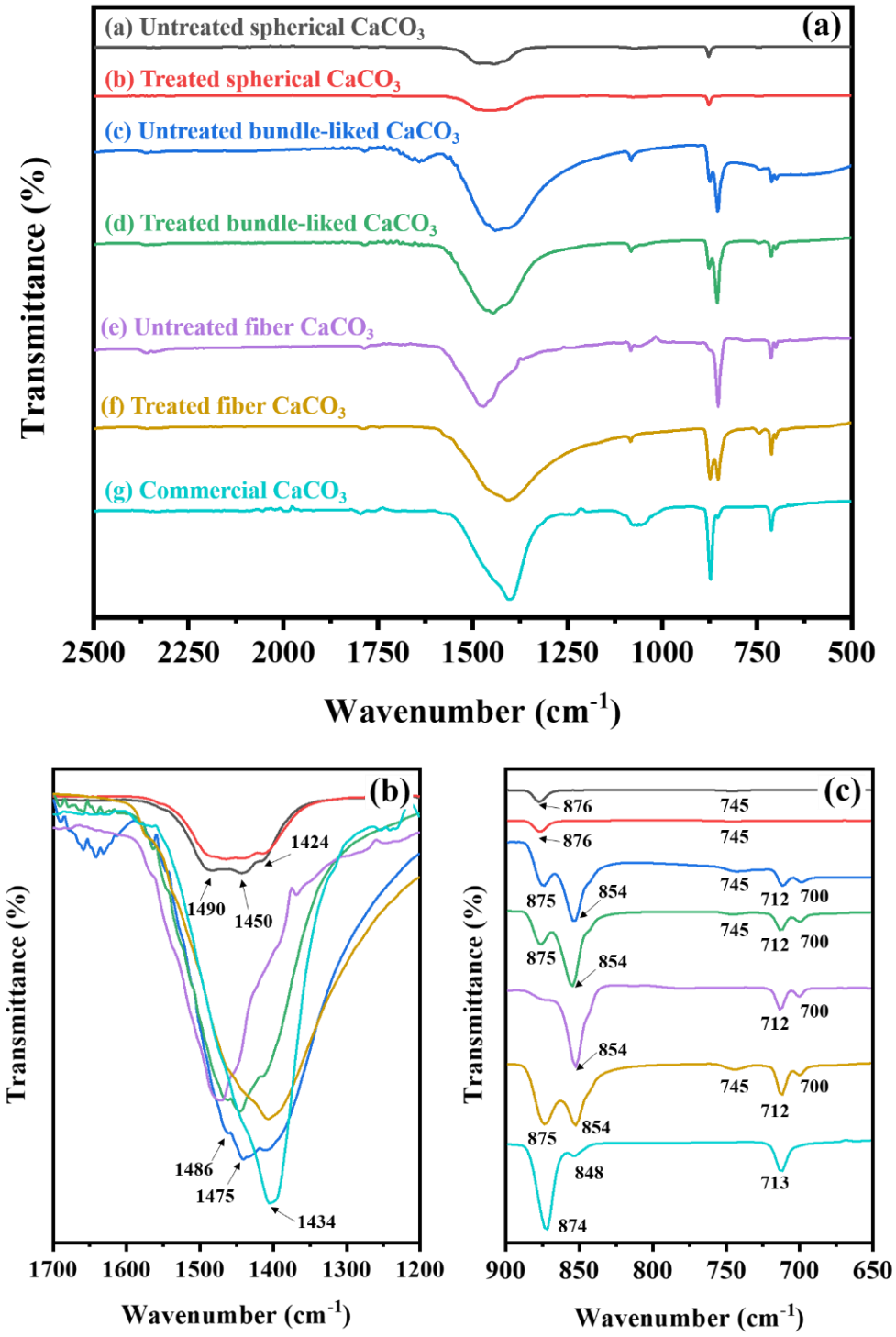


Figure 5.14 FTIR spectra of different types of $CaCO_3$ particles in the range of (a) 500 - 2500 cm^{-1}, (b) 1200 – 1700 cm^{-1}, and (c) 650 – 900 cm^{-1}

Table 5.4 Specific IR wavenumber in cm^{-1} of $CaCO_3$ polymorphs

$CaCO_3$ polymorphs	**Reference absorption band (cm^{-1}) [13]**	**Obtained absorption band (cm^{-1})**	**Vibration mode**
Vaterite	744	745	Doubly degenerate in-plane OCO deformation bending
	849	849	CO_3 out-of-plane bending
	877	876	CO_3 out-of-plane bending
	1090	1090	Symmetric C-O stretching
	1424	1424	C-O stretching
	1450	1450	Doubly degenerated asymmetric C-O stretching
	1465	1465	Doubly degenerated asymmetric C-O stretching
	1490	1490	Doubly degenerated asymmetric C-O stretching
Aragonite	700	700	Doubly degenerate in-plane OCO deformation bending
	712	712	Doubly degenerate in-plane OCO deformation bending
	854	854	CO_3 out-of-plane bending
	1082	1082	Symmetric C-O stretching
	1475	1475	Asymmetric C-O stretching
	1486	1486	C-O stretching
Calcite	712	713	Doubly degenerate in-plane OCO deformation bending
			CO_3 out-of-plane bending
	848	848	CO_3 out-of-plane bending
	877	875	Doubly degenerated asymmetric C-O stretching
	1435	1435	

5.2.3.3 Raman spectroscopy

The polymorphs of $CaCO_3$ phases were also confirmed by Raman spectroscopy as presented in Figure 5.15 in the range of 600 – 1200 cm^{-1}. The Raman

peak maxima (ν_1, ν_3 and ν_4) in cm^{-1} of polymorphic phases of $CaCO_3$ were assigned in Table 5.5. The typical peaks of vaterite polymorph were found at 685, 745, 1075 and 1090 cm^{-1} for untreated and treated spherical $CaCO_3$ (Figure 5.15(a) and 5.15(b)). The typical vibration modes of aragonite at 705 and 1087 cm^{-1} appeared in both shapes of $CaCO_3$ crystal: bundle-liked and fiber $CaCO_3$ particles. The commercial $CaCO_3$ (NCC) shows only the typical bands of calcite polymorphs at 713 and 1085 cm^{-1}.

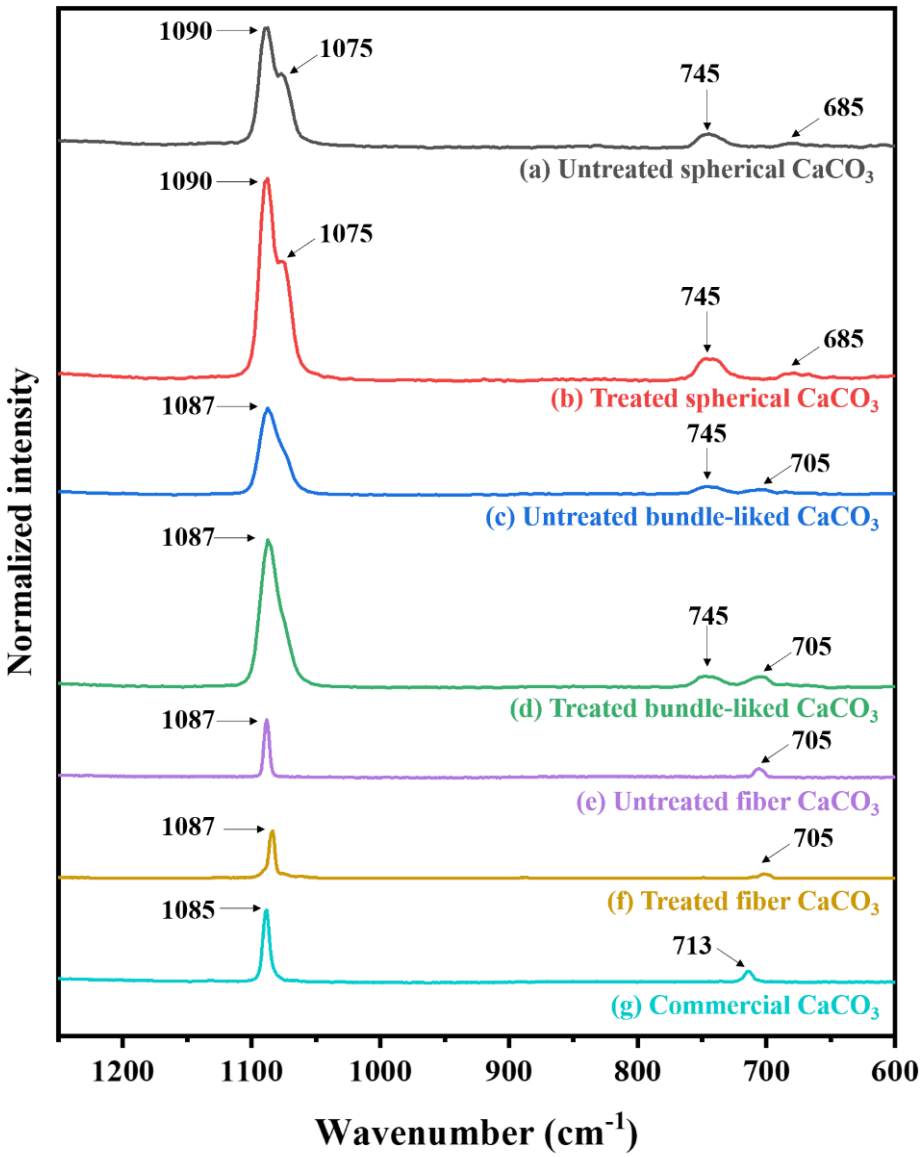


Figure 5.15 Raman spectra of (a) untreated spherical, (b) treated spherical, (c) untreated bundle-liked, (d) treated bundle-liked, (e) untreated fiber, (f) treated fiber, and (g) NCC commercial $CaCO_3$ particles

Table 5.5 Raman peaks maxima in cm^{-1} of polymorphic phases of $CaCO_3$

$CaCO_3$-polymoph	**ν_1 symmetric stretching (CO_3^{2-})**	**ν_3 symmetric stretching (CO_3^{2-})**	**ν_4 in-plane bending (CO_3^{2-})**
Vaterite	1074, 1090	1445, 1495	685, 744
Aragonite	1087	1464	705
Calcite	1085	1435	711

The results corresponding to XRD patterns, FTIR analysis and Raman spectroscopy further confirmed that the different shapes of $CaCO_3$ crystals resulted in the different polymorphs. According to the typical shape of vaterite form which is hexagonal or spherical, the obtained untreated and treated spherical $CaCO_3$ confirmed the typical characteristic peaks of vaterite. On the other hand, as-prepared bundle-liked and fiber-shaped $CaCO_3$ provided a high content of aragonite polymorph whose typical shape is the rhombohedral structure or needle-like shape. The most stable phase of $CaCO_3$: calcite polymorph: present in commercial $CaCO_3$ particles that were prepared from limestone or rock as starting materials. [47] These results can confirm that the mixing procedure plays an important role in the morphological shapes and polymorphic phases of $CaCO_3$ crystals.

5.2.4 Wettability of $CaCO_3$ particles

5.2.4.1 Contact angle

Contact angle measurement is one of the useful techniques to qualitatively measure the polarity of materials. The measurement of the wettability of the $CaCO_3$ powders by a liquid is the way to evaluate whether the surface has a hydrophobic or hydrophilic characteristic if there exists a surface modification. The water is dropped on the powder surface and then the angle of a water droplet on the powder is measured. The contact angle is defined as the angle between a tangent to the liquid surface and the solid surface as seen in Figure 5.16. If the angle is between 0^o to 90^o, the surface is wettable or hydrophilic. An angle higher than 90^o means the surface

is not wettability. It is identified as hydrophobic. If the angle approaches higher than 150^{o}, it is defined as superhydrophobic and is completely liquid-repellent.

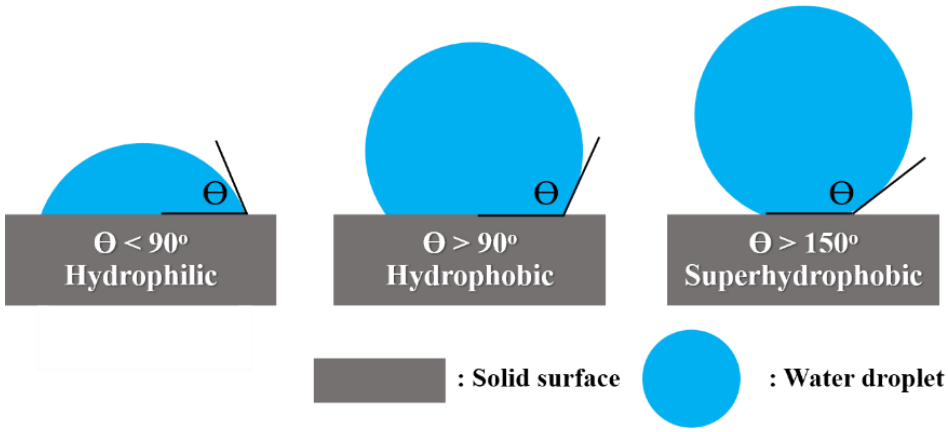


Figure 5.16 The contact angle of water droplets on the solid surface

The water droplet on the surface of the prepared $CaCO_3$ powders was exhibited in Figure 5.17. The contact angles of untreated spherical, bundle-liked and fiber $CaCO_3$ particles are 28 ± 2^{o} (Figure. 5.17(a)), 29 ± 2^{o} (Figure. 5.17(c)) and 31 ± 1^{o} (Figure. 5.17(e)), respectively which are identified as hydrophilic property. While, it was found that the contact angles of treated spherical, treated bundle-liked and treated fiber $CaCO_3$, modified by olive soap are at 163 ± 2^{o} (Figure. 5.17(b)), 167 ± 2^{o} (Figure. 5.17(d)) and 165 ± 5^{o} (Figure. 5.17(f)), respectively. These $CaCO_3$ particles could be defined as superhydrophobic behavior which is similar to the water droplet on lotus leaves. The contact angle of bundle-liked $CaCO_3$ particles provides a higher value than spheroidal ones due to its rougher surface as seen in SEM images. The contact angle of nano calcium carbonate (NCC) and micro-scale 4QC were found at 159 ± 3^{o} (Figure. 5.17(h)) and 164 ± 4^{o} (Figure. 5.17(i)), respectively. They can be classified as superhydrophobic powder. While another micro-scaled commercial $CaCO_3$ powder (9QQ) has an angle between the water droplet and powder surface is 23 ± 1^{o} (Figure. 5.17(g)). It is considered a hydrophilic powder. The contact angle values and wettability classification of different types of $CaCO_3$ powders are listed in Table 5.6.

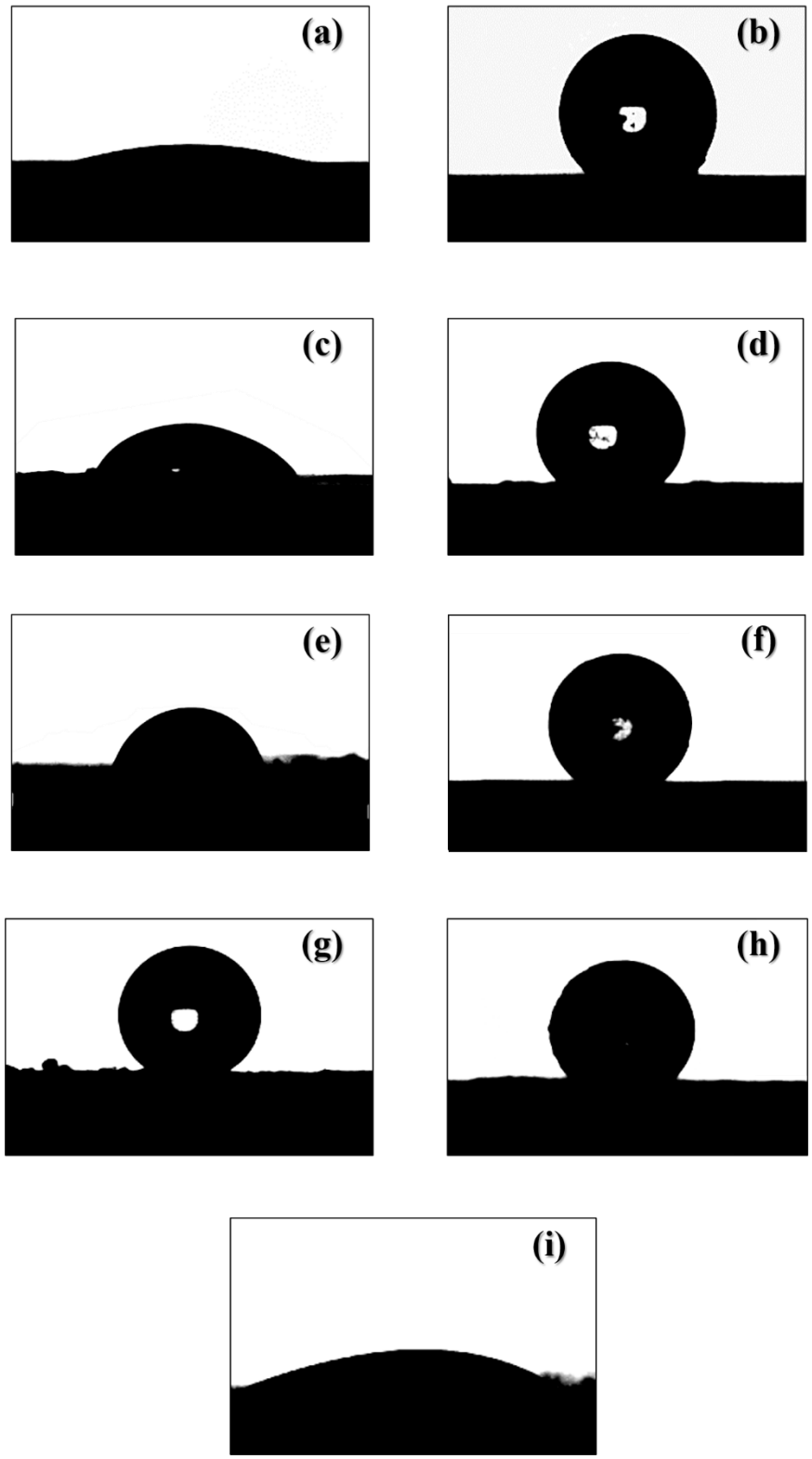


Figure 5.17 Photographs of water droplets of (a) untreated spherical, (b) treated spherical, (c) untreated bundle-liked, (d) treated bundle-liked, (e) untreated fiber, (f) treated fiber, (g) NCC, (h) 4QC, and (i) 9QQ commercial $CaCO_3$ powders

Table 5.6 Contact angle values and wettability classification of different types of $CaCO_3$ powders

Type of $CaCO_3$	Contact angle (°)	Wettability property
1. Untreated spherical $CaCO_3$	< 20	Hydrophilic
2. Treated spherical $CaCO_3$	163 ± 2	Superhydrophobic
3. Untreated bundle-liked $CaCO_3$	< 40	Hydrophilic
4. Treated bundle-liked $CaCO_3$	167 ± 2	Superhydrophobic
5. Untreated fiber $CaCO_3$	< 45	Hydrophilic
6. Treated fiber $CaCO_3$	165 ± 5	Superhydrophobic
7. NCC	159 ± 3	Superhydrophobic
8. 4QC	164 ± 4	Superhydrophobic
9. 9QQ	< 20	Hydrophilic

5.2.5 Thermal property of $CaCO_3$ particles

5.2.5.1 Thermogravimetric analysis

The thermal properties of $CaCO_3$ particles were investigated by thermogravimetric analysis (TGA). The TGA curves and derivative thermogravimetric (DTG) curves of as-prepared and commercial $CaCO_3$ powders were illustrated in Figure 5.18. The thermal decomposition profiles of all $CaCO_3$ powders reveal the decomposition of calcination of $CaCO_3$ to CaO and CO_2 in the range of 600 – 800 °C. The result of untreated spherical $CaCO_3$ revealed a two-step degradation process in Figure 5.18(a). The first step (200 – 250°C) was the decomposition of sucrose with 3 – 4 % weight loss. The second stage (650 – 750°C) demonstrated calcination of $CaCO_3$ with 42% weight loss. For the treated spherical $CaCO_3$ powders, there is another step of decomposition of an organic fuel in soap in the range of 400 – 500°C (Figure 5.18(b)). It was found for all treated $CaCO_3$ powders. Consider the commercial $CaCO_3$ particles which were normally treated with stearic acid: NCC and 4QC, there is a decomposition step of stearic acid at the range of 320 – 500°C in Figure 5.18(g) and 5.18(h). The thermal decomposition temperature of different components in different types of $CaCO_3$ powders is listed in Table 5.7.

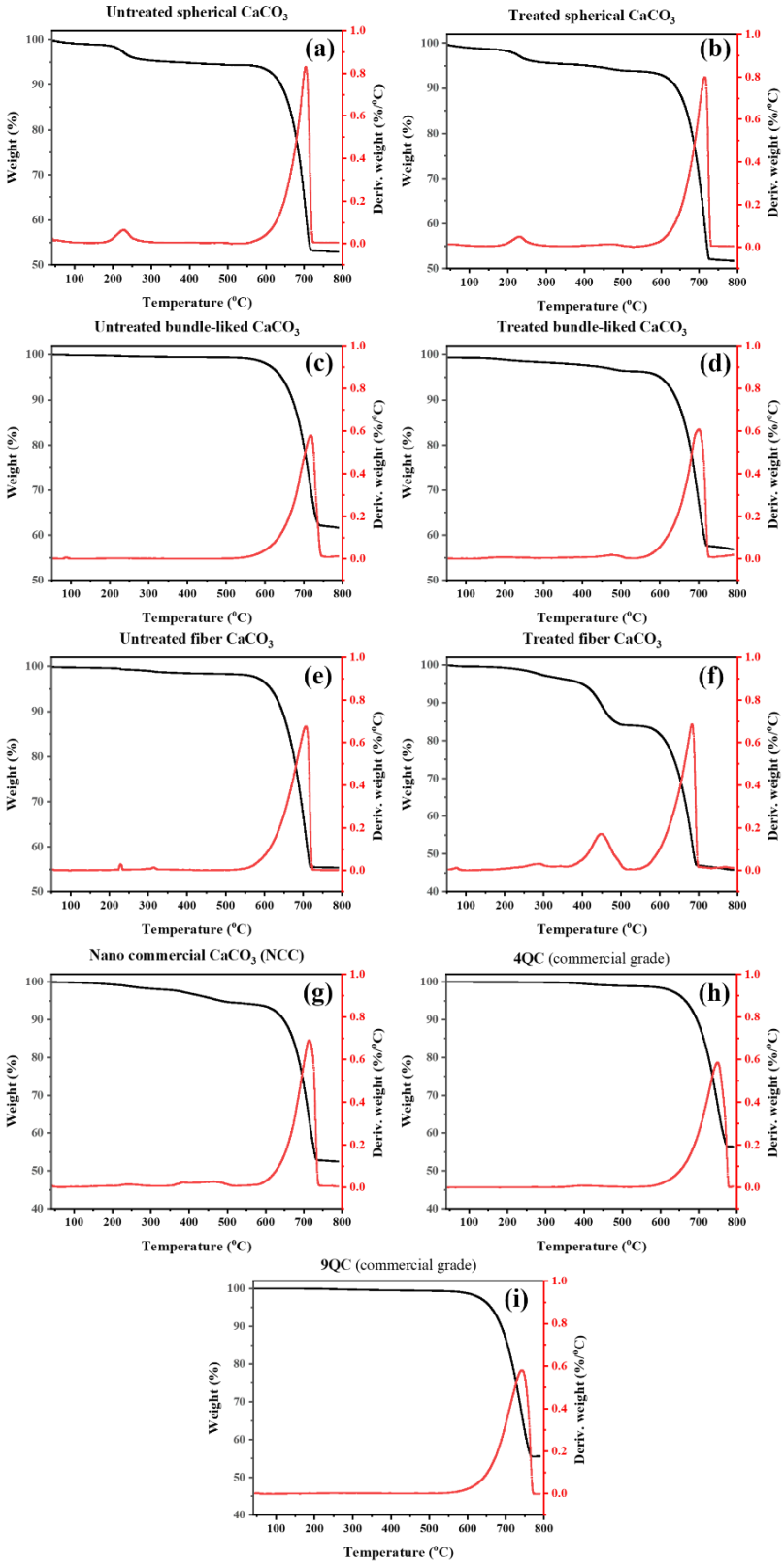


Figure 5.18 TGA thermograms and derivative thermogravimetric curves of (a) untreated spherical, (b) treated spherical, (c) untreated bundle-liked, (d) treated bundle-

liked, (e) untreated fiber, (f) treated fiber, (g) NCC, (h) 4QC, and (i) 9QQ commercial $CaCO_3$ powders

Table 5.7 Thermal decomposition temperature of different types of $CaCO_3$

Types of $CaCO_3$	**Decomposition temperature (^oC)**	**Decomposition component**
1. Untreated spherical $CaCO_3$	227	Sucrose
	703	Calcination of $CaCO_3$ to CaO and CO_2
2. Treated spherical $CaCO_3$	230	Sucrose
	469	Organic fuel in soap
	714	Calcination of $CaCO_3$
3. Untreated bundle-liked $CaCO_3$	718	Calcination of $CaCO_3$
4. Treated bundle-liked $CaCO_3$	475	Organic fuel in soap
	700	Calcination of $CaCO_3$
5. Untreated fiber $CaCO_3$	313	Elimination of crystal water in aragonite
	706	Calcination of $CaCO_3$
6. Treated fiber $CaCO_3$	289	Elimination of crystal water in aragonite
	448	Organic fuel in soap
	682	Calcination of $CaCO_3$
7. NCC	320 - 500	Stearic acid
	713	Calcination of $CaCO_3$
8. 4QC	320 – 500	Stearic acid
	749	Calcination of $CaCO_3$
9. 9QQ	741	Calcination of $CaCO_3$

Part II: Preparation of NR/$CaCO_3$ composites and their mechanical properties

In this part, the different types of prepared calcium carbonate ($CaCO_3$) powders (spherical, bundle-liked and fiber obtained from Part I) were filled in NR to investigate their reinforcing efficacy in NR vulcanizates. Both untreated and treated $CaCO_3$ and commercial $CaCO_3$ in nano and micro-scale (NCC, 4QC and 9QQ) were incorporated in NR latex. The chemical structure and crystal analysis of NR/$CaCO_3$ composites were studied. The mechanical properties including tensile properties, tear strength, and hardness of the composites were evaluated compared to the carbon black (CB, N330) filled NR vulcanizates.

5.3 Chemical and physical properties of NR/$CaCO_3$ compound

5.3.1 Physical appearance of pre-dispersed NR/$CaCO_3$ and NR/CB compounds

The different amounts (0, 5, 10, 20, 40, and 60 phr) of $CaCO_3$ particles were mixed with NR in latex form, and then dried before being subjected to compounding with vulcanizing agents on a 2-roll mill. It was reported in section 5.2.4 that the $CaCO_3$ is hydrophilic while treated $CaCO_3$ is hydrophobic, evidenced by contact angle measurement. The contact angle of the dried NR sheet was also evaluated by the deposition of a water droplet on an NR vulcanizate sheet (Figure 5.19). As a result, the contact angle of the NR is found at $113^o \pm 3$, which is considered a hydrophobic character corresponding to its polyisoprene structure.

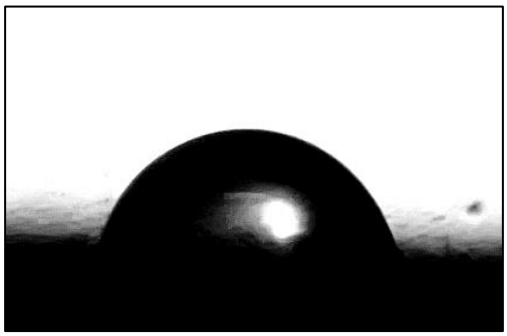


Figure 5.19 Photograph of a water droplet on NR vulcanizate sheet without filler

The physical appearance of pre-dispersed NR/$CaCO_3$ and NR/CB compounds at 20 phr of filler loading was presented in Figure 5.20. It was seen that the hydrophilic fillers consisting of untreated spherical $CaCO_3$ (Figure 5.20(a)), untreated bundle-liked $CaCO_3$ (Figure 5.20(c)), untreated fiber $CaCO_3$ (Figure 5.20(e)), 9QQ (Figure 5.20(i)), and N330 CB (Figure 5.20(j)) were agglomerated. Meanwhile, the good dispersion of fillers in the rubber matrix was exhibited in the pre-dispersed NR compounds filled with treated or superhydrophobic $CaCO_3$ powders following: treated spherical $CaCO_3$ (Figure 5.20(b)), treated bundle-liked $CaCO_3$ (Figure 5.20(d)), treated fiber $CaCO_3$ (Figure 5.20(f)), NCC (Figure 5.20(g)), and 4QC (Figure 5.20(h)). Consequently, this result strongly indicated that the hydrophobic powders dispersed homogeneously in the NR matrix due to the hydrophobic property of NR.

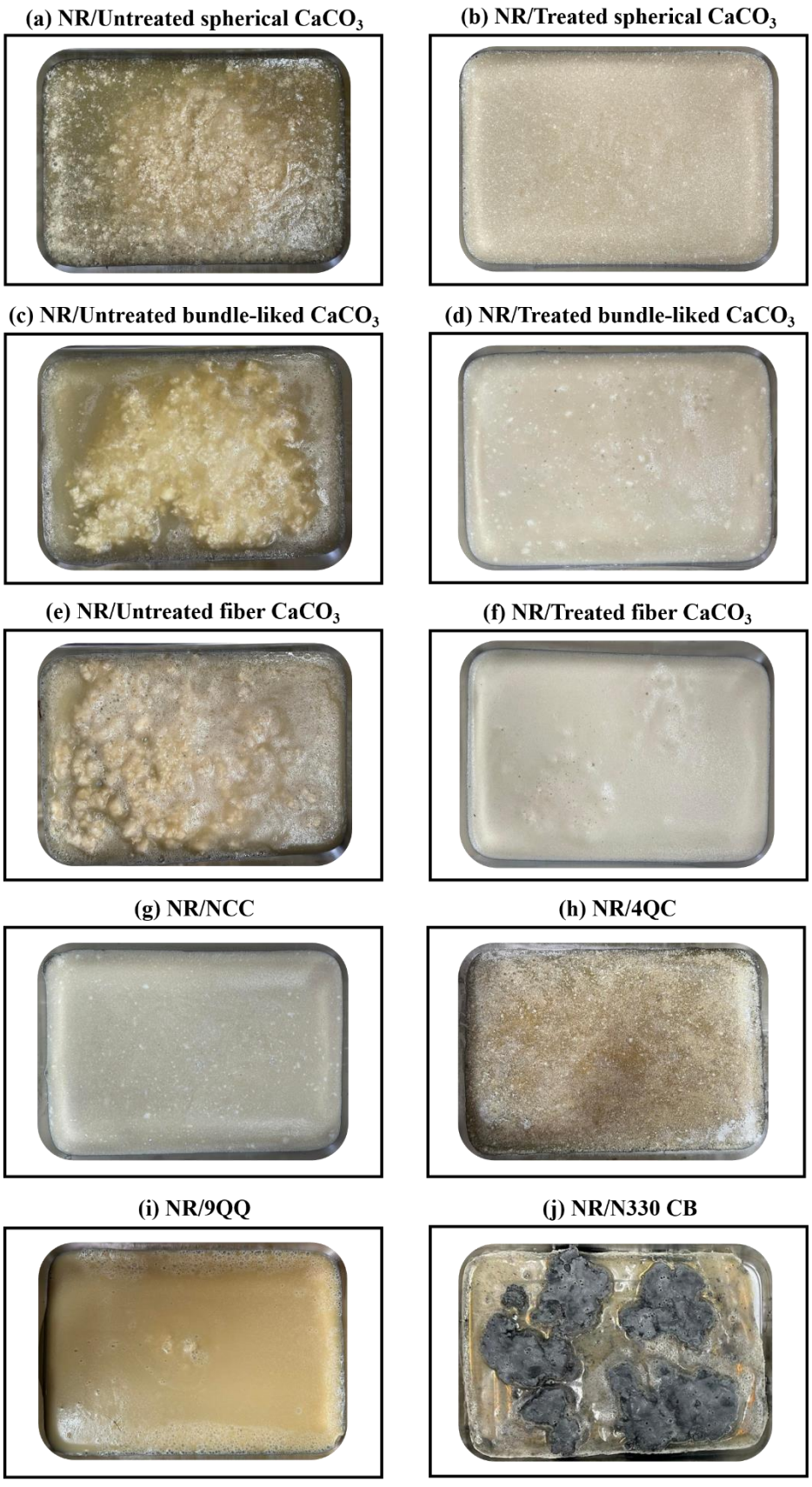


Figure 5.20 Physical appearance of different types of pre-dispersed $CaCO_3$ in NR latex

5.3.1.1 Morphology of $CaCO_3$ in NR and water

As discussed earlier the metastability polymorph vaterite $CaCO_3$ is thermodynamically transformed to a higher stage aragonite or cubical calcite in water. [14] The stability of vaterite $CaCO_3$ particles in the rubber matrix was studied and compared to the aqueous medium. Figure 5.21 presents the SEM images of initials untreated spherical $CaCO_3$ particles, $CaCO_3$ particles dispersed in water and $CaCO_3$ incorporated in NR latex after drying for 7 days. The morphology presented that the initial spherical $CaCO_3$ (Figure 5.21(a)) was transformed into cubical calcite crystals when it was dispersed in water (Figure 5.21(b)). In comparison, the spherical $CaCO_3$ particles could maintain their round shape when they were loaded NR latex (Figure 5.21(c)).

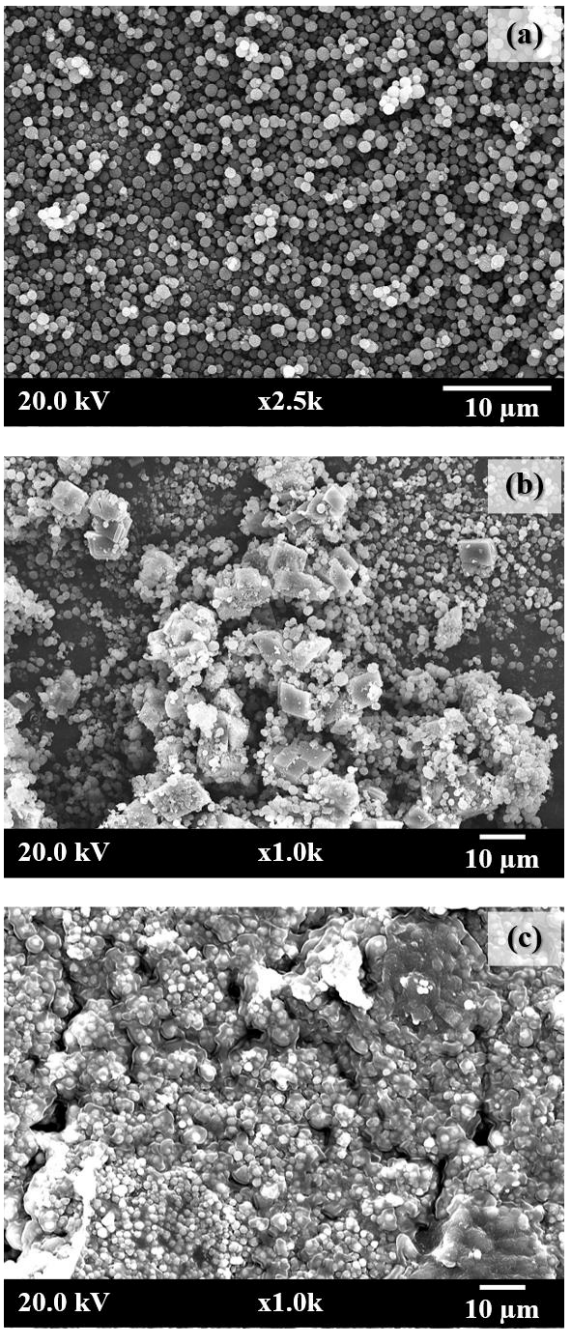


Figure 5.21 SEM images at 1000x, 10 µm scale bar of (a) as-prepared untreated spherical $CaCO_3$, (b) spherical $CaCO_3$ dispersed in water, and (c) untreated spherical $CaCO_3$ incorporated in NR

Figure 5.22 shows the XRD patterns of polymorphic phases of $CaCO_3$ particles dispersed in water and incorporated in NR. From section 5.2.3, the prepared spherical $CaCO_3$ particles provided 99% of vaterite form. The XRD diffraction of

$CaCO_3$ in Figure 5.22(a) shows that the polymorph of $CaCO_3$ could be maintained in the original polymorph which appeared only in the typical peaks of vaterite in NR. On the other hand, the vaterite $CaCO_3$ was transformed into the calcite form evidenced by the appearance of the peak at 29.3 in 2Θ of calcite. The percentage of crystalline via Rietveld analysis of spherical $CaCO_3$ in water (Figure 5.22(b)), was 81.5% of calcite and 18.94% of vaterite.

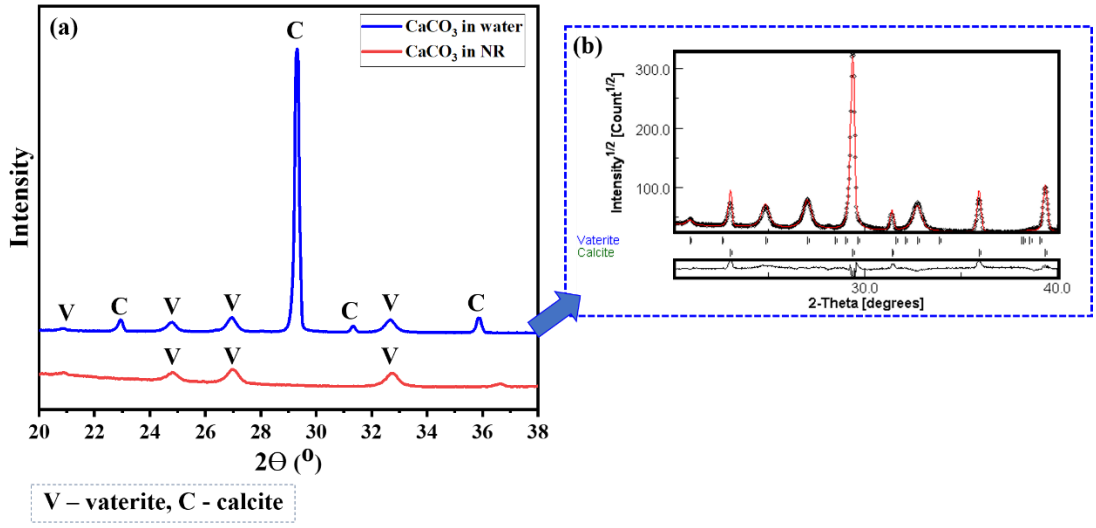


Figure 5.22 (a) XRD diffractions of $CaCO_3$ particles in water and NR, and (b) XRD refinement deduced from the Rietveld analysis for MAUD software of $CaCO_3$ in water for calculating the percentage of polymorph transformation

The ATR-FTIR spectra in Figure 5.23 supported our finding that the spherical $CaCO_3$ particles did not reform the polymorphic phase when it was incorporated in NR latex. [10] Figure 5.23(b) reveals the typical peak of calcite at 713 cm^{-1} in the case of $CaCO_3$ particles dispersed in water and only a vaterite peak at 745, and 1450 cm^{-1} appeared in the case of $CaCO_3$ incorporated in NR. Besides, the FTIR spectrum of NR structure in Figure 2.23(a) was evidenced at 2853, 2960, and 3340 cm^{-1} represented $-CH_2$ symmetric stretching, $-CH_3$ asymmetric stretching, and =C-H stretching, respectively, assigned in Table 5.8. As a result, a good accordance from SEM images, XRD patterns and ATR-FTIR confirm that $CaCO_3$ can stabilize its polymorphs in NR without transformation even though it is in an NR latex aqueous form. This can be inferred that the Ca^{2+} ion of the $CaCO_3$ particle might be adsorbed on the surface of

rubber particles benefit from the negative charges of NR particle, which results in prohibition of $CaCO_3$ crystals and polymorphic phase transformation.

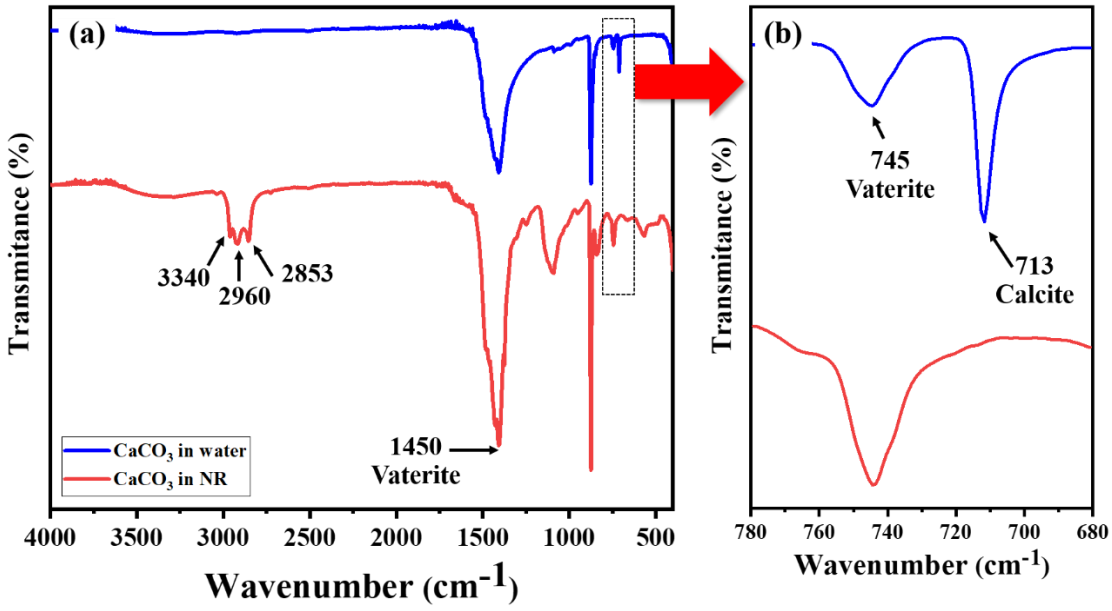


Figure 5.23 ATR-FTIR spectra of $CaCO_3$ particles in water and in NR in the range of (a) 500 – 4000 cm^{-1}, and (b) 680 – 780 cm^{-1}

Table 5.8 ATR-FTIR peak assignment of NR in NR/$CaCO_3$

Assignment	Wavenumber (cm^{-1})
=C-H bending (out of plane)	836
C=C stretching	1666
-CH_2 symmetric stretching	2853
-CH_3 asymmetric stretching	2960
=C-H stretching	3340

5.3.2 Cure measurement of NR/$CaCO_3$ and NR/N330 compounds

Different types of $CaCO_3$ (0, 5, 10, 20, 40 and 60 phr) were incorporated in NR to compare their reinforcing efficacy compared to the carbon black N330 reinforced NR. The cure behavior of NR/$CaCO_3$ and NR/N330 composites was investigated by a Moving die rheometer (MDR) and the results are shown in Figure 5.24. The cure

characteristics of rubber filled with fillers were measured including maximum torque (M_H), minimum torque (M_L), scorch time (t_{s2}), optimum cure time (t_{c90}), and cure rate index (CRI) which were listed in Table 5.9. The cure curves of NR/$CaCO_3$ and NR/N330 vulcanizates provided higher M_H values when the filler loading increased. As a consequence, M_H depends strongly on the type of filler. The N330 carbon black filler is stiffer than the $CaCO_3$ filler, therefore, the torque of NR/N330 composites (Figure 5.24(j)) is higher than NR/$CaCO_3$ (Figure 5.24(a) – 5.24(i)) at all the variations of filler loading. The CRI is a measure of the rate of vulcanization of rubber based on the difference between optimum vulcanization and incipient scorch time. The CRI value of neat NR is 27.55. When filler content increases, the CRI increases. At 10 – 20 phr of $CaCO_3$ filler loading, the rate of vulcanization or CRI value of NR/ $CaCO_3$ composites increased. At high filler loading (40 – 60 phr), the CRI was dropped due to the filler agglomeration. On the other hand, the CRI values of NR/N330 composite were decreased when the carbon black loading increased, resulting in a decrease in the rate of vulcanization. Due to its nanoparticles and ions on the surface of the CB particle, induced the agglomeration of fillers.

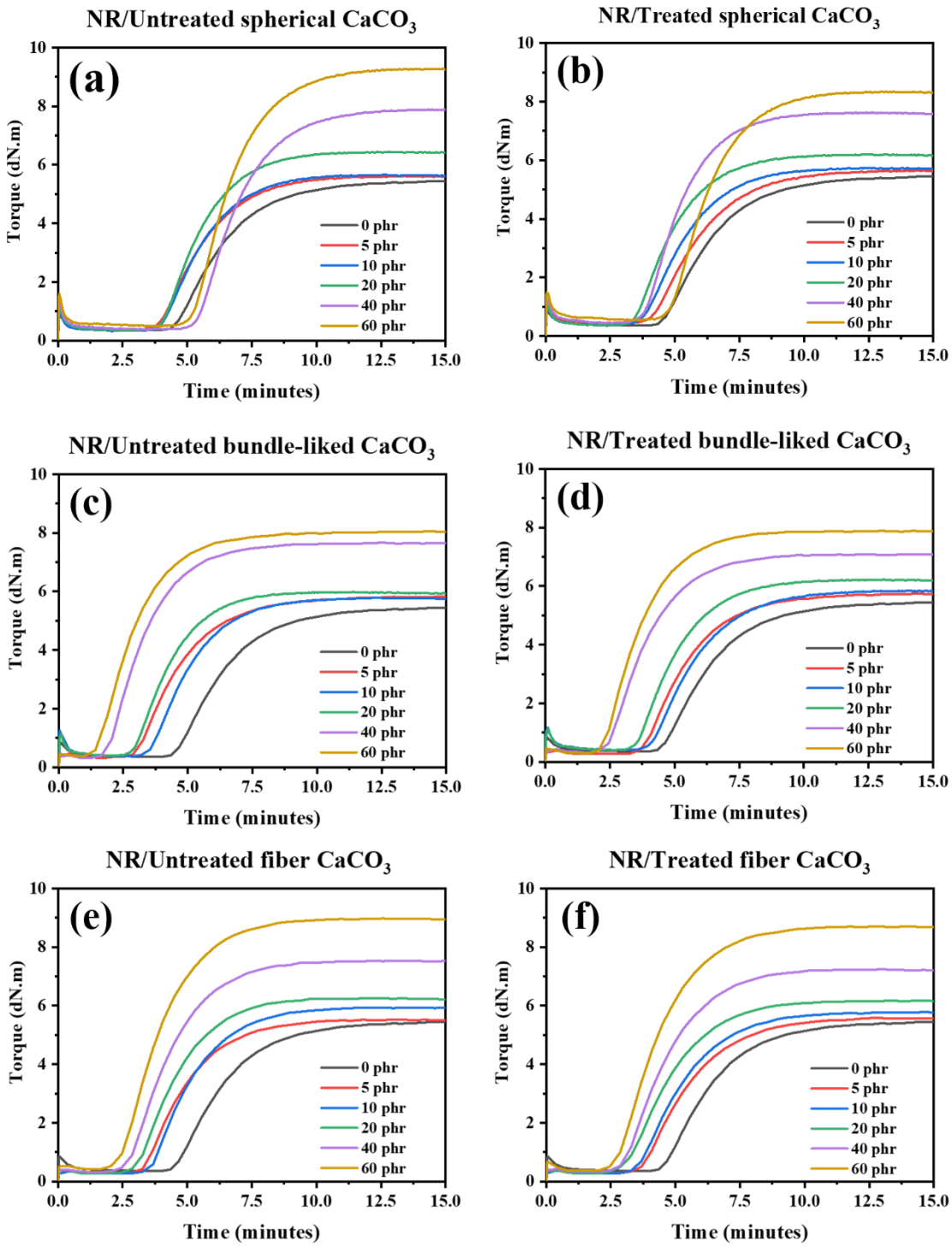


Figure 5.24 Cure behaviors of rubber compounds: (a) NR/Untreated spherical $CaCO_3$, (b) NR/Treated spherical $CaCO_3$, (c) NR/Untreated bundle-liked $CaCO_3$, (d) NR/Treated bundle-liked $CaCO_3$, (e) NR/Untreated fiber $CaCO_3$, (f) NR/Treated fiber $CaCO_3$, (g) NR/NCC $CaCO_3$, (h) NR/4QC $CaCO_3$, (i) NR/9QQ $CaCO_3$, and (j) NR/N330

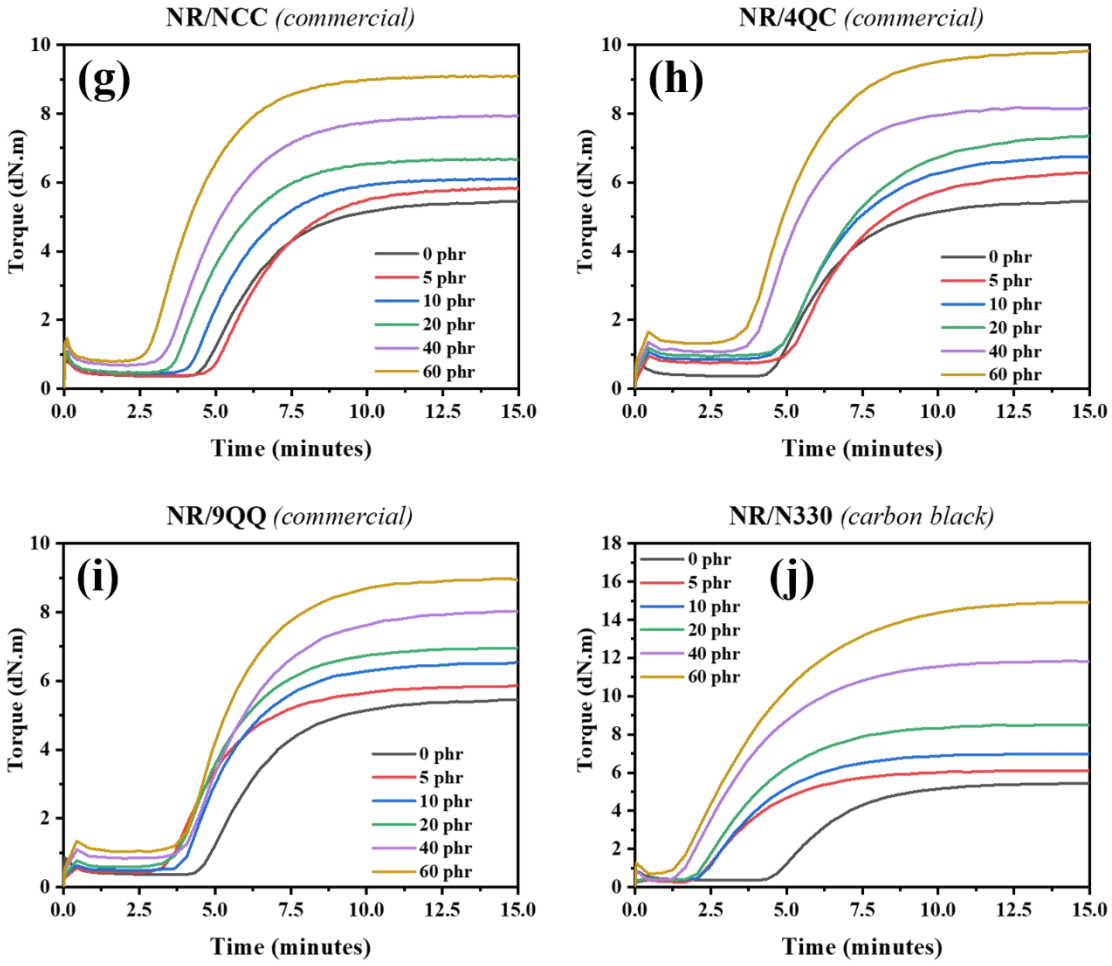


Figure 5.24 (cont.) Cure behaviors of rubber compounds: (a) NR/untreated spherical $CaCO_3$, (b) NR/treated spherical $CaCO_3$, (c) NR/untreated bundle-liked $CaCO_3$, (d) NR/treated bundle-liked $CaCO_3$, (e) NR/untreated fiber $CaCO_3$, (f) NR/treated fiber $CaCO_3$, (g) NR/NCC $CaCO_3$, (h) NR/4QC $CaCO_3$, (i) NR/9QQ $CaCO_3$, and (j) NR/N330

Table 5.9 Cure characteristics of neat NR, NR/$CaCO_3$ and NR/CB composites

Filler loading (phr)	M_H (dN.m)[a]	M_Lb (dN.m)[b]	$M_H - M_L$	t_{s2} (mins)[c]	t_{c90} (mins)[d]	CRI[e]
Neat NR						
0	5.43	0.37	5.06	5.63	9.01	27.55
NR/Untreated spherical $CaCO_3$						
5	5.61	0.36	5.25	4.85	7.88	33.22
10	5.68	0.33	5.35	4.98	7.87	34.01
20	6.43	0.34	6.09	4.82	7.71	34.01
40	7.87	0.38	7.49	6.03	9.24	32.89
60	9.19	0.50	8.69	5.72	8.66	33.67
NR/Treated spherical $CaCO_3$						
5	5.64	0.43	5.21	5.31	8.56	31.75
10	5.75	0.38	5.37	4.76	7.73	33.56
20	6.15	0.35	5.80	4.27	7.06	35.59
40	7.58	0.44	7.14	4.43	7.23	34.72
60	8.36	0.54	7.82	5.39	8.40	33.22
NR/Untreated bundle-liked $CaCO_3$						
5	5.84	0.33	5.51	3.93	7.26	27.78
10	5.86	0.37	5.49	4.44	7.81	32.79
20	6.10	0.39	5.71	3.75	6.74	34.60
40	7.69	0.51	7.18	2.54	5.49	33.67
60	8.04	0.51	7.53	2.13	5.18	33.00
NR/Treated bundle-liked $CaCO_3$						
5	5.80	0.27	5.53	4.76	8.09	27.78
10	5.87	0.39	5.48	5.06	8.39	32.05
20	6.23	0.39	5.84	4.34	7.27	33.78
40	7.10	0.34	6.76	3.11	6.16	33.00
60	7.93	0.36	7.57	2.82	5.80	33.44
NR/Untreated fiber $CaCO_3$						
5	5.54	0.28	5.26	4.35	7.43	32.89
10	5.98	0.27	5.71	4.44	7.56	32.57
20	6.28	0.29	5.99	3.89	6.85	33.56
40	7.59	0.35	7.24	3.46	6.73	31.65
60	8.96	0.49	847	3.04	6.28	31.85
NR/Treated fiber $CaCO_3$						
5	5.63	0.29	534	4.80	8.22	27.40
10	5.80	0.26	554	4.64	7.99	31.15
20	6.25	0.29	5.96	4.09	7.52	30.67

Table 5.9 (cont.) Cure characteristics of neat NR, NR/$CaCO_3$ and NR/CB composites

Filler loading (phr)	M_H (dN.m)[a]	M_Lb (dN.m)[b]	$M_H - M_L$	t_{s2} (mins)[c]	t_{c90} (mins)[d]	CRI[e]
40	7.27	0.35	6.92	3.72	7.07	27.70
60	8.67	0.39	8.28	3.37	6.77	30.86
NR/NCC *(commercial)*						
5	5.87	0.38	5.50	5.89	9.36	27.17
10	6.15	0.45	5.70	5.03	8.34	31.35
20	6.71	0.46	6.25	4.42	7.81	30.96
40	7.95	0.67	7.28	3.92	7.52	26.60
60	9.12	0.79	8.33	3.41	6.84	30.67
NR/4QC *(commercial)*						
5	6.30	0.75	5.55	6.05	9.91	25.91
10	6.77	0.84	5.92	5.70	9.57	25.77
20	7.44	0.92	6.51	5.65	9.79	24.21
40	5.85	1.11	4.74	4.73	6.99	20.83
60	9.81	1.31	8.50	4.29	8.08	26.46
NR/9QQ *(commercial)*						
5	5.85	0.43	5.42	4.35	7.83	28.74
10	6.58	0.49	6.09	4.75	8.31	28.09
20	6.99	0.58	6.41	4.63	8.41	26.46
40	8.08	0.85	7.24	4.76	8.76	25.00
60	9.01	1.05	7.96	4.52	8.30	26.46
NR/N330 carbon black						
5	6.09	0.27	5.82	3.03	6.60	32.68
10	6.99	0.37	6.62	3.08	6.92	25.58
20	8.51	0.39	8.12	2.76	7.05	17.39
40	11.89	0.44	11.45	2.14	7.29	10.29
60	15.00	0.78	14.22	2.01	8.11	7.70

[a]: Maximum torque, [b]: Minimum torque, [c]: Scorch time, [d]: Curing time, [e]: Cure Rate index

The neat NR, and NR/fillers compounds were compressed into 1 mm thickness sheets by using a compression machine at 140^{o}C. [152] Figure 5.25 showed the physical appearance of neat NR, NR/$CaCO_3$, NR/N330 CB composites with 40 phr filler loading. The NR vulcanizate without any filler presented in brown color. While the NR/$CaCO_3$ composites showed more brighter brown color than the neat NR. The commercial

$CaCO_3$ including NCC, 4QC, and 9QQ filled NR provided the brightest shade of brown color. As aforementioned in the introduction chapter, the calcite $CaCO_3$ is widely used to improve the brightness property of a material. In the case of NR/N330 composite, the rubber sheet's color is black corresponding to the black color of carbon black.

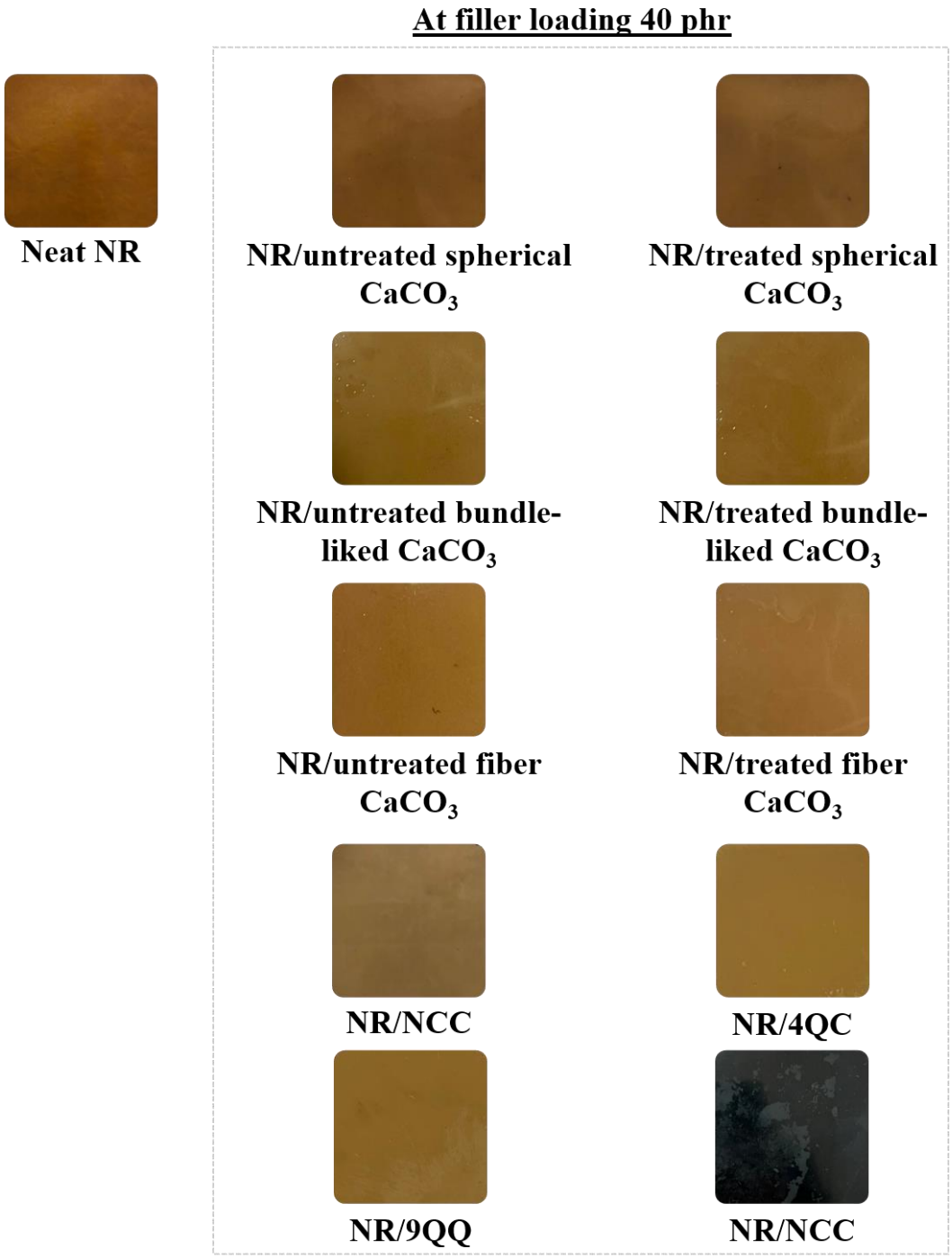


Figure 5.25 Physical appearance of neat NR, NR/$CaCO_3$, and NR/N330 CB sheets

5.3.3 Chemical and crystal characterization of NR/$CaCO_3$ composites

5.3.3.1 XRD analysis

As discussed in section 5.3.1, the morphological shapes and polymorphic phases of vaterite $CaCO_3$ particles could stabilize and not reform when they were incorporated in NR latex. To investigate the crystalline phases of other types of $CaCO_3$ particles, the XRD diffractograms of neat NR and NR/$CaCO_3$ at 20 phr of filler loading were chosen to be carried out as shown in Figure 5.26. As in the rubber vulcanization, oxide (ZnO) was used as one of the activators in the sulfur vulcanization system, the crystalline phases of ZnO were investigated and found located at 31.8^o, 34.0^o, and 36.3^o in 2Θ for neat NR (Figure 5.26(a)) and all NR/$CaCO_3$ composites. [158] The typical crystalline phases of vaterite polymorph for NR/untreated spherical $CaCO_3$ (Figure 5.26(b)) and NR/treated spherical $CaCO_3$ (Figure 5.26(c)) were found without the characteristic peak of calcite appearing in XRD patterns. In the case of rubber/bundle-liked $CaCO_3$ (Figure 5.26(d) and (e)) and rubber/fiber $CaCO_3$ (Figure 5.26(f) and (g)), similar characteristic patterns of vaterite, aragonite and calcite polymorphs were revealed as in the original $CaCO_3$. In the NR/NCC commercial composite (Figure 5.26(h)), only calcite peaks appeared.

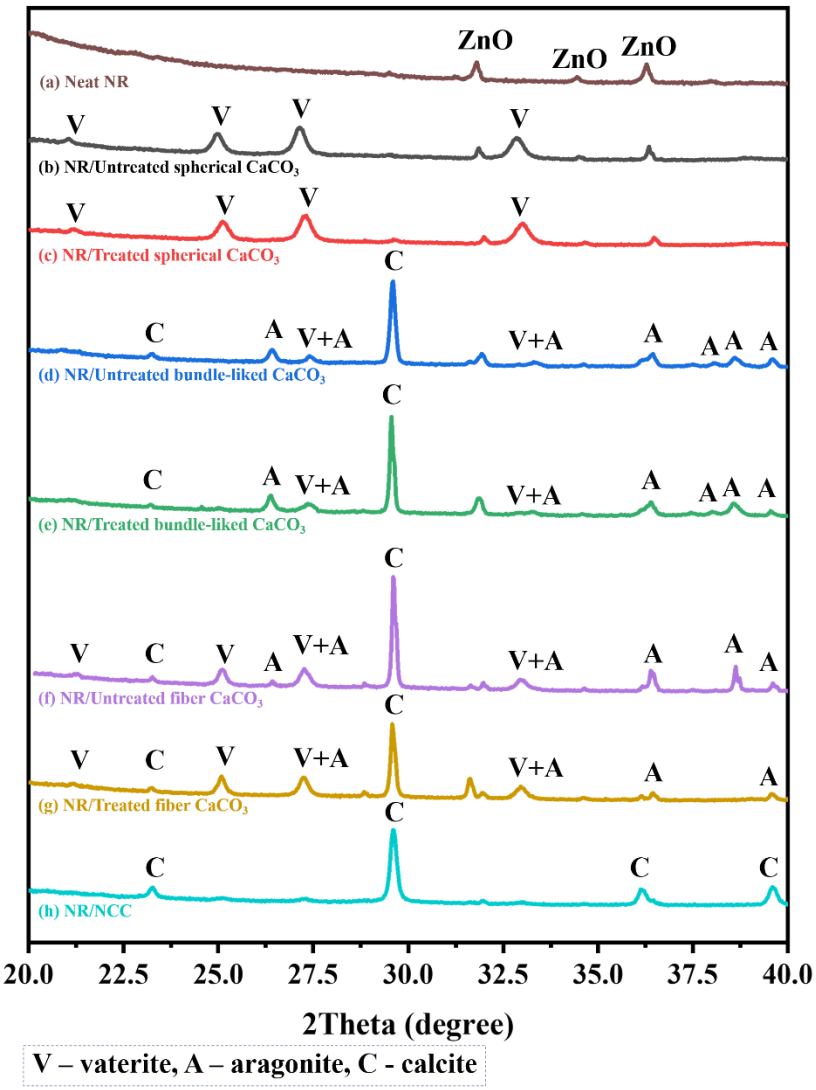


Figure 5.26 The XRD diffractions of neat NR and NR/$CaCO_3$ composites at 20 phr filler loading

To use N330 carbon black (CB) as filler to compare the mechanical properties with NR/$CaCO_3$ composites, the crystalline phase of NR/N330 composite was also investigated. The XRD patterns of N330 powder and NR/N330 were demonstrated in Figure 5.27. The XRD characteristic peak of the amorphous feature of N330 powder was exhibited as a broad peak. [159] The highest intensity of the amorphous phase of N330 was located at 24.5^{o} in 2Θ with crystalline plane (002). [138] The neat NR provided ZnO peaks as aforementioned. The XRD diffractogram of

NR/N330 composite consisted of typical crystalline phases of ZnO and the amorphous feature of N330.

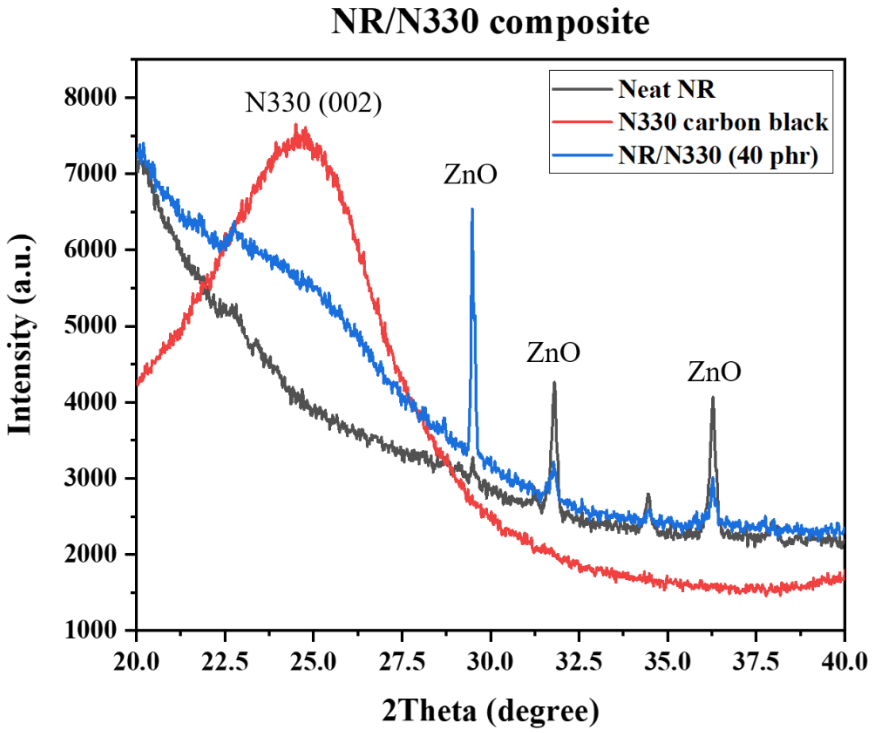


Figure 5.27 The XRD patterns of neat NR, N330 carbon black and NR/N330 composite at 40 phr filler loading

5.3.3.2 ATR-FTIR analysis of NR/$CaCO_3$ composites

The ATR-FTIR spectra of neat NR and NR/$CaCO_3$ composites are presented in Figure 5.28. The FTIR spectrum of neat NR (brown line) showed characteristic signals of C=C of isoprene, CH_2 stretching, CH_3 stretching, and =C-H stretching group of NR structure located at 1642, 2853, 2926, and 2961 cm^{-1}, respectively. The appearance of doubly degenerate in-plane OCO deformation bending at 745 cm^{-1} corresponded to typical vaterite peaks in both NR/untreated and treated spherical $CaCO_3$ composites (Figure 5.28(c)). The typical peaks of aragonite appeared in NR/bundle-liked and NR/fiber $CaCO_3$ composites at 700, 712, and 854 cm^{-1}. The typical peaks of calcite polymorph 874 (Figure 5.28(b)) and 713 cm^{-1} vibration modes (Figure 5.28(c)) were presented obviously in NR/NCC commercial $CaCO_3$ composite.

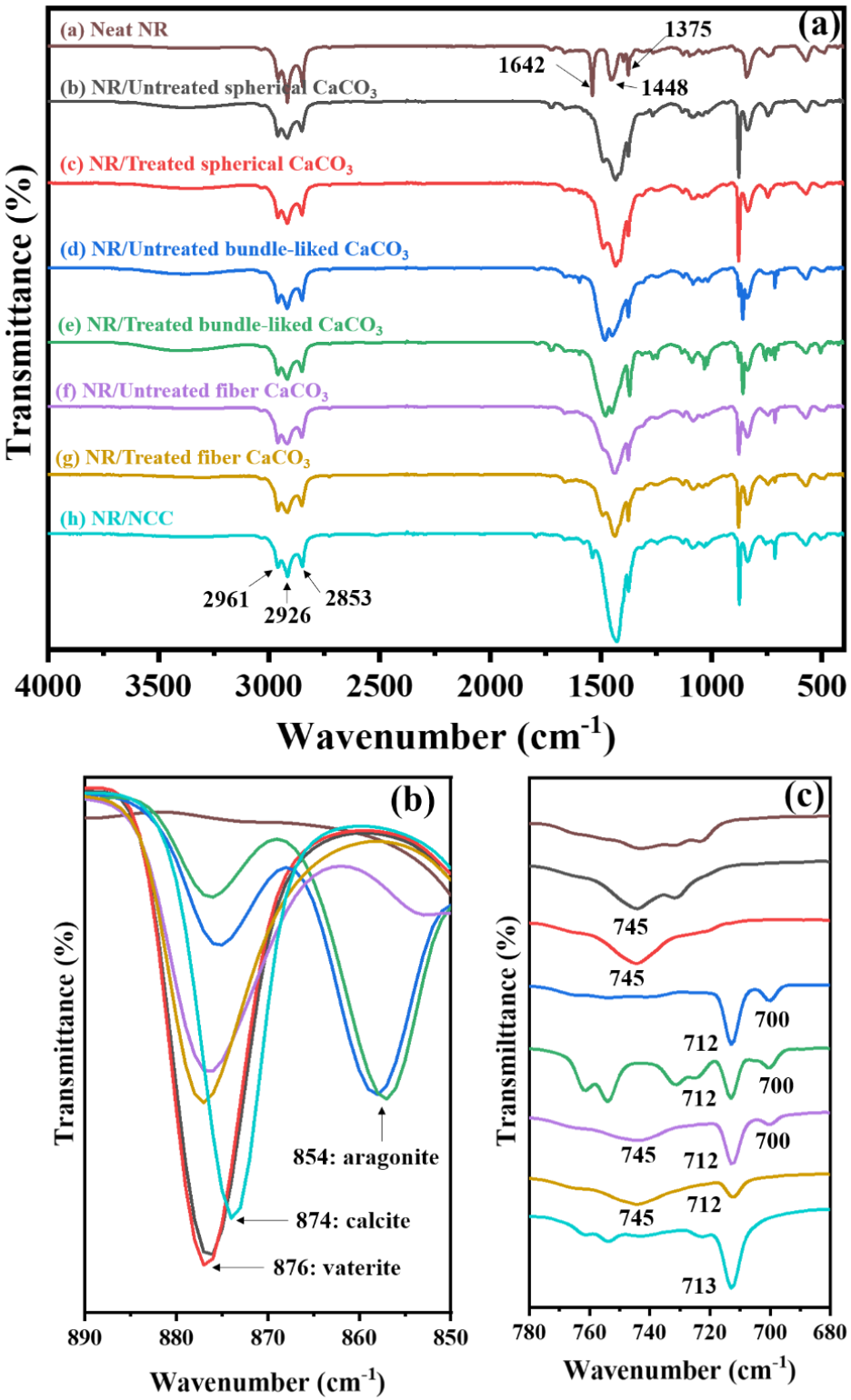


Figure 5.28 ATR-IR spectra of neat NR and NR/$CaCO_3$ composites at filler loading of 40 phr in the range of (a) 500 – 4000 cm^{-1}, (b) 850 – 890 cm^{-1}, and (c) 680 – 780 cm^{-1}

5.3.4 Morphology of NR/$CaCO_3$ composites

The morphology of the tensile-fractured surface of neat NR and NR/$CaCO_3$ composites at 20 phr filler loading was explored and exhibited in Figure 5.29. Figure 5.29(a) presented the smooth surface of the NR matrix without filler (neat NR). The NR/untreated spherical $CaCO_3$ in Figure 5.29(b) and NR/treated spherical $CaCO_3$ in Figure 5.29(c) morphological surfaces demonstrated both smooth surfaces from rubber matrix together with sphere particles of $CaCO_3$ fillers. In the case of NR filled with bundle-liked $CaCO_3$ with untreated in Figure 5.29(d) and treated in Figure 5.29(e), the filler presented in wire shape or rod-liked shape. This was caused by the rubber matrix wetted on the surface of bundle-liked $CaCO_3$ particles. For NR/fiber $CaCO_3$, some fiber $CaCO_3$ particles were broken during the tensile testing, but the fiber particles were still observed in the SEM image (Figure 5.29(f)). In the case of NR/ treated fiber $CaCO_3$, the mixture of spherical, cubical and fiber shapes was observed in Figure 5.29(g). The morphology of NR filled with nano commercial $CaCO_3$ particles was presented in Figure 5.29(h). Meanwhile, the micro-scaled and cubical shape of commercial $CaCO_3$ particles were demonstrated in Figure 5.29(i) for NR/4QC composite, and in Figure 5.29(j) for NR/9QQ composite. The results from SEM images and XRD patterns could support that the polymorph and morphology of $CaCO_3$ can maintain in NR latex and NR composites without transformation.

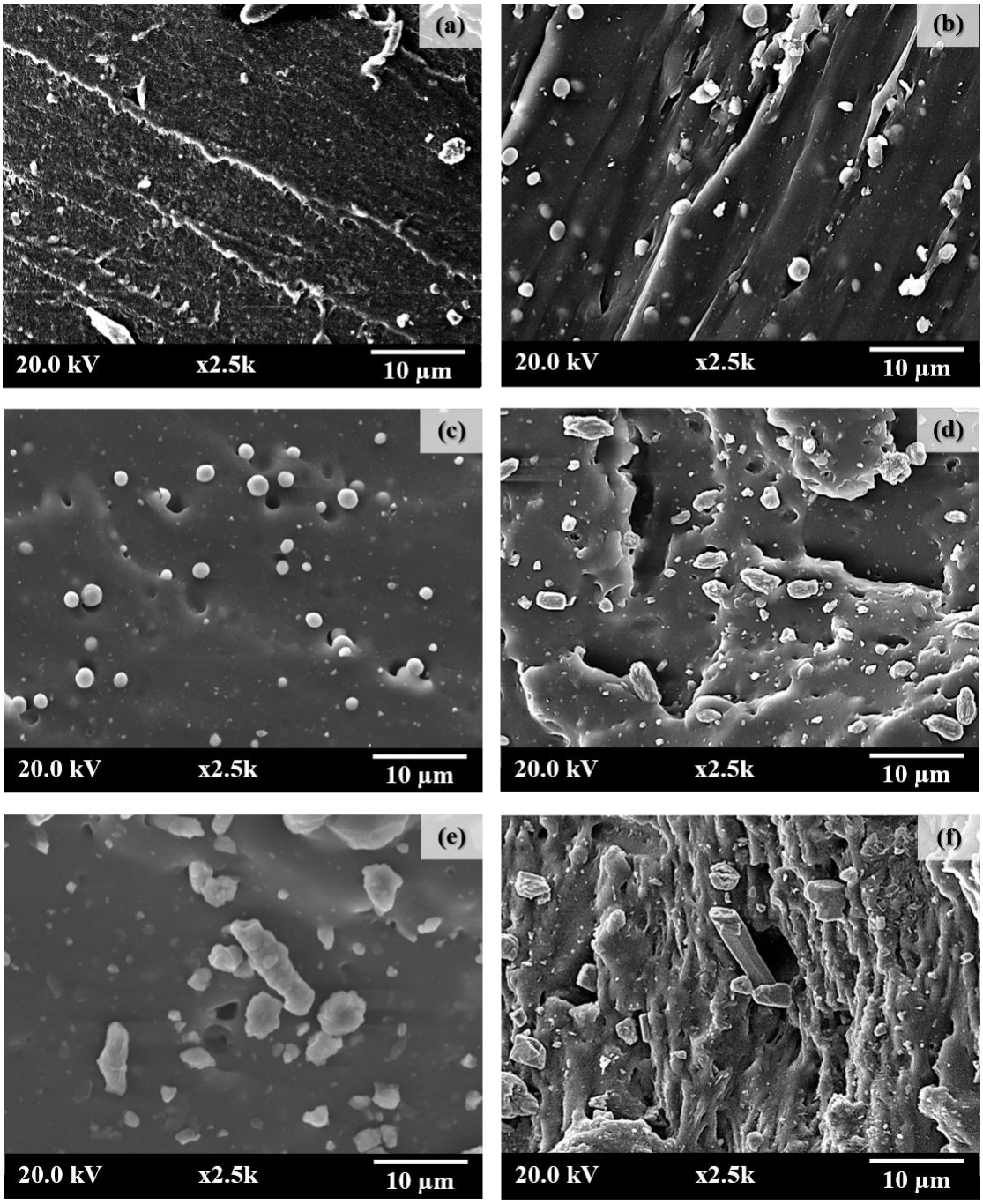


Figure 5.29 SEM images of tensile-fractured surface at 2500x, 10 µm scale bar of (a) Neat NR, (b) NR/Untreated spherical $CaCO_3$, (c) NR/Treated spherical $CaCO_3$, (d) NR/Untreated bundle-liked $CaCO_3$, (e) NR/Treated bundle-liked $CaCO_3$, (f) NR/Untreated fiber $CaCO_3$, (g) NR/Treated fiber $CaCO_3$, (h) NR/NCC $CaCO_3$, (i) NR/4QC $CaCO_3$, and (j) NR/9QQ $CaCO_3$ composites at 20 phr filler loading

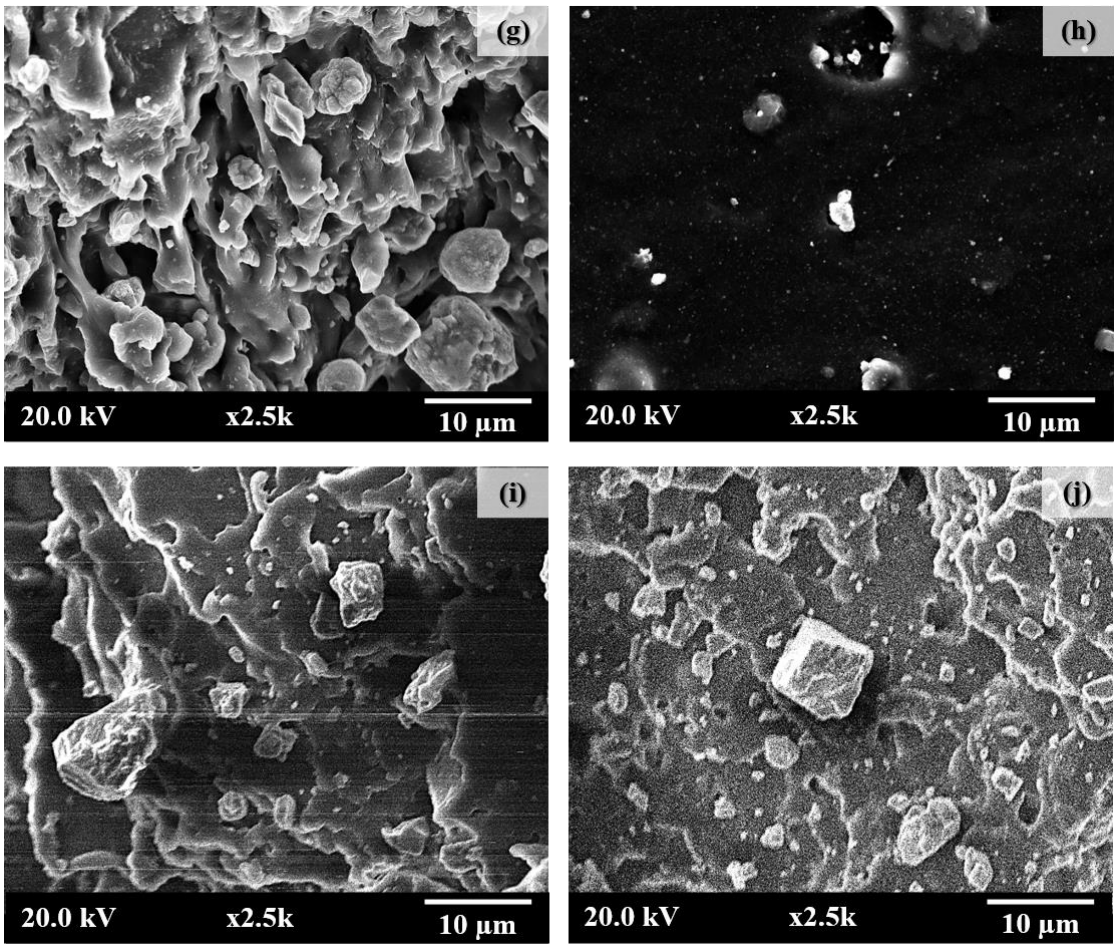


Figure 5.29 (cont.) SEM images of tensile-fractured surface at 2500x, 10 µm scale bar of (a) Neat NR, (b) NR/Untreated spherical $CaCO_3$, (c) NR/Treated spherical $CaCO_3$, (d) NR/Untreated bundle-liked $CaCO_3$, (e) NR/Treated bundle-liked $CaCO_3$, (f) NR/Untreated fiber $CaCO_3$, (g) NR/Treated fiber $CaCO_3$, (h) NR/NCC $CaCO_3$, (i) NR/4QC $CaCO_3$, and (j) NR/9QQ $CaCO_3$ composites at 20 phr filler loading

5.3.5 Element distribution analysis of NR/$CaCO_3$ composites

The X-ray Fluorescence results reported the chemical composition and element distribution. The XRF imaging and components analysis of NR/$CaCO_3$ composites at filler loading of 5, and 20 phr were presented in Figures 5.30 and 5.31, respectively. The elements detected were calcium (Ca), Zinc (Zn), and sulfur (S). In this work, ZnO was used as an activator and S as a curing agent. The XRF imaging of NR/$CaCO_3$ composites at filler loading (20 phr) displayed a brighter in green color of Ca element distribution than at 5 phr of filler loading in all different types of $CaCO_3$. In the meantime, the shades

of Zn and S element distribution were the same. This means that the intensity of the Ca element is increased when $CaCO_3$ loading increases.

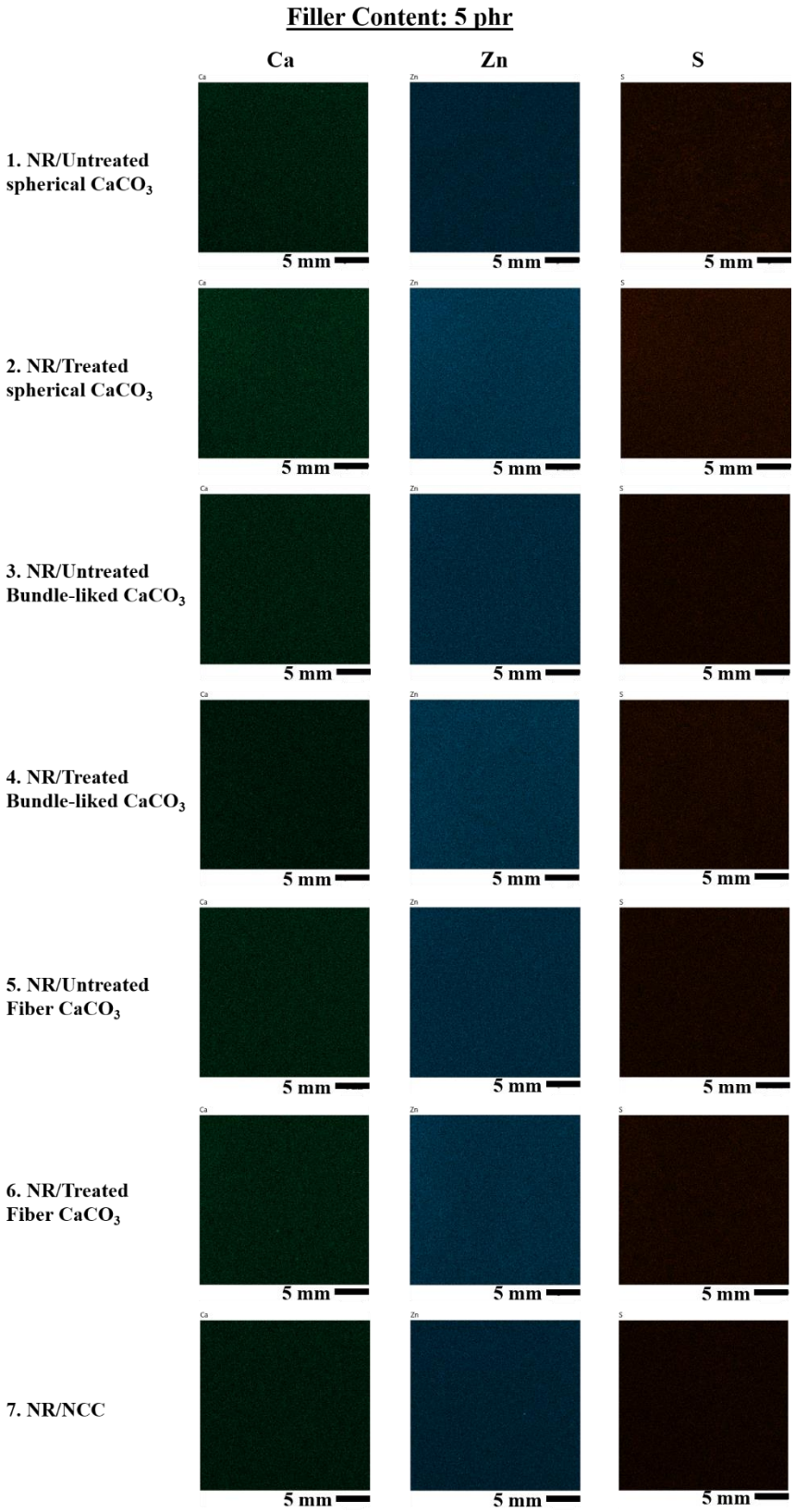


Figure 5.30 XRF imaging and components analysis of detailed element distribution images including Ca, Zn and S of NR/$CaCO_3$ composites at 5 phr filler loading

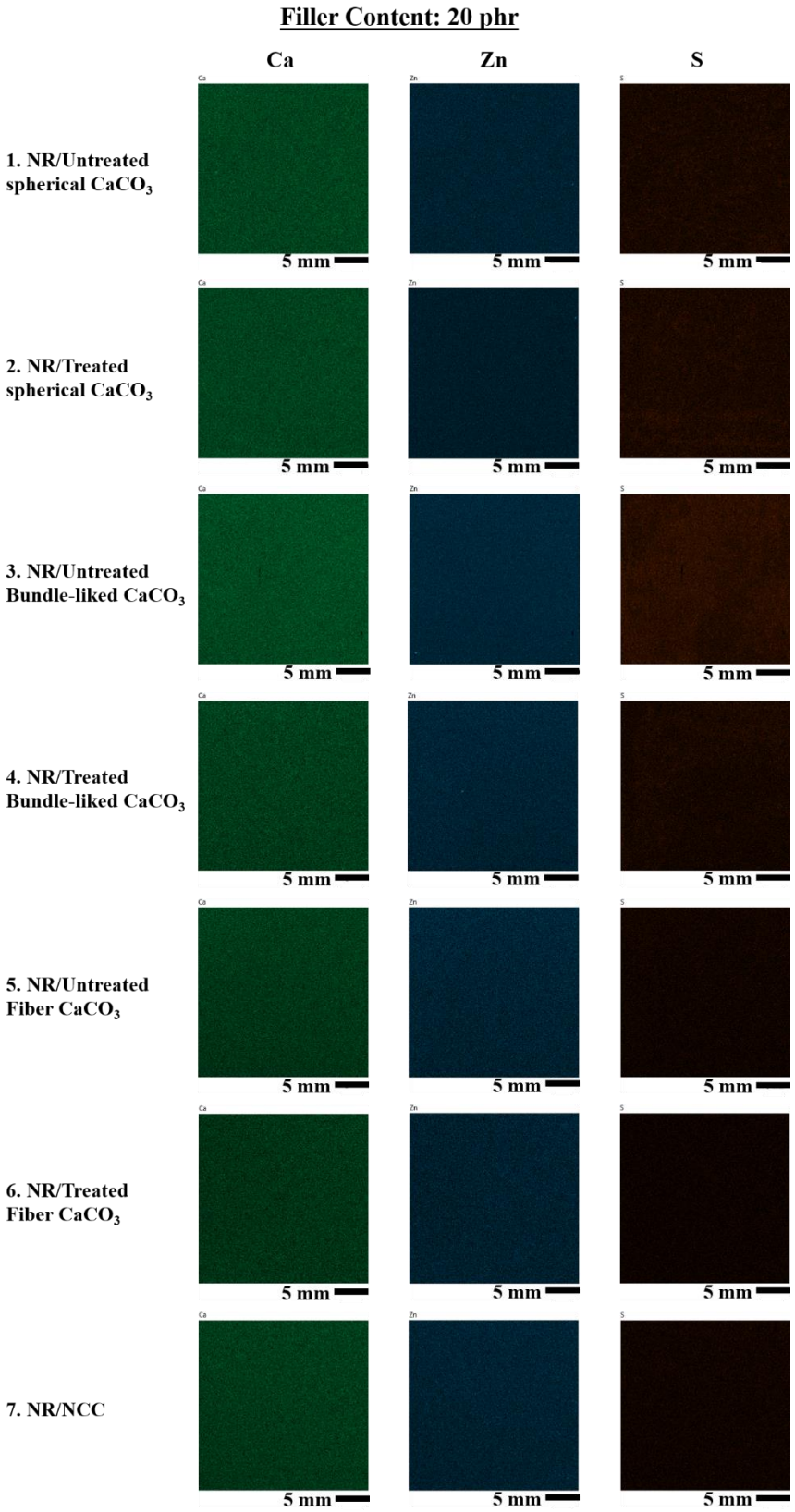


Figure 5.31 XRF imaging and components analysis of detailed element distribution images including Ca, Zn and S of NR/$CaCO_3$ composites at 20 phr filler loading

5.4 Mechanical properties of NR/$CaCO_3$ composites

The mechanical properties including tensile strength, elongation at break, modulus, tear strength, and hardness Shore A of NR/$CaCO_3$ composites at filler loading 5, 10, 20, 40, and 60 phr were investigated in this section. These mechanical values are listed in Table 5.10.

5.4.1 Tensile strength

The tensile strength of NR/$CaCO_3$ composites with all filler loading variations was conducted and presented in Figure 5.32. The stress and strain curves of NR/$CaCO_3$ demonstrated s-curves as presented in Figure 5.33 for all variation of filler loadings. As a result, the neat NR revealed a tensile strength of 22.68 ± 2.22 MPa. After adding $CaCO_3$ powders in NR, the tensile strength of rubber composites increased. At 5 phr of filler loading, the tensile strength of NR/untreated spherical $CaCO_3$ was 21.87 ± 3.98 MPa. When the treated spherical $CaCO_3$ was used to incorporate in the NR, the tensile strength was increased to 23.03 ± 1.14 MPa. A similar achievement was obtained in the case of NR/untreated bundle-liked $CaCO_3$ (24.91 ± 3.68 MPa) and NR/treated bundle-liked $CaCO_3$ (29.88 ± 0.34 MPa) that the tensile strength was improved when the surface of $CaCO_3$ was treated with olive soap. In the case of fiber $CaCO_3$, the tensile strength of NR/untreated fiber $CaCO_3$ was 30.93 ± 1.15 MPa, which is higher than that of NR/treated fiber $CaCO_3$ (28.66 ± 1.83 MPa). The tensile strength of NR/NCC was 22.54 ± 3.58 MPa, but that of NR/9QQ was 24.82 ± 0.14 MPa, and NR/4QC was 26.27 ± 0.06 MPa. The particle size, shape and aspect ratio play an important role in the strengthening of rubber composite, untreated fiber $CaCO_3$ filled NR vulcanizate provided the highest tensile strength due to its nanoparticle and the highest aspect ratio (156.9) over other types of $CaCO_3$ powders. From the definition, the nanoparticle is a particle which has at least one nanoscale dimension from 1 to 100 nm. [160] As a consequence, the particles with a high aspect ratio such as fibrous particles, result in greater reinforcement of the rubber compound. [161] To improve the compatibility and filler dispersion in the matrix between NR and $CaCO_3$ particles, NR composites filled with treated or superhydrophobic $CaCO_3$ had a tensile strength higher than NR/untreated $CaCO_3$ composites for all different shapes except the fiber $CaCO_3$ particles. The good

dispersion of filler particles in the polymer matrix can improve the mechanical properties, especially strength significantly. The untreated or hydrophilic $CaCO_3$ particles are easily aggregated in a polymer matrix resulting in induced poor mechanical properties. In the case of NR/treated fiber $CaCO_3$ exhibited a tensile value lower than NR/untreated fiber $CaCO_3$, it was caused by the treated fiber $CaCO_3$ being the mixture of sphere, cubic and needle-liked particles resulting in poor filler dispersion.

For 10 phr of $CaCO_3$ filler loading, the tensile strength value of NR/$CaCO_3$ composites demonstrated the same trend as at filler loading of 5 phr. The tensile strength of NR/untreated spherical $CaCO_3$ was raised to 22.97 ± 3.87 MPa, NR/treated spherical $CaCO_3$ was 23.74 ± 0.87 MPa, NR/untreated bundle-liked $CaCO_3$ was 24.84 ± 5.03 MPa, NR/treated bundle-liked $CaCO_3$ was 26.95 ± 3.04 MPa, NR/untreated fiber $CaCO_3$ was 31.66 ± 1.80 MPa, NR/treated fiber $CaCO_3$ was 28.30 ± 0.74 MPa, NR/NCC was 23.78 ± 0.54 MPa, NR/9QQ was 23.66 ± 0.46 MPa, and NR/4QC was 26.79 ± 0.91 MPa.

The tensile strength of NR/untreated spherical and NR/treated spherical $CaCO_3$ increased until the maximum loading of filler of 20 phr which were 23.94 ± 0.97, and 25.28 ± 0.80 MPa and decreased at high filler loading of 40 and 60 phr. The agglomeration of filler at high loading showed a significant effect on tensile strength. The presence of agglomeration or large particles of filler in rubber matrix are important concern in rubber. The agglomeration not only reduces the contact between filler and rubber matrix but also affects as failure initiations site leading to the premature failure of rubber materials. The maximum loading of bundle-liked $CaCO_3$ fillers for both different surface treatments was in the range 20 – 40 phr which provided the highest tensile strength values. The maximum of untreated fiber $CaCO_3$ in NR vulcanizates is 10 phr and the fiber particles were agglomerated at 20 – 60 phr of filler loading resulting in a decrease of tensile strength. Meanwhile, the tensile strength of NR/treated fiber $CaCO_3$ fluctuated due to the inhomogeneous of its particle size and shape.

Table 5.10 Results of tensile properties of NR/$CaCO_3$ composites at different types and loading of $CaCO_3$

Filler loading (phr)	Tensile strength (MPa)	Elongation at break (%)	M100 (MPa)	M300 (MPa)	Tear strength (N/mm)	Hardness (Shore A)
0	22.68±2.22	821.63±10.25	0.90±0.03	2.08±0.07	54.76±1.35	40.5±0.3
NR/Untreated spherical $CaCO_3$ (Filler aspect ratio = 1.04)						
5	21.87±3.98	802.06±29.90	0.90±0.07	2.17±0.20	57.70±4.58	41.7±0.4
10	22.97±3.87	800.45±33.19	087±0.02	2.19±0.03	59.47±5.12	43.1±0.4
20	23.94±0.97	765.83±1.30	0.98±0.06	2.70±0.15	60.62±1.63	44.4±0.5
40	21.41±0.85	669.30±0.20	1.21±0.01	3.75±0.10	63.50±3.83	46.7±0.4
60	19.66±0.51	594.06±3.24	1.50±0.02	5.16±0.08	72.83±2.10	50.9±0.2
NR/Treated spherical $CaCO_3$ (Filler aspect ratio = 0.98)						
5	23.03±1.14	785.30±14.72	1.02±0.06	2.46±0.19	55.53±4.27	42.8±0.3
10	23.74±0.87	795.96±27.19	0.88±0.04	2.14±0.12	53.07±0.65	42.9±0.2
20	25.28±0.80	735.46±1.36	0.88±0.03	2.35±0.08	60.00±1.64	46.0±0.4
40	23.14±1.11	733.60±14.20	1.03±0.01	3.03±0.05	72.30±3.89	48.5±0.4
60	23.18±2.15	713.36±31.56	1.18±0.06	3.55±0.14	75.40±9.29	50.2±0.5
NR/Untreated bundle-liked $CaCO_3$ (Filler aspect ratio = 9.06)						
5	24.91±3.68	804.66±29.97	0.99±0.02	2.36±0.06	62.35± 4.71	42.9±0.5
10	24.84±5.03	794.43±63.15	0.85±0.03	2.12±0.14	67.16±11.66	44.1±0.2
20	29.98±0.44	852.26±15.80	0.89±0.02	2.18±0.29	60.16±3.06	45.2±0.5
40	30.59±3.50	777.46±22.41	1.43±0.02	3.51±0.18	59.50±2.33	49.6±0.4
60	29.31±1.69	750.23±6.60	1.52±0.07	3.89±0.15	62.00±2.33	50.4±0.5
NR/Treated bundle-liked $CaCO_3$ (Filler aspect ratio = 8.42)						
5	29.88±0.34	857.43±4.50	0.98±0.10	2.35±0.23	45.75±4.45	43.5±0.4
10	26.95±3.04	828.56±13.80	0.85±0.02	2.10±0.01	54.93±1.58	45.0±0.6
20	31.51±1.02	868.30±4.45	0.94±0.02	2.29±0.05	58.37±0.37	45.6±0.4

Table 5.10 (cont.) Results of tensile properties of NR/$CaCO_3$ composites at different types and loading of $CaCO_3$

Filler loading (phr)	Tensile strength (MPa)	Elongation at break (%)	M100 (MPa)	M300 (MPa)	Tear strength (N/mm)	Hardness (Shore A)
40	29.73±0.51	781.83±9.30	1.28±0.03	3.23±0.10	63.00±0.52	48.3±0.6
60	25.78±1.49	732.03±23.55	1.41±0.01	3.69±0.05	83.10±0.34	51.3±0.4
NR/Untreated fiber $CaCO_3$ (Filler aspect ratio = 156.9)						
5	30.93±1.15	876.17±10.03	0.90±0.04	2.14±0.10	54.43±2.49	42.3±0.5
10	31.66±1.80	852.10±2.71	0.99±0.05	2.36±0.14	56.47±2.05	43.4±0.4
20	29.82±0.32	834.27±2.20	1.06±0.01	2.55±0.02	65.93±2.86	44.4±0.4
40	29.43±1.04	764.43±8.30	1.31±0.07	3.41±0.18	57.03±2.85	47.5±0.5
60	24.50±0.79	708.70±17.33	1.49±0.02	3.94±0.05	60.57±1.85	51.0±0.3
NR/Treated fiber $CaCO_3$ (Filler aspect ratio = 35.9)						
5	28.66±1.83	850.86±13.47	0.94±0.07	2.31±0.17	54.27±4.01	41.4±0.4
10	28.30±0.74	853.76±3.87	0.91±0.04	2.18±0.09	59.40±1.75	43.1±0.3
20	30.02±2.59	823.63±10.51	1.11±0.08	2.68±0.17	61.87±7.31	44.5±0.4
40	24.15±3.98	735.20±37.64	1.30±0.04	3.27±0.11	59.57±2.61	47.0±0.4
60	29.88±1.49	734.17±7.17	1.74±0.09	4.45±0.16	61.97±0.90	52.3±0.4
NR/NCC *(commercial)* (Filler aspect ratio = 1.38)						
5	22.54±3.58	801.06±26.78	0.87±0.01	2.12±0.01	61.20±2.25	43.9±0.2
10	23.78±0.54	803.86±24.54	0.90±0.05	2.27±0.12	62.67±1.64	44.9±0.2
20	30.20±1.01	824.90±12.41	0.94±0.04	2.53±0.08	61.10±1.45	46.5±0.2
40	32.40±1.47	787.52±9.33	1.19±0.06	3.52±0.20	105.20±1.21	50.0±0.0
60	32.20±1.03	743.86±11.77	1.44±0.01	4.48±0.04	108.77±1.51	53.7±0.3
NR/9QQ *(commercial)* (Filler aspect ratio = 1.29)						
5	24.82±0.14	711.88±13.08	0.83±0.01	1.80±0.02	59.77±1.59	42.8±0.3
10	23.66±0.46	664.94±10.56	0.94±0.01	2.14±0.03	64.90±3.43	45.3±0.4
20	24.81±0.73	690.33±5.32	0.98±0.01	2.21±0.02	70.95±3.21	46.9±0.2
40	22.57±0.47	656.85±9.10	1.13±0.02	2.45±0.05	67.43±1.93	48.9±0.4
60	20.60±0.84	640.64±13.41	1.33±0.01	2.87±0.04	68.57±0.63	53.2±0.4

Table 5.10 (cont.) Results of tensile properties of NR/$CaCO_3$ composites at different types and loading of $CaCO_3$

Filler loading (phr)	Tensile strength (MPa)	Elongation at break (%)	M100 (MPa)	M300 (MPa)	Tear strength (N/mm)	Hardness (Shore A)
NR/4QC *(commercial)* (Filler aspect ratio = 1.58)						
5	26.27±0.06	692.35±10.03	0.89±0.02	2.08±0.07	74.60±5.20	44.5±0.4
10	26.79±0.91	672.83±10.21	0.96±0.02	2.30±0.08	76.86±2.66	45.8±0.3
20	26.75±0.20	671.07±4.61	1.05±0.01	2.48±0.03	75.60±1.21	47.4±0.4
40	18.26±0.77	733.47±5.12	0.78±0.01	1.64±0.02	62.73±2.36	49.7±0.6
60	21.08±1.17	600.48±15.89	1.46±0.07	3.59±0.22	81.20±1.67	53.0±0.7

In the case of commercial $CaCO_3$: NCC, 9QQ and 4QC, the tensile strength of NR/NCC increased when NCC filler loading increased. Meanwhile, the maximum loading of 9QQ and 4QC filler was 20 phr similar to as-prepared $CaCO_3$ filled NR composites. In the same manner, the tensile strength of superhydrophobic 4QC filled hydrophobic NR was higher than NR/hydrophilic 9QQ composites. Many studies have summarized that the loading percentage of micro-scale $CaCO_3$ was in the range of 10 – 50 % affecting mechanical property improvement weaker than nanoscale $CaCO_3$ filled in polymer composites whose loading percentage is about 5 – 10 %. [32]

To put it simply, the linear plots of the tensile strength value of NR/$CaCO_3$ composites at all filler variations were demonstrated in Figure 5.36 to describe the effect of particle size on the tensile strength of rubber composites. These results could be summed up that the particle size or aspect ratio and shape of the filler play the primary factor on the strength of the rubber composite while the surface treatment of the filler is a secondary factor. Corresponding to the reinforcing mechanism of the composite, the nanoparticle filler has a high surface area that is in contact with the rubber phase leading to an increase in reinforcement. [32] Moreover, reducing the particle size of the filler also results in greater polymer-filler interaction. Plus, the particle distribution also effects on reinforcement. Generally, the $CaCO_3$ powders are used as an additive to reduce the cost of products, our finding is that the as-prepared $CaCO_3$ powders play the role of reinforcing fillers, thus the results could lead to

broadening the applications of $CaCO_3$ to improve the mechanical property of different material industry.

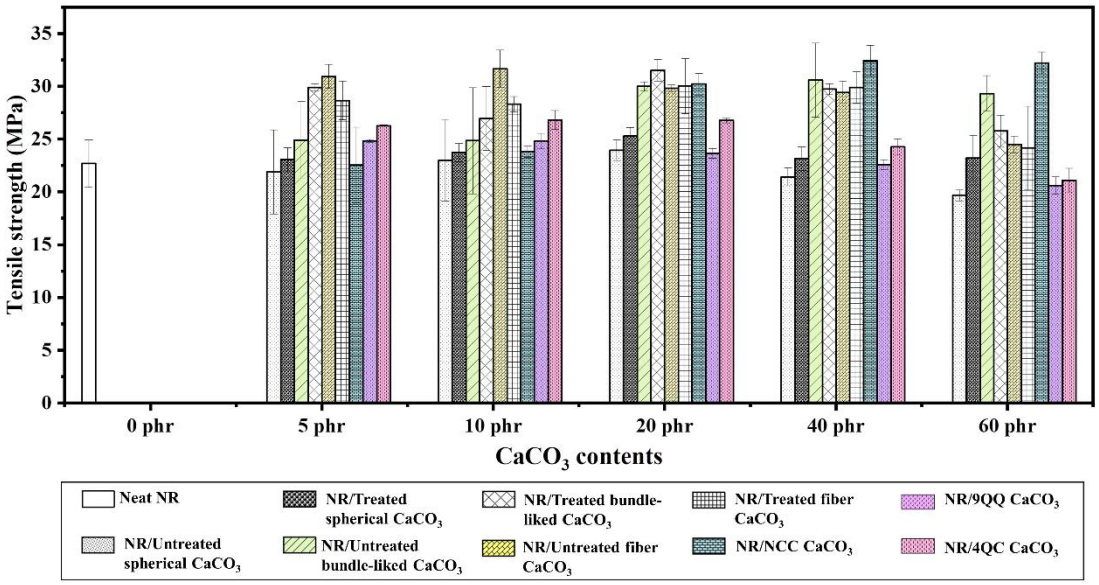


Figure 5.32 Tensile strength of NR/$CaCO_3$ composites at different types and loading

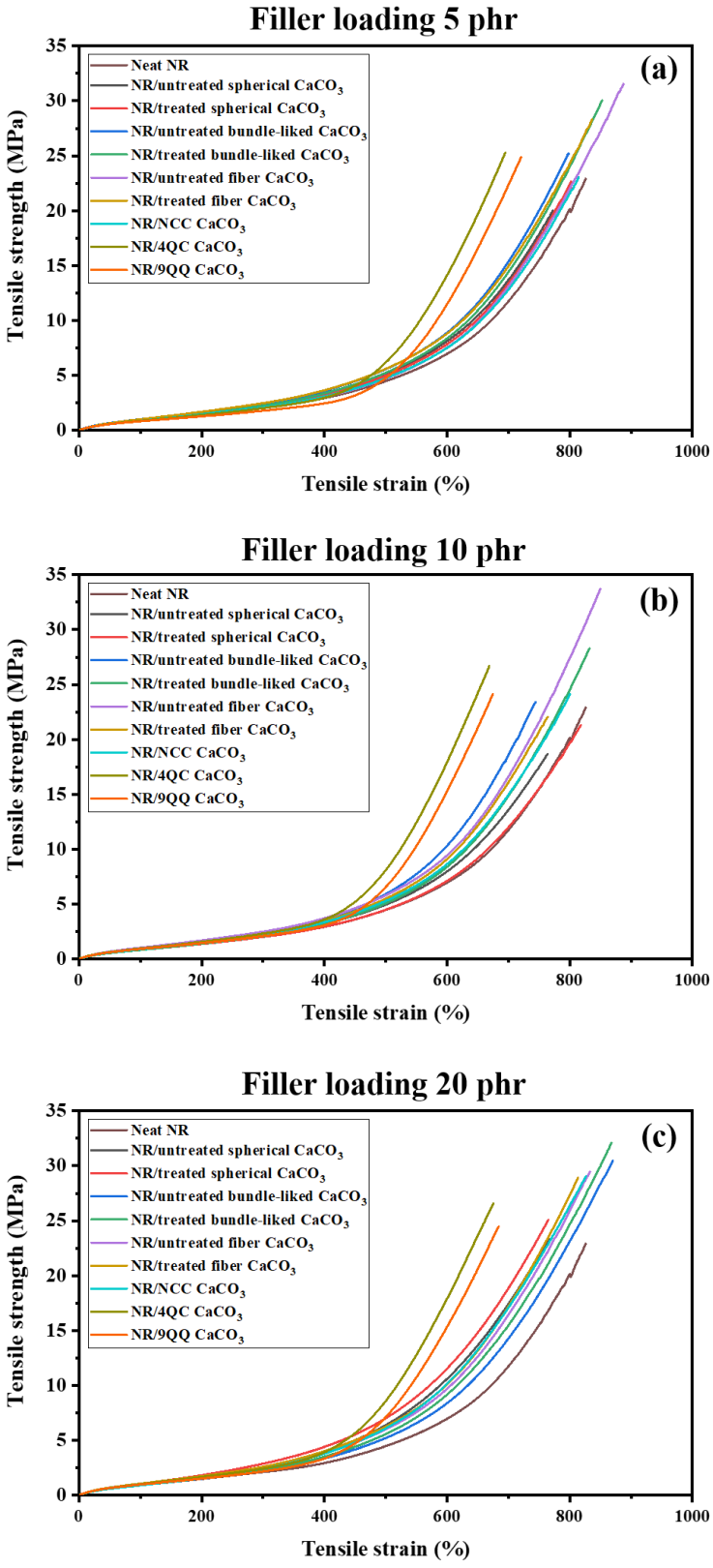


Figure 5.33 Plots of tensile strain and tensile strength of NR/$CaCO_3$ composites at different types and filler loading of (a) 5, (b) 10, (c) 20, (d) 40, and (e) 60 phr

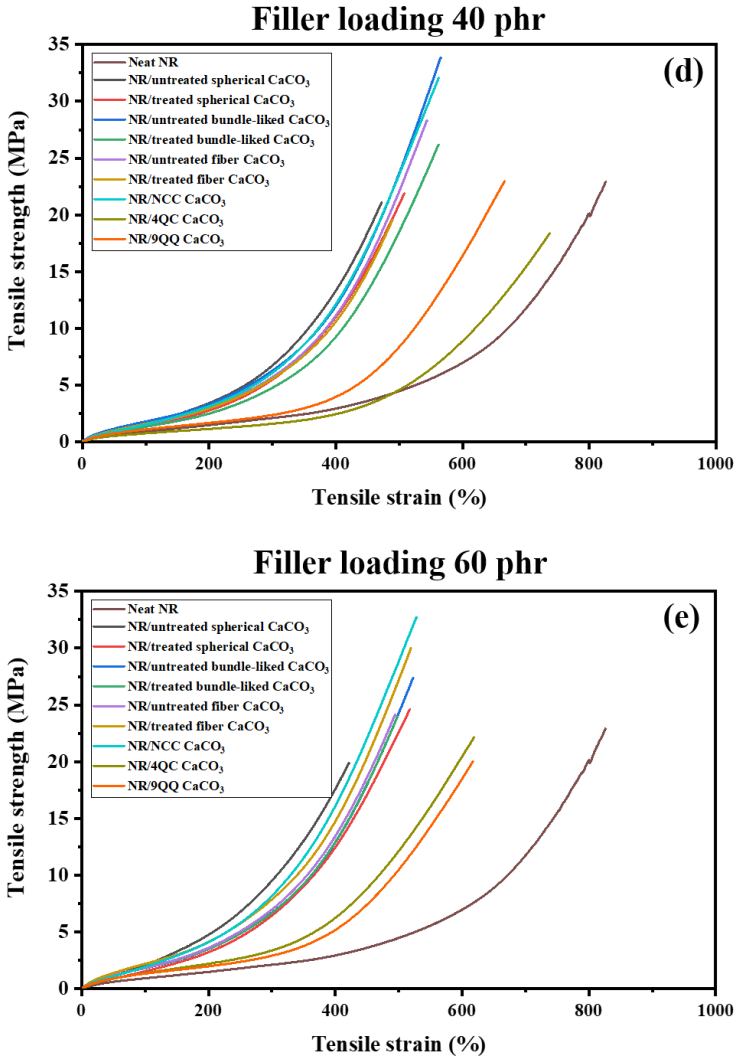


Figure 5.33 (cont.) Plots of tensile strain and tensile strength of NR/$CaCO_3$ composites at different types and filler loading of (a) 5, (b) 10, (c) 20, (d) 40, and (e) 60 phr

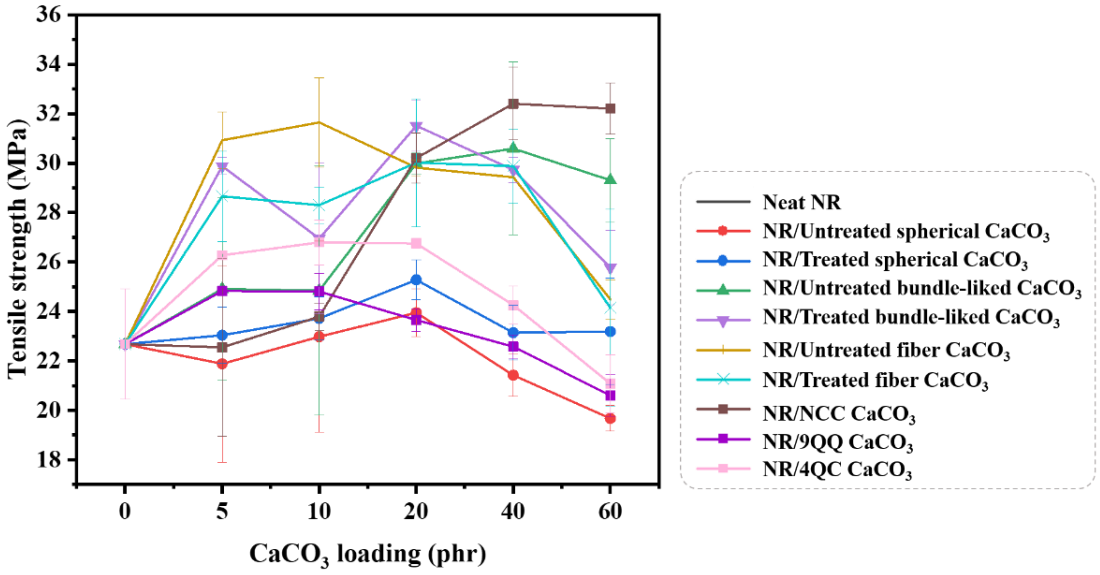


Figure 5.34 Plots of tensile strength values of NR/$CaCO_3$ composites at different types and loading of $CaCO_3$

The surface treatment or surface activity of filler provides the chemical contribution while the particle size is considered as a physical contribution. The ability of filler which could react or chemically bond with polymer matrix results in increasing the strength of composite significantly. According to the nature of $CaCO_3$ as a hydrophilic filler and NR as a hydrophobic material, the surface activity of $CaCO_3$ was transformed to superhydrophobic inducing the mechanical properties' improvement of the rubber composites. The surface activity of superhydrophobic $CaCO_3$ is reflected in the increased tensile strength of the rubber composites. The plots between tensile strength values and different shapes of $CaCO_3$ particles were presented in Figure 5.35. The results in Figure 5.35(a) showed that the spherical $CaCO_3$, the superhydrophobic (treated) presented a higher tensile strength value than the hydrophilic (untreated) one. Likewise, the tensile strength of NR/treated bundle-liked $CaCO_3$ composites was higher than NR/untreated bundle-liked $CaCO_3$ composites (Figure 5.35(b)). However, the treated fiber $CaCO_3$-filled NR exhibited a lower tensile strength than the untreated one due to its mixture of large particles as aforementioned (Figure 5.35(c)). Furthermore, NR/4QC provided the higher tensile strength than NR/9QQ composites caused by the hydrophobicity of 4QC (Figure 5.35(d)).

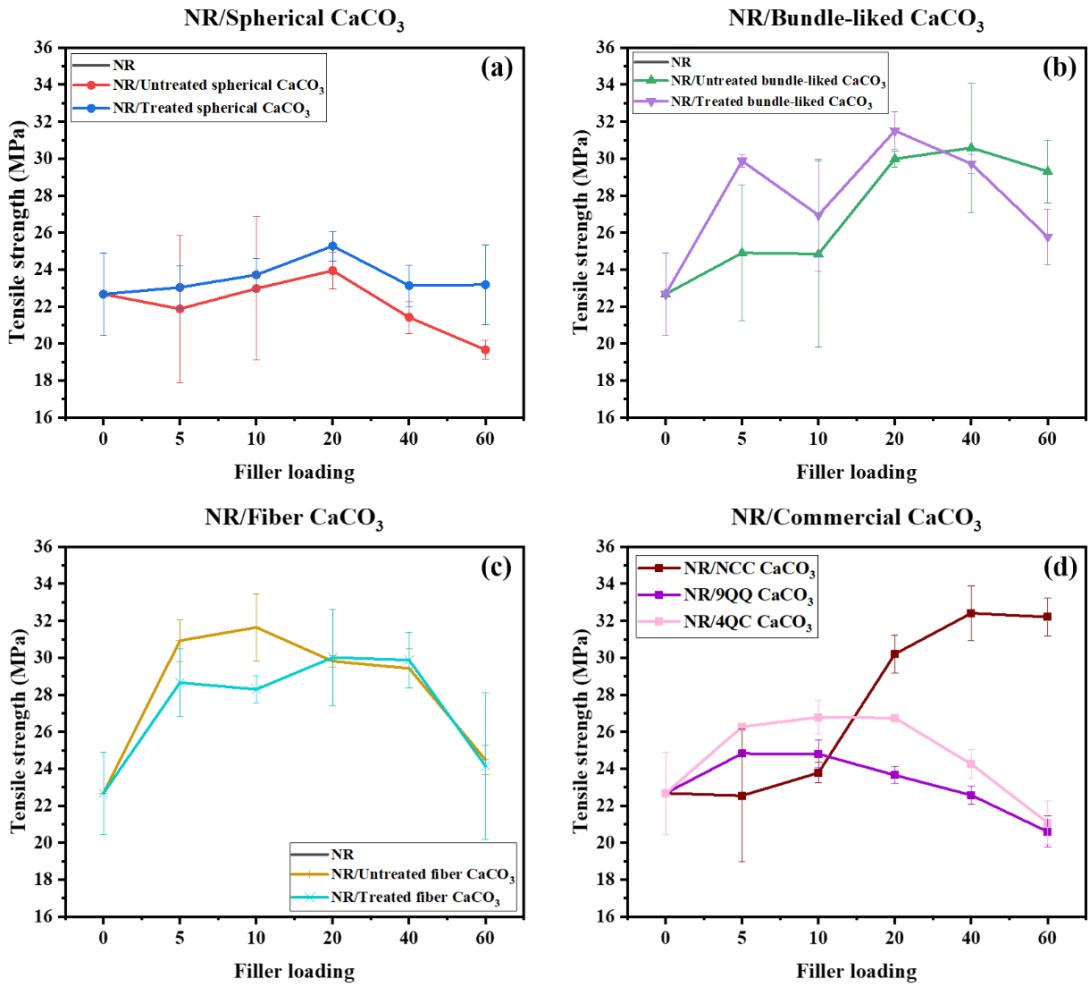


Figure 5.35 Plots of tensile strength values of NR/$CaCO_3$ composites comparing the different shapes of filler and surface treatment: (a) NR/spherical $CaCO_3$, (b) NR/bundle-liked $CaCO_3$, (c) NR/fiber $CaCO_3$, and (e) NR/commercial (rhombohedral) $CaCO_3$ composites

5.4.2 Elongation at break

Figure 5.36 shows the results of elongation at break of the NR/filler composites. It was found the decrement of elongation ability of NR/$CaCO_3$ composites at high filler loading (40 – 60 phr). The elongation at break value of neat NR is 821.63 ± 10.25 %. When the spherical $CaCO_3$ particles were loaded in NR, the elongation at break decreased down to 594.06 ± 3.24 % of NR/untreated sphere and 713.36 ± 31.56 % of NR/treated sphere at 60 phr. These results could indicate that the addition of rigid inorganic particles in the rubber matrix resulted in a reduction of the ductility of rubber

composites. In the case of NR/untreated bundle-liked, NR/treated bundle-liked and NR/untreated fiber $CaCO_3$ composites, the elongation at break increased at maximum loading of 20 phr. It may be caused by its rod-liked, needle-liked, or fibrous particles. The elongation at break decreased at high filler loading due to the agglomeration effect. The highest elongation at break of NR/NCC is also at using 20 phr filler loading (824.90 ± 12.41%) and slightly dropped after 40 – 60 phr loading. Meanwhile, the elongation at break of NR/9QQ and NR/4QC composites was dropped at the filler loading beyond 5 phr. Their large size of micro-scale commercial $CaCO_3$ particles effect on inducing the resistance to stretch when the strain was applied.

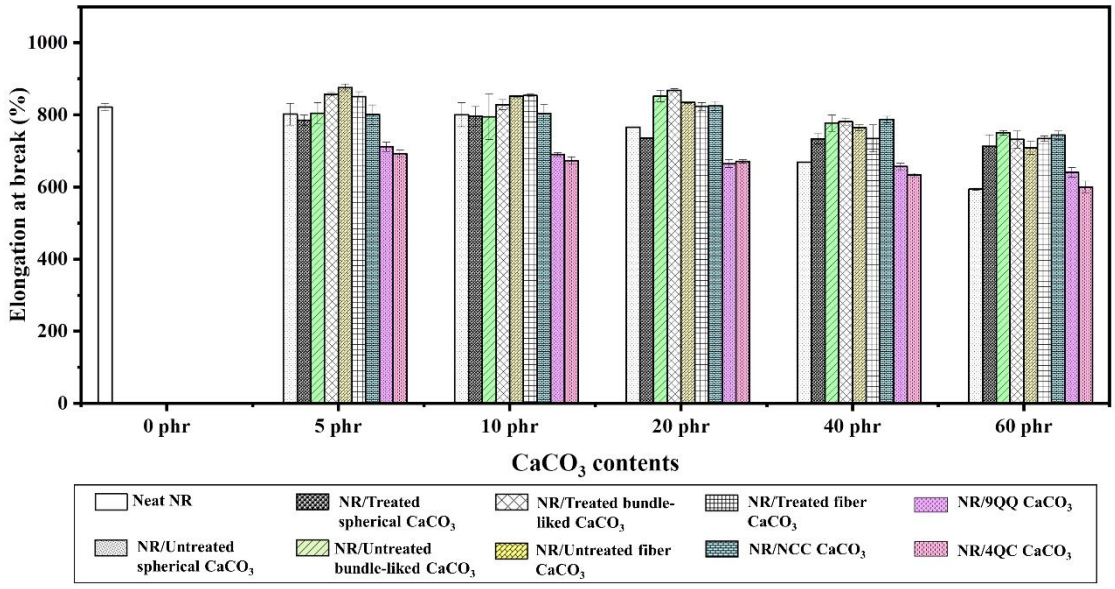


Figure 5.36 Elongation at break of NR/$CaCO_3$ composites at different types and loading of $CaCO_3$

5.4.3 Modulus

The 100% (M100) and 300% Modulus (M300) of NR/$CaCO_3$ composites were presented in Figures 5.37 and 5.38, respectively. The M100 and M300 of neat NR is 0.90 ± 0.03, 2.08 ± 0.07 MPa. As a result, the presence of $CaCO_3$ filler for all loading variations can promote the modulus values. This result could indicate that the rigid $CaCO_3$ crystals resulted in the increase stiffness of rubber composites.

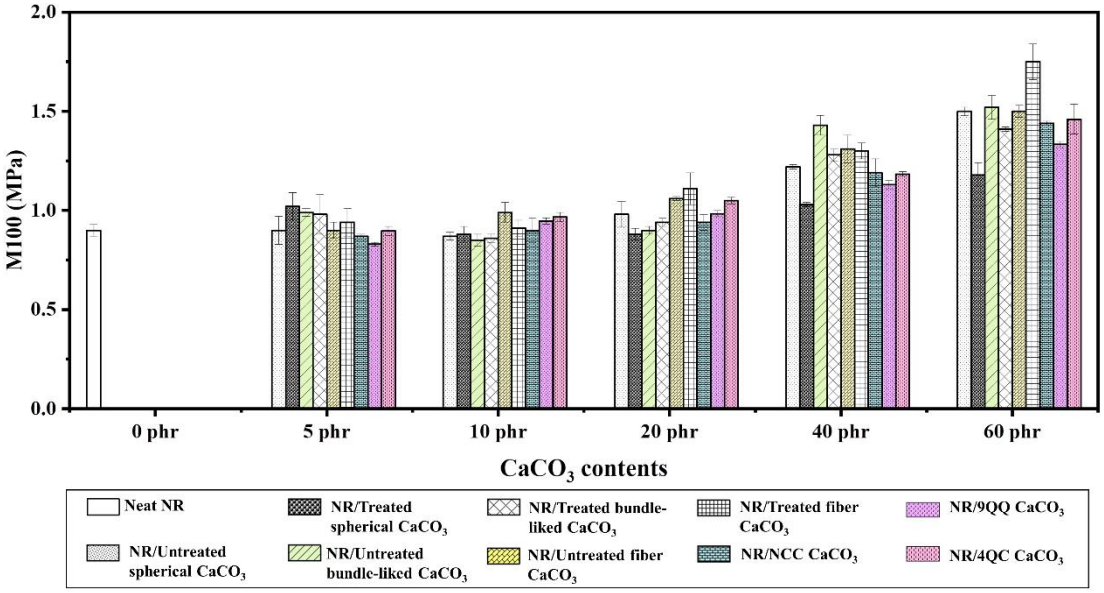


Figure 5.37 100% Modulus (M100) of NR/$CaCO_3$ composites at different types and loading of $CaCO_3$

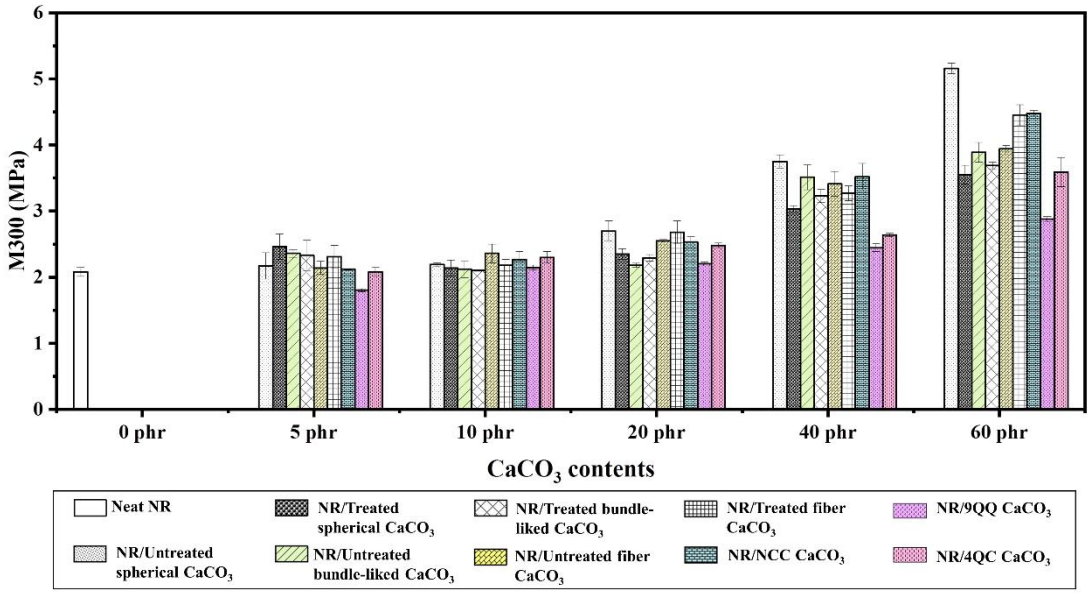


Figure 5.38 300% Modulus (M300) of NR/$CaCO_3$ composites at different types and loading of $CaCO_3$

5.4.4 Tear strength

The tear strength in the rubber/$CaCO_3$ sheet is related to the propagation of a crack cut in the test sample. The tear strength of NR/$CaCO_3$ composites at 0, 5, 10, 20, 40, and 60 phr filler loading was demonstrated in Figure 5.39. The tear strength of neat NR is 54.76 ± 1.35 N/mm. There were increments of tear strength when the $CaCO_3$ particles were loading. Improvement in tear properties was observed even though the agglomerations occurred at high filler loading. Our results are in good agreement with other work that the $CaCO_3$ particles can improve the tear resistance of the materials. [162] It was reported that ultrafine grounded $CaCO_3$ could improve tear strength of NR film effectively. Under applied force, the $CaCO_3$ mineral can induce a dissipation of energy which could increase the tear strength.

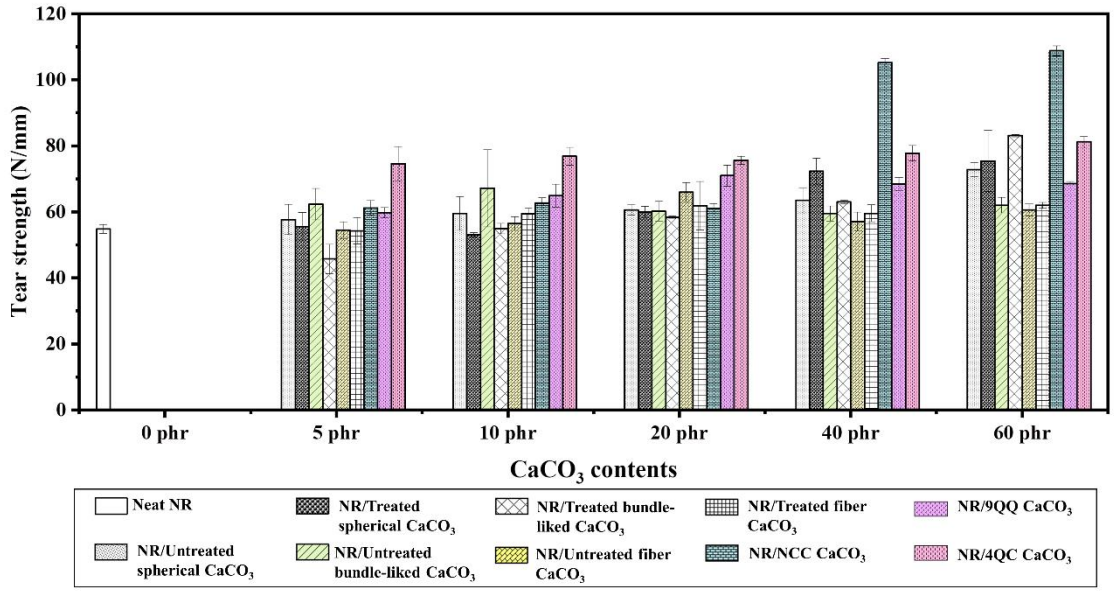


Figure 5.39 Tear strength of NR/$CaCO_3$ composites at different types and loading of $CaCO_3$

5.4.5 Hardness Shore A

Figure 5.40 revealed the hardness Shore A of NR/$CaCO_3$ composites. The hardness Shore A is used to measure the hardness of elastomers to indicate their resistance to indentation. The higher numbers on the scale mean greater hardness, while lower numbers indicate softer materials. The hardness Shore A of neat NR is 40.5 ± 0.

When $CaCO_3$ filler contents in the rubber matrix increased, the hardness of NR composites increased. At 60 phr of $CaCO_3$ powder loading, the hardness Shore A was significantly raised in the range of 50 – 54.

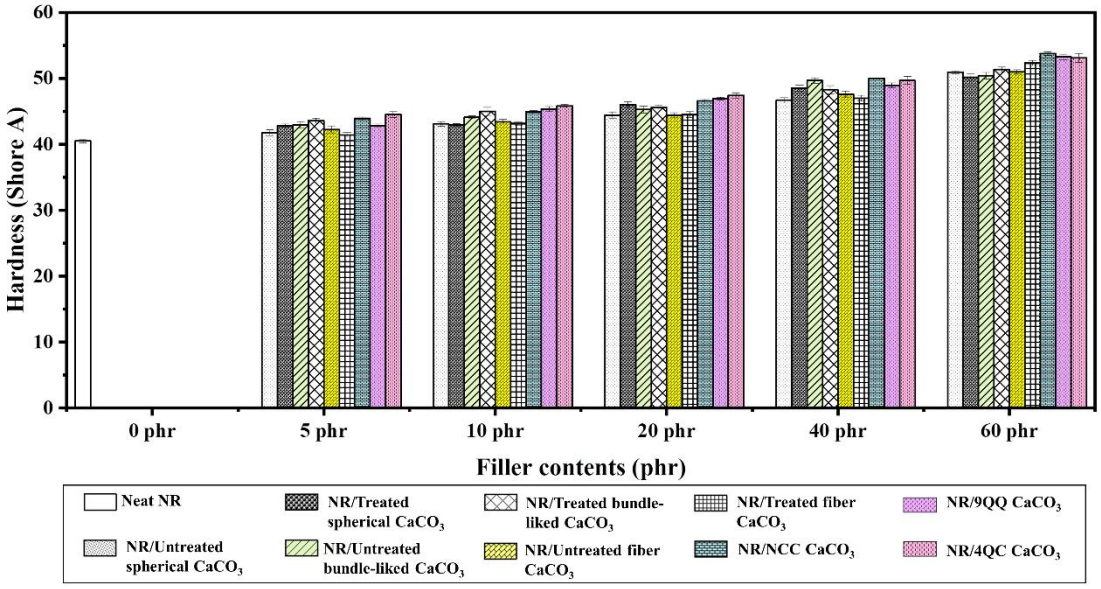


Figure 5.40 Hardness (Shore A) of NR/$CaCO_3$ composites at different types and loading of $CaCO_3$

5.5 Thermal properties of NR/$CaCO_3$ composites

Thermal stability and glass transition temperature of NR and NR/$CaCO_3$ composites were investigated by TGA and DSC analyses, respectively.

5.5.1 Thermogravimetric analysis (TGA)

The thermal decomposition profiles of all NR/$CaCO_3$ samples in terms of thermogravimetric analysis (TGA) curves and derivative thermogravimetric (DTG) curves are illustrated in Figure 5.41. The result in Figure 5.41(a) showed that the neat NR revealed a single-step degradation process in the range of 360 – 420^{o}C which was assigned as the polymer pyrolysis. All rubbers filled with $CaCO_3$ powders provided a two-step degradation process shown in Figure 5.41(b) – 5.41(j). In the first step (360 – 420^{o}C), a weight loss of about 65% occurred due to the decomposition of NR. The second stage (650 – 750^{o}C) demonstrated the thermal decomposition region of $CaCO_3$

inorganic fillers with a weight loss of 16 – 20%. In addition, there is another decomposition step of sucrose used as an aqueous medium in the range of 200 – 300^{o}C for the preparation of spherical $CaCO_3$ to be used in NR/ $CaCO_3$ (Figure 5.41(b) and 5.41(c)).

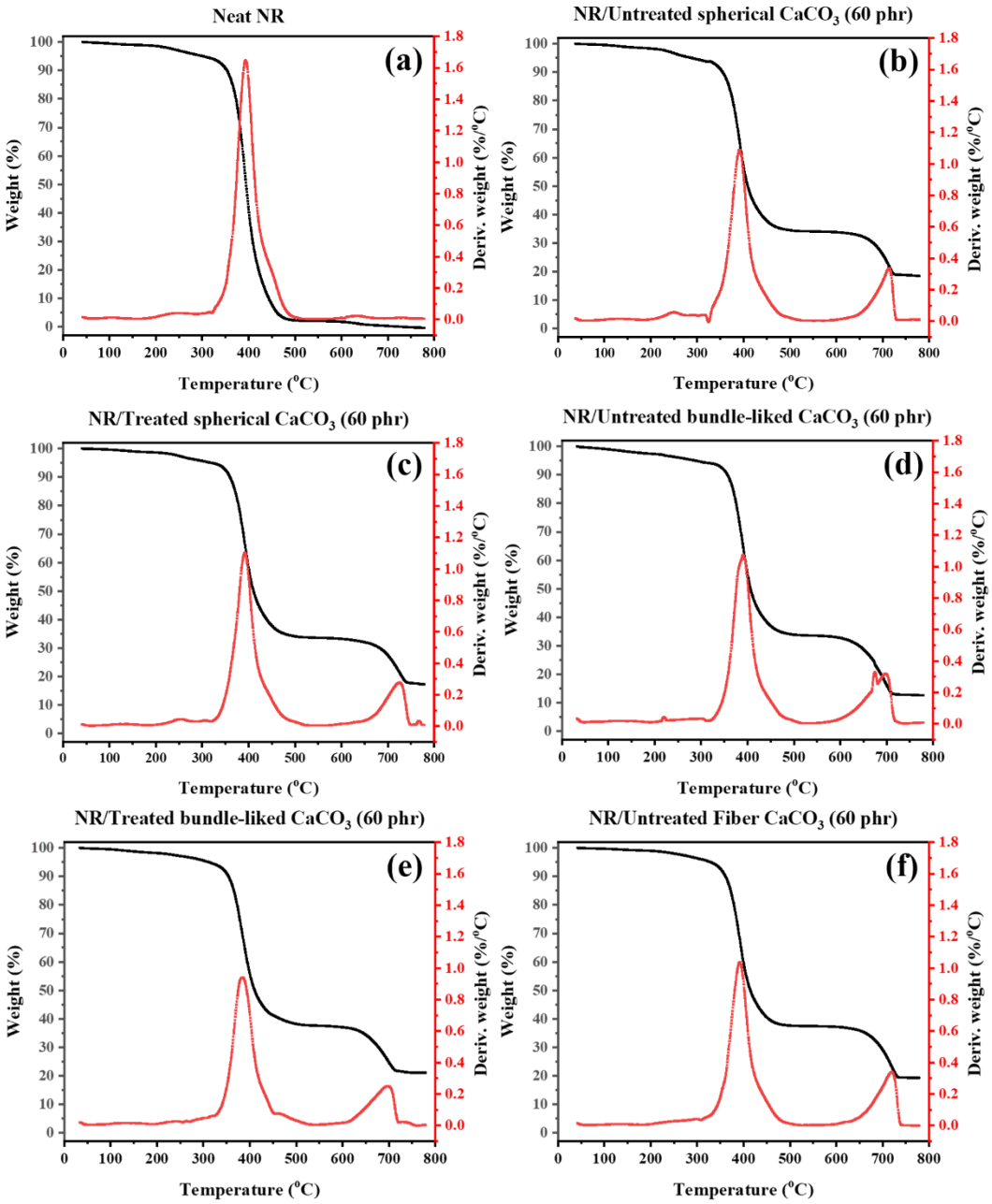


Figure 5.41 TGA thermograms of (a) neat NR, and NR/$CaCO_3$ composites at 60 phr (b) NR/Untreated spherical, (c) NR/Treated spherical, (d) NR/Untreated bundle-liked, (e) NR/Treated bundle-liked, (f) NR/Untreated fiber, (g) NR/Treated fiber, (h) NR/NCC, (i) NR/4QC, and (j) NR/9QQ composites

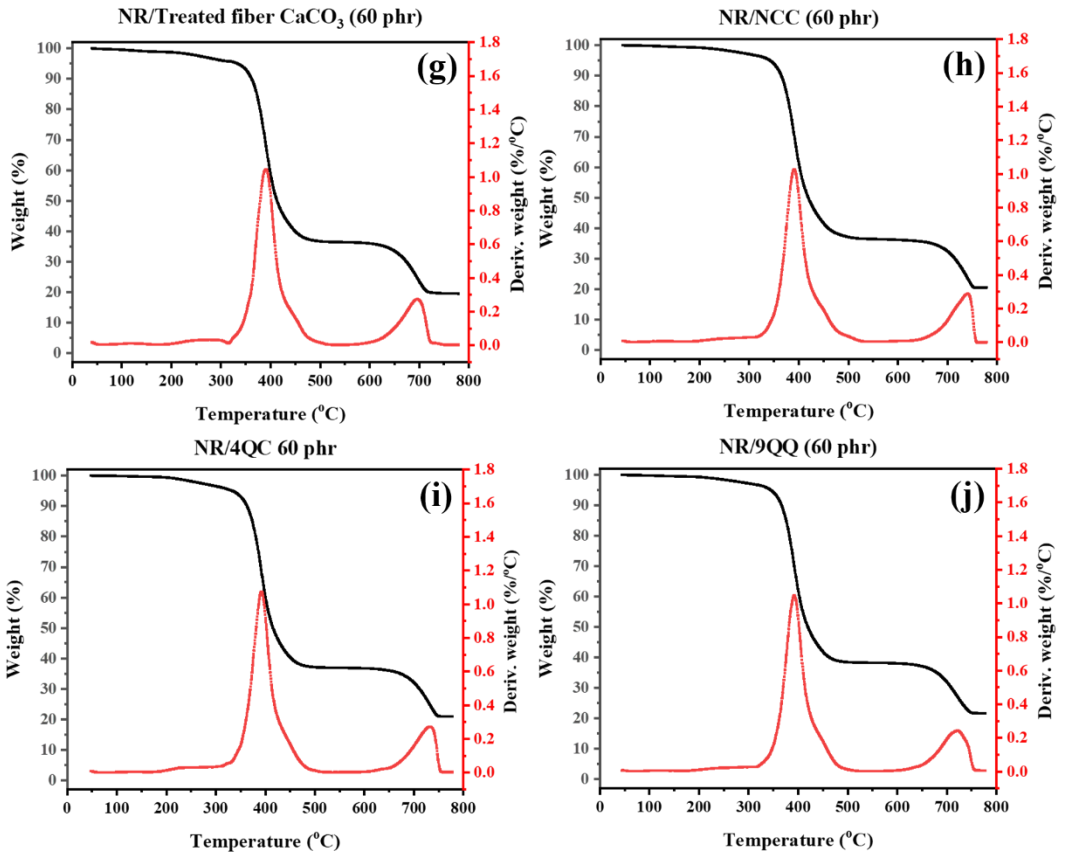


Figure 5.41 (cont.) TGA thermograms of (a) neat NR, and NR/$CaCO_3$ composites at 60 phr (b) NR/Untreated spherical, (c) NR/Treated spherical, (d) NR/Untreated bundle-liked, (e) NR/Treated bundle-liked, (f) NR/Untreated fiber, (g) NR/Treated fiber, (h) NR/NCC, (i) NR/4QC, and (j) NR/9QQ composites

5.5.2 Differential scanning calorimeter (DSC)

Figure 5.42 demonstrated the DSC thermograms of NR, NR/$CaCO_3$ composites at filler content 20 phr. The glass transition temperature (T_g) of rubber composites is listed in Table 5.11. The T_g of neat NR was found at approximately -59.68°C. Upon adding $CaCO_3$ filler in NR, the T_g value did not observe significant alteration or change. The average T_g of NR/$CaCO_3$ at filler loading 20 phr is -59.75 ± 0.25°C. This result could be ascribed to the $CaCO_3$ fillers did not affect the rubber backbone or rubber chain motion.

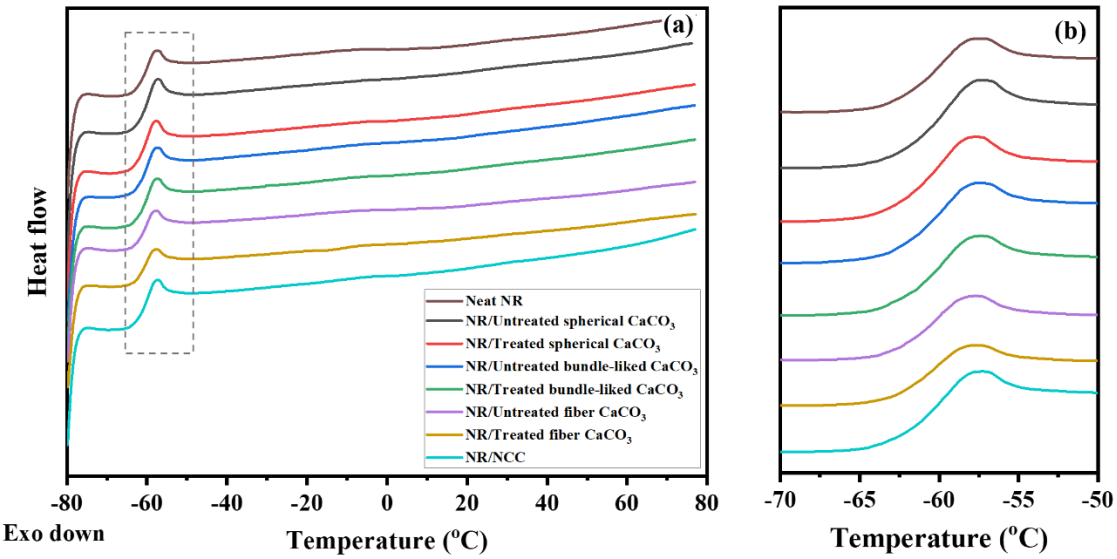


Figure 5.42 DSC thermograms of neat NR and NR/$CaCO_3$ (20 phr) composites in the range of (-80) – 80°C, and (-70) – (-50) °C for the glass transition temperature (T_g) of rubber vulcanizates

Table 5.11 Glass transition temperature (T_g) of NR/$CaCO_3$ composites at filler loading of 20 phr

Sample	Tg (°C)
1. Neat NR	-59.68
2. NR/Untreated spherical $CaCO_3$	-59.60
3. NR/Treated spherical $CaCO_3$	-59.65
4. NR/Untreated bundle-liked $CaCO_3$	-59.63
5. NR/Treated bundle-liked $CaCO_3$	-59.84
6. NR/Untreated fiber $CaCO_3$	-59.99
7. NR/Treated fiber $CaCO_3$	-60.20
8. NR/NCC	-59.35

5.6 Mechanical properties of NR/$CaCO_3$ compared with NR/N330 composites

In this study, the N330 carbon black (CB) was selected as a filler to compare the mechanical properties with $CaCO_3$ fillers used in this work. The physical and chemical properties of N330 CB used in this study are shown in Table 5.12.

Table 5.12 Physical and chemical properties of N330 CB used in this study (From BIRLA N330 company)

Physical properties	
Color	Black
Particle size (nm)	28 – 36
Average surface area (m^2/g)	76 – 80
Oil absorption number (OAN) (cc/100g)	104.7
Oil absorption number on the compressed sample (COAN) (cc/100g)	85.1
Pour density (kh/m^3)	368.1
Heating loss (%)	0.5
Sieve Residue (%)	0.100
Hardness (gf)	21.2
Ash content (%)	0.42
Chemical properties	
Iodine No. (mg/g)	82.2

It was reported that CB has reinforcing efficiency on rubber materials resulting in high tensile strength, high abrasion, proper modulus, and sufficient elongation. [138] In this research, the CB filler loading was varied 0, 5, 10, 20, 40, and 60 phr same as $CaCO_3$ used in the NR composite formula. The mechanical properties of NR/N330 composites were compared with NR/$CaCO_3$ composites including tensile strength, elongation at break, 100% and 300% modulus. The plot between tensile strain and

tensile strength of NR/N330 composites was presented in Figure 5.43. The tensile properties of NR/N330 composites were listed in Table 5.13.

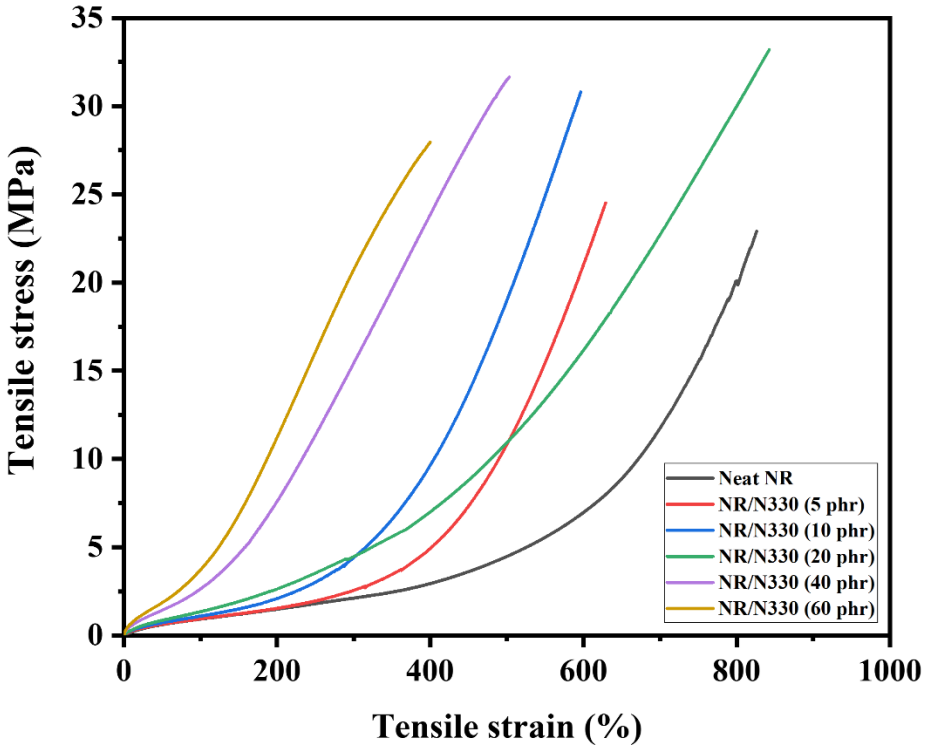


Figure 5.43 Plots of tensile strain and tensile strength of NR/N330 composites

Table 5.13 Tensile properties of NR/N330 composites

NR/N330 (phr)	Tensile strength (MPa)	Elongation at break (%)	100% Modulus (MPa)	300% Modulus (MPa)
1. Neat NR	22.68 ± 2.22	821.63 ± 10.25	0.90 ± 0.03	2.08 ± 0.07
2. NR/N330 (5)	24.32 ± 0.36	623.04 ± 9.09	0.91 ± 0.06	2.59 ± 0.03
3. NR/N330 (10)	31.20 ± 1.28	610.29 ± 18.39	1.10 ± 0.01	4.32 ± 0.09
4. NR/N330 (20)	33.03 ± 0.30	596.00 ± 15.62	1.39 ± 0.02	7.50 ± 0.42
5. NR/N330 (40)	31.33 ± 0.28	487.50 ± 14.35	2.72 ± 0.08	16.23 ± 0.71
6. NR/N330 (60)	27.82 ± 0.16	413.26 ± 6.57	4.01 ± 0.07	20.71 ± 0.34

5.6.1 Tensile strength of NR/N330 composites

Figure 5.44 presented the tensile strength of NR/untreated $CaCO_3$ (spherical, bundle-liked, fiber) composites compared with NR/330 CB composites for all filler loading variations. At 5 and 10 phr of filler loading, the tensile strength of NR/untreated fiber $CaCO_3$ exhibited the highest tensile strength value of 30.93 ± 1.15 and 31.66 ± 1.80 MPa, respectively. The tensile strength of NR/N330 composites at 5 and 10 phr were 24.32 ± 0.36 and 31.20 ± 1.28 MPa, respectively. These results depended on the particle shape and average particle size of the filler. The untreated fiber is a nanofiber particle resulting in high aspect ratio. The tensile strength of NR/N330 composites increased until the maximum loading value was equal to 20 phr. At 20 phr of filler loading, the NR/N330 composite provided the highest tensile strength (33.03 ± 0.30 MPa) over all other NR/$CaCO_3$ composites. This is caused by the nano-size and high surface area of CB which is well distributed and interact with rubber. [163] At 40 and 60 phr, the tensile strength of the rubber/filler composites decreased due to the agglomeration of filler resulting in unwell distribution and dispersion.

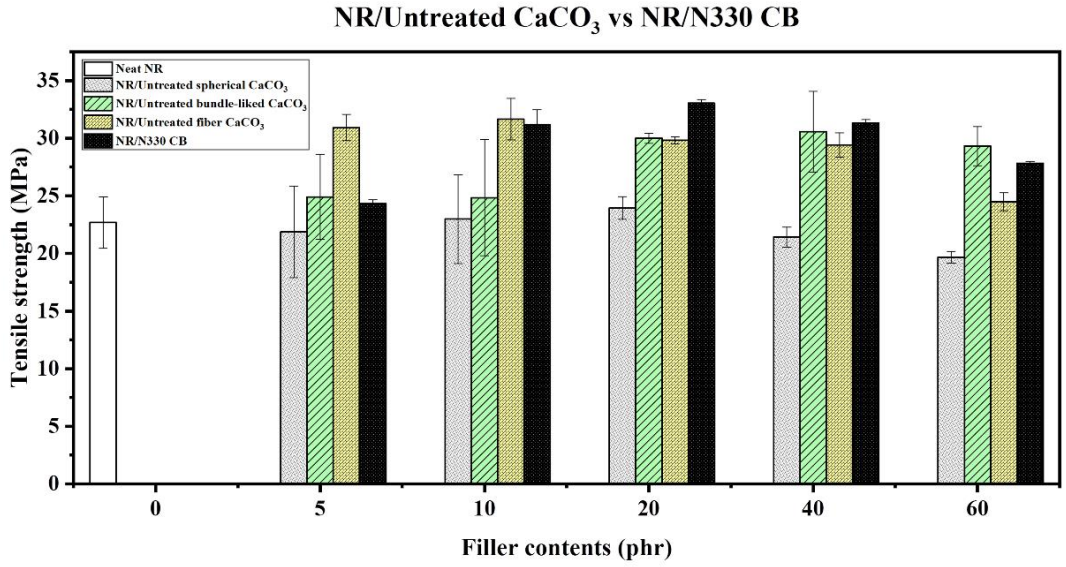


Figure 5.44 Tensile strength of NR/N330 carbon black composites compared with NR/untreated (spherical, bundle-liked and fiber shaped) $CaCO_3$ composites

Figure 5.45 demonstrated the tensile strength of NR/treated $CaCO_3$ (spherical, bundle-liked, fiber) composites together with NR/N330 composites. At 5 phr, the tensile strength of NR/treated bundle-liked $CaCO_3$ sample gave the highest tensile strength of 29.88 ± 0.34 MPa while that of NR/N330 was 24.32 ± 0.36 MPa. The aspect ratio of bundle-liked is 8.42 which is higher than treated spherical (0.98) might influence this property. At 10 and 20 phr of filler loading, the NR/N330 composites revealed a high tensile strength over NR/$CaCO_3$ due to its nanoparticles. The maximum loading of CB is 20 phr and the tensile strength decreased slightly when filler loading is 30 phr. The tensile strength of NR/N330 composite at 60 phr was significantly decreased due to particle agglomeration.

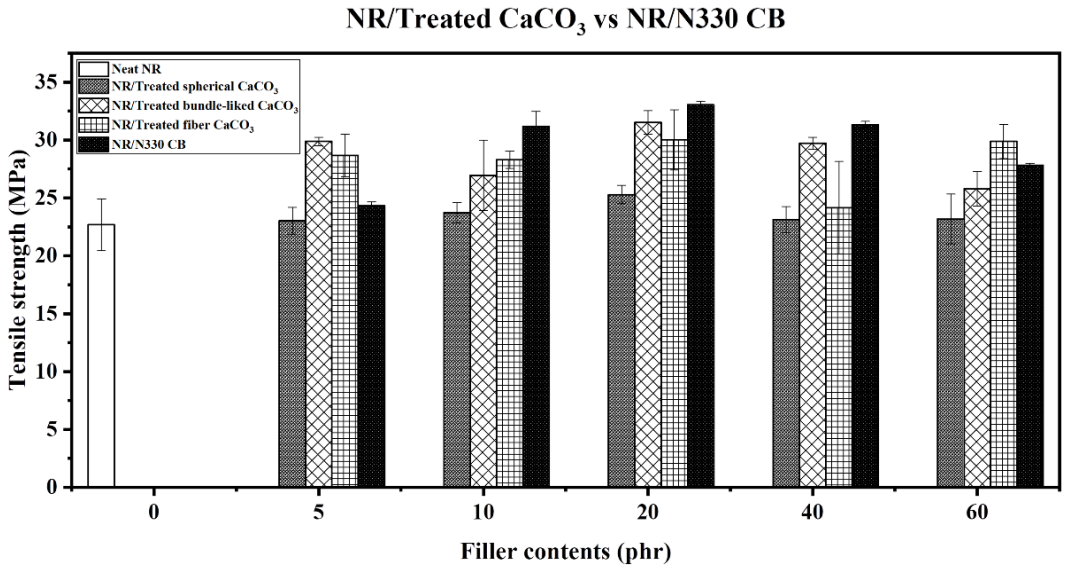


Figure 5.45 Tensile strength of NR/N330 carbon black composite compared with NR/treated (spherical, bundle-liked and fiber shaped) $CaCO_3$ composites

5.6.2 Elongation at break of NR/N330 composites

The elongation at break of NR/N330 composite compared to NR/untreated $CaCO_3$ composites was presented in Figure 5.46(a) and NR/treated $CaCO_3$ composites in Figure 5.46(b). When the filler content increased, the elongation of composites decreased. The filler might adhere to the rubber matrix inhibiting the flexibility of the rubber composite. Compared to the elongation at break of neat NR

which is 821.63 ± 10.25 %, the elongation at break of rubber when filled with N330 fillers were decreased to 623.04 ± 9.09, 610.29 ± 18.39, 596.00 ± 15.62, 487.50 ± 14.35, and 413.26 ± 6.57% at N330 loading of 5, 10, 20, 40, and 60 phr, respectively. It was seen that at all filler loading variations of untreated and treated $CaCO_3$ fillers, the elongation at break of NR/N330 composites is lower than those of the NR/$CaCO_3$ composites. According to the stiffness of CB which is higher than $CaCO_3$ particles, these led to the stiffening of the polymer chain hence resistance to stretch when strain was applied for NR/N330 composites.

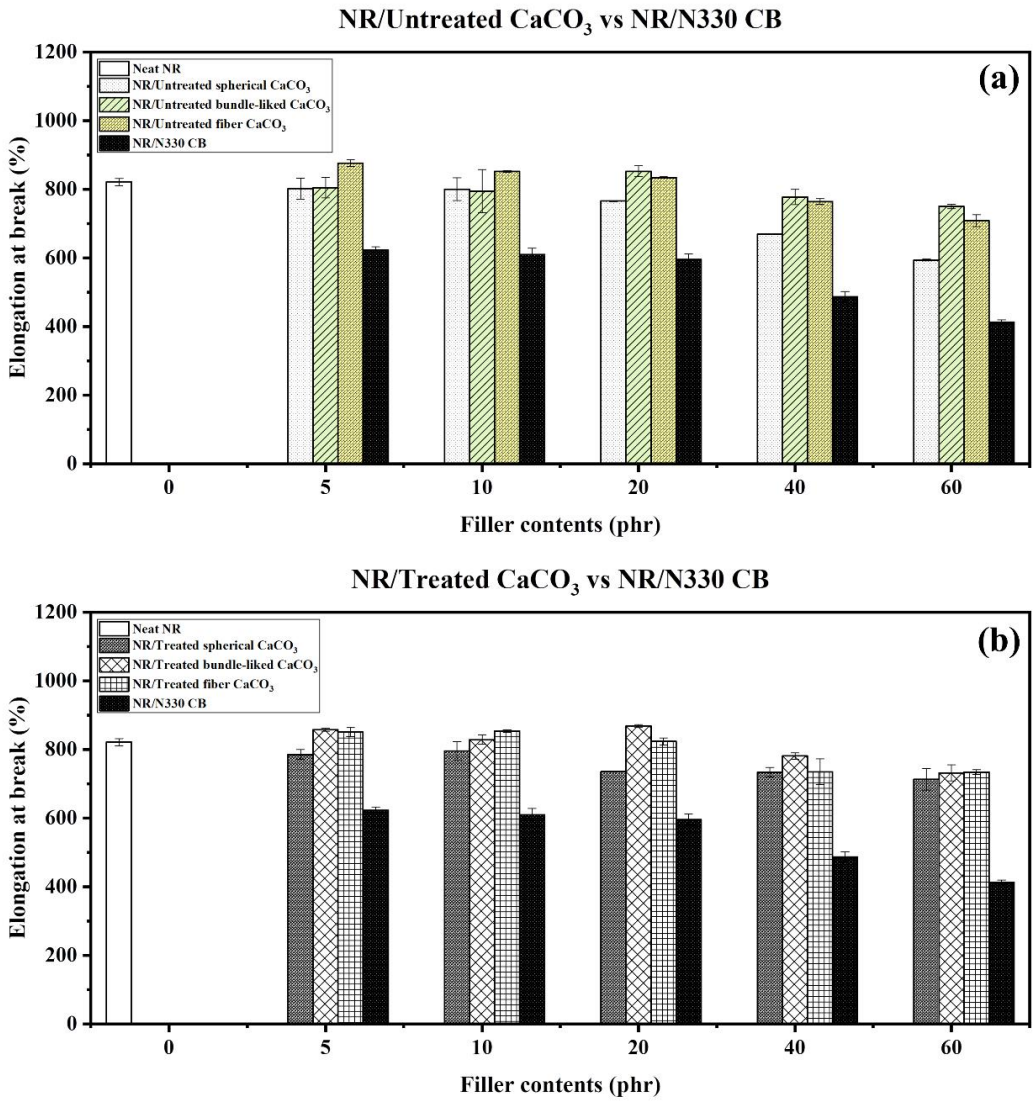


Figure 5.46 Elongation at break of NR/N330 carbon black composites compared with different shapes of $CaCO_3$: spherical, bundle-liked and fiber filled rubber vulcanizates (a) NR/untreated $CaCO_3$, and (b) NR/treated $CaCO_3$ composites

5.6.3 Modulus of NR/N330 composite

The 100% modulus and 300% modulus of NR/N330 compared to the NR/$CaCO_3$ composites were shown in Figure 5.47 and 5.48, respectively. The modulus of all composites increased when the filler contents increased. The 100% modulus of neat NR was 0.90 ± 0.03% while the 100% modulus of NR/N330 composites were 0.91 ± 0.06, 1.10 ± 0.01, 1.39 ± 0.02, 2.72 ± 0.08, and 4.01 ± 0.07 MPa, at 5, 10, 20, 40, and 60 phr filler loading, respectively. Similar to M100, the 300% modulus of NR/N330 composite at 5, 10, 20, 40, and 60 phr were raised to 2.59 ± 0.03, 4.32 ± 0.09, 7.50 ± 0.42, 16.23 ± 0.71, and 20.71 ± 0.34 MPa, respectively, compared to that of neat NR (2.08 ± 0.07 MPa). The modulus of rubber composites is an indication of the relative stiffness of the composite, the 100% and 300% moduli of NR/N330 composites at all filler loading were higher than NR/$CaCO_3$ composites. This is also due to the high stiffness of CB particles; the filler restricted and entrapped the mobility of rubber chains resulting in an increment of rigidity of the composites.

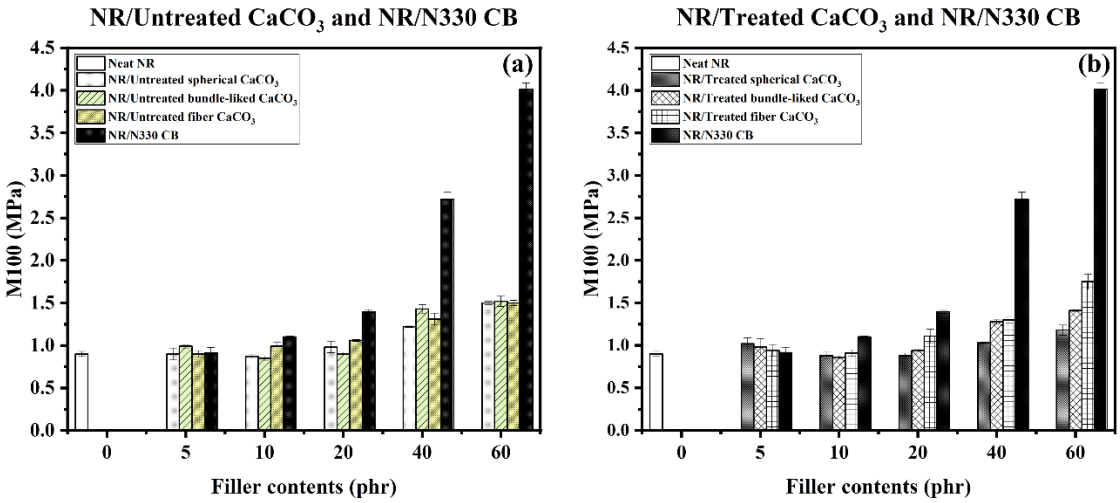


Figure 5.47 M100 of NR/N330 CB composites and NR/$CaCO_3$ composites: (a) NR/untreated $CaCO_3$ and (b) NR/treated $CaCO_3$ composites

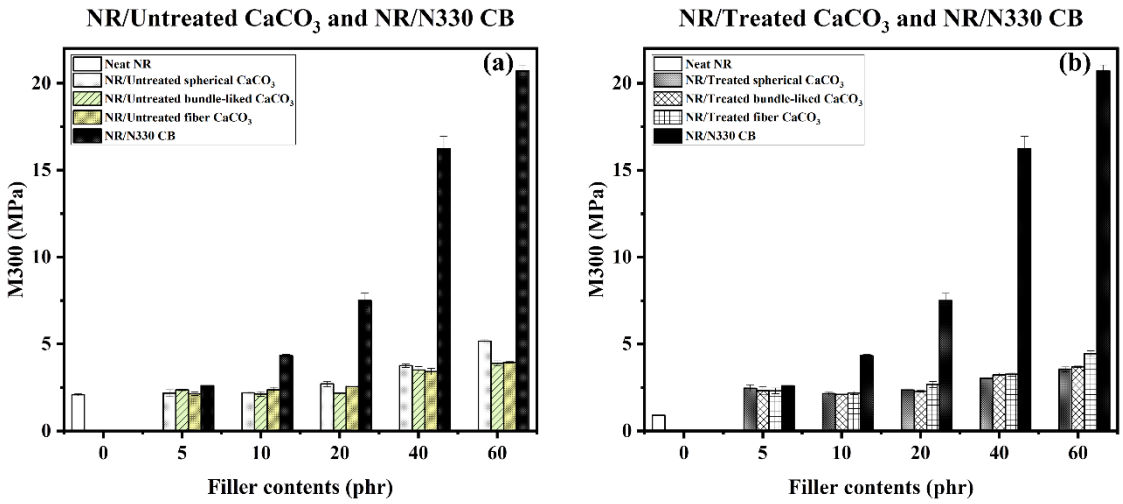


Figure 5.48 300% Modulus (M300) of NR/N300 composites and NR/$CaCO_3$ composites: (a) NR/Untreated $CaCO_3$, and (b) NR/Treated $CaCO_3$ composites

These mechanical property results can be summarized that 10 phr of untreated fiber $CaCO_3$ filler loading provided the highest tensile strength and elongation at break over not only other types of $CaCO_3$ powders but also N330 CB (Figure 5.49). The fiber shaped $CaCO_3$ powder enhanced the mechanical properties of NR vulcanizate due to its nanoscale particle size, fiber shape with high aspect ratio. In the material's stiffness point of view, the CB provided higher modulus values than the $CaCO_3$ filled NR composites.

At 20 and 40 phr, the NR/N330 composites demonstrated the highest tensile strength due to their nanoparticles and well distributed in the rubber matrix. The $CaCO_3$ particles will agglomerate together disrupting the mobility of the rubber chain at a high content of filler loading.

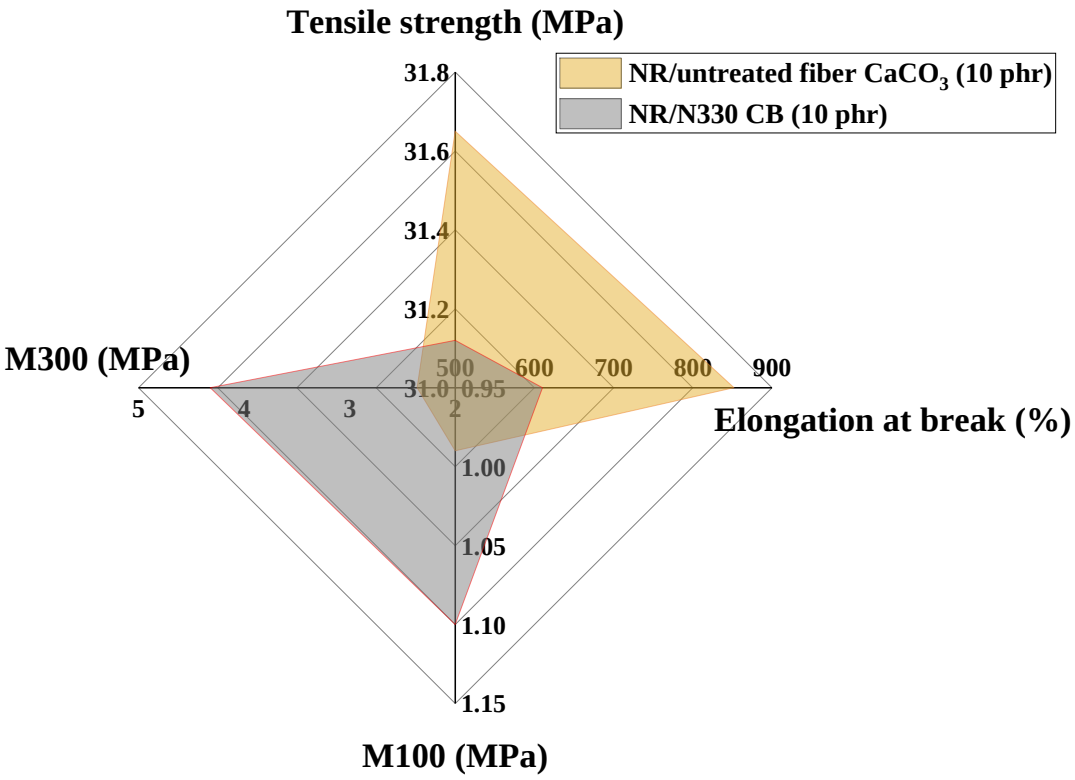


Figure 5.49 Radar chart comparison the mechanical properties of NR/untreated fiber $CaCO_3$ and NR/N330 composites at filler content 10 phr including tensile strength, elongation at break, M100 and M300

From the view point of environmental and health issues, the CB powders are toxic nanoparticles that can cause lung organ problem of front-line operators. Meanwhile, $CaCO_3$ powders are non-toxicological concern. It can infer that $CaCO_3$ can be used as reinforcing fillers in rubber materials with environmentally friendly property.

CHAPTER VI
CONCLUSIONS

This research synthesized the different shapes, particle sizes, aspect ratios, and surface modifications of calcium carbonate ($CaCO_3$) particles via the precipitation process using different mixing conditions. Then, the as-synthesized $CaCO_3$ particles were incorporated in natural rubber (NR) to investigate their reinforcing efficacy. The mechanical properties of NR/$CaCO_3$ composites were investigated and compared with commercial micro and nano sizes $CaCO_3$ and N330 carbon black (CB). Several synthetic parameters and analyses were conducted. The results obtained are concluded as follows.

Part I: Preparation and polymorphic characterization of calcium carbonate ($CaCO_3$) particles

The $CaCO_3$ particles were achieved via the solution precipitation method between carbonate (CO_3^{2-}) ions and calcium (Ca^{2+}) ions. The polymorphic phases and chemical structure of $CaCO_3$ were characterized by XRD, ATR-FTIR, and Raman spectroscopy. The SEM was employed to confirm the morphological shape of as-synthesized and commercial $CaCO_3$ particles. The TEM technique was used to measure the average particle size, diameter, length, and aspect ratio of the $CaCO_3$ particles. The surface hydrophilicity of the $CaCO_3$ particles was investigated by measuring the water contact angle.

It was found that the reaction of $(NH_4)_2CO_3$ and $CaCl_2$ dissolved in 50% by weight of sucrose as the aqueous medium resulted in spherical $CaCO_3$ with an aspect ratio of about 1, evidenced by SEM technique. This condition provided the particle size on a nanoscale (0.42 ± 0.14 μm). This is caused by the increment of viscosity of the

mixing system from sucrose playing the key factor in reducing the particle size of spherical $CaCO_3$. It limited the diffusion of Ca^{2+} ions and prevented the further growth of $CaCO_3$ particles. When the precipitation reaction occurred in the presence of olive soap, the average particle size of treated spherical $CaCO_3$ particles was obtained at 0.51 ± 0.16 µm which is larger than untreated spherical $CaCO_3$. This is caused by the soap as a surface modifying agent being trapped inside and also coated on the surface of the particles. The bigger particle size resulted in a lower specific surface area with porous property which was confirmed by BET and TEM techniques. Both untreated and treated spherical $CaCO_3$ provided the high percentage of vaterite phase about 99% and no typical peak of calcite is presented. The wettability of untreated spherical $CaCO_3$ is assigned as hydrophilic with a water contact angle of 28 ± 2°. In contrast, the treated spherical $CaCO_3$ gave a water contact angle of 163 ± 2°, categorized as superhydrophobic powder.

The precipitation process of 1.0 M Na_2CO_3 and 1.0 M $CaCl_2$ solutions using water as a medium was performed at 80 ± 1°C. At the high temperature of the mixing system, the morphology demonstrated rod-liked particles agglomerating into bundles, revealed by SEM and TEM techniques. The length of bundle-liked $CaCO_3$ was about 4 µm and the diameter of 0.5 µm, resulting in the aspect ratio in the range of 8 – 9. This type of $CaCO_3$ demonstrated the high content of aragonite phase (75 – 85%), followed by 10 – 20% of vaterite, and 2% of calcite phase, respectively. The superhydrophobic bundle-liked $CaCO_3$ was also successfully synthesized by soap treatment as well. The water contact angle of untreated and treated bundle-liked are 29 ± 2°, and 167 ± 2°, respectively. Due to the rough surface of the bundle type, it obtained a higher contact angle than the spherical shape.

The fiber $CaCO_3$ nanoparticles were successfully synthesized through the polymorph transformation in water from spherical vaterite to long nano-wired aragonite at 80°C of dispersing temperature with stirring. The average length of untreated fiber $CaCO_3$ particles was 20.40 ± 7.72 µm and the diameter was 0.13 ± 0.04 µm or 130 nm resulting in the highest aspect ratio of 156.9 over other shapes of $CaCO_3$. However, the soap-treated fiber $CaCO_3$ contained a mixture of spherical, cubic, and fiber forms. This affected the decreased aspect ratio of the $CaCO_3$. The Rietveld refinement patterns of

both untreated and treated fiber $CaCO_3$ showed the highest %crystallinity of the aragonite phase of about 70 – 80%. The hydrophilicity of untreated fiber CaCO3 was 31 ± 1º. The treated fiber $CaCO_3$ provided 165 ± 5º of water contact angle, hence it is considered as a superhydrophobic property similar to other synthesized $CaCO_3$ polymorphs.

The commercial $CaCO_3$ in micro- and nanoscale were also investigated. All the commercial $CaCO_3$ morphology is cubic with 99% of calcite crystallinity. The nano $CaCO_3$ particles revealed 5 nm of particle size with a hydrophobic surface of 159 ± 3º. The 4QC and 9QQ gave the microscale of diameter in the range of 2 – 4 μm. The 4QC powders are superhydrophobic with 164 ± 4º while the hydrophilicity of 9QQ is 23 ± 1º.

The thermal stability of both synthesized and commercial $CaCO_3$ powders revealed the main step of calcination decomposition of inorganic $CaCO_3$ powder in the range of 600 – 800ºC.

Part II: Preparation of NR/$CaCO_3$ composites and their mechanical properties

Different types of $CaCO_3$ including as-synthesized and commercial $CaCO_3$ powders were incorporated into natural rubber (NR) as fillers. The variation of $CaCO_3$ filler in NR was 0, 5, 10, 20, 40, and 60 phr. The polymorph of $CaCO_3$ particles is found to stabilize their starting phase in NR without any transformation. The vaterite $CaCO_3$ was found stable when it was incorporated in the NR latex stage. Other polymorphs of untreated and treated bundle-liked and fiber-shaped $CaCO_3$ revealed the same forms when they were added to NR latex. The mechanical properties of NR/$CaCO_3$ including tensile strength, elongation at break, tear strength, and hardness Shore A were investigated. The surface-modified $CaCO_3$-filled NR vulcanizates successfully improved the mechanical properties of NR vulcanizates according to the nature of hydrophobicity of NR (113 ± 3º) and superhydrophobic $CaCO_3$ particles. The

hydrophobic $CaCO_3$ particles including treated spherical, treated bundle-liked, treated fiber, NCC, and 9QQ presented the homogenous dispersion in NR compound compared to the agglomeration of fillers for NR/hydrophilic $CaCO_3$ compounds.

The tensile strength of NR/$CaCO_3$ composites increased with increasing the $CaCO_3$ loading. In the case of spherical-shaped $CaCO_3$ particles, the treated spherical $CaCO_3$ has good compatibility with NR resulting in higher tensile strength compared with untreated spherical $CaCO_3$ filled in NR. The highest tensile strength of NR/treated vaterite $CaCO_3$ was 25.28 ± 0.80 MPa, and the NR/untreated vaterite $CaCO_3$ was 23.94 ± 0.97 MPa at 20 phr loading, compared to the neat NR (22.68 ± 2.22 MPa). The highest tensile strength of treated bundle-liked shape $CaCO_3$ filled NR was 31.51 ± 1.02 MPa (20 phr of filler loading), while the untreated bundle-liked shape resulted in the tensile strength of 29.98 ± 0.44 MPa at the same filler loading. The maximum improvement in mechanical properties of NR/$CaCO_3$ composites was achieved by adding untreated fiber $CaCO_3$ at loading only 10 phr providing the highest tensile strength of 31.66 ± 1.80 MPa compared to other composites and neat NR. This was caused by the particle size in the nanoscale and the high aspect ratio of fiber $CaCO_3$ enhancing the interfacial adhesion between filler and rubber matrix which improves the mechanical properties of NR vulcanizates. The treated fiber $CaCO_3$ gave lower tensile strength (28.30 ± 0.74 MPa) than the untreated powder due to the appearance of the mixture of polymorphs. As a result, the optimum loading $CaCO_3$ filler in NR raised at 10 phr for fiber-shape $CaCO_3$ and 20 phr for bundle-shape $CaCO_3$, which affected the improved mechanical properties. Not only tensile strength was improved but the elongation at break also increased when the bundle-liked and fiber-shaped $CaCO_3$ were added into NR. At high loading (40 and 60 phr), the agglomeration of filler occurred disturbing the stress transfer during strain applied. Hence, decreased mechanical properties of the NR/$CaCO_3$ composites.

In comparison with synthesized $CaCO_3$ and commercial $CaCO_3$ used in this work, the NR/bundle-liked $CaCO_3$ and NR/ fiber $CaCO_3$ composites with and without filler surface treatment resulted in higher tensile strength, elongation at break, and modulus than all types of commercial $CaCO_3$ (NCC, 9QQ, and 4QC) at filler loading 5

– 20 phr. It was found that the commercial $CaCO_3$-filled NR vulcanizates provided slightly higher tear strength than synthesized $CaCO_3$ powders in this work.

The thermal stability of $CaCO_3$ powders and NR/$CaCO_3$ composites was studied by using TGA. The peak of polymer pyrolysis of NR was shifted from 391^oC to 388^oC. The thermal decomposition profiles showed that $CaCO_3$ can improve the thermal resistance of rubber composites. The DSC results demonstrated that loading $CaCO_3$ in NR does not affect the backbone or disrupt the rubber chain motions.

In addition, the NR/N330 CB composites were prepared and compared the mechanical properties with NR/untreated and treated $CaCO_3$ composites. At 20 phr of N330 CB loading provided the highest tensile strength of 33.03 ± 0.30 MPa which is slightly higher than the NR/untreated fiber $CaCO_3$ at 10 phr. This might be due to the particle size of N330 (28 – 36 nm) being smaller than the untreated fiber $CaCO_3$ (0.53 ± 0.05 μm). It can be seen that a lower loading of $CaCO_3$ than N330 could effectively reinforce the NR composites at a similar tensile strength. Consequently, the prepared $CaCO_3$ powders have the potential to broaden their application not only as diluents or additives but also as reinforcing agents. Considering environmental and health issues and the toxicity of CB used in rubber factories, the prepared $CaCO_3$ is a good option for use as a reinforcing filler in NR composites and the filler loading could be carried out in the NR latex form.

In conclusion, these finding provides knowledge of the synthetic procedures and surface modification of $CaCO_3$ particles and the preparation of NR/$CaCO_3$ composites. The improvement of mechanical properties of NR filled with $CaCO_3$ particles has been tested, and fiber shape with long nanowire of $CaCO_3$ could be the potential reinforcing filler to widen or broaden the application of $CaCO_3$ not only used as additive or diluting fillers. Furthermore, the application of hydrophilic and hydrophobic with different shapes of $CaCO_3$ will have the potential to be applied as filler in many materials which can be manipulated by their surface property such as in synthetic rubbers i.e. SBR, BR or in plastics such as polyolefine (polypropylene (PP) or polyethylene (PE), poly(lactic acid)) and so on.

Future perspectives

The successful development of untreated and treated $CaCO_3$ with different polymorphs in this study has opened an opportunity and is challenging to further an investigation in other types of bio-based or biodegradable plastics such as poly(lactic acid) and cellulosic materials.

REFERENCES

1. Sato, Y., & Komaru, A. (2019). Pearl formation in the Japanese pearl oyster (Pinctada fucata) by CaCO3 polymorphs: Pearl quality-specific biomineralization processes and their similarity to shell regeneration. *Aquaculture Research, 50*(6), 1710-1717. doi:https://doi.org/10.1111/are.14057
2. Sulpis, O., Jeansson, E., Dinauer, A., Lauvset, S. K., & Middelburg, J. J. (2021). Calcium carbonate dissolution patterns in the ocean. *Nature Geoscience, 14*(6), 423-428. doi:10.1038/s41561-021-00743-y
3. Boyjoo, Y., Pareek, V. K., & Liu, J. (2014). Synthesis of micro and nano-sized calcium carbonate particles and their applications. *Journal of Materials Chemistry A, 2*(35), 14270-14288. doi:10.1039/C4TA02070G
4. Konopacka-Łyskawa, D. (2019). Synthesis Methods and Favorable Conditions for Spherical Vaterite Precipitation: A Review. *Crystals, 9*(4). Retrieved from doi:10.3390/cryst9040223
5. Hu, Y.-B., Wolf-Gladrow, D. A., Dieckmann, G. S., Völker, C., & Nehrke, G. (2014). A laboratory study of ikaite (CaCO3·6H2O) precipitation as a function of pH, salinity, temperature and phosphate concentration. *Marine Chemistry, 162*, 10-18. doi:https://doi.org/10.1016/j.marchem.2014.02.003
6. Maleki Dizaj, S., Barzegar-Jalali, M., Zarrintan, M. H., Adibkia, K., & Lotfipour, F. (2015). Calcium carbonate nanoparticles as cancer drug delivery system. *Expert Opinion on Drug Delivery, 12*(10), 1649-1660. doi:10.1517/17425247.2015.1049530
7. Pouget, E. M., Bomans, P. H. H., Dey, A., Frederik, P. M., de With, G., & Sommerdijk, N. A. J. M. (2010). The Development of Morphology and Structure in Hexagonal Vaterite. *Journal of the American Chemical Society, 132*(33), 11560-11565. doi:10.1021/ja102439r

8. Wang, L., Sondi, I. I., & Matijevic, E. (1999). Preparation of Uniform Needle-Like Aragonite Particles by Homogeneous Precipitation. *J Colloid Interface Sci, 218*(2), 545-553. doi:10.1006/jcis.1999.6463
9. Ferreira, A. M., Vikulina, A. S., & Volodkin, D. (2020). CaCO3 crystals as versatile carriers for controlled delivery of antimicrobials. *Journal of Controlled Release, 328*, 470-489. doi:https://doi.org/10.1016/j.jconrel.2020.08.061
10. Longkaew, K., Tessanan, W., Daniel, P., Phinyocheep, P., & Gibaud, A. (2023). Using sucrose to prepare submicrometric CaCO3 vaterite particles stable in natural rubber. *Advanced Powder Technology, 34*(1), 103924. doi:https://doi.org/10.1016/j.apt.2022.103924
11. Pérez-Villarejo, L., Takabait, F., Mahtout, L., Carrasco-Hurtado, B., Eliche-Quesada, D., & Sánchez-Soto, P. J. (2018). Synthesis of vaterite CaCO3 as submicron and nanosized particles using inorganic precursors and sucrose in aqueous medium. *Ceramics International, 44*(5), 5291-5296. doi:https://doi.org/10.1016/j.ceramint.2017.12.142
12. Chen, J., & Xiang, L. (2009). Controllable synthesis of calcium carbonate polymorphs at different temperatures. *Powder Technology, 189*(1), 64-69. doi:https://doi.org/10.1016/j.powtec.2008.06.004
13. Abidi, L., Amiard, F., Delorme, N., Ouhenia, S., & Gibaud, A. (2022). Using saponified olive oil to make cost effective calcium carbonate particles superhydrophobic. *Advanced Powder Technology, 33*(2), 103399. doi:https://doi.org/10.1016/j.apt.2021.103399
14. Cherkas, O., Beuvier, T., Zontone, F., Chushkin, Y., Demoulin, L., Rousseau, A., et al. (2018). On the kinetics of phase transformations of dried porous vaterite particles immersed in deionized and tap water. *Advanced Powder Technology, 29*(11), 2872-2880. doi:https://doi.org/10.1016/j.apt.2018.08.008
15. Mattila, H.-P., & Zevenhoven, R. (2014). Chapter Ten - Production of Precipitated Calcium Carbonate from Steel Converter Slag and Other Calcium-Containing Industrial Wastes and Residues. In M. Aresta & R. van Eldik (Eds.), *Advances in Inorganic Chemistry* (Vol. 66, pp. 347-384): Academic Press.

16. Jafari, R., & Farzaneh, M. (2012). Development a simple method to create the superhydrophobic composite coatings. *Journal of Composite Materials, 47*(25), 3125-3129. doi:10.1177/0021998312462429
17. Ali, M., Abdullah, M. S., & Saad, S. A. (2015). Effect of Calcium Carbonate Replacement on Workability and Mechanical Strength of Portland Cement Concrete. *Advanced Materials Research, 1115*, 137-141. doi:10.4028/www.scientific.net/AMR.1115.137
18. Chen, J., Cheng, G., Chai, Y., Han, W., Zong, W., Chen, J., et al. (2018). Preparation of nano-CaCO(3)/polystyrene nanocomposite beads for efficient bilirubin removal. *Colloids Surf B Biointerfaces, 161*, 480-487. doi:10.1016/j.colsurfb.2017.11.017
19. Cherkas, O., Beuvier, T., Fall, S., & Gibaud, A. (2016). X-ray absorption and diffraction analysis for determination of the amount of calcium carbonate and porosity in paper sheets. *Cellulose, 23*(5), 2831-2840. doi:10.1007/s10570-016-1001-3
20. Choe, H., Lee, J. H., & Kim, J. H. (2020). Polyurethane composite foams including CaCO3 fillers for enhanced sound absorption and compression properties. *Composites Science and Technology, 194*, 108153. doi:https://doi.org/10.1016/j.compscitech.2020.108153
21. Hassani, L. N., Hindré, F., Beuvier, T., Calvignac, B., Lautram, N., Gibaud, A., et al. (2013). Lysozyme encapsulation into nanostructured CaCO3 microparticles using a supercritical CO2 process and comparison with the normal route. *Journal of Materials Chemistry B, 1*(32), 4011-4019. doi:10.1039/C3TB20467G
22. Li, L., Yang, Y., Lv, Y., Yin, P., & Lei, T. (2020). Porous calcite CaCO3 microspheres: Preparation, characterization and release behavior as doxorubicin carrier. *Colloids and Surfaces B: Biointerfaces, 186*, 110720. doi:https://doi.org/10.1016/j.colsurfb.2019.110720
23. Son, C., Kim, S. Y., Bahn, S. Y., Cha, H. J., & Choi, Y. S. (2017). CaCO3 thin-film formation mediated by a synthetic protein-lysozyme coacervate. *RSC Advances, 7*(25), 15302-15308. doi:10.1039/C6RA28808A

24. Zhou, G.-T., Yu, J. C., Wang, X.-C., & Zhang, L.-Z. (2004). Sonochemical synthesis of aragonite-type calcium carbonate with different morphologies. *New Journal of Chemistry, 28*(8), 1027-1031. doi:10.1039/B315198K

25. Hirata, Y., Kondo, H., & Ozawa, Y. (2014). 12 - Natural rubber (NR) for the tyre industry. In S. Kohjiya & Y. Ikeda (Eds.), *Chemistry, Manufacture and Applications of Natural Rubber* (pp. 325-352): Woodhead Publishing.

26. Yip, E., & Cacioli, P. (2002). The manufacture of gloves from natural rubber latex. *J Allergy Clin Immunol, 110*(2 Suppl), S3-14. doi:10.1067/mai.2002.124499

27. Ho, C. C. (2013). *CHAPTER 4:The Production of Natural Rubber from Hevea brasiliensis Latex: Colloidal Properties, Preservation, Purification and Processing*.

28. Nawamawat, K., Sakdapipanich, J. T., Ho, C. C., Ma, Y., Song, J., & Vancso, J. G. (2011). Surface nanostructure of Hevea brasiliensis natural rubber latex particles. *Colloids and Surfaces A: Physicochemical and Engineering Aspects, 390*(1), 157-166. doi:https://doi.org/10.1016/j.colsurfa.2011.09.021

29. Kumarn, S., Churinthorn, N., Nimpaiboon, A., Sriring, M., Ho, C.-C., Takahara, A., et al. (2018). Investigating the Mechanistic and Structural Role of Lipid Hydrolysis in the Stabilization of Ammonia-Preserved Hevea Rubber Latex. *Langmuir, 34*(43), 12730-12738. doi:10.1021/acs.langmuir.8b02321

30. Fang, Q., Song, B., Tee, T.-T., Sin, L. T., Hui, D., & Bee, S.-T. (2014). Investigation of dynamic characteristics of nano-size calcium carbonate added in natural rubber vulcanizate. *Composites Part B: Engineering, 60*, 561-567. doi:https://doi.org/10.1016/j.compositesb.2014.01.010

31. Jong, L. (2020). Synergistic Effect of Calcium Carbonate and Biobased Particles for Rubber Reinforcement and Comparison to Silica Reinforced Rubber. *Journal of Composites Science, 4*(3). Retrieved from doi:10.3390/jcs4030113

32. Khan, I., & Bhat, A. H. (2014). Micro and Nano Calcium Carbonate Filled Natural Rubber Composites and Nanocomposites (pp. 467-487).

33. Lay, M., Hamran, N., & Rashid, A. A. (2019). Ultrafine calcium carbonate-filled natural rubber latex film: mechanical and post-processing properties. *Iranian Polymer Journal, 28*(10), 849-858. doi:10.1007/s13726-019-00748-w

34. Guo, B., Chen, F., Lei, Y., & Chen, W. (2010). Significantly improved performance of rubber/silica composites by addition of sorbic acid. *Polymer Journal, 42*(4), 319-326. doi:10.1038/pj.2010.4

35. Khodabakhshi, S., Fulvio, P. F., & Andreoli, E. (2020). Carbon black reborn: Structure and chemistry for renewable energy harnessing. *Carbon, 162*, 604-649. doi:https://doi.org/10.1016/j.carbon.2020.02.058

36. Leblanc, J. L. (2002). Rubber–filler interactions and rheological properties in filled compounds. *Progress in Polymer Science, 27*(4), 627-687. doi:https://doi.org/10.1016/S0079-6700(01)00040-5

37. Ananthapadmanabha, G. S., & Deshpande, V. (2018). Influence of aspect ratio of fillers on the properties of acrylonitrile butadiene styrene composites. *Journal of Applied Polymer Science, 135*(11), 46023. doi:https://doi.org/10.1002/app.46023

38. Supaphol, P., Harnsiri, W., & Junkasem, J. (2004). Effects of calcium carbonate and its purity on crystallization and melting behavior, mechanical properties, and processability of syndiotactic polypropylene. *Journal of Applied Polymer Science, 92*(1), 201-212. doi:https://doi.org/10.1002/app.13432

39. Turku, I., & Kärki, T. (2013). Research progress in wood-plastic nanocomposites: A review. *Journal of Thermoplastic Composite Materials, 27*(2), 180-204. doi:10.1177/0892705713486131

40. Sae-oui, P., Sirisinha, C., Thepsuwan, U., & Hatthapanit, K. (2006). Roles of silane coupling agents on properties of silica-filled polychloroprene. *European Polymer Journal, 42*(3), 479-486. doi:https://doi.org/10.1016/j.eurpolymj.2005.09.003

41. Surya, I., & Sinaga, R. (2019). Tensile and rheometric properties of calcium carbonate-filled natural rubber compounds without/with lauryl alcohol. *IOP Conference Series: Materials Science and Engineering, 505*(1), 012146. doi:10.1088/1757-899X/505/1/012146

42. Falini, G., Fermani, S., Reggi, M., Njegić Džakula, B., & Kralj, D. (2014). Evidence of structural variability among synthetic and biogenic vaterite. *Chemical Communications, 50*(97), 15370-15373. doi:10.1039/C4CC05054A

43. Xu, Y., Ye, J., Zhou, D., & Su, L. (2020). Research progress on applications of calcium derived from marine organisms. *Scientific Reports, 10*(1), 18425. doi:10.1038/s41598-020-75575-8

44. Chakoumakos, B. C., Pracheil, B. M., Koenigs, R. P., Bruch, R. M., & Feygenson, M. (2016). Empirically testing vaterite structural models using neutron diffraction and thermal analysis. *Scientific Reports, 6*(1), 36799. doi:10.1038/srep36799

45. Portugal, S. J., Bowen, J., & Riehl, C. (2018). A rare mineral, vaterite, acts as a shock absorber in the eggshell of a communally nesting bird. *Ibis, 160*(1), 173-178. doi:https://doi.org/10.1111/ibi.12527

46. Basfar, S., & Elkatatny, S. (2023). Micronized calcium carbonate to enhance water-based drilling fluid properties. *Scientific Reports, 13*(1), 18295. doi:10.1038/s41598-023-45776-y

47. Gaber, M. A. W. (2018). Characterizations of El Minia limestone for manufacturing paper filler and coating. *Egyptian Journal of Petroleum, 27*(4), 437-443. doi:https://doi.org/10.1016/j.ejpe.2017.07.007

48. Christy, A. G. (2017). A Review of the Structures of Vaterite: The Impossible, the Possible, and the Likely. *Crystal Growth & Design, 17*(6), 3567-3578. doi:10.1021/acs.cgd.7b00481

49. Kamhi, S. R. (1963). On the structure of vaterite CaCO3. *Acta Crystallographica, 16*(8), 770-772. doi:https://doi.org/10.1107/S0365110X63002000

50. Rodriguez-Blanco, J. D., Shaw, S., & Benning, L. G. (2011). The kinetics and mechanisms of amorphous calcium carbonate (ACC) crystallization to calcite, viavaterite. *Nanoscale, 3*(1), 265-271. doi:10.1039/C0NR00589D

51. Qi, R. J., & Zhu, Y. J. (2006). Microwave-assisted synthesis of calcium carbonate (vaterite) of various morphologies in water-ethylene glycol mixed solvents. *J Phys Chem B, 110*(16), 8302-8306. doi:10.1021/jp060939s

52. Ulkeryildiz, E., Kilic, S., & Ozdemir, E. (2016). Rice-like hollow nano-CaCO3 synthesis. *Journal of Crystal Growth, 450*, 174-180. doi:https://doi.org/10.1016/j.jcrysgro.2016.06.032

53. Myszka, B., Hurle, K., Zheng, K., Wolf, S. E., & Boccaccini, A. R. (2019). Mechanical improvement of calcium carbonate cements by in situ HEMA

polymerization during hardening. *Journal of Materials Chemistry B, 7*(21), 3403-3411. doi:10.1039/C9TB00237E

54. Tom, S., Jin, H.-E., Heo, K., & Lee, S.-W. (2016). Engineered phage films as scaffolds for CaCO3 biomineralization. *Nanoscale, 8*(34), 15696-15701. doi:10.1039/C6NR04322D
55. Woldetsadik, A. D., Sharma, S. K., Khapli, S., Jagannathan, R., & Magzoub, M. (2017). Hierarchically Porous Calcium Carbonate Scaffolds for Bone Tissue Engineering. *ACS Biomater Sci Eng, 3*(10), 2457-2469. doi:10.1021/acsbiomaterials.7b00301
56. Wei, M. C. T., Tran, C., Meredith, N., & Walsh, L. J. (2017). Effectiveness of implant surface debridement using particle beams at differing air pressures. *Clin Exp Dent Res, 3*(4), 148-153. doi:10.1002/cre2.74
57. Trushina, D. B., Bukreeva, T. V., Kovalchuk, M. V., & Antipina, M. N. (2014). $CaCO_3$ vaterite microparticles for biomedical and personal care applications. *Mater Sci Eng C Mater Biol Appl, 45*, 644-658. doi:10.1016/j.msec.2014.04.050
58. Brecevic, L., & Kralj, D. (2007). On Calcium Carbonates: From Fundamental Research to Application. *Croatica Chemica Acta, 80*, 467-484.
59. Xu, B., & Poduska, K. M. (2014). Linking crystal structure with temperature-sensitive vibrational modes in calcium carbonate minerals. *Physical Chemistry Chemical Physics, 16*(33), 17634-17639. doi:10.1039/C4CP01772B
60. Trushina, D. B., Bukreeva, T. V., & Antipina, M. N. (2016). Size-Controlled Synthesis of Vaterite Calcium Carbonate by the Mixing Method: Aiming for Nanosized Particles. *Crystal Growth & Design, 16*(3), 1311-1319. doi:10.1021/acs.cgd.5b01422
61. Dupont, L., Portemer, F., & late Michel Figlarz, t. (1997). Synthesis and study of a well crystallized CaCO3 vaterite showing a new habitus. *Journal of Materials Chemistry, 7*(5), 797-800. doi:10.1039/A607761G
62. Struktur und Fehlordnung des Vaterits*. (1969). *128*(3-6), 183-212. doi:doi:10.1524/zkri.1969.128.3-6.183
63. Wolf, G., Königsberger, E., Schmidt, H. G., Königsberger, L. C., & Gamsjäger, H. (2000). Thermodynamic Aspects of the Vaterite-Calcite Phase Transition.

Journal of Thermal Analysis and Calorimetry, 60(2), 463-472. doi:10.1023/A:1010114131577

64. Burgess, K. M. N., & Bryce, D. L. (2015). On the crystal structure of the vaterite polymorph of CaCO3: A calcium-43 solid-state NMR and computational assessment. *Solid State Nuclear Magnetic Resonance, 65*, 75-83. doi:https://doi.org/10.1016/j.ssnmr.2014.08.003
65. Won, Y.-H., Jang, H. S., Chung, D.-W., & Stanciu, L. A. (2010). Multifunctional calcium carbonate microparticles: Synthesis and biological applications. *Journal of Materials Chemistry, 20*(36), 7728-7733. doi:10.1039/C0JM01231A
66. Volodkin, D. V., Larionova, N. I., & Sukhorukov, G. B. (2004). Protein Encapsulation via Porous CaCO3 Microparticles Templating. *Biomacromolecules, 5*(5), 1962-1972. doi:10.1021/bm049669e
67. Beuvier, T., Calvignac, B., Delcroix, G. J.-R., Tran, M. K., Kodjikian, S., Delorme, N., et al. (2011). Synthesis of hollow vaterite CaCO3 microspheres in supercritical carbon dioxide medium. *Journal of Materials Chemistry, 21*(26), 9757-9761. doi:10.1039/C1JM10770D
68. Sun, R., Willhammar, T., Svensson Grape, E., Strømme, M., & Cheung, O. (2019). Mesoscale Transformation of Amorphous Calcium Carbonate to Porous Vaterite Microparticles with Morphology Control. *Crystal Growth & Design, 19*(9), 5075-5087. doi:10.1021/acs.cgd.9b00438
69. Hu, Q., Zhang, J., Teng, H., & Becker, U. (2012). Growth process and crystallographic properties of ammonia-induced vaterite. *American Mineralogist, 97*. doi:10.2138/?am.2012.3983
70. Yang, L.-f., Chu, D.-q., Sun, H.-l., & Ge, G. (2016). Room temperature synthesis of flower-like CaCO3 architectures. *New Journal of Chemistry, 40*(1), 571-577. doi:10.1039/C5NJ02141C
71. Ševčík, R., Viani, A., Machová, D., Lanzafame, G., Mancini, L., & Appavou, M.-S. (2019). Synthetic calcium carbonate improves the effectiveness of treatments with nanolime to contrast decay in highly porous limestone. *Scientific Reports, 9*(1), 15278. doi:10.1038/s41598-019-51836-z
72. Njegić-Dzakula, B., Falini, G., Brecević, L., Skoko, Z., & Kralj, D. (2010). Effects of initial supersaturation on spontaneous precipitation of calcium carbonate in

the presence of charged poly-L-amino acids. *J Colloid Interface Sci, 343*(2), 553-563. doi:10.1016/j.jcis.2009.12.010

73. Gehrke, N., Cölfen, H., Pinna, N., Antonietti, M., & Nassif, N. (2005). Superstructures of Calcium Carbonate Crystals by Oriented Attachment. *Crystal Growth & Design, 5*(4), 1317-1319. doi:10.1021/cg050051d
74. Plummer, L. N., & Busenberg, E. (1982). The solubilities of calcite, aragonite and vaterite in CO2-H2O solutions between 0 and 90°C, and an evaluation of the aqueous model for the system CaCO3-CO2-H2O. *Geochimica et Cosmochimica Acta, 46*(6), 1011-1040. doi:https://doi.org/10.1016/0016-7037(82)90056-4
75. Parkin, S. J., Vogel, R., Persson, M., Funk, M., Loke, V. L. Y., Nieminen, T. A., et al. (2009). Highly birefringent vaterite microspheres: production, characterization and applications for optical micromanipulation. *Optics Express, 17*(24), 21944-21955. doi:10.1364/OE.17.021944
76. Manoli, F., & Dalas, E. (2000). Spontaneous precipitation of calcium carbonate in the presence of ethanol, isopropanol and diethylene glycol. *Journal of Crystal Growth, 218*(2), 359-364. doi:https://doi.org/10.1016/S0022-0248(00)00560-1
77. Udrea, I., Capat, C., Olaru, E. A., Isopescu, R., Mihai, M., Mateescu, C. D., et al. (2012). Vaterite Synthesis via Gas–Liquid Route under Controlled pH Conditions. *Industrial & Engineering Chemistry Research, 51*(24), 8185-8193. doi:10.1021/ie202221m
78. Song, X., Cao, Y., Bu, X., & Luo, X. (2021). Porous vaterite and cubic calcite aggregated calcium carbonate obtained from steamed ammonia liquid waste for Cu2+ heavy metal ions removal by adsorption process. *Applied Surface Science, 536*, 147958. doi:https://doi.org/10.1016/j.apsusc.2020.147958
79. Trushina, D. B., Borodina, T. N., Belyakov, S., & Antipina, M. N. (2022). Calcium carbonate vaterite particles for drug delivery: Advances and challenges. *Materials Today Advances, 14*, 100214. doi:https://doi.org/10.1016/j.mtadv.2022.100214
80. Binevski, P. V., Balabushevich, N. G., Uvarova, V. I., Vikulina, A. S., & Volodkin, D. (2019). Bio-friendly encapsulation of superoxide dismutase into vaterite CaCO3 crystals. Enzyme activity, release mechanism, and perspectives for

ophthalmology. *Colloids and Surfaces B: Biointerfaces, 181*, 437-449. doi:https://doi.org/10.1016/j.colsurfb.2019.05.077

81. Ulian, G., & Valdrè, G. (2023). The effect of long-range interactions on the infrared and Raman spectra of aragonite (CaCO3, Pmcn) up to 25 GPa. *Scientific Reports, 13*(1), 2725. doi:10.1038/s41598-023-29783-7
82. Zhou, G.-T., Yao, Q.-Z., Ni, J., & Jin, G. (2009). Formation of aragonite mesocrystals and implication for biomineralization. *94*(2-3), 293-302. doi:doi:10.2138/am.2009.2957
83. Niu, T., Xu, J., & Huang, J. (2014). Growth of aragonite phase calcium carbonate on the surface of a titania-modified filter paper. *CrystEngComm, 16*(12), 2424-2431. doi:10.1039/C3CE42322K
84. Ramakrishna, C., Thenepalli, T., Huh, J.-H., & Ahn, J. W. (2016). Precipitated Calcium Carbonate Synthesis by Simultaneous Injection to Produce Nano Whisker Aragonite. *J. Korean Ceram. Soc, 53*(2), 222-226. doi:10.4191/kcers.2016.53.2.222
85. Sinkankas, J. (1964). *Mineralogy for Amateurs*: Van Nostrand.
86. Du, X., Wu, M., Tse, J. S., & Pan, Y. (2018). Structures and Transport Properties of CaCO3 Melts under Earth's Mantle Conditions. *ACS Earth and Space Chemistry, 2*(1), 1-8. doi:10.1021/acsearthspacechem.7b00100
87. McLaren, S. J. (2011). Aragonite. In D. Hopley (Ed.), *Encyclopedia of Modern Coral Reefs: Structure, Form and Process* (pp. 47-47). Dordrecht: Springer Netherlands.
88. Hassani, L. N., Buchtová, N., Cordonnier, T., Ramalapa, B., Garcion, E., Hindre, F., et al. (2022). Chapter 1 - Hybrid systems in bio-encapsulation. In G. Castro, A. Nadda, T. Nguyen, S. Sharma, & R. Gupta (Eds.), *Smart Nanomaterials for Bioencapsulation* (pp. 1-23): Elsevier.
89. Liendo, F., Arduino, M., Deorsola, F. A., & Bensaid, S. (2022). Factors controlling and influencing polymorphism, morphology and size of calcium carbonate synthesized through the carbonation route: A review. *Powder Technology, 398*, 117050. doi:https://doi.org/10.1016/j.powtec.2021.117050
90. Cai, G., Phillips, A. E., Tucker, M. G., & Dove, M. T. (2020). Neutron scattering study of the orientational disorder and phase transitions in barium carbonate.

Journal of Physics: Condensed Matter, 32(37), 374014. doi:10.1088/1361-648X/ab8cde

91. Beck, R., & Andreassen, J.-P. (2010). The onset of spherulitic growth in crystallization of calcium carbonate. *Journal of Crystal Growth, 312*(15), 2226-2238. doi:https://doi.org/10.1016/j.jcrysgro.2010.04.037
92. Guo, X., Liu, L., Wang, W., Zhang, J., Wang, Y., & Yu, S.-H. (2011). Controlled crystallization of hierarchical and porous calcium carbonate crystals using polypeptide type block copolymer as crystal growth modifier in a mixed solution. *CrystEngComm, 13*(6), 2054-2061. doi:10.1039/C0CE00202J
93. Kezuka, Y., Kawai, K., Eguchi, K., & Tajika, M. (2017). Fabrication of Single-Crystalline Calcite Needle-Like Particles Using the Aragonite–Calcite Phase Transition. *Minerals, 7*(8). Retrieved from doi:10.3390/min7080133
94. Thriveni, T., Nam, S. Y., Ahn, J.-W., & Um, N. (2014). Enhancement of arsenic removal efficiency from mining waste water by accelerated carbonation. *IMPC 2014 - 27th International Mineral Processing Congress*.
95. Haldar, S. K. (2020). Chapter 1 - Minerals and rocks. In S. K. Haldar (Ed.), *Introduction to Mineralogy and Petrology (Second Edition)* (pp. 1-51). Oxford: Elsevier.
96. Zeynep, E. Y., Antoine, D., Brice, C., Frank, B., & Christine, J. (2015). Double hydrophilic polyphosphoester containing copolymers as efficient templating agents for calcium carbonate microparticles. *Journal of Materials Chemistry B, 3*(36), 7227-7236. doi:10.1039/C5TB00887E
97. Kawano, J., Miyake, A., Shimobayashi, N., & Kitamura, M. (2009). Molecular dynamics simulation of the phase transition between calcite and CaCO(3)-II. *J Phys Condens Matter, 21*(27), 275403. doi:10.1088/0953-8984/21/27/275403
98. Ogino, T., Suzuki, T., & Sawada, K. (1987). The formation and transformation mechanism of calcium carbonate in water. *Geochimica et Cosmochimica Acta, 51*(10), 2757-2767. doi:https://doi.org/10.1016/0016-7037(87)90155-4
99. Njegić-Džakula, B., Falini, G., Brečević, L., Skoko, Ž., & Kralj, D. (2010). Effects of initial supersaturation on spontaneous precipitation of calcium carbonate in the presence of charged poly-l-amino acids. *Journal of Colloid and Interface Science, 343*(2), 553-563. doi:https://doi.org/10.1016/j.jcis.2009.12.010

100. Svenskaya, Y. I., Fattah, H., Zakharevich, A. M., Gorin, D. A., Sukhorukov, G. B., & Parakhonskiy, B. V. (2016). Ultrasonically assisted fabrication of vaterite submicron-sized carriers. *Advanced Powder Technology, 27*(2), 618-624. doi:https://doi.org/10.1016/j.apt.2016.02.014

101. Hou, W., & Feng, Q. (2006). Morphology and formation mechanism of vaterite particles grown in glycine-containing aqueous solutions. *Materials Science and Engineering: C, 26*(4), 644-647. doi:https://doi.org/10.1016/j.msec.2005.09.098

102. Beck, R., & Andreassen, J.-P. (2010). Spherulitic Growth of Calcium Carbonate. *Crystal Growth & Design, 10*(7), 2934-2947. doi:10.1021/cg901460g

103. Myszka, B., Schüßler, M., Hurle, K., Demmert, B., Detsch, R., Boccaccini, A. R., et al. (2019). Phase-specific bioactivity and altered Ostwald ripening pathways of calcium carbonate polymorphs in simulated body fluid. *RSC Advances, 9*(32), 18232-18244. doi:10.1039/C9RA01473J

104. Cherkas, O., Beuvier, T., Breiby, D. W., Chushkin, Y., Zontone, F., & Gibaud, A. (2017). Direct Observation of Microparticle Porosity Changes in Solid-State Vaterite to Calcite Transformation by Coherent X-ray Diffraction Imaging. *Crystal Growth & Design, 17*(8), 4183-4188. doi:10.1021/acs.cgd.7b00476

105. Prah, J., Maček, J., & Dražič, G. (2011). Precipitation of calcium carbonate from a calcium acetate and ammonium carbamate batch system. *Journal of Crystal Growth, 324*(1), 229-234. doi:https://doi.org/10.1016/j.jcrysgro.2011.03.020

106. Bots, P., Benning, L. G., Rodriguez-Blanco, J.-D., Roncal-Herrero, T., & Shaw, S. (2012). Mechanistic Insights into the Crystallization of Amorphous Calcium Carbonate (ACC). *Crystal Growth & Design, 12*(7), 3806-3814. doi:10.1021/cg300676b

107. Lassin, A., André, L., Devau, N., Lach, A., Beuvier, T., Gibaud, A., et al. (2018). Dynamics of calcium carbonate formation: Geochemical modeling of a two-step mechanism. *Geochimica et Cosmochimica Acta, 240*, 236-254. doi:https://doi.org/10.1016/j.gca.2018.08.033

108. Flaten, E. M., Seiersten, M., & Andreassen, J.-P. (2010). Induction time studies of calcium carbonate in ethylene glycol and water. *Chemical Engineering Research and Design, 88*(12), 1659-1668. doi:https://doi.org/10.1016/j.cherd.2010.01.028

109. Li, S., Yu, L., Geng, F., Shi, L., Zheng, L., & Yuan, S. (2010). Facile preparation of diversified patterns of calcium carbonate in the presence of DTAB. *Journal of Crystal Growth, 312*(10), 1766-1773. doi:https://doi.org/10.1016/j.jcrysgro.2010.02.019

110. Yu, J. G., Guo, H., Davis, S. A., & Mann, S. (2006). Fabrication of Hollow Inorganic Microspheres by Chemically Induced Self-Transformation. *Advanced Functional Materials, 16*(15), 2035-2041. doi:https://doi.org/10.1002/adfm.200600552

111. Barhoum, A., Ibrahim, H. M., Hassanein, T. F., Hill, G., Reniers, F., Dufour, T., et al. (2014). Preparation and characterization of ultra-hydrophobic calcium carbonate nanoparticles. *IOP Conference Series: Materials Science and Engineering, 64*(1), 012037. doi:10.1088/1757-899X/64/1/012037

112. Lin, Y., & Chan, C. M. (2012). 3 - Calcium carbonate nanocomposites. In F. Gao (Ed.), *Advances in Polymer Nanocomposites* (pp. 55-90): Woodhead Publishing.

113. Wadeesirisak, K., Castano, S., Berthelot, K., Vaysse, L., Bonfils, F., Peruch, F., et al. (2017). Rubber particle proteins REF1 and SRPP1 interact differently with native lipids extracted from Hevea brasiliensis latex. *Biochimica et Biophysica Acta (BBA) - Biomembranes, 1859*(2), 201-210. doi:https://doi.org/10.1016/j.bbamem.2016.11.010

114. Mohapatra, S., & Nando, G. B. (2013). Chemical Modification of Natural Rubber in the Latex Stage by Grafting Cardanol, a Waste from the Cashew Industry and a Renewable Resource. *Industrial & Engineering Chemistry Research, 52*(17), 5951-5957. doi:10.1021/ie400195v

115. Smitthipong, W., Suethao, S., Shah, D., & Vollrath, F. (2016). Interesting green elastomeric composites: Silk textile reinforced natural rubber. *Polymer Testing, 55*, 17-24. doi:https://doi.org/10.1016/j.polymertesting.2016.08.007

116. Loos, K., Aydogdu, A. B., Lion, A., Johlitz, M., & Calipel, J. (2021). Strain-induced crystallisation in natural rubber: a thermodynamically consistent model of the material behaviour using a serial connection of phases. *Continuum Mechanics and Thermodynamics, 33*(4), 1107-1140. doi:10.1007/s00161-020-00950-9

117. Persson, B. N. J., Albohr, O., Heinrich, G., & Ueba, H. (2005). Crack propagation in rubber-like materials. *Journal of Physics: Condensed Matter, 17*(44), R1071. doi:10.1088/0953-8984/17/44/R01

118. Toki, S., Fujimaki, T., & Okuyama, M. (2000). Strain-induced crystallization of natural rubber as detected real-time by wide-angle X-ray diffraction technique. *Polymer, 41*(14), 5423-5429. doi:https://doi.org/10.1016/S0032-3861(99)00724-7

119. Alarifi, I. M. (2022). Chapter 4 - Synthetic rubber. In I. M. Alarifi (Ed.), *Synthetic Engineering Materials and Nanotechnology* (pp. 79-100): Elsevier.

120. Rasid, H. M., Azhar, N. H. A., & Yusoff, S. F. M. (2017). Physicochemical properties of liquid natural rubber bearing fluoro groups for hydrophobic surfaces. *Journal of Polymer Research, 24*(7), 106. doi:10.1007/s10965-017-1270-z

121. Wang, T., Gui, H.-X., Zhang, W.-F., Zhang, K.-X., Yu, W.-Q., Li, Y.-M., et al. (2015). Novel nonammonia preservative for concentrated natural rubber latex. *Journal of Applied Polymer Science, 132*(15). doi:https://doi.org/10.1002/app.41749

122. Dafader, N. C., Haque, M. E., Akhtar, F., Ahmad, M. U., & Utama, M. (1996). Evaluation of the Properties of Natural Rubber Latex Concentrated by Creaming Method for Gamma Ray Irradiation. *Journal of Macromolecular Science, Part A, 33*(sup2), 73-81. doi:10.1080/10601329608020361

123. George, N., Venugopal, B., John, H., Mathiazhagan, A., & Joseph, R. (2019). Nanosilica decorated multiwalled carbon nanotubes (CS hybrids) in natural rubber latex. *Polymer, 161*, 170-180. doi:https://doi.org/10.1016/j.polymer.2018.12.014

124. Fisher, H. L. (1939). VULCANIZATION OF RUBBER Vulcanization of Rubber. *Industrial & Engineering Chemistry, 31*(11), 1381-1389. doi:10.1021/ie50359a015

125. Kruželák, J., Kvasničáková, A., & Hudec, I. (2020). Peroxide curing systems applied for cross-linking of rubber compounds based on SBR. *Advanced Industrial and Engineering Polymer Research, 3*(3), 120-128. doi:https://doi.org/10.1016/j.aiepr.2020.05.001

126. Kruželák, J., Sýkora, R., & Hudec, I. (2016). Sulphur and peroxide vulcanisation of rubber compounds – overview. *70*(12), 1533-1555. doi:doi:10.1515/chempap-2016-0093

127. Isayev, A. I. (2014). 16 - Recycling of natural and synthetic isoprene rubbers. In S. Kohjiya & Y. Ikeda (Eds.), *Chemistry, Manufacture and Applications of Natural Rubber* (pp. 395-435): Woodhead Publishing.

128. Gilmour, M. E., & Lavers, J. L. (2021). Latex balloons do not degrade uniformly in freshwater, marine and composting environments. *Journal of Hazardous Materials, 403*, 123629. doi:https://doi.org/10.1016/j.jhazmat.2020.123629

129. Sarih, N. M., Dzulkafly, N. S., Maher, S., & Rashid, A. A. (2022). Wearable Natural Rubber Latex Gloves with Curcumin for Torn Glove Detection in Clinical Settings. *Polymers, 14*(15). Retrieved from doi:10.3390/polym14153048

130. Bin Samsuri, A., & Abdullahi, A. A. (2017). Degradation of Natural Rubber and Synthetic Elastomers *Reference Module in Materials Science and Materials Engineering*: Elsevier.

131. Ikeda, Y., Yasuda, Y., Ohashi, T., Yokohama, H., Minoda, S., Kobayashi, H., et al. (2015). Dinuclear Bridging Bidentate Zinc/Stearate Complex in Sulfur Cross-Linking of Rubber. *Macromolecules, 48*(3), 462-475. doi:10.1021/ma502063m

132. Ciullo, P. A., & Hewitt, N. (1999). COMPOUNDING MATERIALS. In P. A. Ciullo & N. Hewitt (Eds.), *The Rubber Formulary* (pp. 4-49). Norwich, NY: William Andrew Publishing.

133. Mohammad, A., & Simon, G. P. (2006). 12 - Rubber-clay nanocomposites. In Y.-W. Mai & Z.-Z. Yu (Eds.), *Polymer Nanocomposites* (pp. 297-325): Woodhead Publishing.

134. Chandrasekaran, V. C. (2007). 2 - Brief Notes on Compounding Ingredients. In V. C. Chandrasekaran (Ed.), *Essential Rubber Formulary* (pp. 5-7). Norwich, NY: William Andrew Publishing.

135. Coran, A. Y. (2013). Chapter 7 - Vulcanization. In J. E. Mark, B. Erman, & C. M. Roland (Eds.), *The Science and Technology of Rubber (Fourth Edition)* (pp. 337-381). Boston: Academic Press.

136. Noordermeer, J. W. M. (2015). Vulcanization. In S. Kobayashi & K. Müllen (Eds.), *Encyclopedia of Polymeric Nanomaterials* (pp. 2577-2590). Berlin, Heidelberg: Springer Berlin Heidelberg.

137. Robertson, C. G., & Hardman, N. J. (2021). Nature of Carbon Black Reinforcement of Rubber: Perspective on the Original Polymer Nanocomposite. *Polymers, 13*(4). Retrieved from doi:10.3390/polym13040538

138. Fan, C., Liu, Y., Zhu, J., Wang, L., Chen, X., Zhang, S., et al. (2019). Understanding the structural transformation of carbon black from solid spheres to hollow polyhedra during high temperature treatment. *RSC Advances, 9*(51), 29779-29783. doi:10.1039/C9RA06828G

139. Azura, A. R., & Leow, S. L. (2019). Effect of carbon black loading on mechanical, conductivity and ageing properties of Natural Rubber composites. *Materials Today: Proceedings, 17*, 1056-1063. doi:https://doi.org/10.1016/j.matpr.2019.06.512

140. da Costa, H. M., Ramos, V. D., Visconte, L. L. Y., & Furtado, C. R. G. (2007). Design and analysis of single-factor experiments: Analysis of variance of the effect of rice husk ash and commercial fillers in NR compounds. *Polymer Bulletin, 58*(3), 597-610. doi:10.1007/s00289-006-0684-2

141. Baan, R. A. (2007). Carcinogenic Hazards from Inhaled Carbon Black, Titanium Dioxide, and Talc not Containing Asbestos or Asbestiform Fibers: Recent Evaluations by an IARC Monographs Working Group. *Inhalation Toxicology, 19*(sup1), 213-228. doi:10.1080/08958370701497903

142. Phumnok, E., Khongprom, P., & Ratanawilai, S. (2022). Preparation of Natural Rubber Composites with High Silica Contents Using a Wet Mixing Process. *ACS Omega, 7*(10), 8364-8376. doi:10.1021/acsomega.1c05848

143. Zheng, J., Han, D., Ye, X., Wu, X., Wu, Y., Wang, Y., et al. (2018). Chemical and physical interaction between silane coupling agent with long arms and silica and its effect on silica/natural rubber composites. *Polymer, 135*, 200-210. doi:https://doi.org/10.1016/j.polymer.2017.12.010

144. Campbell, F. C. (2004). Chapter 1 - Introduction to Composite Materials and Processes: Unique Materials that Require Unique Processes. In F. C. Campbell

(Ed.), *Manufacturing Processes for Advanced Composites* (pp. 1-37). Amsterdam: Elsevier Science.

145. Ren, X., & Sancaktar, E. (2019). Use of fly ash as eco-friendly filler in synthetic rubber for tire applications. *Journal of Cleaner Production, 206*, 374-382. doi:https://doi.org/10.1016/j.jclepro.2018.09.202
146. Kan, T., Strezov, V., & Evans, T. (2017). Fuel production from pyrolysis of natural and synthetic rubbers. *Fuel, 191*, 403-410. doi:https://doi.org/10.1016/j.fuel.2016.11.100
147. Jiang, L., Lam, Y. C., Tam, K. C., Chua, T. H., Sim, G. W., & Ang, L. S. (2005). Strengthening acrylonitrile-butadiene-styrene (ABS) with nano-sized and micron-sized calcium carbonate. *Polymer*, *46*(1), 243-252. doi:https://doi.org/10.1016/j.polymer.2004.11.001
148. Jin, F.-L., & Park, S.-J. (2008). Thermo-mechanical behaviors of butadiene rubber reinforced with nano-sized calcium carbonate. *Materials Science and Engineering: A*, *478*(1), 406-408. doi:https://doi.org/10.1016/j.msea.2007.05.102
149. Azrem, A. A., Noriman, N. Z., & Razif, M. N. (2014). The Effects of Carbon Black and Calcium Carbonate as a Filler on Cure Characteristic and Physical Properties of SBR/CRr Blends. *Key Engineering Materials, 594-595*, 867-871. doi:10.4028/www.scientific.net/KEM.594-595.867
150. Longkaew, K., Gibaud, A., Tessanan, W., Daniel, P., & Phinyocheep, P. (2023). Spherical CaCO3: Synthesis, Characterization, Surface Modification and Efficacy as a Reinforcing Filler in Natural Rubber Composites. *Polymers, 15*(21). Retrieved from doi:10.3390/polym15214287
151. Blekas, G., Tsimidou, M., & Boskou, D. (2006). Olive Oil Composition.
152. Ikeda, Y., Phakkeeree, T., Junkong, P., Yokohama, H., Phinyocheep, P., Kitano, R., et al. (2017). Reinforcing biofiller “Lignin” for high performance green natural rubber nanocomposites. *RSC Advances, 7*(9), 5222-5231. doi:10.1039/C6RA26359C
153. Valentín, J. L., Carretero-González, J., Mora-Barrantes, I., Chassé, W., & Saalwächter, K. (2008). Uncertainties in the Determination of Cross-Link

Density by Equilibrium Swelling Experiments in Natural Rubber. *Macromolecules, 41*(13), 4717-4729. doi:10.1021/ma8005087

154. Olsson, C., & Swenson, J. (2020). Structural Comparison between Sucrose and Trehalose in Aqueous Solution. *The Journal of Physical Chemistry B, 124*(15), 3074-3082. doi:10.1021/acs.jpcb.9b09701

155. Labgairi, K., Jourani, A., & Kaddami, M. (2011). An isothermal (30°C) study of heterogeneous equilibria in the sucrose (C12H22O11)–calcium hydroxide (Ca(OH)2)–water system. *Fluid Phase Equilibria, 307*(1), 100-103. doi:https://doi.org/10.1016/j.fluid.2011.03.009

156. Song, Y. H., Park, J. C., Kim, C. S., Hwang, D. S., Cha, H. J., & Seo, J. H. (2018). Sucrose-calcium Complexation for the Durable Biomass Pellet. *Biotechnology and Bioprocess Engineering, 23*(3), 341-348. doi:10.1007/s12257-018-0118-7

157. Evans, J. S. O., & Evans, I. R. (2021). Structure Analysis from Powder Diffraction Data: Rietveld Refinement in Excel. *Journal of Chemical Education, 98*(2), 495-505. doi:10.1021/acs.jchemed.0c01016

158. Arefi, M. R., & Rezaei-Zarchi, S. (2012). Synthesis of Zinc Oxide Nanoparticles and Their Effect on the Compressive Strength and Setting Time of Self-Compacted Concrete Paste as Cementitious Composites. *International Journal of Molecular Sciences, 13*(4), 4340-4350. Retrieved from doi:10.3390/ijms13044340

159. Ungár, T., Gubicza, J., Ribárik, G., Pantea, C., & Zerda, T. W. (2002). Microstructure of carbon blacks determined by X-ray diffraction profile analysis. *Carbon, 40*(6), 929-937. doi:https://doi.org/10.1016/S0008-6223(01)00224-X

160. Khan, I., Saeed, K., & Khan, I. (2019). Nanoparticles: Properties, applications and toxicities. *Arabian Journal of Chemistry, 12*(7), 908-931. doi:https://doi.org/10.1016/j.arabjc.2017.05.011

161. Roy, K., Debnath, S. C., Pongwisuthiruchte, A., & Potiyaraj, P. (2021). Recent advances of natural fibers based green rubber composites: Properties, current status, and future perspectives. *Journal of Applied Polymer Science, 138*(35), 50866. doi:https://doi.org/10.1002/app.50866

162. Singh, M., & Azahari, B. (2004). *THE EFFECT OF CALCIUM CARBONATE ON THE MECHANICAL PROPERTIES AND MORPHOLOGY OF NATURAL RUBBER LATEX FILMS*.

163. Gao, M., Zheng, F., Xu, J., Zhang, S., Bhosale, S. S., Gu, J., et al. (2019). Surface modification of nano-sized carbon black for reinforcement of rubber. *8*(1), 405-414. doi:doi:10.1515/ntrev-2019-0036

APPENDIX

PUBLICATION #1

Advanced Powder Technology 34 (2023) 103924

Contents lists available at ScienceDirect

Advanced Powder Technology

journal homepage: www.elsevier.com/locate/apt

Using sucrose to prepare submicrometric $CaCO_3$ vaterite particles stable in natural rubber

Khansinee Longkaew [a,b], Wasan Tessanan [a], Philippe Daniel [b], Pranee Phinyocheep [a,*], Alain Gibaud [b]

[a] Department of Chemistry, Faculty of Science, Mahidol University, Rama VI Road, Phayatai, Bangkok 10400, Thailand
[b] Institut des Molécules et Matériaux du Mans, UMR CNRS 6283, Avenue Olivier Messiaen, 72085 Le Mans Cedex 9, France

ARTICLE INFO

Article history:
Received 20 August 2022
Received in revised form 18 November 2022
Accepted 16 December 2022

Keywords:
Calcium carbonate
Calcite
Natural rubber
Sucrose
Vaterite

ABSTRACT

Vaterite with submicrometer particles was successfully synthesized by adding sucrose at certain amounts (x = 0–50 %) to the aqueous solutions of ammonium carbonate ($(NH_4)_2CO_3$) and calcium chloride ($CaCl_2$) precursors prior to the precipitation. Typical polymorphic phases and morphological shapes of $CaCO_3$ particles were characterized by XRD, FTIR, Raman spectroscopy, SEM, and TEM techniques. It is evident that when the sucrose concentration is increased, the average particle size of $CaCO_3$ is decreased which was reduced from 0.81 μm at x = 0 % to 0.42 μm at x = 50 %. Simultaneously, the % quantitative of the vaterite phase was increased from 92.52 % at x = 0 % to 99.10 % at x = 50 %. In addition, the regular round shape of the vaterite particles was evidenced by SEM and TEM images. Generally, commercial $CaCO_3$ which is a calcite polymorph with cubic form was used as an extender without reinforcing efficiency in rubber material. It is therefore challenging to incorporate the obtained round shape vaterite in natural rubber (NR) latex and it is interesting to find a stable vaterite $CaCO_3$ polymorph in the NR, evidenced by XRD and FTIR results. The negative charges on the surface of NR particles were proposed to play an important role to stabilize the vaterite particles.

© 2022 The Society of Powder Technology Japan. Published by Elsevier BV and The Society of Powder Technology Japan. All rights reserved.

1. Introduction

Calcium carbonate ($CaCO_3$) is one of the abundant mineral materials which exist in nature (e.g., crustaceans [1], fish organs [2] or bird eggs [3] and limestone [4]) and it can be also obtained by synthetic method [5,6]. $CaCO_3$ is widely used in various industrial fields (e.g., construction [7], medical treatments such as bone cement [8], dental implants [9] and scaffolds [10,11] due to its simple synthesis, no toxicological concerns, biocompatibility, high surface area and inexpensive cost [12]. Moreover, $CaCO_3$ has a strong demand for use as abrasives, absorbents and fillers in papers, plastics, rubbers, paints and adhesives with the aim to improve the rheology and mechanical properties of the products [13–15]. Generally, $CaCO_3$ has six polymorphs; amorphous calcium carbonate (ACC), calcium carbonate monohydrate (MCC), calcium carbonate hexahydrate (ikaite), vaterite, aragonite and calcite [16]. According to thermodynamics, calcite is the most stable phase among the other polymorphs but vaterite is kinetically favored [5,6]. $CaCO_3$ exhibits different morphological shapes depending on the type of polymorph. Vaterite shows a hexagonal, a spherulitic or a framboid morphology. Aragonite displays orthorhombic or needle-liked shape and calcite has a typical trigonal morphology [17–19]. Nevertheless, these morphologies and shapes can be changed by altering the condition and reaction methods [20,21].

Vaterite is a thermodynamically metastable phase of $CaCO_3$. In the precipitation, the primary factors influencing vaterite formation are supersaturation, temperature, stirring rate and seed crystals. However, additives, mixed solvent composition and pH are found as secondary factors [5,6]. The vaterite phase can easily transform or recrystallize into a more stable phase in water such as calcite or aragonite due to its higher solubility and greater hydrophilicity [22–24]. The spherical shape, the porous structure and the high surface area of vaterite confer to this polymorph a real advantage over calcite and aragonite in terms of biomedical application [5,6]. This polymorphic $CaCO_3$ form has attracted considerable attention for use in personal care and biomedical products such as drug delivery [25], encapsulation of proteins [26], enzymes [27], DNA and growth factors [28] etc. Besides varying the synthesis factors mentioned above, many approaches have been developed to control the particle size, morphology and polymorphs of $CaCO_3$ for optimal use. Generally, the suitable temperature for synthesizing vaterite is 25–50 °C [29]. Different additives added such as polymers [30,31], surfactants [32,33] and mixed solvents [34,35]

* Corresponding author.
E-mail address: pranee.phi@mahidol.ac.th (P. Phinyocheep).

https://doi.org/10.1016/j.apt.2022.103924
0921-8831/© 2022 The Society of Powder Technology Japan. Published by Elsevier BV and The Society of Powder Technology Japan. All rights reserved.

can stabilize the vaterite phase crystallization. H. Tang et al. studied the influence of polyelectrolyte poly-(sodium4-styrene-sulfate) (PSSS) copolymer as an additive on morphogenesis and phase changes of $CaCO_3$ [34]. In the presence of PSSS, most rhombohedral calcite particles disappeared and a large number of spherical aggregates were produced with the smallest $CaCO_3$ spherical particles. PSSS copolymer would inhibit the precipitation of calcite by absorbing on the surface of Ca^{2+} ions and prevent further growth of particles. D. B. Trushina et al. added polyol additives; ethylene glycol, glycerol (EG) and erythritol bearing two, three and four hydroxyl groups, respectively in the mixing system [36]. The smallest particle size from 1.1 μm to 350 nm was performed by EG 83.3 % V/V. As a result, it can be mentioned that hydroxyl groups of the additives and viscosity of the mixing system were the main factors that affected the promotion of vaterite formation together with a reduction of the vaterite particle size. In the case of erythritol and glycerol, there is a limitation of solubility in water at high additives concentrations. Their observed data confirm that the role of a higher viscosity decreases the size of forming vaterite by favoring the nucleation process due to the limited diffusion of Ca^{2+} ions. Promising results of using sucrose as an aqueous medium also showed a significant effect of its hydroxyl groups on particle size and polymorphs of $CaCO_3$. L. P. Villarejo et al. used calcium nitrate tetrahydrate [$Ca(NO_3)_2{\cdot}4H_2O$ and sodium bicarbonate ($NaHCO_3$) as reactants and sucrose as an additive in the mixing system [37]. Increasing the sucrose content up to 67 % can promote a high percentage of vaterite having an irregular shape and a particle size in the range of 0.5 -1.0 μm.

Although various works on the control of morphology have been reported, it is still challenging to stabilize and synthesize vaterite with small particle sizes in the range of submicrometer to nanometer and explore its utilization. Indeed, it has been shown that reducing the particle size of fillers in the submicron range is necessary to increase the mechanical properties of filled polymeric materials such as for instance natural rubber (NR) [38]. NR is one of the important elastomers with the chemical structure *cis*-1,4 polyisoprene, obtained from the rubber tree: *Hevea brasiliensis* [39]. Freshly collected NR latex tapped from the rubber tree is in the colloidal form which is stabilized by negative charges surrounded on the surface of the rubber particles [40]. The negative charge distributed on the surface of the NR particles is the key parameter of the rubber colloidal stability [41]. Hence, ammonia solution is commonly added to maintain the negative charges for preservation of NR colloidal particles in latex for commercial [42]. To prepare rubber products especially rubber tyres, NR has to be mixed with crosslinking agents and fillers to improve its mechanical properties [43]. Many fillers can potentially improve rubber's mechanical properties such as carbon black, precipitated silica (SiO_2) and $CaCO_3$ [43–45]. Among many types of fillers, $CaCO_3$ is categorized as a semi-reinforcing filler or non-reinforcing filler due to its particle size larger than 100 nm which has not the capability to be a reinforcing filler. In the use of fillers, particle size, surface area and shape of filler are the most important factors in reinforcing efficiency [44,46]. It was found that the spherical-shaped $CaCO_3$ provided the most mechanical properties of NR compared to the chain-shaped or the cube-shaped $CaCO_3$ due to its high specific surface area compared to other shapes [44]. Filler with particle size smaller than 100 nm can be classified to be able to reinforce elastomer resulting from a greater polymer-filler interaction [47,48]. This causes $CaCO_3$ to be merely used as processing aids, or mechanical modifiers in rubber products. However, the cost and processability of some applications are the greatest concerns, so $CaCO_3$ remains a good option. Generally, the loading percentage of $CaCO_3$ in rubber was in the range of 5–50 % depending on the size of the fillers [38]. It was also reported that using $CaCO_3$ of less than 1 μm particle size required 10–50 wt% to have comparable improved mechanical properties of the rubber composites to the nanosized (1–100 nm) $CaCO_3$ using only 5–10 wt%. It is therefore still challenging to further study the incorporation of submicrometer size $CaCO_3$ with spherical shape in the rubber composite. Moreover, it has not been studied whether $CaCO_3$ maintains the spherical vaterite form in NR or not. Hence, reducing the particle size of $CaCO_3$ and stabilizing the spheroidal vaterite form in NR was the purpose of this challenging study.

In this paper, we report a simple synthesis route for vaterite precipitation with sub-micrometer particle size by adding sucrose at different concentrations to the aqueous solutions of the initial precursors. The effect of sucrose concentrations on particle size, morphology and polymorphs was examined by SEM, TEM, XRD, FTIR and Raman spectroscopy. Furthermore, to the best of our knowledge, there is no literature reporting incorporating vaterite as a filler in natural rubber (NR). Therefore, the prepared vaterite $CaCO_3$ polymorph was explored for the first time its stability in NR latex.

2. Experimental section

2.1. Materials

Calcium chloride dihydrate ($CaCl_2{\cdot}2H_2O$) and ammonium carbonate ($(NH_4)_2CO_3$) were used as the reagents for $CaCO_3$ precipitation. These chemical reagents of analytical grade were purchased from Acros-Organics. Sucrose in solid form was obtained from commercial sugar (Pulverent Sugar Poedersuiker, Massy, France). NR latex with 60 % dried rubber contents (DRC), stabilized with 0.7 % by weight ammonia solution was supplied by Thai Rubber Latex Co. Ltd., Thailand.

2.2. Submicrometric $CaCO_3$ synthesis

In a typical $CaCO_3$ synthesis, sucrose at concentrations varying from 0,10, 20, 30, 40, and 50 wt% dissolved in deionized water was used. The maximum concentration was limited to 50 wt% because the viscosity of the solutions drastically increased with the sucrose content and was therefore limiting the mixing. $CaCl_2{\cdot}2H_2O$ and $(NH_4)_2CO_3$ reagents were dissolved at a concentration of 1 M in two separate glass beakers each of them containing sucrose at a given concentration at 25 ± 1 °C. The reactants dissolved in sucrose solution were rapidly mixed in a commercial blender (KENWOOD brand SB327 at a mixing speed > 10000 rpm) at 25 ± 1 °C for 60 s. After continuous stirring, a turbid solution containing precipitated $CaCO_3$ particles was obtained. Particles in suspension were centrifuged (Allegra X-22 Centrifuge, Beckman Coulter) for 6 min at 4200 rpm and were washed three times with ethanol to remove nonreacted ions. The solid particles were collected by drying at 70 °C for 2 h in an oven and stored in a dried form.

2.3. Loading $CaCO_3$ particles in NR

Different amounts (10 and 20 phr (part per hundred rubber)) of vaterite $CaCO_3$ particles were added into 60 % DRC NR latex, with stirring for 10 min. Afterward, the NR/$CaCO_3$ latex was poured into a plate and dried in an oven at 70 °C for 7 days. The obtained NR/$CaCO_3$ after drying was analyzed using X-ray diffraction (XRD) and FTIR. For comparison, the vaterite particle was put in water with stirring for 10 min and dried in an oven at 70 °C for 7 days, before analysis using XRD and FTIR.

2.4. Characterization

Morphology of $CaCO_3$ particles was imaged by using the JEOL JSM 65 VL scanning electron microscope (SEM) which was operated at 20 kV with a working distance of 11 mm. The particle size was determined by ImageJ software in which the straight-line function was used to drag a line for measuring the diameter of the particles. Setting the scale value in SEM images scale bar as a standard scale for particle size measurement. The number of analyzed particles exceeded 150 particles in each sample.

X-ray powder diffraction was performed to identify the crystal phases with a Panalytical Empyrean diffractometer working with the monochromatic Cu-Kα radiation (λ = 1.54 Å), 40 kV-30 mA. X-ray diffraction (XRD) patterns were obtained from 2Θ from 20° to 40° in step size 0.052°. To quantitatively ascertain the quantitative percentage of vaterite and calcite phases from the diffraction patterns of $CaCO_3$ particles, MAUD software based on Rietveld refinement was used [49]. The Rietveld software MAUD was designed especially for refining both the structural, microstructural and phase parameters.

Fourier Transform Infrared (FTIR) spectra of prepared particles were measured from 4000 to 400 cm^{-1} with a resolution of 4 cm^{-1} using 20 scans by Bruker Vertex 70v equipment in attenuated total reflectance infrared (ATR-IR) mode to characterize vibration bands of the polymorphs, vaterite and calcite.

Raman spectroscopy was used to detect the polymorphs of particles by XploRA Raman Microscope. The spectra were recorded from 400 to 3700 cm^{-1}, 785 nm and detector 1200 gr/mm.

Transmission electron microscopy (TEM) and high-resolution transmission electron microscopy (HRTEM) were carried out by using a JEM-2100 Electron Microscope to image the particle structure and study the properties of particles on the atomic scale. To prepare samples for TEM analysis, the $CaCO_3$ particles were dispersed in ethanol solution first and then deposited as a droplet onto a TEM grid coated with a layer of carbon film.

Viscosity behavior was assessed by AR-G2 Magnetic Bearing Rheometer using aluminum plate core 994327, 40 mm at temperature 20 °C.

3. Results and discussion

3.1. Effect of sucrose concentration on the particle size of vaterite calcium carbonate polymorph

The precipitation reaction of $CaCO_3$ follows equations (1) to (3). In a typical synthesis, CO_3^{2-} ions and Ca^{2+} ions will be contacting each other to quickly form solid $CaCO_3$ particles.

$$(NH_4)_2CO_3 \rightarrow 2NH_4^+ + CO_3^{2-} \quad (1)$$

$$CaCl_2 \rightarrow Ca^{2+} + 2Cl^- \quad (2)$$

$$(NH_4)_2CO_3 + CaCl_2 \rightarrow CaCO_3\,(s) + 2NH_4Cl \quad (3)$$

Morphology, average particle size and histogram size distribution of prepared precipitated $CaCO_3$ at different sucrose concentrations obtained by SEM at low (2,500×) and high (30,000×) magnification are shown in Fig. 1. Some rhombohedral calcite particles are observed in very small quantities only in water system without sucrose at low magnification (Fig. 1a). The majority of $CaCO_3$ particles is assigned to spherical vaterite with rough surface in the presence of sucrose 10–50 wt% aqueous medium. Due to the high solubility of vaterite in water and its metastability, vaterite easily transforms into more stable thermodynamically polymorphs such as calcite or aragonite. Thus, the presence of water in the precipitated system can induce a polymorphic transformation from spherical vaterite to rhombohedral calcite [23]. The mean values of spherulitic particle size were 0.81, 0.72, 0.52, 0.46, 0.44 and 0.42 μm at various sucrose concentrations 0, 10, 20, 30, 40 and 50 wt%, respectively. The highest % sucrose concentration (50 wt %) yielded the smallest particle size with the narrowest particle size distribution (see Fig. 1g-l) Sucrose is a disaccharide that is composed of two monosaccharides: glucose and fructose. Sucrose contains plenty of hydroxyl polar groups and is miscible in water. The interaction of the hydroxyl of sucrose and Ca^{2+} might form calcium saccharide, leading to the decreased affinity of CO_3^{2-} towards Ca^{2+}, hence favorite the vaterite precipitation. Upon increasing the sugar concentration, the viscosity drastically increases by more than one order of magnitude (see Fig. 2). This in turn prevents contact between the reactants molecules and slows down the kinetics of precipitation. As shown in Table 1, this synthetic route was quite successful to achieve a high yield of spherical sub-micrometer $CaCO_3$ particles. The use of sucrose in the aqueous medium was earlier reported by L. Pérez-Villarejo et al. at a sucrose concentration of 67 % yielding 100 % of vaterite. Yet, their particle size was in the range of 0.5–1 μm with irregular shape and rough surface [37]. Meanwhile, starting from 30 wt% of sucrose as the aqueous medium in our study could provide the average particle size of vaterite smaller than 0.5 μm with a regular spherical shape (Table 1).

Fig. 2a. shows Newtonian behavior of aqueous medium with and without sucrose. The viscosity of 1 M $CaCl_2$ in the water system, 1 M $CaCl_2$ in 50 wt% sucrose medium and pure 50 wt% sucrose were 0.0008, 0.0240 and 0.0152 Pa.s, respectively. Soluble sucrose in water can form three-dimensional networks of hydrogen-bonded molecules; proton donors hydroxyl groups of sucrose molecules can act as proton acceptors in hydrogen bonds. The possible interaction model between sucrose and calcium ions is equivalent to a polymer-like complex involving more than one calcium cation per sucrose molecule [50–52]. This interaction induces a stronger viscosity than in the case of a pure sucrose solution (see Fig. 2). Thus, the viscosity positively correlates both to the amount of sucrose and calcium ions in the sucrose solution. The change in viscosity of the solutions can be indicated by the higher slope between shear stress and shear rate in Fig. 2b. The increase of viscosity that is about 30 times bigger for 1 M $CaCl_2$ (0.0240 Pa.s) with sucrose than without sucrose (0.0008 Pa.s) can prevent the contact between CO_3^{2-} and Ca^{2+} ions to form further bigger particles made of aggregated nanograins of $CaCO_3$.

The activation energy for forming nuclei in the nucleation and growth theory is presented in equation (4) [34].

$$\Delta G_N = 16\pi(\Delta G_1)^3/3(kTlnS)^2 \quad (4)$$

where ΔG_N is an activation energy, ΔG_1 is the required surface energy for forming new interfaces and maintaining the crystal growth, k is the Boltzman constant, T is temperature and S is the degree of supersaturation of the solution given by [6,36].

In the presence of sugar in the aqueous medium, the surface energy that is needed to form the new interface (ΔG_1) decreases.

$$S = \left(\left(a_{Ca^{2+}} + a_{CO_3^{2-}}\right)/K_{sp}\right)^{1/2} \quad (5)$$

where $a_{Ca^{2+}}$ and $a_{CO_3^{2-}}$ are the activities of a Ca^{2+} and CO_3^{2-} ions, respectively, and K_{sp} is a thermodynamic solubility of the product.

In the presence of sucrose in the aqueous medium, the activity of Ca^{2+} ions remains high during the onset of precipitation due to high viscosity and so does the supersaturation. In a solution, the size of the critical nuclei during precipitation is inversely related to the logarithm of the supersaturation as seen in equation (6) [36].

$$r_c = 2\gamma v/KTlnS \quad (6)$$

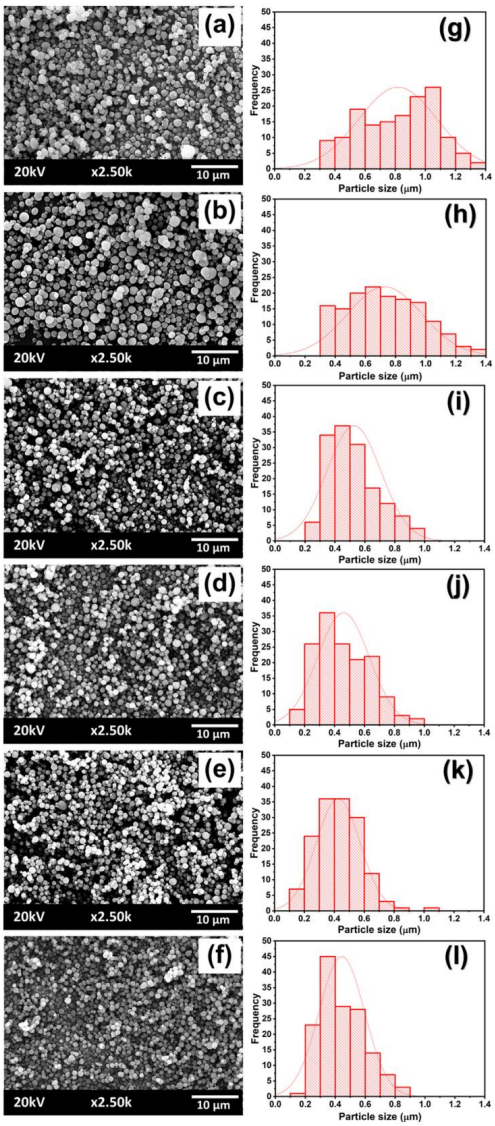


Fig. 1. SEM micrographs and histograms size distribution of $CaCO_3$ at sucrose different concentrations by wt%; (a, g) 0%, (b, h) 10%, (c, i) 20%, (d, j) 30%, (e, k) 40% and (f, l) 50%.

where r_c is the radius of critical nucleus, γ is the interfacial tension and v is the volume of a molecule inside the nucleus. Therefore, a high degree of supersaturation (S) would induce smaller particles. These factors allowed us to propose that sucrose plays an important role in promoting the viscosity of the mixing system which led to reducing the particle size of $CaCO_3$.

Fig. 3 presents XRD patterns of the $CaCO_3$ particles at different sucrose concentrations. In the range of 20–40, the XRD patterns

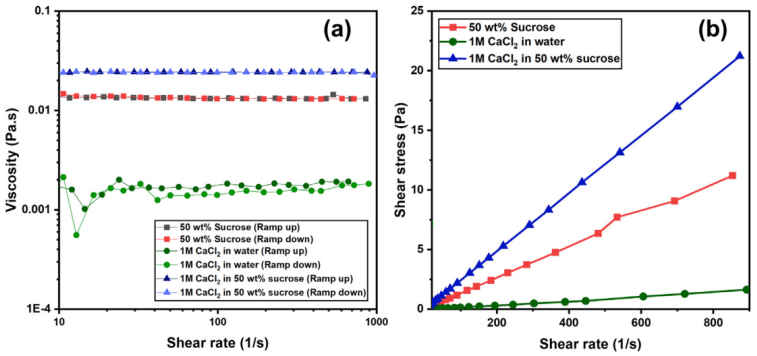


Fig. 2. Plots of (a) viscosity and (b) shear stress vs shear rate of 50 wt% sucrose, 1 M $CaCl_2$ in water and 1 M $CaCl_2$ in 50 wt% sucrose.

Table 1
Results of average particle sizes and % vaterite and calcite of prepared $CaCO_3$ at different sucrose concentrations.

Sucrose concentration (wt%)	Particle size (μm)	% Vaterite*	% Calcite*
0	0.81 ± 0.26	92.52	7.74
10	0.72 ± 0.24	97.50	2.49
20	0.52 ± 0.18	98.06	1.93
30	0.46 ± 0.17	98.43	1.56
40	0.44 ± 0.15	99.08	0.91
50	0.42 ± 0.14	99.10	0.89

* Calculated by MAUD software by carrying CIF files information of crystal structures: calcite, vaterite as initial inputs.

exhibited vaterite, located at 24.9, 27 and 32.7 in 2Θ with the reflection of XRD patterns: (100), (101) and (102), respectively. The crystal planes following (012), (104), (110) and (113) where the main diffraction peaks of calcite were located respectively at 23, 29.3, 35.9 and 39.5 in 2Θ. The XRD data clearly showed that the obtained product at 0 wt% sucrose concentration consisted of vaterite and calcite crystals. This result is in good agreement with SEM images. When the content of sucrose was further increased, the Bragg peak located at 2Θ = 23° corresponding to calcite disappeared and the intensity of the strongest one located at 2Θ = 29.3° almost disappeared. The XRD patterns suggest that the presence of sucrose has an obvious influence on the phase structure of $CaCO_3$ particles, i.e., promoting vaterite and inhibiting the formation of calcite. Quantitative analysis of XRD results for the two polymorphs was calculated by using the MAUD program (Fig. 3c and 3d). The absence of sucrose gave a percentage of vaterite 92.5 % and calcite with a percentage of 7.5 %. As it can be seen from Table 1, the percentage of vaterite increased from 97.50 to 99.1 % and concomitantly the percentage of calcite decreased from 2.49 to 0.9 % when sucrose concentrations were increased from 10 % to 50 % respectively. The increase of sucrose concentration means that the proportion of water was reduced. When the content of water in the system decreases, the phase transformation of $CaCO_3$ from vaterite into calcite is decreased. This supports the idea that sucrose can stabilize vaterite polymorph.

Table 1 summarizes % vaterite and % calcite at different sucrose concentrations. It can be seen that increasing the sucrose concentration resulted in a decrease in the particle size with an increased percentage of vaterite form. The reaction yield is one of the impor-

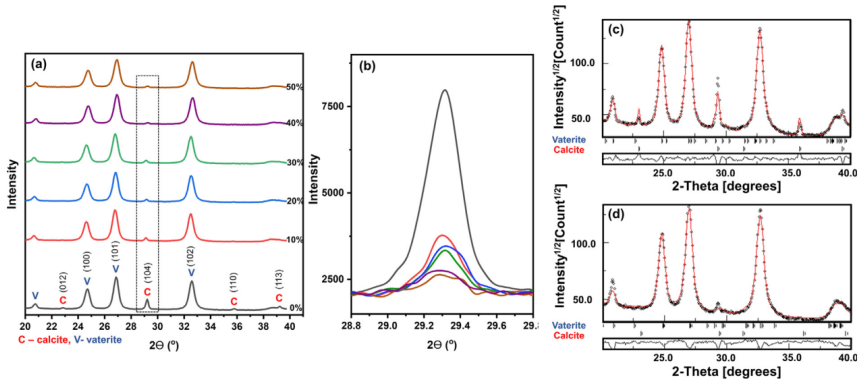


Fig. 3. X-ray diffractograms of obtained $CaCO_3$ particles at different sucrose concentrations; (a,b) 10–50 wt% and Rietveld refinement patterns of X-ray diffraction from MAUD software: (c) 0 wt% sucrose and (d) 50 wt% sucrose medium.

tant parameters for practical application on an industrial scale. The reaction yields at all varied conditions are estimated by weighing the synthesized dry particles. The results show yields higher than 87 % for all series. The smallest particle (0.42 μm) was obtained at a high concentration of 50 % sugar concentration which is lower than in previous report carried out by L. Pérez-Villarejo and coworkers [37].

The characteristic bands of vaterite and calcite were identified by FTIR in Fig. 4. The typical bands of vaterite are located at 745 cm^{-1}, 877 cm^{-1} and 1076–1089 cm^{-1} for doubly degenerate in-plane OCO deformation bending, CO_3 out-of-plane bending and symmetric C—O stretching and symmetric C—O stretching, respectively. On the other hand, the doubly degenerate in-plane of OCO deformation bending and CO_3 out-of-plane bending typical bands of calcite normally appear at 713 and 848 cm^{-1}, respectively. Fig. 4b shows the FTIR spectra in the absence and presence of sucrose in the system of $CaCO_3$ precipitation in the range of 500–1300 cm^{-1}. The absorption band corresponding to calcite at 713 cm^{-1} is present in the 0 wt% sucrose spectrum and is absent when sucrose was used as an aqueous medium for all variations of sucrose concentrations (10–50 wt%). The intensity of C—H symmetric and asymmetric stretching at 2918 cm^{-1} and 2974 cm^{-1} increased when increasing the sucrose concentration. These C—H stretching peaks were obtained from the disaccharide structure of sucrose which contained glucose 1 molecule and fructose 1 molecule [53].

Similar to FTIR analysis, the two polymorphs of $CaCO_3$ phases were also confirmed by Raman spectroscopy (Fig. 5). The presence

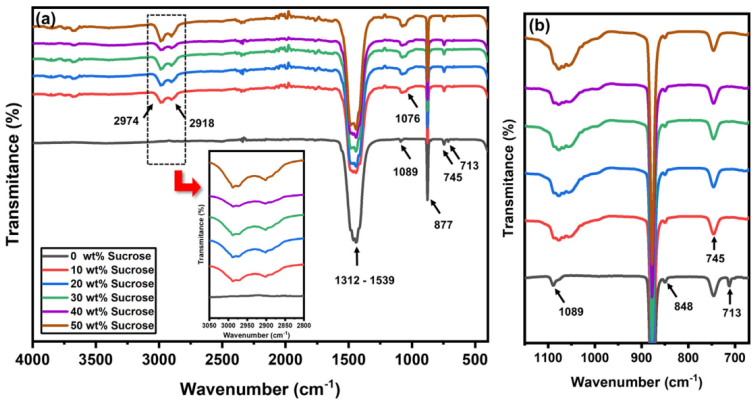


Fig. 4. FTIR spectra of $CaCO_3$ obtained particles by varying wt% of sucrose medium: 0, 10, 20, 30, 40 and 50 wt%, in the range of (a) 500–4000 cm^{-1} and (b) 700–1100 cm^{-1}.

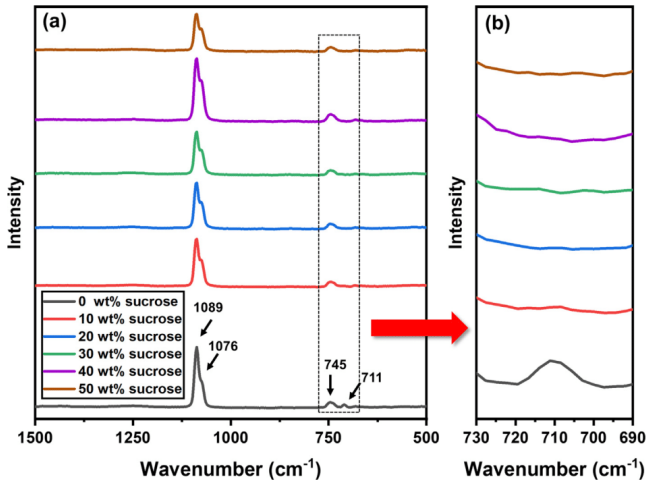


Fig. 5. Raman spectra of obtained $CaCO_3$ at different sucrose concentrations (wt%): 0, 10, 20, 30, 40 and 50 in the range of (a) 500–1500 cm^{-1} and (b) 690–730 cm^{-1}.

of vaterite in $CaCO_3$ can be determined at 745, 1076 and 1089 cm^{-1} and calcite at 711 cm^{-1}. The calcite peak at 711 cm^{-1} appeared in the aqueous system without added sugar and disappeared when sugar was used in the mixing systems as seen in Fig. 5b. The corresponding XRD patterns, FTIR analysis and Raman spectroscopy further confirmed that sugar has a considerable high impact on polymorphs of $CaCO_3$.

In order to characterize the structure of $CaCO_3$ particles, TEM was conducted. Fig. 6 shows TEM images of $CaCO_3$ prepared by using 50 wt% sugar in the aqueous solutions. It can be observed that the particles are spherical in good agreement with what was observed in SEM images in Fig. 1. The porous structure is demonstrated by an obvious contrast difference between the paler edges and darker centers (Fig. 6b).

3.2. Incorporation of vaterite in natural rubber

Generally, fabrication of polymeric products often requires inorganic fillers to reinforce the properties. Commercial $CaCO_3$ having particle size larger than 100 nm is incorporated in polymeric materials as a filler without reinforcing efficacy. The $CaCO_3$ is an irregular cubic form, hence agglomeration normally occurs, resulting in the deterioration of the final product properties. In addition, the size and shape of the inorganic reinforcing filler play an important role in the properties of the filled product in particular natural rubber (NR). Qinghong Fang et al. revealed that the spherical-shaped $CaCO_3$ having a high specific surface area could provide the highest mechanical properties of filled NR, compared to the chain-shaped or cube-shaped $CaCO_3$ [44]. While Makara Lay and co-workers attempted to reduce the particle size of $CaCO_3$ by grinding and ultrasonication, in a ball mill [46]. They could optimize the grinding process (ultrasonication of 120 min. and ball mill for 72 h.) to obtain 1.5 μm size of $CaCO_3$ before addition in NR latex. However, the broad particle-size distribution was obtained by this technique, hence reducing the mechanical properties of the filled NR product. Hence, it is interesting for the first time to incorporate the obtained vaterite $CaCO_3$ polymorph in the form of regular spherical sub-micrometer size in natural rubber (NR) latex. To investigate the vaterite stability in concentrated NR latex, the $CaCO_3$ particles prepared with 50 wt% sucrose in the aqueous medium were chosen in this study since they contained the highest % of vaterite and the smallest particle size. Different amounts (10 and 20 phr) of $CaCO_3$ were dispersed in NR latex by simple stirring, compared to the $CaCO_3$ dispersed in water. As mentioned in the introduction section, vaterite has a higher solubility than calcite. This metastability is the driving force for the phase transformation occurring when vaterite particles are put in contact with water. The resident time of vaterite form was fully transformed into calcite is 2 days in water at room temperature [23]. To compare the stability of $CaCO_3$ in water and in NR latex, the dispersed $CaCO_3$ in water, then dried in an oven at 70 °C as in the case of $CaCO_3$ dispersed in NR latex had experimented. It was found that the water was almost evaporated within one hour in the case of $CaCO_3$ in water. XRD patterns in Fig. 7 revealed that the powders were not completely transformed, as 81.5 % calcite and 18.94 % vaterite were found. While $CaCO_3$ particles were maintaining their vaterite polymorph when they were loaded into NR as the calcite peak located at $2\Theta = 29.3°$ was not detected in the case of $CaCO_3$ in NR. There are only the vaterite phases appeared in all contents of $CaCO_3$ loading NR.

The results of FTIR spectra (Fig. 8) supported that the prepared $CaCO_3$ particles do not reform when they were dispersed in NR latex. Corresponding to FTIR spectra in Fig. 8, the typical peak of calcite was evidenced at 713 cm^{-1} with the $CaCO_3$ in water, while only a vaterite peak at 745 cm^{-1} was apparent for $CaCO_3$ in NR. Different amounts (10 and 20 phr) of $CaCO_3$ could be incorporated in NR latex without the transformation of vaterite polymorph into calcite. Besides, the CH_2 stretching, CH_3 stretching and =C–H

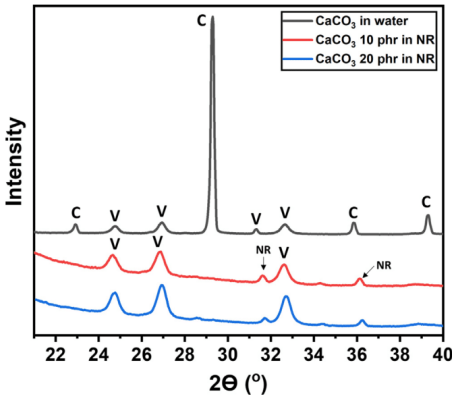


Fig. 7. XRD patterns of $CaCO_3$ in water, and 10 and 20 phr $CaCO_3$ in NR.

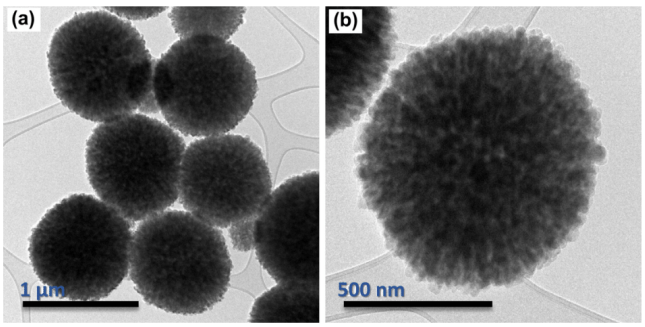


Fig. 6. TEM images of (a) and (b) $CaCO_3$ particles prepared from 50 wt% sucrose as an aqueous medium at different magnification.

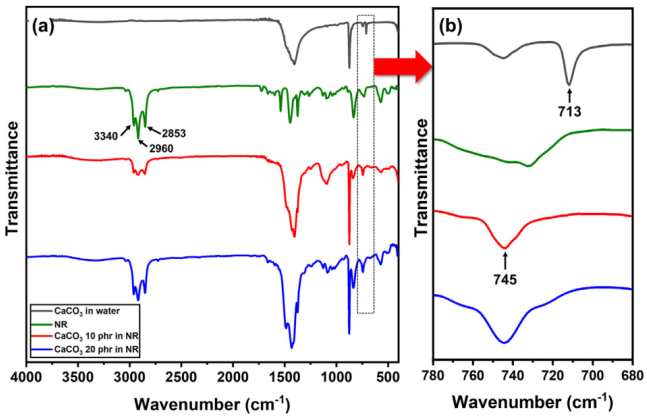


Fig. 8. FTIR spectra of $CaCO_3$ in water and NR at different content (10 and 20 phr) of $CaCO_3$ loading in the range of (a) 500–4000 cm^{-1} and (b) 680–780 cm^{-1}.

stretching group from the NR structure were located at 2853, 2960 and 3340 cm^{-1}, respectively. The stability of vaterite polymorph in NR latex even though it is in an aqueous medium, might be due to the adsorption of Ca^{2+} on the surface of the rubber particles that contain negative charges [41,42], resulting in the limitation of crystal transformation of the vaterite polymorph.

4. Conclusion

In this work, we have successfully shown that sub-micrometer sized $CaCO_3$ particles with a high content of vaterite form could be prepared when a high content of sugar was initially present in the aqueous solutions of the precursors. The optimum condition was obtained when 50 wt% sugar was added to the 1 M $CaCl_2$ and $(NH_4)_2CO_3$ reactants solutions with a stirring speed of 10000 rpm in a blender working at 25 °C for 60 s. The SEM images, XRD patterns, FTIR analysis, Raman spectroscopy and TEM image results converge towards the formation of submicrometer spherical vaterite particles having a porous structure when the amount of sugar was increased up to 50 wt%. The percentage of vaterite calculated from the XRD patterns was more than 99 % and the particle size was reduced down to 0.4 μm when the content of sugar was 50 wt%. The viscosity of the sugar solutions was shown to positively correlate with the amount of sugar added to the solutions. We consider that not only the interaction of the hydroxyl groups of sucrose with the Ca^{2+} but the viscosity was another key factor to reduce the particle size due to the limited diffusion of Ca^{2+} ions. Our finding shows that this protocol for $CaCO_3$ synthesis using sugar yielding a high content and regular spherical shape of vaterite is an advantage over simple and rapid mixing methods. This route is additionally harmless and low-cost suitable for industrial-scale production. Moreover, there is no report on the stability of vaterite polymorph in NR latex, it is very challenging to use these particles as reinforcing fillers, especially in the rubber industry because the prepared vaterite did not transform when dispersed in NR latex. The negative charges of the surface NR particles were proposed to play an important role to stabilize the vaterite particles. The effect of using submicron vaterite $CaCO_3$ particles on the mechanical properties of NR is now in progress.

Declaration of Competing Interest

The authors declare that they have no known competing financial interests or personal relationships that could have appeared to influence the work reported in this paper.

Acknowledgements

We would like to gratefully thank ERASMUS + Thailand (2019-1-FR01-KA107-062076) between Mahidol University and Le Mans University and the Sritrangtong Scholarship Program from the Faculty of Science, Mahidol University to K. Longkaew.

References

[1] G. Falini, S. Fermani, M. Reggi, B. Njegić Džakula, D. Kralj, Evidence of structural variability among synthetic and biogenic vaterite, Chem. Commun. 50 (2014) 15370–15373.
[2] B.C. Chakoumakos, B.M. Pracheil, R.P. Koenigs, R.M. Bruch, M. Feygenson, Empirically testing vaterite structural models using neutron diffraction and thermal analysis, Sci. Rep. 6 (2016) 36799.
[3] S.J. Portugal, J. Bowen, C. Riehl, A rare mineral, vaterite, acts as a shock absorber in the eggshell of a communally nesting bird, Ibis 160 (2018) 173–178.
[4] M.A.W. Gaber, Characterizations of El Minia limestone for manufacturing paper filler and coating, Egypt. J. Pet. 27 (2018) 437–443.
[5] Y. Boyjoo, V.K. Pareek, J. Liu, Synthesis of micro and nano-sized calcium carbonate particles and their applications, J. Mater. Chem. A 2 (2014) 14270–14288.
[6] D. Konopacka-Łyskawa, Synthesis methods and favorable conditions for spherical vaterite precipitation: A review, Crystals 9 (2019).
[7] M. Ali, M.S. Abdullah, S.A. Saad, Effect of calcium carbonate replacement on workability and mechanical strength of Portland cement concrete, Adv. Mat. Res. 1115 (2015) 137–141.
[8] B. Myszka, K. Hurle, K. Zheng, S.E. Wolf, A.R. Boccaccini, Mechanical improvement of calcium carbonate cements by in situ HEMA polymerization during hardening, J. Mater. Chem. B 7 (2019) 3403–3411.
[9] M.C.T. Wei, C. Tran, N. Meredith, L.J. Walsh, Effectiveness of implant surface debridement using particle beams at differing air pressures, Clin. Exp. Dental Res. 3 (2017) 148–153.
[10] S. Tom, H.-E. Jin, K. Heo, S.-W. Lee, Engineered phage films as scaffolds for $CaCO_3$ biomineralization, Nanoscale 8 (2016) 15696–15701.
[11] A.D. Woldetsadik, S.K. Sharma, S. Khapli, R. Jagannathan, M. Magzoub, Hierarchically porous calcium carbonate scaffolds for bone tissue engineering, ACS Biomater Sci. Eng. 3 (2017) 2457–2469.
[12] A.M. Ferreira, A.S. Vikulina, D. Volodkin, $CaCO_3$ crystals as versatile carriers for controlled delivery of antimicrobials, J. Control. Release 328 (2020) 470–489.

[13] J. Chen, G. Cheng, Y. Chai, W. Han, W. Zong, J. Chen, C. Li, W. Wang, L. Ou, Y. Yu, Preparation of nano-$CaCO_3$/polystyrene nanocomposite beads for efficient bilirubin removal, Colloids Surf. B Biointerfaces 161 (2018) 480–487.

[14] O. Cherkas, T. Beuvier, S. Fall, A. Gibaud, X-ray absorption and diffraction analysis for determination of the amount of calcium carbonate and porosity in paper sheets, Cellul. 23 (2016) 2831–2840.

[15] H. Choe, J.H. Lee, J.H. Kim, Polyurethane composite foams including CaCO3 fillers for enhanced sound absorption and compression properties, Compos. Sci. Technol. 194 (2020) 108153.

[16] Y.-B. Hu, D.A. Wolf-Gladrow, G.S. Dieckmann, C. Völker, G. Nehrke, A laboratory study of ikaite ($CaCO_3{\cdot}6H_2O$) precipitation as a function of pH, salinity, temperature and phosphate concentration, Mar. Chem. 162 (2014) 10–18.

[17] A.G. Christy, A review of the structures of vaterite: the impossible, the possible, and the likely, Cryst. Growth Des. 17 (2017) 3567–3578.

[18] S. Kamhi, On the structure of vaterite $CaCO_3$, Acta Crystallogr. 16 (1963) 770–772.

[19] J.D. Rodriguez-Blanco, S. Shaw, L.G. Benning, The kinetics and mechanisms of amorphous calcium carbonate (ACC) crystallization to calcite, viavaterite, Nanoscale 3 (2011) 265–271.

[20] R.-J. Qi, Y.-J. Zhu, Microwave-assisted synthesis of calcium carbonate (vaterite) of various morphologies in water–ethylene glycol mixed solvents, J. Phys. Chem. B 110 (2006) 8302–8306.

[21] E. Ulkeryildiz, S. Kilic, E. Ozdemir, Rice-like hollow nano-CaCO3 synthesis, J. Cryst. Growth 450 (2016) 174–180.

[22] O. Cherkas, T. Beuvier, D.W. Breiby, Y. Chushkin, F. Zontone, A. Gibaud, Direct observation of microparticle porosity changes in solid-state vaterite to calcite transformation by coherent X-ray diffraction imaging, Cryst. Growth Des. 17 (2017) 4183–4188.

[23] O. Cherkas, T. Beuvier, F. Zontone, Y. Chushkin, L. Demoulin, A. Rousseau, A. Gibaud, On the kinetics of phase transformations of dried porous vaterite particles immersed in deionized and tap water, Adv. Powder Technol. 29 (2018) 2872–2880.

[24] G. Nehrke, P. Van Cappellen, Framboidal vaterite aggregates and their transformation into calcite: A morphological study, J. Cryst. Growth 287 (2006) 528–530.

[25] L. Li, Y. Yang, Y. Lv, P. Yin, T. Lei, Porous calcite $CaCO_3$ microspheres: Preparation, characterization and release behavior as doxorubicin carrier, Colloids Surf. B Biointerfaces 186 (2020) 110720.

[26] C. Son, S.Y. Kim, S.Y. Bahn, H.J. Cha, Y.S. Choi, CaCO3 thin-film formation mediated by a synthetic protein-lysozyme coacervate, RSC Adv. 7 (2017) 15302–15308.

[27] L.N. Hassani, F. Hindré, T. Beuvier, B. Calvignac, N. Lautram, A. Gibaud, F. Boury, Lysozyme encapsulation into nanostructured $CaCO_3$ microparticles using a supercritical CO_2 process and comparison with the normal route, J. Mater. Chem. B 1 (2013) 4011–4019.

[28] Y.-Z. Tian, Y.-L. Li, Z.-F. Wang, Y. Jiang, Nuclease-responsive DNA–PEI hollow microcapsules for bio-stimuli controlled release, J. Mater. Chem. B 2 (2014) 1667–1672.

[29] J. Chen, L. Xiang, Controllable synthesis of calcium carbonate polymorphs at different temperatures, Powder Technol. 189 (2009) 64–69.

[30] M. El-Shahate Ismaiel Saraya, H. Hassan Abdel Latif Rokbaa, Preparation of vaterite calcium carbonate in the form of spherical nano-size particles with the aid of polycarboxylate superplasticizer as a capping agent, Am. J. Nanomater. 4 (2022) 44–51.

[31] J. Yu, M. Lei, B. Cheng, X. Zhao, Effects of PAA additive and temperature on morphology of calcium carbonate particles, J. Solid State Chem. 177 (2004) 681–689.

[32] Y. Zhao, W. Du, L. Sun, L. Yu, J. Jiao, R. Wang, Facile synthesis of calcium carbonate with an absolutely pure crystal form using 1-butyl-3-methylimidazolium dodecyl sulfate as the modifier, Colloid Polym. Sci. 291 (2013) 2191–2202.

[33] Y. Zhao, S. Li, L. Yu, Y. Liu, X. Wang, J. Jiao, The preparation of calcium carbonate crystals regulated by mixed cationic/cationic surfactants, J. Cryst. Growth 324 (2011) 278–283.

[34] H. Tang, J. Yu, X. Zhao, D.H.L. Ng, Influence of PSSS on the morphology and polymorph of calcium carbonate in the ethanol–water mixed system, J. Alloy. Compd. 463 (2008) 343–349.

[35] L. Zhang, L.-H. Yue, F. Wang, Q. Wang, Divisive effect of alcohol–water mixed solvents on growth morphology of calcium carbonate crystals, J. Phys. Chem. B 112 (2008) 10668–10674.

[36] D.B. Trushina, T.V. Bukreeva, M.N. Antipina, Size-controlled synthesis of vaterite calcium carbonate by the mixing method: aiming for nanosized particles, Cryst. Growth Des. 16 (2016) 1311–1319.

[37] L. Pérez-Villarejo, F. Takabait, L. Mahtout, B. Carrasco-Hurtado, D. Eliche-Quesada, P.J. Sánchez-Soto, Synthesis of vaterite $CaCO_3$ as submicron and nanosized particles using inorganic precursors and sucrose in aqueous medium, Ceram. Int. 44 (2018) 5291–5296.

[38] I. Khan, A.H. Bhat, CHAPTER 16 Micro and Nano Calcium Carbonate Filled Natural Rubber Composites and Nanocomposites, in: Natural Rubber Materials: Volume 2: Composites and Nanocomposites, The Royal Society of Chemistry, 2014, pp. 467–487.

[39] C.C. Ho, CHAPTER 4 The Production of Natural Rubber from Hevea brasiliensis Latex: Colloidal Properties, Preservation, Purification and Processing, in: Natural Rubber Materials: Volume 1: Blends and IPNs, The Royal Society of Chemistry, 2014, pp. 73–106.

[40] K. Nawamawat, J.T. Sakdapipanich, C.C. Ho, Y. Ma, J. Song, J.G. Vancso, Surface nanostructure of Hevea brasiliensis natural rubber latex particles, Colloids Surf. A Physicochem. Eng. Asp. 390 (2011) 157–166.

[41] C.N. Rochette, J.J. Crassous, M. Drechsler, F. Gaboriaud, M. Eloy, B. de Gaudemaris, J.F.L. Duval, Shell structure of natural rubber particles: evidence of chemical stratification by electrokinetics and cryo-TEM, Langmuir 29 (2013) 14655–14665.

[42] S. Kumarn, N. Churinthorn, A. Nimpaiboon, M. Sriring, C.-C. Ho, A. Takahara, J. Sakdapipanich, Investigating the mechanistic and structural role of lipid hydrolysis in the stabilization of ammonia-preserved Hevea rubber latex, Langmuir 34 (2018) 12730–12738.

[43] Y. Hirata, H. Kondo, Y. Ozawa, 12 - Natural rubber (NR) for the tyre industry, in: S. Kohjiya, Y. Ikeda (Eds.), Chemistry, Manufacture and Applications of Natural Rubber, Woodhead Publishing, 2014, pp. 325–352.

[44] Q. Fang, B. Song, T.-T. Tee, L.T. Sin, D. Hui, S.-T. Bee, Investigation of dynamic characteristics of nano-size calcium carbonate added in natural rubber vulcanizate, Compos. B Eng. 60 (2014) 561–567.

[45] L. Jong, Synergistic effect of calcium carbonate and biobased particles for rubber reinforcement and comparison to silica reinforced rubber, J. Compos. Sci. 4 (2020).

[46] M. Lay, N. Hamran, A.A. Rashid, Ultrafine calcium carbonate-filled natural rubber latex film: mechanical and post-processing properties, Iran. Polym. J. 28 (2019) 849–858.

[47] G.S. Ananthapadmanabha, V. Deshpande, Influence of aspect ratio of fillers on the properties of acrylonitrile butadiene styrene composites, J. Appl. Polym. Sci. 135 (2018) 46023.

[48] J.L. Leblanc, Rubber–filler interactions and rheological properties in filled compounds, Prog. Polym. Sci. 27 (2002) 627–687.

[49] I.A. Lira-Hernández, F.R. Barrientos-Hernández, M. Pérez-Labra, A.M. García-Mercado, J.A. Romero-Serrano, Comments about rietveld analysis and tolerance factor: Y Doped $BaTiO_3$, Preprints (2016).

[50] K. Labgairi, A. Jourani, M. Kaddami, An isothermal (30°C) study of heterogeneous equilibria in the sucrose ($C_{12}H_{22}O_{11}$)–calcium hydroxide ($Ca(OH)_2$)–water system, Fluid Phase Equilib. 307 (2011) 100–103.

[51] N. Pannetier, A. Khoukh, J. François, Physico-chemical study of sucrose and calcium ions interactions in alkaline aqueous solutions, Macromol. Symp. 166 (2001) 203–208.

[52] Y.H. Song, J.C. Park, C.S. Kim, D.S. Hwang, H.J. Cha, J.H. Seo, Sucrose-calcium complexation for the durable biomass pellet, Biotechnol. Bioprocess Eng. 23 (2018) 341–348.

[53] A.B. Brizuela, L.C. Bichara, E. Romano, A. Yurquina, S. Locatelli, S.A. Brandán, A complete characterization of the vibrational spectra of sucrose, Carbohydr. Res. 361 (2012) 212–218.

PUBLICATION #2

polymers

MDPI

Article

Spherical $CaCO_3$: Synthesis, Characterization, Surface Modification and Efficacy as a Reinforcing Filler in Natural Rubber Composites

Khansinee Longkaew [1], Alain Gibaud [2], Wasan Tessanan [1], Philippe Daniel [2] and Pranee Phinyocheep [1,*]

[1] Department of Chemistry, Faculty of Science, Mahidol University, Rama VI Road, Payathai, Bangkok 10400, Thailand; khansinee.lon@gmail.com (K.L.); t.wasan18@gmail.com (W.T.)
[2] Institute of Molecules and Materials of Le Mans (IMMM), UMR CNRS 6283, Avenue Olivier Messiaen, CEDEX 9, 72085 Le Mans, France; alain.gibaud@univ-lemans.fr (A.G.); philippe.daniel@univ-lemans.fr (P.D.)
* Correspondence: pranee.phi@mahidol.ac.th

Abstract: Natural rubber (NR), an important natural polymer derived from the *Hevea brasiliensis* tree, has been widely used in the rubber industry owing to its excellent elastic properties. However, it requires reinforcing fillers to improve its mechanical properties for the manufacturing of rubber products. Generally, calcium carbonate ($CaCO_3$) is employed as a non-reinforcing filler. This work aimed to synthesize spherical-shaped $CaCO_3$ at a submicrometric scale without and with surface treatment and explore its utilization as a reinforcing filler in NR composites. The morphological shape and polymorphic phase of $CaCO_3$ were investigated using SEM, TEM, XRD, ATR-FTIR and Raman techniques. The mechanical properties of various amounts (0 to 60 phr) of $CaCO_3$-filled NR composites were explored. As a result, the NR/treated $CaCO_3$ composites provided higher tensile strength than the NR/untreated $CaCO_3$ composites and pure NR at all filler loadings. This may have been due to the improved interfacial interaction between NR and $CaCO_3$ with the improved hydrophobicity of $CaCO_3$ after treatment with olive soap. The optimal filler loading was 20 phr for the highest tensile strength of the rubber composites. In addition, the elongation at break of the NR/treated $CaCO_3$ was slightly decreased. Evidence from SEM and FTIR revealed the vaterite polymorph and shape stability of $CaCO_3$ particles in the NR matrix. The results demonstrate that the particle size and surface treatment of the filler have essential effects on the mechanical property enhancement of the rubber composites. Synthesized spherical $CaCO_3$ could be a potential reinforcing filler with broader application in polymer composites.

Keywords: calcium carbonate; spherical shape; natural rubber; reinforcing filler; surface treatment

check for updates

Citation: Longkaew, K.; Gibaud, A.; Tessanan, W.; Daniel, P.; Phinyocheep, P. Spherical $CaCO_3$: Synthesis, Characterization, Surface Modification and Efficacy as a Reinforcing Filler in Natural Rubber Composites. *Polymers* **2023**, *15*, 4287. https://doi.org/10.3390/polym15214287

Academic Editors: Huihuang Ding and Zhaojun Wang

Received: 30 September 2023
Revised: 19 October 2023
Accepted: 25 October 2023
Published: 31 October 2023

Copyright: © 2023 by the authors. Licensee MDPI, Basel, Switzerland. This article is an open access article distributed under the terms and conditions of the Creative Commons Attribution (CC BY) license (https://creativecommons.org/licenses/by/4.0/).

1. Introduction

Natural rubber (NR) is a valuable natural elastomer that is obtained in colloidal form from the rubber tree *Hevea brasiliensis*. Rubber particles are dispersed in water in the latex form of 30% dry rubber content (DRC). In general, NR latex is concentrated into 60% DRC for commercial applications. The chemical structure of NR is that of a non-polar hydrocarbon with a cis-1,4-polyisoprenic structure [1–3]. It possesses excellent elastic properties and good mechanical properties. However, NR latex or solid NR must be mixed with curing chemicals and reinforced by fillers to improve its mechanical properties, including tensile strength, elongation, modulus, and tear resistance [4,5]. Normally, fillers are divided into reinforcing, semi-reinforcing, and non-reinforcing categories [5,6]. The reinforcing efficiency of a filler in a polymer depends on the particle size, shape, specific surface area, and compatibility between the polymer matrix and filler [7]. There are several fillers used in the rubber industry depending on the target application, such as carbon black [8–10], precipitated silica (SiO_2) [11], calcium carbonate ($CaCO_3$) [12,13], clay [14], talc [15], etc. Carbon black is one of the most widely used reinforcing fillers in the

automotive industry, especially tire manufacturing, and has the potential to improve the strength of rubber due to its nanoscale particle size (<100 nm) [5]. Silica is incorporated into rubber, particularly for tire treads, to lower the rolling resistance. However, owing to the polarity difference between silica and rubber, modification of the silica surface is required to reduce its polarity and enhance the composite performance. In contrast, $CaCO_3$ is mostly used as a semi-reinforcing or non-reinforcing filler [5]. This is due to the major drawback of $CaCO_3$ having a particle size larger than 100 nm. It is therefore useful as a cost-effective dilution filler and for processability for some applications [16]. Consequently, many attempts have been made to reduce the particle size of $CaCO_3$ to the submicrometric or nanometric scale to enhance its degree of reinforcement [17–20].

$CaCO_3$ is an abundant inorganic material that can be obtained from nature [21,22] or by chemical synthesis [23–25]. Among many chemical syntheses, the simplest method of $CaCO_3$ synthesis is solution precipitation from a mixture of calcium ions (Ca^{2+}) and carbonate ions (CO_3^{2-}). The crystal shape and polymorph of the $CaCO_3$ particle can be changed by adjusting various parameters, such as the concentration of reactants, mixing temperature, mixing speed, and organic or aqueous medium. The crystal polymorphs of $CaCO_3$ are known as vaterite, aragonite, and calcite. The different polymorphic phases exhibit different shapes. Vaterite has a typical hexagonal shape, demonstrating a spherulitic or framboid morphology [26], while aragonite demonstrates an orthorhombic or needle-like shape [27,28]. The most thermodynamically stable phase is calcite, which has a typical trigonal morphology, showing a cubical shape [29,30]. An aqueous medium containing hydroxyl groups, such as glycerol, ethylene glycol, or sucrose, is the key factor in increasing the viscosity of the mixing system, influencing the decrement in particle size [17,20]. Using sucrose as the aqueous medium in the mixing procedure can reduce the particle size of $CaCO_3$ to the submicron scale, with a spherical shape and homogeneous distribution [20]. Moreover, $CaCO_3$ can be incorporated in the NR latex stage and maintain its vaterite polymorph. Q. Fang and coworkers investigated different shapes, namely spherical, chain-shaped, and cubic, of $CaCO_3$ in NR vulcanizates [12]. The results showed that spherical-shaped $CaCO_3$, having a high specific surface area, exhibited the best mechanical properties for loaded NR composites compared with chain-shaped and cube-shaped $CaCO_3$. However, the authors did not show the properties of unfilled NR vulcanizates. The particle shape and size of the filler are not the only key factors in the reinforcing efficiency: the interaction between the matrix and filler of the polymer composite also plays an important role [12,31,32]. To improve the reinforcing efficacy of $CaCO_3$ in an NR composite, the interfacial interaction between the two phases can be enhanced by adding a compatibilizer to the $CaCO_3$-filled NR or modifying the surface of hydrophilic $CaCO_3$ to provide it with a hydrophobic character. It was reported that the addition of lauryl alcohol to NR incorporated with $CaCO_3$ resulted in improved $CaCO_3$ dispersion in the NR matrix, hence increasing the tensile strength of the rubber composite [33]. The surface modification of hydrophilic $CaCO_3$ to produce hydrophobic properties has been explored by several researchers using stearic acid and soaps [34–36]. However, the utilization of a hydrophobic $CaCO_3$-filled NR composite is rarely found. Accordingly, it is challenging to synthesize submicrometric $CaCO_3$ particles with a spherical shape (vaterite polymorph) together with hydrophobic surface modification for further use as a reinforcing agent in a rubber composite.

This work, therefore, was focused firstly on $CaCO_3$ preparation using a precipitation process to produce submicron spherical-shaped $CaCO_3$ with a high percentage of the vaterite phase. The surface modification of the synthesized vaterite $CaCO_3$ using olive soap was also carried out. The morphological shape, particle size, and polymorphic phase of the obtained $CaCO_3$ particles were examined by scanning electron microscopy (SEM), transmission electron microscopy (TEM), X-ray diffraction (XRD), Brunauer–Emmett–Teller (BET) analysis, attenuated total reflectance–Fourier transform infrared (ATR-FTIR) spectroscopy, and Raman spectroscopy. The wettability of the particle surface was measured by its optical contact angle. Then, the untreated and treated spherical $CaCO_3$ particles

were incorporated into NR with varying filler content and compared with the neat NR. The mechanical and thermal properties of NR/untreated $CaCO_3$ and NR/treated $CaCO_3$ composites were investigated, including phase morphology by SEM.

2. Materials and Methods

2.1. Materials

The reactants for calcium carbonate ($CaCO_3$) synthesis, namely ammonium carbonate ($(NH_4)_2CO_3$) and calcium chloride dihydrate ($CaCl_2 \cdot 2H_2O$), were purchased from Acros Organics (Roissy Charles de Gaulle, Paris, France). Commercial-grade granulated sugar was purchased from Pulverent Sugar Poedersuiker (Picardie, Paris, France). Olive oil was obtained from Carrefour BIO Huile d'Olive Vierge Extra Extraite a Froid (Massy Cedex, France). Reagent-grade sodium hydroxide (NaOH) was obtained from Honeywell (Offenbach, Germany). High-ammonia NR latex with 60% DRC was purchased from the Thai Rubber Latex Corporation (Chonburi, Thailand). Commercial-grade curing agents, specifically ZnO, stearic acid, N-cyclohexyl benzothiazole-2-sulfenamide (CBS), and sulfur, were supplied by Kitpiboon Chemical Ltd. (Bangkok, Thailand).

2.2. Methods

2.2.1. Untreated $CaCO_3$ Synthesis

The untreated $CaCO_3$ powder was prepared following the synthesis procedure from our previous work [20]. Briefly, 50% by weight of sucrose solution was used as an aqueous medium to dissolve 1.0 M of $(NH_4)_2CO_3$ solution and 1.0 M of $CaCl_2$ solution. Both reactants were mixed at high speed (>10,000 rpm) using a blender under 25 ± 1 °C for 60 s. The obtained $CaCO_3$ powders were collected by centrifugation at 4200 rpm for 6 min, using an Allegra X-22 Centrifuge (Beckman Coulter, IN, USA). Then, the powder was washed several times with ethanol before drying at 70 °C for 3 h in an oven.

2.2.2. Olive Soap Preparation

The olive soap used for the surface modification of $CaCO_3$ was prepared by saponification between olive oil and NaOH. First, 1.3 g NaOH was dissolved in 3.9 mL of DI water, which was then mixed with olive oil (10 g) while stirring at 500 rpm for 3 h at room temperature. The obtained solid soap was dried at room temperature for a few days before further use.

2.2.3. Treated $CaCO_3$ Synthesis

Next, 0.4 g of solid olive soap was dissolved in 10 mL of ethanol at 80 °C. Then, the olive soap solution was cooled down to room temperature before adding 100 mL of 1.0 M $(NH_4)_2CO_3$ dissolved in sucrose solution. The mixture was then added to 100 mL of 1.0 M $CaCl_2$ dissolved in sucrose solution, followed by blending at high speed (>10,000 rpm) under 25 ± 1 °C for 60 s. The treated $CaCO_3$ was obtained by centrifugation, in the same manner as untreated $CaCO_3$.

2.2.4. Preparation of NR/$CaCO_3$ Composites

- NR/$CaCO_3$ compound preparation

For both the untreated and treated samples, 10, 20, 40, or 60 parts per hundred rubbers (phr) were added to 60% DRC NR latex and mixed by mechanical stirring at 600 rpm for 10 min. The NR/$CaCO_3$ latex compounds were poured into aluminum plates and dried at room temperature under an ambient atmosphere for approximately 2 weeks.

- NR/$CaCO_3$ composite preparation

The NR/$CaCO_3$ composites were prepared following the mixing formulation in Table 1. All ingredients were mixed using a 2-roll mill mixing machine (W100T, Collin GmbH, Mühldorf, Germany) at room temperature. The mixing process was performed as follows: mastication of the NR or NR/$CaCO_3$ compounds was performed on the roll

for 5 min, and then ZnO and stearic acid were added and mixed for 5 min. Thereafter, the curative agents CBS and sulfur were added and mixed for 5 min. The overall mixing time was kept constant at 15 min. After mixing, 10 end-roll passes were made before sheeting the compound off the 2-roll mill. The neat NR and NR/$CaCO_3$ composites were compressed into a sheet of 1 mm thickness by heat pressing at 140 °C, following their optimal cure times (t_{c90}), which were obtained using a moving die rheometer (MDR) (Dynisco MDR-CGM, Franklin, MA, USA) operated at 140 °C. The rubber sheets were cut into dumbbell-shaped specimens and stored at room temperature for at least 8 h before testing.

Table 1. Mixing formulation of NR/$CaCO_3$ composites.

Chemicals	Content (phr*)
NR	100
$CaCO_3$	0, 10, 20, 40, 60
ZnO	1.8
Stearic acid	2.0
CBS	1.0
Sulfur	1.5

* phr, parts per hundred rubber.

2.3. *Characterization of $CaCO_3$ Fillers and NR/$CaCO_3$ Composites*

2.3.1. Optical Contact Angle

The contact angle measurement of $CaCO_3$ powders was performed using an optical contact angle instrument (SL200KS, Kino, Boston, MA, USA). A water droplet was applied on the surface of the powder following the sessile drop method, with a capture speed of 7 frames per second, and axisymmetric drop shape analysis was performed with the Young–Laplace equation in fitting mode.

2.3.2. Scanning Electron Microscopy (SEM)

The morphology of the samples, namely the $CaCO_3$ particle surfaces and tensile-fractured surfaces of NR/$CaCO_3$ composites coated with gold, was visualized by SEM (JEOL JSM 65 VL, Peabody, MA, USA) at 20 kV with a 10 mm working distance. The average particle size and distribution of $CaCO_3$ particles were determined using the ImageJ software (v1.8.0). In each $CaCO_3$ sample, the number of particles examined exceeded 150.

2.3.3. Transmission Electron Microscopy (TEM)

TEM (JEM-2100, Peabody, MA, USA) was performed to further examine the particle surfaces. The obtained $CaCO_3$ particles were dispersed in ethanol before being deposited as droplets onto TEM grids coated with a carbon film.

2.3.4. Attenuated Total Reflectance–Fourier Transform Infrared (ATR-FTIR) Spectroscopy

The ATR-FTIR spectra were obtained to study the chemical structure and vibration bands of the filler and rubber composites using Bruker Vertex 70v equipment (Billerica, MA, USA) in the ATR-IR mode, working with 20 scans at a resolution of 1 cm^{-1}, in the range of 400–4000 cm^{-1}.

2.3.5. Raman Spectroscopy

A Raman microscope (XploRA, Horiba, Lyon, France) was used to characterize the polymorphs of $CaCO_3$ particles. The spectra were recorded from 400 to 4000 cm^{-1}, using a wavelength of 785 nm and a detector value of 1200 gr/mm.

2.3.6. X-ray Diffraction (XRD) Analysis

XRD analysis of the $CaCO_3$ powders, NR, and NR/$CaCO_3$ composites was conducted using a Panalytical Empyrean diffractometer (Malvern, UK) with a 2θ range of 20–40°, step size of 0.052°, monochromatic Cu-Kα radiation (λ = 1.54 Å), acceleration voltage of

40 kV, and 30 mA beam current. The crystalline percentage of the $CaCO_3$ polymorphs was calculated using the MAUD software (v2.94) based on Rietveld refinement, which was designed especially for calculating both the structural and phase parameters.

2.3.7. Thermogravimetric Analysis (TGA)

Thermogravimetric analysis (TGA) (SDT 296, Universal V3.4C TA instrument, New Castle, DE, USA) was performed to investigate the thermal stability of the $CaCO_3$ powders and NR/$CaCO_3$ composites, using 10 mg of each sample. The samples were investigated in the heating range of 40–800 °C under a N_2 atmosphere. A heating rate of 10 °C/min was used for $CaCO_3$ powder [37]. As the heating rate can affect the decomposition of a polymer, the heating rate used for polymer composites is generally higher than that for the filler [38]. Thus, the heating rate of 20 °C/min was used for NR/$CaCO_3$ composites, referring to NR/cellulose nanocrystal composites [39].

2.3.8. Brunauer–Emmett–Teller (BET) Analysis

The BET-specific surface area in m^2/g unit was measured using a TriStar II 3020 V1.03 Micromeritics Instrument (Norcross, GA, USA), based on N_2 adsorption, using a sample mass of 2.5 g.

2.4. Mechanical Properties of NR/$CaCO_3$ Composites

2.4.1. Tensile Properties

The tensile properties, namely the tensile strength, elongation at break, and 100% (M100) and 300% moduli (M300), of neat NR and NR/$CaCO_3$ for all variations of filler loading were determined according to the ASTM D 412-98 [40] standard test using dumbbell-shaped specimens with 1 mm thickness and a type C die for cutting. A tensile machine (Instron 5566, Instron, High Wycombe, UK) was used with a crosshead speed rate of 500 mm/min. The average results were taken from 5 testing specimens.

2.4.2. Hardness (Shore A)

The hardness (Shore A) of rubber vulcanizates with and without filler was evaluated using a hardness tester (Wallace H17A, Surrey, UK) in accordance with the ASTM D2240-97 standard [41]. The specimen thickness was 6 mm. The testing was conducted at different positions on the specimen, and the average hardness value of each specimen was calculated using 6 positions.

2.4.3. Statistical Analysis

An analysis of variance (ANOVA) was performed using the Single Factor program with the Data Analysis tool in Microsoft Excel 2019. The *t*-test method was used for the comparison of two samples, assuming unequal variance to determine the significant differences among the mean values ($p < 0.05$).

3. Results and Discussion

3.1. Untreated and Treated $CaCO_3$ Powders

The features of untreated and treated $CaCO_3$ obtained by precipitation in the sugar solution are demonstrated in Figure 1a,b, respectively. Figure 1a shows that, without the olive soap surface treatment, the $CaCO_3$ powders settled in the bottom of the container, whereas the treated $CaCO_3$ particles floated on the surface of the sugar solution (Figure 1b). This is a simple indication that the surface of the $CaCO_3$ was altered. Then, the surface wettability was evaluated by considering the contact angle of the untreated and treated $CaCO_3$, as shown in Figure 1c,d, respectively. The average contact angle of untreated $CaCO_3$ powder is 16.5°, indicating hydrophilic particles. Conversely, the contact angle of $CaCO_3$ powder treated with olive soap is 145.4° (Figure 1d), revealing hydrophobic behavior. The fatty acid composition of olive oil consists of 55–83% oleic acid, 3.5–21% linoleic acid, and 7.5–20% palmitic ester [42]. These fatty acids interact with sodium hydroxide

(NaOH) by saponification, producing sodium carboxylate (RCOONa) and glycerol. The formation of soap molecules adsorbed on the surface of $CaCO_3$ particles is demonstrated in Figure 2. The soap molecules contain two parts, a hydrophilic head and a hydrophobic tail. The hydrophilic heads are located at the $CaCO_3$ surface, while the hydrophobic tails extend out into the surroundings. After the addition of the soap solution into the $CaCl_2$ reactant solution, the sodium carboxylate chains could be interchanged with Ca^{2+} ions, forming Ca carboxylate ($R(COO^-)_2Ca$). During the precipitation between Ca^{2+} and CO_3^{2+} ions, some of the carboxylate chains were adsorbed on the surfaces of the $CaCO_3$ particles, resulting in hydrophobic surface behavior. Therefore, the agreement between the physical appearance of the precipitated $CaCO_3$ solution and the contact angle confirmed that the surface wettability of $CaCO_3$ can be changed from hydrophilic to hydrophobic by precipitation using olive soap.

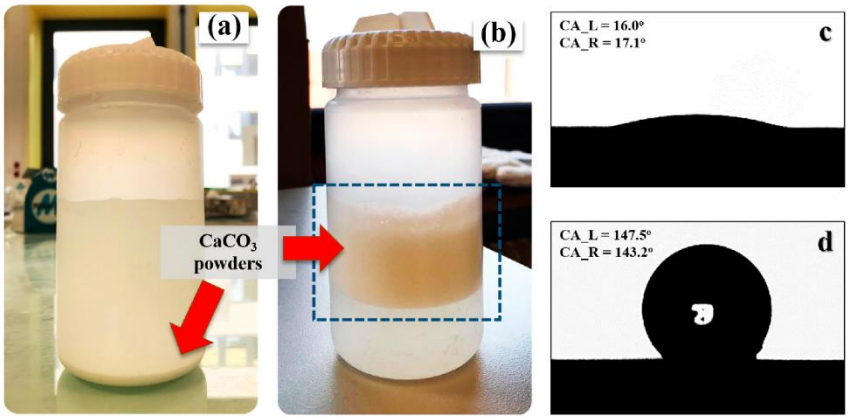


Figure 1. Physical appearance of $CaCO_3$ powder in solution before centrifugation: (**a**) untreated $CaCO_3$ powder and (**b**) treated $CaCO_3$ powder. The contact angle (CA) behavior of (**c**) untreated and (**d**) treated $CaCO_3$ powders, presenting CA values for the left (L) and right (R) sides of the droplet.

The morphological shape and particle size distribution of the prepared $CaCO_3$ particles were investigated by SEM and TEM, as shown in Figure 3. The spherical shape of untreated and treated $CaCO_3$ was observed by SEM, as shown in Figure 3a,d, respectively. Both samples also exhibited narrow particle size distributions. The histograms in Figure 3c,e reveal the particle sizes of untreated and treated $CaCO_3$ particles, respectively. The particles of untreated $CaCO_3$ were on the submicron scale (0.42 ± 0.14 µm), which was due to the use of sucrose as a medium in the precipitation process [18,20]. The addition of olive soap in the precipitation system during $CaCO_3$ preparation affected the surface modification of $CaCO_3$, as discussed earlier, and increased the particle size of $CaCO_3$ (0.52 ± 0.16 µm), as shown in Table 2, although the particles remained in the submicron range.

Table 2. Particle size, BET-specific surface area, contact angle, and polymorphic phase percentage of obtained $CaCO_3$.

Types of $CaCO_3$	Particle Size (µm) *	BET Value (m^2/g)	Contact Angle (°)	Polymorphic Phase (%)	
				Vaterite	Calcite
Untreated	0.42 ± 0.14	39.32	16.5	99.1	0.9
Treated	0.52 ± 0.16	34.45	145.4	99.8	0.2

* The data are presented as means ± standard deviations.

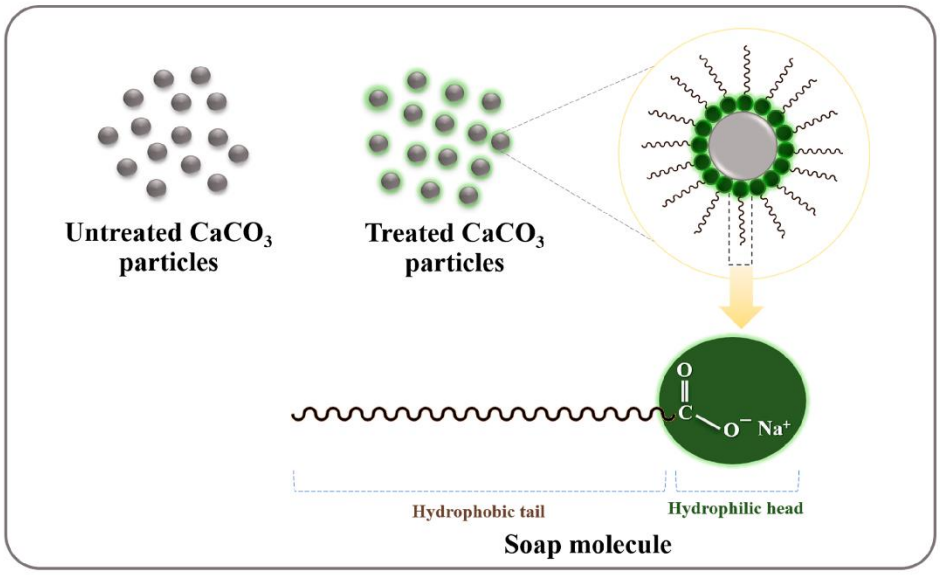


Figure 2. Proposed schematic adsorption of soap molecules on the surface of $CaCO_3$ particles.

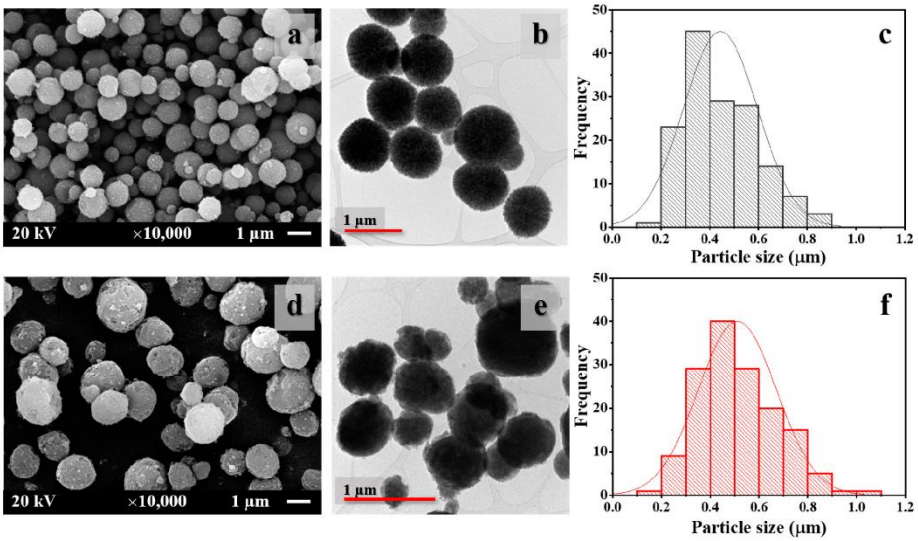


Figure 3. SEM micrographs at 10,000× magnification (1 μm scale bar), TEM micrographs with 1 μm scale bar, and particle size distribution histograms of (**a**–**c**) untreated $CaCO_3$ and (**d**–**f**) treated $CaCO_3$ powders.

The TEM micrographs of untreated $CaCO_3$ (Figure 3b) and treated $CaCO_3$ (Figure 3e) particles were obtained. The surface morphology of $CaCO_3$ particles after treatment with olive soap was changed, presenting rougher and larger particles than the untreated particles. This may be attributed to not only the adsorbed soap on the surface of treated $CaCO_3$ but also the penetration of soap inside the particles.

The specific surface area of the untreated and treated $CaCO_3$ was analyzed by the BET technique. The BET values shown in Table 2 reveal that the specific surface area of untreated $CaCO_3$ powders (39.32 m^2/g) was higher than that of the treated $CaCO_3$ powders (34.45 m^2/g). The lower surface area is consistent with the larger particle size of treated $CaCO_3$ particles. Moreover, the obtained BET values indicate that the $CaCO_3$ particles were porous, which is typical and unique to the vaterite polymorph.

The ATR-FTIR and Raman spectra of the $CaCO_3$ samples are shown in Figure 4. In Figure 4a, the ATR-FTIR spectra of both $CaCO_3$ particle types show the typical bands of vaterite, corresponding to doubly degenerate in-plane OCO deformation bending and CO_3 out-of-plane bending at 745 and 875 cm^{-1}, respectively [36]. In contrast, the characteristic peak of calcite was not observed at 713 cm^{-1}, corresponding to the doubly degenerate in-plane OCO bending deformation [43]. The Raman spectra in Figure 4b support the findings of the FTIR spectra. The typical peaks of the vaterite polymorph appear at 744, 1076, and 1089 cm^{-1}, corresponding to the ν_4 in-plane bending, ν_1 symmetric stretching, and ν_3 symmetric stretching of CO_3^{2-}, respectively [44,45]. Furthermore, the characteristic peak of calcite at 711 cm^{-1} (ν_4 in-plane bending) was absent.

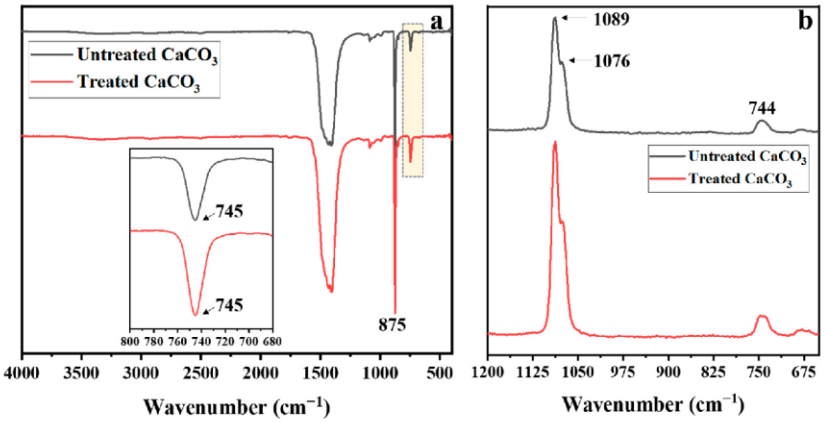


Figure 4. (**a**) ATR-FTIR spectra in the wavenumber range of 400–4000 cm^{-1} and (**b**) Raman spectra (650–1200 cm^{-1}) of untreated and treated $CaCO_3$ particles.

The XRD patterns of untreated and treated $CaCO_3$ powders were investigated in the 2θ range of 20–40°, as shown in Figure 5a,b, respectively. The typical peaks of vaterite located at 20.0°, 24.9°, 27.0°, and 32.7° are attributed to the reflections of the (004), (100), (101), and (102) crystalline planes, respectively [46]. Additionally, the typical peak of the calcite polymorph at 29.3° was not found [47]. Powder diffraction analysis coupled with Rietveld analysis (using the MAUD software) is a powerful technique to clarify the structure and polymorphic phase content of powders. The XRD refinement of untreated spherical $CaCO_3$ powder revealed a volume fraction of 99.1% for vaterite and 0.9% for calcite, whereas the treated $CaCO_3$ powder contained 99.8% vaterite and 0.2% calcite. The minimization of the particle size and maximization of the vaterite content depend strongly on the use of sucrose

as an aqueous medium [20,48]. The results confirmed that adding olive soap in the mixing system resulted in a hydrophobic powder and provided high content of the vaterite phase.

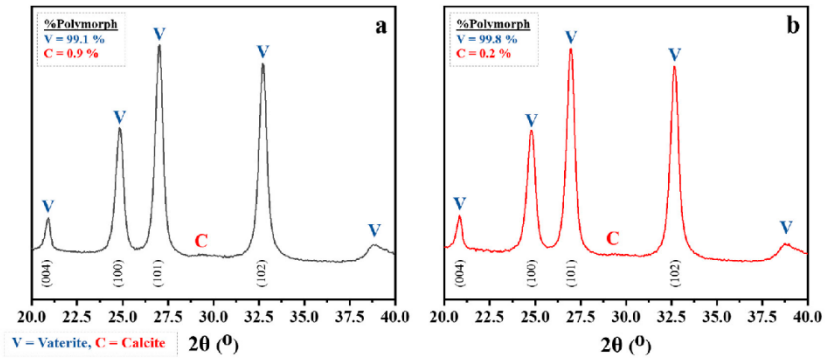


Figure 5. XRD patterns of the obtained $CaCO_3$ powders: (**a**) untreated $CaCO_3$ and (**b**) treated $CaCO_3$, with calculated percentages of the polymorphic phases via Rietveld refinement using MAUD software.

The thermal properties of the $CaCO_3$ powders were examined by TGA, as presented in Figure 6. The mass change of the sample during heating as a function of temperature (40–800 °C) was demonstrated in TGA thermograms and derivative thermogravimetric (DTG) curves. For both the untreated (Figure 6a) and treated $CaCO_3$ (Figure 6b), the decomposition started around 200 °C and was completed at 250 °C, with weight losses of 3–4%, which may have arisen from the decomposition of the sucrose used as an aqueous medium in the preparation process. In the case of hydrophobic $CaCO_3$ powder, the decomposition of organic fuel in the soap occurred in the range of 400–500 °C (see Figure 6b). Moreover, the decomposition of $CaCO_3$ to CaO and CO_2 occurred for both the untreated and treated samples in the range of 650–750 °C [49].

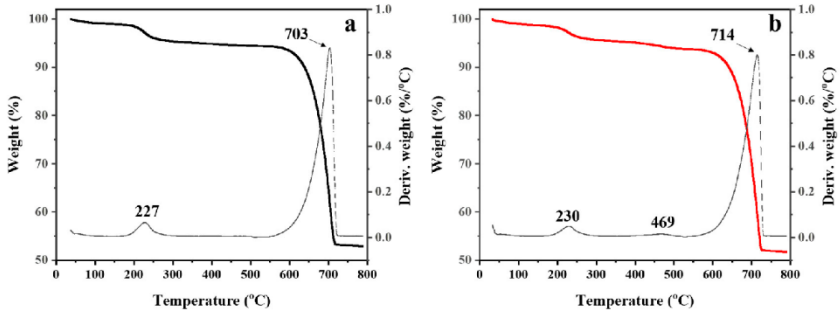


Figure 6. TGA thermograms (black and red solid lines) and DTG curves (dashed line) of (**a**) untreated $CaCO_3$ and (**b**) treated $CaCO_3$ powders.

3.2. *NR/Untreated $CaCO_3$ and NR/Treated $CaCO_3$ Composites*

The NR/untreated $CaCO_3$ and NR/treated $CaCO_3$ composites were prepared, and their characteristics were analyzed by ATR-FTIR spectroscopy. Figure 7a shows the ATR-FTIR spectra of neat NR and NR/$CaCO_3$ composites filled with 20 phr of $CaCO_3$. The chemical structure of NR comprises cis 1,4-polyisoprene. The characteristic peaks of the

isoprene unit in NR were found at 837, 1642, 2853, 2926, and 2961 cm^{-1}, assigned to the =C-H out-of-plane deformation, C=C stretching, CH_2 stretching, CH_3 stretching, and =C-H stretching, respectively. The FTIR spectra of NR/$CaCO_3$ composites exhibited an additional peak of $CaCO_3$ at 745 cm^{-1} (Figure 7b), indicating the typical band of vaterite for doubly degenerate in-plane OCO. As a result, the vaterite polymorph of $CaCO_3$ incorporated in NR latex in the preparation of NR/$CaCO_3$ compounds did not convert into the more thermodynamically stable form of calcite. This is because the negative charges of NR particles limit the polymorphic phase transformation of $CaCO_3$ fillers [20]. The XRD patterns of $CaCO_3$ fillers incorporated in NR are shown in Figure 7c. The typical crystalline phases of vaterite $CaCO_3$ were present at 21.0°, 24.9°, 27.1°, and 32.8°. Meanwhile, the typical calcite peak in the range of 28–29° was not detected. Additionally, peaks were observed at 29.5°, 31.5°, and 36.3° for the ZnO that was used in the curing agents. The FTIR and XRD results agree well, demonstrating that no characteristic peaks of calcite were found in the rubber/$CaCO_3$ composites.

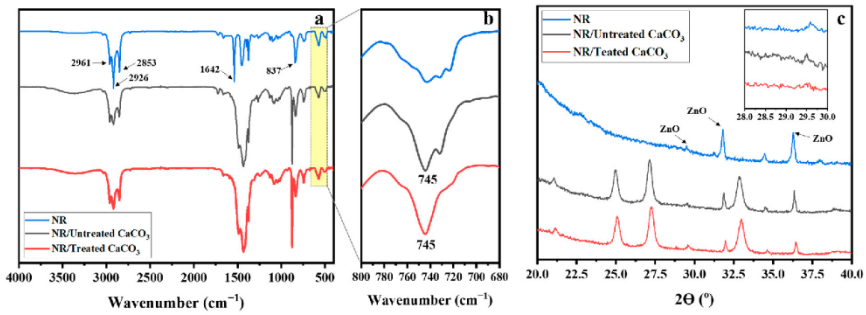


Figure 7. ATR-FTIR spectra of neat NR and NR/$CaCO_3$ composites (at filler loading of 20 phr) in the range of wavenumbers (**a**) 400–4000 cm^{-1} and (**b**) 680–800 cm^{-1}, and (**c**) X-ray diffractogram of NR and NR/$CaCO_3$ composite at filler loading of 20 phr.

The morphologies of the tensile-fractured surfaces of neat NR and NR/$CaCO_3$ composites at 20 phr filler loading are shown in Figure 8. Figure 8a shows the smooth surface of the NR matrix without filler. The NR/untreated $CaCO_3$ (Figure 8b) and NR/treated $CaCO_3$ (Figure 8c) morphological surfaces exhibit both smooth surfaces from the rubber and roughness from the $CaCO_3$ particles, and they maintained their initial spherical shape and vaterite polymorph in NR without any transformation.

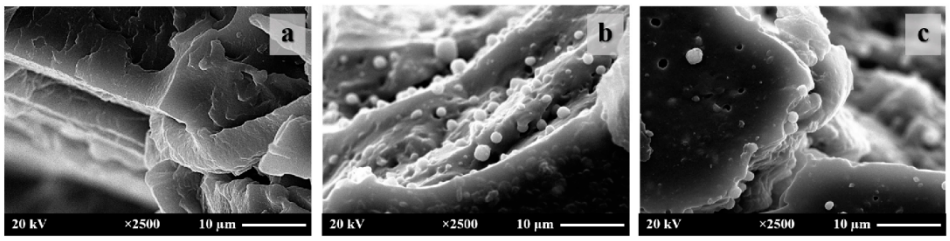


Figure 8. SEM images of the tensile-fractured surface at 2500×, with 10 µm scale bar, of (**a**) neat NR, (**b**) NR/untreated $CaCO_3$ composite (20 phr), and (**c**) NR/treated $CaCO_3$ composite (20 phr).

The mechanical properties of NR filled with untreated and treated spherical $CaCO_3$ powders at different loadings (0, 10, 20, 40, and 60 phr) were investigated, including the 100% and 300% moduli, tensile strength, elongation at break, and hardness. The 100% (M100) and 300% (M300) moduli of neat NR, NR/untreated $CaCO_3$, and NR/treated $CaCO_3$ composites are presented in Figure 9a,b, respectively. The modulus is an indication of the relative stiffness of the composite. The incorporation of 10 phr $CaCO_3$ filler did not result in a significant change in the moduli of the composites. However, increasing the filler loading increased the moduli of the rubber composites, which can be ascribed to the rigidity of the $CaCO_3$. Notably, NR/untreated $CaCO_3$ exhibited a higher modulus than NR/treated $CaCO_3$ composites, which may be attributed to an effect of the soap molecules.

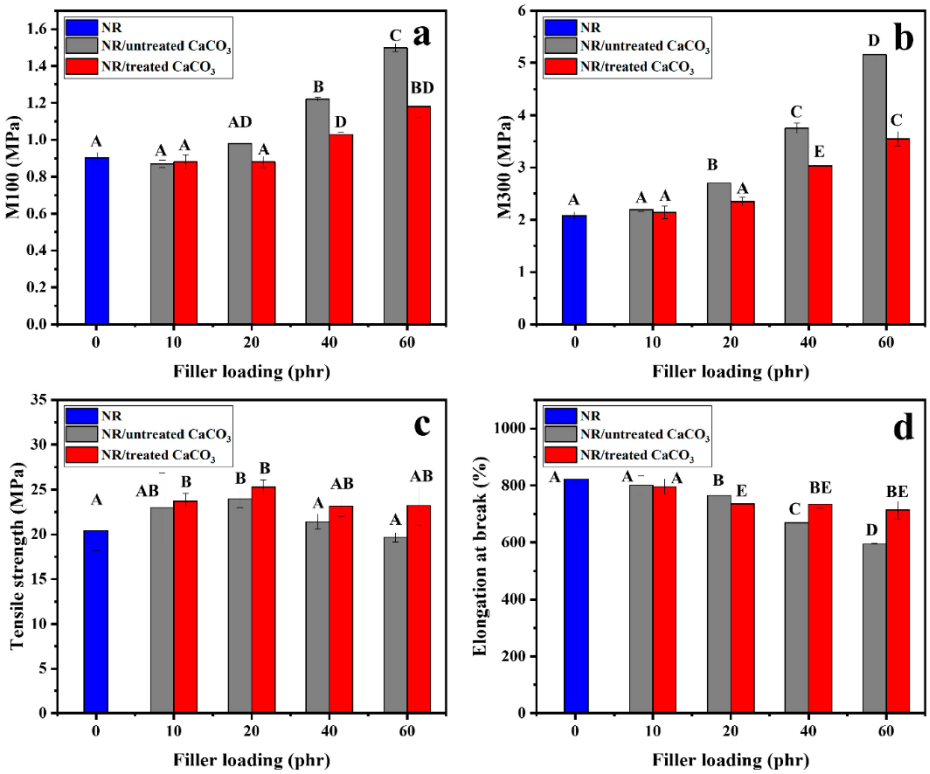


Figure 9. Mechanical properties of neat NR, NR/untreated $CaCO_3$, and NR/treated $CaCO_3$ composites for filler loadings of 0–60 phr: (**a**) M100, (**b**) M300, (**c**) elongation at break, and (**d**) tensile strength. The results were analyzed by ANOVA, and the different letters (A, AB, C, D, E, AD, BD, BE) above bars refer to significant differences among the means, $p < 0.05$.

The tensile strengths of NR/$CaCO_3$ composites with different filler loadings (0–60 phr) are presented in Figure 9c, as analyzed by ANOVA. The tensile strength of neat NR was 20.35 ± 2.22 MPa. After adding spherical $CaCO_3$ powders to the NR, the tensile strength was significantly increased compared with the neat NR (as shown using the different letters above the bars). This result is contrary to the use of $CaCO_3$ in plastic, which decreases the

tensile strength [50]. Moreover, in the case of the same filler content, the tensile strength of untreated and treated $CaCO_3$ added to NR results in significantly different elongation at break. The addition of untreated $CaCO_3$ powder at 20 phr provided the highest tensile strength value (23.95 ± 0.97 MPa). Further increases in the filler loading of untreated $CaCO_3$ to 40 and 60 phr decreased the tensile strength. This may be due to the poor dispersion of the filler in the rubber composites owing to the polarity difference between NR and $CaCO_3$. This can also be explained by the non-homogeneous distributions for high filler concentrations in the rubber matrix, possibly resulting in filler aggregation, which can cause stress concentration and accelerate failure under tension. The tensile strength of the NR/treated $CaCO_3$ composites was higher than that of the NR/untreated $CaCO_3$ composite at all filler loadings. This may be due to the improved interfacial interaction between the NR and treated $CaCO_3$. The highest tensile strength was obtained for NR/treated $CaCO_3$ composites with 20 phr loading (25.28 ± 0.81 MPa). Similarly, Y. Yu and coworkers loaded NR with silanized silica-encapsulated $CaCO_3$ or untreated $CaCO_3$ [51]. Their results showed that the tensile strength of the NR/silanized silica-encapsulated $CaCO_3$ vulcanizate was improved compared with the NR/$CaCO_3$ vulcanizate, which was attributed to the enhancements in the interfacial compatibility and dispersion of the $CaCO_3$ in the rubber matrix. Herein, when the treated $CaCO_3$ loading was increased further to 40 and 60 phr, the tensile strength was slightly decreased but still significantly higher than that for the NR/untreated $CaCO_3$. The decreased tensile strength at high filler loadings may be due to filler–filler aggregation.

Regarding the elongation of NR/$CaCO_3$ composites, as shown in Figure 9d, there was a decrease in the strain at break in NR composites loaded with the $CaCO_3$ filler. The elongation at break for neat NR was 821.63 ± 10.25%. For 10 phr of $CaCO_3$ particles, the elongation at break of the filled NR composites was similar to that of the neat NR. This is because the low amount of the filler did not disrupt the elongation of rubber chain entanglements during extension. Increasing the filler loading to 20, 40, and 60 phr gradually decreased the elongation at break in the NR/filler composites. The elongation at break decreased to 594.06 ± 3.24% in NR/untreated $CaCO_3$ composites and 713.36 ± 31.56% in NR/treated $CaCO_3$ composites at 60 phr loading. These results indicate that the addition of rigid inorganic particles reduced the ductility of the rubber composites. In addition, the formation of filler–filler aggregation may have increased the discontinuity of the rubber matrix, resulting in reduced elongation. Furthermore, the elongation of NR/treated $CaCO_3$ composites was higher than that of the NR/untreated $CaCO_3$ composites at all filler loadings. This can be explained by the presence of the soap on the surface of the treated $CaCO_3$, which can serve as a lubricant to facilitate the flow of rubber chains during elongation. Moreover, the spherical-shaped $CaCO_3$ treated with olive soap did not show significantly decreased elongation at break even when a large amount (40–60 phr) of the filler was added.

Figure 10 shows the Shore A hardness values of neat NR and NR/$CaCO_3$ composites. Generally, the Shore A hardness is used to evaluate the resistance of rubbers and elastomers to indentation. Higher values imply greater hardness, while lower values indicate softer materials. Therefore, it is not surprising that the hardness of NR composites increased when the $CaCO_3$ filler content increased. The Shore A hardness of neat NR was 40.5 ± 0.3, but the Shore A hardness increased to 50.9 ± 0.2 for NR/untreated $CaCO_3$ and 50.2 ± 0.5 for NR/treated $CaCO_3$ composites at a loading of 60 phr. At 20 and 40 phr loadings, the Shore A hardness values of NR/treated $CaCO_3$ were higher than those of NR/untreated $CaCO_3$. This is attributed to the enhanced distribution of the treated $CaCO_3$ filler in the rubber matrix compared with the case of untreated $CaCO_3$.

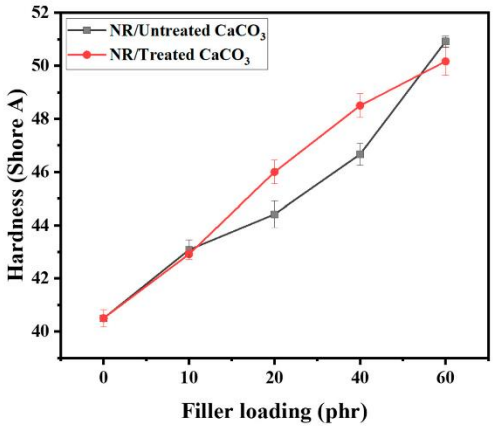


Figure 10. Shore A hardness of NR/$CaCO_3$ composites.

The thermal decomposition profiles of neat NR, NR/untreated $CaCO_3$, and NR/treated $CaCO_3$ samples at 20 phr filler loading in terms of TGA curves (Figure 11a) and DTG curves (Figure 11b) were determined. The NR revealed significant degradation in the range of 360–450 °C, which was ascribed to the polymer's pyrolysis, with a peak at 391 °C. NR filled with $CaCO_3$ powders exhibited major degradation in a similar range, resulting in weight loss of approximately 65% due to the decomposition of NR. A second stage (650–750 °C) of thermal decomposition appeared for NR/$CaCO_3$ composites, with weight losses of 16–20%. In addition, in the range of 200–320 °C, the weight loss of the NR was slightly higher than that of the NR/$CaCO_3$ composites. The results suggest that $CaCO_3$ improved the thermal resistance of the rubber composites. This result is consistent with the work of Umunakwe et al., who investigated NR filled with carbon black and calcium carbonate. They demonstrated that calcium carbonate could improve the thermal resistance of the rubber vulcanizate compared with the carbon black-filled rubber [52].

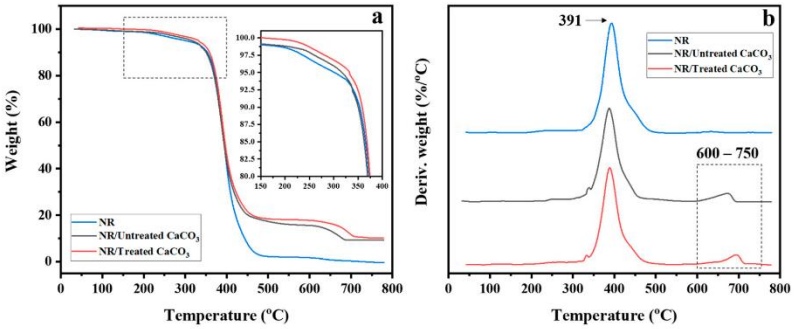


Figure 11. (**a**) TGA curves and (**b**) DTG curves of neat NR, NR/untreated $CaCO_3$, and NR/treated $CaCO_3$ composites at 20 phr loading in the temperature range of 40–800 °C, with scanning rate of 20 °C min^{-1}.

4. Conclusions

Spheroidal-shaped $CaCO_3$ particles with and without surface treatment were easily synthesized by precipitation using sucrose as an aqueous medium to reduce the particle size to the submicron scale, and olive soap was used to modify the surface properties of the $CaCO_3$ particles. The optical contact angle of $CaCO_3$ without treatment was 16.5°, which reflects the general nature of $CaCO_3$, while that of treated $CaCO_3$ was 145.4°, which is considered hydrophobic. The $CaCO_3$ particles were larger and rougher after treatment with olive soap because of the soap molecules adsorbed on the surfaces of $CaCO_3$ particles. The percentage of the vaterite crystalline phase was higher than 99% for both the untreated and treated $CaCO_3$ powders. The mechanical properties of NR vulcanizates were enhanced when $CaCO_3$ fillers (0–60 phr) were applied. The NR/treated $CaCO_3$ composites provided higher tensile strength than the NR/untreated $CaCO_3$ composites for all variations of filler loading. This may have been due to the improved interfacial interaction between the NR and hydrophobic $CaCO_3$. The filler loading of 20 phr was optimal in obtaining the highest tensile strength in the rubber composites. In addition, the elongation ability of the NR/treated $CaCO_3$ only decreased slightly, while the hardness of the NR composites was significantly improved. In summary, spherical $CaCO_3$ particles can be used to effectively reinforce and improve the mechanical properties of NR. The facile method for the surface modification of the spherical-shaped $CaCO_3$ using olive soap resulted in enhanced hardness and tensile strength. These findings can broaden the application of $CaCO_3$ in polymer composites.

Author Contributions: Conceptualization, K.L., A.G., P.D. and P.P.; methodology, K.L. and W.T.; validation and data curation, K.L.; writing—original draft preparation—K.L.; writing—review and editing, P.P.; funding acquisition, A.G., P.D. and P.P. All authors have read and agreed to the published version of the manuscript.

Funding: This research project is supported by ERASMUS+ Thailand (2019-1-FR01-KA107-062076) between Mahidol University (Thailand) and Le Mans University (France), and the Sritrangtong Scholarship Program from the Faculty of Science, Mahidol University.

Institutional Review Board Statement: Not applicable.

Data Availability Statement: The data presented in this research are available on request from the corresponding author.

Acknowledgments: We would like to gratefully thank the Sritrangtong Scholarship Program from the Faculty of Science, Mahidol University to K. Longkaew. The authors acknowledge the facilities and technical support of the Rubber Technology Research Centre (RTEC), Faculty of Science, Mahidol University, and the Mahidol University Frontier Research Facility (MU-FRF), including its scientists (Napawol Udpuay, Chawalit Takoon, Suwilai Chaveanghong, and Bancha Panyacharoen).

Conflicts of Interest: The authors declare no conflict of interest.

References

1. Phinyocheep, P.; Phetphaisit, C.W.; Derouet, D.; Campistron, I.; Brosse, J.C. Chemical degradation of epoxidized natural rubber using periodic acid: Preparation of epoxidized liquid natural rubber. *J. Appl. Polym. Sci.* **2005**, *95*, 6–15. [CrossRef]
2. Phinyocheep, P. 3—Chemical modification of natural rubber (NR) for improved performance. In *Chemistry, Manufacture and Applications of Natural Rubber*; Kohjiya, S., Ikeda, Y., Eds.; Woodhead Publishing: Cambridge, UK, 2014; pp. 68–118.
3. Singh, M. The Colloidal Properties of Commercial Natural Rubber Latex Concentrates. *J. Rubber Res.* **2018**, *21*, 119–134. [CrossRef]
4. Fisher, H.L. Vulcanization of rubber vulcanization of rubber. *Ind. Eng. Chem.* **1939**, *31*, 1381–1389. [CrossRef]
5. Leblanc, J.L. Rubber–filler interactions and rheological properties in filled compounds. *Prog. Polym. Sci.* **2002**, *27*, 627–687. [CrossRef]
6. Rothon, R. Particulate Fillers in Elastomers. In *Fillers for Polymer Applications*; Rothon, R., Ed.; Springer International Publishing: Cham, Switzerland, 2017; pp. 125–146.
7. Turku, I.; Kärki, T. Research progress in wood-plastic nanocomposites: A review. *J. Thermoplast. Compos. Mater.* **2013**, *27*, 180–204. [CrossRef]
8. Kim, J.H.; Jeong, H.Y. A study on the material properties and fatigue life of natural rubber with different carbon blacks. *Int. J. Fatigue* **2005**, *27*, 263–272. [CrossRef]

9. Kaliyathan, A.V.; Rane, A.V.; Huskic, M.; Kunaver, M.; Kalarikkal, N.; Rouxel, D.; Thomas, S. Carbon black distribution in natural rubber/butadiene rubber blend composites: Distribution driven by morphology. *Compos. Sci. Technol.* **2020**, *200*, 108484. [CrossRef]
10. Robertson, C.G.; Hardman, N.J. Nature of Carbon Black Reinforcement of Rubber: Perspective on the Original Polymer Nanocomposite. *Polymers* **2021**, *13*, 538. [CrossRef]
11. Sarkawi, S.S.; Dierkes, W.K.; Noordermeer, J.W.M. Reinforcement of natural rubber by precipitated silica: The influence of processing temperature. *Rubber Chem. Technol.* **2014**, *87*, 103–119. [CrossRef]
12. Fang, Q.; Song, B.; Tee, T.-T.; Sin, L.T.; Hui, D.; Bee, S.-T. Investigation of dynamic characteristics of nano-size calcium carbonate added in natural rubber vulcanizate. *Compos. Part. B Eng.* **2014**, *60*, 561–567. [CrossRef]
13. Lay, M.; Hamran, N.; Rashid, A.A. Ultrafine calcium carbonate-filled natural rubber latex film: Mechanical and post-processing properties. *Iran. Polym. J.* **2019**, *28*, 849–858. [CrossRef]
14. Sadeghi Ghari, H.; Jalali-Arani, A. Nanocomposites based on natural rubber, organoclay and nano-calcium carbonate: Study on the structure, cure behavior, static and dynamic-mechanical properties. *Appl. Clay Sci.* **2016**, *119*, 348–357. [CrossRef]
15. Akbari, A.; Jawaid, M.; Hassan, A.; Balakrishnan, H. Epoxidized natural rubber toughened polylactic acid/talc composites: Mechanical, thermal, and morphological properties. *J. Compos. Mater.* **2013**, *48*, 769–781. [CrossRef]
16. Khan, I.; Bhat, A.H. Micro and Nano Calcium Carbonate Filled Natural Rubber Composites and Nanocomposites. In *Natural Rubber Materials, Volume 2: Composites and Nanocomposites*; Thomas, S., Maria, H.J., Joy, J., Chan, C.H., Pothen, L.A., Eds.; The Royal Society of Chemistry: Cambridge, UK, 2013; Volume 2.
17. Konopacka-Łyskawa, D.; Lackowski, M. Influence of ethylene glycol on $CaCO_3$ particles formation via carbonation in the gas–slurry system. *J. Cryst. Growth* **2011**, *321*, 136–141. [CrossRef]
18. Pérez-Villarejo, L.; Takabait, F.; Mahtout, L.; Carrasco-Hurtado, B.; Eliche-Quesada, D.; Sánchez-Soto, P.J. Synthesis of vaterite $CaCO_3$ as submicron and nanosized particles using inorganic precursors and sucrose in aqueous medium. *Ceram. Int.* **2018**, *44*, 5291–5296. [CrossRef]
19. Gibaud, A.; Younas, D.; Matthews, L.; Narayanan, T.; Longkaew, K.; Hageberg, I.U.; Chushkin, Y.; Breiby, D.W.; Chattopadhyay, B. Insights into the precipitation kinetics of $CaCO_3$ particles in the presence of polystyrene sulfonate using in situ small-angle X-ray scattering. *J. Appl. Crystallogr.* **2023**, *56*, 1114–1124. [CrossRef]
20. Longkaew, K.; Tessanan, W.; Daniel, P.; Phinyocheep, P.; Gibaud, A. Using sucrose to prepare submicrometric $CaCO_3$ vaterite particles stable in natural rubber. *Adv. Powder Technol.* **2023**, *34*, 103924. [CrossRef]
21. Baqiya, M.A.; Lailiyah, Q.; Riyanto, A.; Arifin, Z.; Triwikantoro; Zainuri, M.; Pratapa, S.; Darminto. Precipitation Process of $CaCO_3$ from Natural Limestone for Functional Materials. *J. AOAC Int.* **2020**, *103*, 373–381. [CrossRef]
22. Owuamanam, S.; Cree, D. Progress of Bio-Calcium Carbonate Waste Eggshell and Seashell Fillers in Polymer Composites: A Review. *J. Compos. Sci.* **2020**, *4*, 70. [CrossRef]
23. Rodriguez-Blanco, J.D.; Shaw, S.; Benning, L.G. The kinetics and mechanisms of amorphous calcium carbonate (ACC) crystallization to calcite, viavaterite. *Nanoscale* **2011**, *3*, 265–271. [CrossRef]
24. Boyjoo, Y.; Pareek, V.K.; Liu, J. Synthesis of micro and nano-sized calcium carbonate particles and their applications. *J. Mater. Chem. A* **2014**, *2*, 14270–14288. [CrossRef]
25. Jimoh, O.A.; Ariffin, K.S.; Hussin, H.B.; Temitope, A.E. Synthesis of precipitated calcium carbonate: A review. *Carbonates Evaporites* **2018**, *33*, 331–346. [CrossRef]
26. Nehrke, G.; Van Cappellen, P. Framboidal vaterite aggregates and their transformation into calcite: A morphological study. *J. Cryst. Growth* **2006**, *287*, 528–530. [CrossRef]
27. Bragg, W.L. The structure of aragonite. *Proc. R. Soc. London Ser. A Contain. Pap. A Math. Phys. Character* **1997**, *105*, 16–39. [CrossRef]
28. Kogo, M.; Suzuki, K.; Umegaki, T.; Kojima, Y. Control of aragonite formation and its crystal shape in $CaCl_2$-Na_2CO_3-H_2O reaction system. *J. Cryst. Growth* **2021**, *559*, 125964. [CrossRef]
29. Tas, A.C. Monodisperse Calcium Carbonate Microtablets Forming at 70 °C in Prerefrigerated CaCl2–Gelatin–Urea Solutions. *Int. J. Appl. Ceram. Technol.* **2009**, *6*, 53–59. [CrossRef]
30. Lu, J.; Ruan, S.; Liu, Y.; Wang, T.; Zeng, Q.; Yan, D. Morphological characteristics of calcium carbonate crystallization in CO_2 pre-cured aerated concrete. *RSC Adv.* **2022**, *12*, 14610–14620. [CrossRef]
31. Utrera-Barrios, S.; Perera, R.; León, N.; Santana, M.H.; Martínez, N. Reinforcement of natural rubber using a novel combination of conventional and in situ generated fillers. *Compos. Part C Open Access* **2021**, *5*, 100133. [CrossRef]
32. Zhao, R.; Yin, Z.; Zou, W.; Yang, H.; Yan, J.; Zheng, W.; Li, H. Preparation of High-Strength and Excellent Compatibility Fluorine/Silicone Rubber Composites under the Synergistic Effect of Fillers. *ACS Omega* **2023**, *8*, 3905–3916. [CrossRef]
33. Surya, I.; Sinaga, R. Tensile and rheometric properties of calcium carbonate-filled natural rubber compounds without/with lauryl alcohol. *IOP Conf. Ser. Mater. Sci. Eng.* **2019**, *505*, 012146. [CrossRef]
34. Shi, X.; Rosa, R.; Lazzeri, A. On the Coating of Precipitated Calcium Carbonate with Stearic Acid in Aqueous Medium. *Langmuir* **2010**, *26*, 8474–8482. [CrossRef] [PubMed]
35. Cao, Z.; Daly, M.; Clémence, L.; Geever, L.M.; Major, I.; Higginbotham, C.L.; Devine, D.M. Chemical surface modification of calcium carbonate particles with stearic acid using different treating methods. *Appl. Surf. Sci.* **2016**, *378*, 320–329. [CrossRef]

36. Abidi, L.; Amiard, F.; Delorme, N.; Ouhenia, S.; Gibaud, A. Using saponified olive oil to make cost effective calcium carbonate particles superhydrophobic. *Adv. Powder Technol.* **2022**, *33*, 103399. [CrossRef]
37. Subagjo; Wulandari, W.; Adinata, P.M.; Fajrin, A. Thermal decomposition of dolomite under CO_2-air atmosphere. *AIP Conf. Proc.* **2017**, *1805*, 040006. [CrossRef]
38. Erickson, K.L. Application of Low-Heating Rate TGA Results to Hazard Analyses Involving High-Heating Rates. In Proceedings of the SAMPE'08 Conference, Albuquerque, NM, USA, 18–22 May 2008.
39. Koeipudsa, N.; Chanthateyanonth, R.; Daniel, P.; Phinyocheep, P. Development of natural rubber nanocomposites reinforced with cellulose nanocrystal isolated from oil palm biomass. *J. Polym. Res.* **2022**, *29*, 403. [CrossRef]
40. *ASTM D412-98*; Standard Test Methods for Vulcanized Rubber and Thermoplastic Rubbers and Thermoplastic Elastomers-Tension. American Society for Testing and Materials (ASTM): West Conshohocken, PA, USA, 2002.
41. *ASTM D2240-97*; Standard Test Method for Rubber Property—Durometer Hardness. American Society for Testing and Materials (ASTM): West Conshohocken, PA, USA, 2015.
42. Rodrigues, N.; Casal, S.; Pinho, T.; Cruz, R.; Peres, A.M.; Baptista, P.; Pereira, J.A. Fatty Acid Composition from Olive Oils of Portuguese Centenarian Trees Is Highly Dependent on Olive Cultivar and Crop Year. *Foods* **2021**, *10*, 496. [CrossRef]
43. Reig, F.B.; Adelantado, J.V.; Moya Moreno, M.C. FTIR quantitative analysis of calcium carbonate (calcite) and silica (quartz) mixtures using the constant ratio method. Application to geological samples. *Talanta* **2002**, *58*, 811–821. [CrossRef]
44. Dupont, L.; Portemer, F.; late Michel Figlarz, T. Synthesis and study of a well crystallized $CaCO_3$ vaterite showing a new habitus. *J. Mater. Chem.* **1997**, *7*, 797–800. [CrossRef]
45. Trushina, D.B.; Bukreeva, T.V.; Kovalchuk, M.V.; Antipina, M.N. $CaCO_3$ vaterite microparticles for biomedical and personal care applications. *Mater. Sci. Eng. C Mater. Biol. Appl.* **2014**, *45*, 644–658. [CrossRef]
46. Yang, L.-F.; Chu, D.-Q.; Sun, H.-L.; Ge, G. Room temperature synthesis of flower-like $CaCO_3$ architectures. *New J. Chem.* **2016**, *40*, 571–577. [CrossRef]
47. Thriveni, T.; Nam, S.Y.; Ahn, J.-W.; Um, N. Enhancement of arsenic removal efficiency from mining waste water by accelerated carbonation. In Proceedings of the IMPC 2014—27th International Mineral Processing Congress, Santiago, Chile, 20–24 October 2014.
48. Konopacka-Łyskawa, D.; Czaplicka, N.; Kościelska, B.; Łapiński, M.; Gębicki, J. Influence of Selected Saccharides on the Precipitation of Calcium-Vaterite Mixtures by the CO_2 Bubbling Method. *Crystals* **2019**, *9*, 117. [CrossRef]
49. Abdolmohammadi, S.; Siyamak, S.; Ibrahim, N.A.; Yunus, W.M.Z.W.; Rahman, M.Z.A.; Azizi, S.; Fatehi, A. Enhancement of Mechanical and Thermal Properties of Polycaprolactone/Chitosan Blend by Calcium Carbonate Nanoparticles. *Int. J. Mol. Sci.* **2012**, *13*, 4508–4522. [CrossRef] [PubMed]
50. Buasri, A.; Chaiyut, N.; Borvornchettanuwat, K.; Chantanachai, N.; Thonglor, K. Thermal and Mechanical Properties of Modified $CaCO_3$/PP Nanocomposites. *World Acad. Sci. Eng. Technol. Int. J. Chem. Mol. Nucl. Mater. Metall. Eng.* **2012**, *6*, 689–692.
51. Yu, Y.; Zhang, J.; Wang, H.; Xin, Z. Silanized Silica-Encapsulated Calcium Carbonate@Natural Rubber Composites Prepared by One-Pot Reaction. *Polymers* **2020**, *12*, 2668. [CrossRef]
52. Umunakwe, R.; Oyetunji, A.; Adewuyi, B.; Eze, W.; Nwigwe, S.; Umunakwe, I. Mechanical properties and microstructure of hybrid vulcanized natural rubber filled with carbon black and Nano-$CaCO_3$ from achatina achatina shells. *J. Met. Mater. Miner.* **2019**, *29*, 80–89. [CrossRef]

Disclaimer/Publisher's Note: The statements, opinions and data contained in all publications are solely those of the individual author(s) and contributor(s) and not of MDPI and/or the editor(s). MDPI and/or the editor(s) disclaim responsibility for any injury to people or property resulting from any ideas, methods, instructions or products referred to in the content.

BIOGRAPHY

NAME	Khansinee Longkaew
DATE OF BIRTH	September 2nd, 1995
PLACE OF BIRTH	Trang, Thailand
INSTITUTIONS ATTENDED	Mahidol University, 2014-2017 Bachelor of Science (Chemistry) Mahidol University and Le Mans University, 2018-2024 Doctor of Philosophy (Polymer Science and Technology)
RESEARCH GRANTS	Sritrangthong Scholarship of Faculty of Science, Mahidol University Scholarship for Young scientists, Faculty of Graduate Studies, Mahidol University ERASMUS+ Mobilité Internationale de Crédits (2019-1-FR01-KA107-062076)
HOME ADDRESS	6 Moo 5, Khaokob Tumbon, Huaiyot District, Trang 92130 Tel. +66 92 593 5097 E-mail: Khansinee.lon@gmail.com
PUBLICATION / PRESENTATION	K. Longkaew, W. Tessanan, P. Daniel, P. Phinyocheep, A. Gibaud. Using sucrose to prepare submicrometric $CaCO_3$ vaterite particles stable in natural rubber. Advanced Powder Technology, 34: 103924-103933 (2023). (Publication) K. Longkaew, A. Gibaud. W. Tessanan, P. Daniel, P. Phinyocheep. Spherical $CaCO_3$:

Synthesis, Characterization, Surface Modification and Efficacy as a Reinforcing Filler in Natural Rubber Composites. Polymers 2023, 15, 4287 (2023). (Publication)

COLLEGE DOCTORAL PAYS DE LA LOIRE
ED MATIERE, MOLECULES MATERIAUX ET GEOSCIENCES

Le Mans Université

Titre : Préparation de particules de carbonate de calcium pour application dans un composite de caoutchouc naturel

Mots clés : Carbonate de Calcium / Vatérite / Aragonite / Fibre de carbonate de calcium / Composite de caoutchouc naturel

Résumé : Cette recherche vise à synthétiser différents types et formes de particules de carbonate de calcium ($CaCO_3$) à l'échelle submicrométrique et nanométrique, et à étudier leurs applications en tant que charges renforçantes pour les composites de caoutchouc naturel (NR). L'étude a donc été divisée en deux parties. Premièrement, la procédure de préparation des particules de CaCO3 était basée sur la méthode de précipitation en solution entre les ions carbonate (CO_3^{2-}) et les ions calcium (Ca^{2+}). La deuxième partie concerne l'étude des propriétés mécaniques des composites NR/$CaCO_3$.

La première partie a commencé par la précipitation de $(NH_4)_2CO_3$ et de $CaCl_2$ dissous dans 50 % en poids de saccharose comme milieu aqueux. Cette condition a entraîné la formation de $CaCO_3$ sphérique, ce qui a été mis en évidence au microscope électronique à balayage (MEB). L'analyse au microscope électronique à transmission (TEM) a révélé une taille de particule de 0,42 ± 0,14 µm avec un rapport d'aspect d'environ un. Lorsque la réaction de précipitation s'est produite en présence d'huile d'olive saponifiée, la propriété de surface du $CaCO_3$ est passée d'hydrophile (angle de contact avec l'eau de 28 ± 2°) à superhydrophobe (angle de contact avec l'eau de 163 ± 2°). Les phases polymorphes typiques de $CaCO_3$ ont été caractérisées par diffraction des rayons X (DRX), infrarouge à transformée de Fourier par réflexion totale atténuée (ATR-FTIR) et spectroscopie Raman. Ces techniques ont révélé que le CaCO3 sphérique non traité et traité représentait environ 99 % du polymorphe de la vatérite. Dans le processus de précipitation utilisant des solutions aqueuses 1M de Na_2CO_3 et 1 M de $CaCl_2$ réalisé à 80 ± 1 °C, du $CaCO_3$ sous forme de fibres agglomérées a été obtenu avec un rapport d'aspect compris entre 8 et 9. Le $CaCO_3$ superhydrophobe sous cette forme a également été synthétisé avec succès. L'angle de contact avec l'eau des fibres traitées et non traitées est respectivement de 29 ± 2° et 167 ± 2°. De plus, le $CaCO_3$ sphérique dispersé dans l'eau à 80°C a donné naissance à des nanoparticules de $CaCO_3$ en forme de fibre qui ont été obtenues via la transformation de la vatérite sphérique en aragonite nanofilaire longue avec le rapport d'aspect le plus élevé de 156,9 par rapport aux autres formes de $CaCO_3$. La fibre $CaCO_3$ non traitée était hydrophile avec un angle de contact avec l'eau de 31 ± 1°, tandis que la fibre $CaCO_3$ traitée avec du savon donnait un angle de contact avec l'eau de 165 ± 5° ; elle était donc superhydrophobe similaire aux autres polymorphes de $CaCO_3$ synthétisés. La DRX a révélé que le $CaCO_3$ en forme de fibres, non traitées et traitées, contenait en majorité de l'aragonite et en moindre mesure de la vatérite et de la calcite. La stabilité thermique de différents types de $CaCO_3$ a également été évaluée par analyse thermogravimétrique (TGA). Les résultats ont montré la calcination des cristaux de $CaCO_3$, du saccharose et du savon.

La deuxième partie a consisté à incorporer le $CaCO_3$ préparé (0, 5, 10, 20, 40, à 60 pce) dans du latex naturel (NR). Il a été constaté que la vatérite $CaCO_3$ non traitée et traitée était stable dans le milieu latex NR.

Les propriétés mécaniques du NR/$CaCO_3$ comprenaient la résistance à la traction, l'allongement à la rupture, la résistance à la déchirure et la dureté Shore A. Il a été constaté que la résistance à la traction des composites NR/$CaCO_3$ augmentait lorsque la charge de $CaCO_3$ augmentait. La résistance à la traction du NR s'est améliorée de 22,68 ± 2,22 MPa de NR pur jusqu'à 23,94 ± 0,97 MPa lorsque des poudres de $CaCO_3$ sphériques non traitées (20 phr) ont été ajoutées, et à 25,28 ± 0,80 MPa de $CaCO_3$ sphérique traité (20 phr) de NR rempli. La résistance à la traction maximale de NR/$CaCO_3$ de type faisceau non traité était de 30,59 ± 3,50 MPa à 40 pce de charge, tandis que 31,51 ± 1,02 MPa de NR/$CaCO_3$ de type faisceau traité à une charge de charge de 20 pce ont été obtenues. Les vulcanisats NR chargés de $CaCO_3$ traités ont donné une résistance à la traction plus élevée que ceux non traités. Cela était dû à une meilleure compatibilité de la dispersion de charge entre le caractère hydrophobe du $CaCO_3$ traité et la propriété hydrophobe du NR. En conséquence, il a été constaté que le NR rempli de particules de fibres de $CaCO_3$ non traitées offrait la résistance à la traction la plus élevée de 31,66 ± 1,80 MPa à 10 phr de charge par rapport aux autres types de $CaCO_3$. Les nanoparticules de grande surface et de rapport d'aspect élevé fibre/nano-fil long de $CaCO_3$ ont amélioré l'adhésion interfaciale entre le $CaCO_3$ et la matrice NR, ce qui pourrait transférer efficacement la contrainte du caoutchoucà la charge pendant l'étirement. Cela a permis de renforcer l'efficacité de la fibre $CaCO_3$. À forte charge de charges (> 20 pce), l'agglomération de $CaCO_3$ s'est produite, entraînant l'apparition de vides et réduisant la résistance à la traction des composites. Il était intéressant de constater que les résistances à la traction du NR/$CaCO_3$ commercial composé de composites NCC, 9QQ et 4QC étaient inférieures à celles du NR incorporé avec du $CaCO_3$ en forme de fibre avec et sans traitement de surface au $CaCO_3$. Dans ce travail, les vulcanisats NR commerciaux remplis de $CaCO_3$ ont donné lieu à une résistance à la déchirure légèrement supérieure à celle des poudres NR/$CaCO_3$ synthétisées. Les profils de stabilité thermique des composites NR/$CaCO_3$ issus des résultats TGA ont révélé que les poudres de $CaCO_3$ peuvent améliorer la résistance thermique des composites de caoutchouc.

De plus, les propriétés mécaniques des composites de noir de carbone (CB) NR/N330 ont également été comparées à celles des composites NR/$CaCO_3$. La résistance à la traction la plus élevée du composite NR/N330 était de 33,03 ± 0,30 MPa à une charge de 20 pce. Ce résultat était comparable à celui du NR/fibre $CaCO_3$ avec une charge de charge de 10 phr. Cette découverte a démontré qu'une charge inférieure en $CaCO_3$ par rapport au N330 pourrait renforcer efficacement les composites NR. Par conséquent, les poudres de $CaCO_3$ préparées ont le potentiel d'élargir leur application non seulement en tant que diluants ou additifs, mais également en tant qu'agents de renforcement.

Title : Preparation of calcium carbonate particles for application in natural rubber composites

Keywords : CALCIUM CARBONATE / VATERITE / ARAGONITE / FIBER-SHAPE CALCIUM CARBONATE / NATURAL RUBBER COMPOSITE

Abstract : This research aims to synthesize different types and shapes of calcium carbonate ($CaCO_3$) particles at a submicrometric and nanoscale, and investigate their applications as reinforcing fillers for natural rubber (NR) composites. The study was therefore divided into two parts. Firstly, the preparation procedure of $CaCO_3$ particles was based on the solution precipitation method between carbonate (CO_3^{2-}) ions and calcium (Ca^{2+}) ions. The second part focused on investigating the mechanical properties of NR/$CaCO_3$ composites.

The first part started with the precipitation of $(NH_4)_2CO_3$ and $CaCl_2$ dissolved in 50% by weight of sucrose as the aqueous medium. This condition resulted in spherical $CaCO_3$ which was evidenced by a scanning electron microscope (SEM). Transmission electron microscope (TEM) analysis revealed a particle size of 0.42 ± 0.14 µm with an aspect ratio of about one. When the precipitation reaction occurred in the presence of olive soap, the surface property of the $CaCO_3$ was changed from hydrophilic (water contact angle of 28 ± 2º) to superhydrophobic powders (water contact angle of 163 ± 2º). The typical polymorphic phases of $CaCO_3$ were characterized by X-ray diffraction (XRD), attenuated total reflection-Fourier transform infrared (ATR-FTIR), and Raman spectroscopy. These techniques revealed that both untreated and treated spherical $CaCO_3$ were about 99% of the vaterite polymorph. In the precipitation process using 1.0 M Na_2CO_3 and 1.0 M $CaCl_2$ aqueous solutions performed at 80 ± 1ºC, bundle-liked $CaCO_3$ was obtained with an aspect ratio in the range of 8 – 9. The superhydrophobic bundle-liked $CaCO_3$ was also successfully synthesized by soap treatment. The water contact angle of untreated and treated bundle-liked are 29 ± 2º, and 167 ± 2º, respectively. Furthermore, the spherical $CaCO_3$ dispersed in water at 80ºC resulted in the fiber-shaped $CaCO_3$ nanoparticles which were achieved via the polymorph transformation from spherical vaterite to long nano-wired aragonite with the highest aspect ratio of 156.9 over other shapes of $CaCO_3$. The untreated fiber $CaCO_3$ was hydrophilic with a water contact angle of 31 ± 1º, while the treated fiber $CaCO_3$ with soap resulted in 165 ± 5º of water contact angle, hence it was superhydrophobic similar to other synthesized $CaCO_3$ polymorphs. The XRD revealed that the untreated and treated bundle-liked and fiber-shaped $CaCO_3$ contained the majority of aragonite followed by vaterite and calcite polymorphs. The thermal stability of different types of $CaCO_3$ was also evaluated using thermogravimetric analysis (TGA). The results demonstrated the components in $CaCO_3$ comprising calcination of $CaCO_3$ crystals, sucrose and soap.

The second part was carried out to incorporate the prepared $CaCO_3$ (0, 5, 10, 20, 40, to 60 phr.) in NR latex. It was found that the untreated and treated vaterite $CaCO_3$ were stable in the NR latex medium. Furthermore, the polymorphs of the untreated and treated bundle-liked and fiber-shaped $CaCO_3$ were also stable in their forms when they were added to NR latex. The mechanical properties of NR/$CaCO_3$ included tensile strength, elongation at break, tear strength, and hardness Shore A. It was found that the tensile strength of NR/$CaCO_3$ composites increased when $CaCO_3$ loading was increased. The tensile strength of NR improved from 22.68 ± 2.22 MPa of neat NR up to 23.94 ± 0.97 MPa when untreated spherical $CaCO_3$ powders (20 phr) were added, and to 25.28 ± 0.80 MPa of treated spherical $CaCO_3$ (20 phr) filled NR. The maximum tensile strength of NR/untreated bundle-liked $CaCO_3$ was 30.59 ± 3.50 MPa at 40 phr of loading while 31.51 ± 1.02 MPa of NR/treated bundle-liked $CaCO_3$ at filler loading 20 phr was obtained. The treated $CaCO_3$-filled NR vulcanizates gave higher tensile strength than the untreated ones. This was caused by better compatibility of filler dispersion between the hydrophobicity of treated $CaCO_3$ and hydrophobic property of NR. As a result, it was found that the NR filled with untreated fiber $CaCO_3$ particle provided the highest tensile strength of 31.66 ± 1.80 MPa at 10 phr of filler loading, over other types of $CaCO_3$. The nanoparticle, large surface area, and high aspect ratio of fiber/ long nano wired of $CaCO_3$ enhanced the interfacial adhesion between $CaCO_3$ and NR matrix which could transfer stress from rubber to filler effectively during stretching. This resulted in the reinforcing efficacy of the fiber $CaCO_3$. At high filler loading (> 20 phr), the agglomeration of $CaCO_3$ occurred, resulting in the appearance of voids and reducing the tensile strength of the composites. It was interesting to find that the tensile strengths of NR/commercial $CaCO_3$ consisting of NCC, 9QQ, and 4QC composites were lower than NR incorporated with bundle-liked and fiber-shaped $CaCO_3$ with and without $CaCO_3$ surface treatment. The commercial $CaCO_3$-filled NR vulcanizates resulted in slightly higher tear strength than NR/synthesized $CaCO_3$ powders in this work. The thermal stability profiles of NR/$CaCO_3$ composites from TGA results revealed that $CaCO_3$ powders can improve the thermal resistance of rubber composites. Moreover, the mechanical properties of NR/N330 carbon black (CB) composites were also compared to those of NR/$CaCO_3$ composites. The highest tensile strength of NR/N330 composite was 33.03 ± 0.30 MPa at 20 phr loading. This result was comparable to the NR/fiber $CaCO_3$ at 10 phr filler loading. This finding demonstrated that a lower loading of $CaCO_3$ than N330 could effectively reinforce the NR composites. Consequently, the prepared $CaCO_3$ powders have the potential to broaden their application not only as diluents or additives but also as reinforcing agents.